A High Performance, Microchannel Plate Based, Photon Counting Detector For Space Use

Michael Leonard Edgar

Mullard Space Science Laboratory
Department of Physics and Astronomy
University College London

Submitted to the University of London
for the degree of Doctor of Philosophy

February, 1993

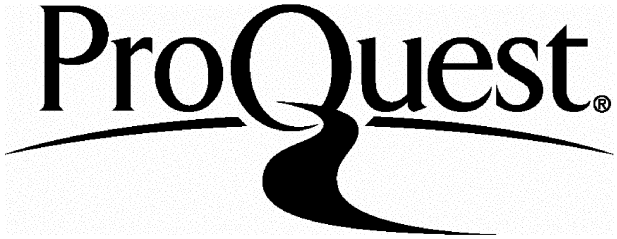

Abstract

This thesis describes the development of a microchannel plate (MCP) based photon counting detector using the Spiral Anode (SPAN) as a readout. This detector was one of two being evaluated for use in the Optical Monitor for ESA's X-ray Multi Mirror satellite. Throughout this thesis, where possible, the underlying physical processes, particularly those of the MCP, have been identified and studied separately.

The first chapter is an introduction to photon counting detectors and includes a review of the various readouts used with MCPs. The second chapter provides a more detailed review and analysis of cyclic, continuous-electrode, charge-division readouts, of which SPAN is an example.

The next two chapters describe the technique for measuring the radial distribution of the MCP charge cloud, which can significantly affect detector imaging performance . Results are presented for various operating conditions. The distribution consists of two parts and the size is dependent on the operating voltages of the MCP stack.

The fifth and sixth chapters describe the procedure for operating a SPAN readout and the decoding necessary for converting the ADC readings into a two dimensional coordinate. Various methods are described and their limitations evaluated. The cause of problems associated with the SPAN readout, such as "ghosting" and fixed patterning and methods of reducing them are discussed in detail. Results are presented which demonstrate the performance of the anode.

The seventh chapter discusses and evaluates the interaction between channels in MCPs and the long range effects an active pore has on the surrounding quiescent pores. This represents the first time that these effects have been measured. The importance of this phenomenon for imaging detectors is discussed and possible mechanisms evaluated.

The last chapter presents the conclusions of this work and discusses the suitability of SPAN detectors for use on satellites.

To my parents,
without whom I'd only have had two chances;
Buckley's and none.

And ye shall hear of wars and rumours of wars, see that you be not troubled, for all of these things must come to pass, but the end is not yet.
For nation shall rise against nation and kingdom against kingdom: and there shall be famines, and pestilences, and earthquakes in diverse places.
All these are the begining of sorrows.
Then shall they deliver you up to be afflicted, and shall kill you:...
And then shall many be offended, and shall betray one another, and shall hate one another.
And many false propets shall rise, and shall decieve many.
And because iniquity shall abound, the love of many shall wax cold.
But he that shall endure unto the end, the same shall be saved.

Matthew 24 : 6-13

Contents

List of Figures

List of Tables

Chapter 1

Review of Two Dimensional Photon Counting Detectors

Figure 1.1 summarizes the performance characteristics of various two dimensional, photon counting, X-ray detectors. Rear illuminated charge coupled devices (CCDs) can be used directly as imaging, X-ray, photon counting detectors without the need of any photon conversion or electron multiplying device. The microcalorimeter also detects an X-ray photon directly, by detecting its thermal energy in a similar manner to an infrared bolometer. At present, these detectors can only be used for photon energies greater than $\sim$ 500 eV (Culhane, 1992 and references therein).

In the most widely used types of photon counting detectors, the incoming photon produces at least one electron by either interacting with a gas, in gas proportional counters, or a photocathode in photomultipliers. In the later case, this photo-electron is then multiplied by a cascade of processes producing secondary electrons. If the gain is $\approx 10^6\ e^-$ or larger, a current or light pulse large enough to be measured individually is produced when the secondary electrons are collected by an anode or phosphor.

In the position sensitive gas-filled proportional counter (PSPC), electron multiplication takes place in the gas, such as either a Xe/CH_4 or Ar/CH_4 mixture, in the region of a high electric field near an anode wire. The generation of a cloud of positive ions near the anode wire induces charge on one or two cathodes which allows the centre of gravity of the resulting charge cloud to be determined.

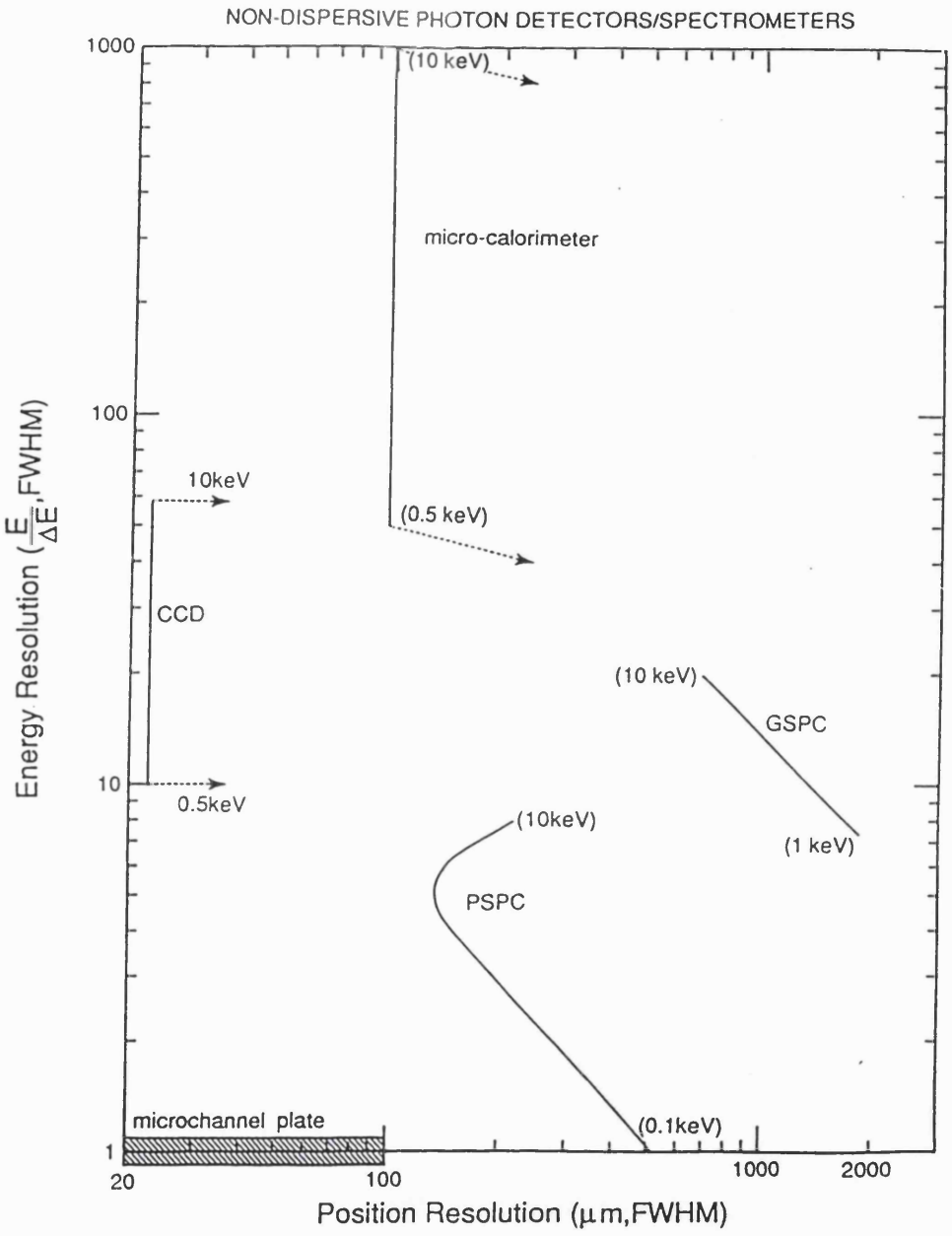

Figure 1.1: Spatial and energy resolution for various two dimensional photon counters. From Culhane (1992).

The total amount of charge collected on the cathodes is proportional to the incident photon's energy. The cathodes are configured as either a crossed wire grid, a wire grid combined with a one dimensional, planar cathode readout such as the "backgammon" or a two dimensional, electrode readout such as the "Wedge and Strip". These and other types of position readout are discussed below.

The gas scintillation proportional counter (GSPC), avoids the need for electron multiplication. Instead photo-electrons are created in a noble gas and pass into a region where the electric field is high enough to cause gas scintillation, producing UV photons, but the gas is not ionized. The number of photons is proportional to the number of photo-electrons and therefore, incident photon energy. By omitting the electron avalanche an improvement in energy resolution of a factor ~ 2 can be achieved. Position is determined by using an array of photomultiplier tubes or a two dimensional photomultiplier (Smith & Bavdaz, 1992)

The most widely used secondary electron multiplier in image intensifiers are the discrete dynode chain photomultiplier tubes (PMTs). Discrete dynode PMTs can produce sufficient gain. However, only mesh dynode PMTs can provide two dimensional images and the resolution is limited to approximately 300 μm FWHM (Kume *et al.*, 1986).

Since about the mid 1960s, position-sensitive photomultipliers have been used in photon counting detectors for astronomical applications. In these detectors, sometimes referred to as first generation image intensifiers, the photo-electrons from a photocathode on the input window, are accelerated by a high voltage, approximately 10 kV, and then electrostatically or magnetically focussed onto a phosphor screen (Baum, 1966). The energy gained by the electrons' traversal of the electric field is converted to a photon pulse. If the phosphor is "sandwiched" together with another photocathode, the photon pulse will produce more photo-electrons. Each sandwich can produce an electron gain of $\approx$ 100 for a 10 kV potential (Randall, 1966).

Gains of up to 10^6 can be obtained by cascading four such stages together, requiring 40 kV. The original Imaging Photon Counting System (IPCS), used on several ground based telescopes and as the Faint Object Camera on the Hubble Space telescope was a 4 stage tube, using a TV camera as the position readout for the optical pulses.

Microchannel plate (MCP) based devices are similar in concept, with the four stage tube being replaced by a MCP electron multiplier. These devices are discussed in detail in the next section.

The gas-filled detectors' spatial resolutions are ultimately limited by the diffusion

of the photo-electrons whereas the other detectors' ultimate resolutions are dependent on their manufacturing processes. Although gas-filled detectors only have moderate spatial resolutions, Figure 1.1, they are widely used because of their good energy resolution. The photomultipliers offer no intrinsic energy resolution, however only the CCD has a spatial resolution comparable with the MCP. Also, only image intensifiers are sensitive to photons with energies $<$ 100 eV and so can be used for EUV and UV/Optical detectors as well as X-rays.

1.1 Microchannel Plate, Secondary Electron Multipliers

An MCP is a secondary electron multiplier consisting of an array of millions of glass tubes, called channels or pores, fused into a disk about 1 mm thick and typically 25 mm diameter. A typical MCP would have cylindrical pores with an internal diameter of 12.5 μm. The pores are hexagonally packed with a spacing of approximately 15 μm. Figure 1.2 shows a schematic representation of an MCP and Table 1.1 shows the wide range of the properties of a selection of MCPs available from just one manufacturer.

Washington *et al.* (1971) describe the manufacturing process of MCPs. The material consists basically of silica glass into which is incorporated Pb and Bi oxides which are then reduced to their metallic form by baking in a hydrogen atmosphere. This produces a high resistance surface layer. Alkali ions are also introduced into the glass to give it the required malleability and annealing temperatures. The electrical properties of metal oxide glasses have been discussed in detail by Trap (1971).

Hill (1976) has carried out Auger analysis on the surface layer of this type of bulk glass that has been treated in the same manner as MCPs during manufacture. Auger analysis can only examine approximately the top nanometre of a surface but by ablating the surface with an argon ion beam, the composition of the material with increasing depth could be probed. Figure 1.3 shows this element composition as a function of depth. The surface region has a high concentration of K but almost no Pb or Bi. The C is a surface contaminant and other contaminants such as S and Ca were also present. The Pb and Bi do not appear until about 10 to 20 nm below the surface. During heat treatment, K is thought to occupy positions at the surface that would normally be occupied by Pb and Bi.

The resistivity was also measured with varying depth. The conducting layer was located from 10 to 20 nm below the surface, which correlated with the appearance of Pb and

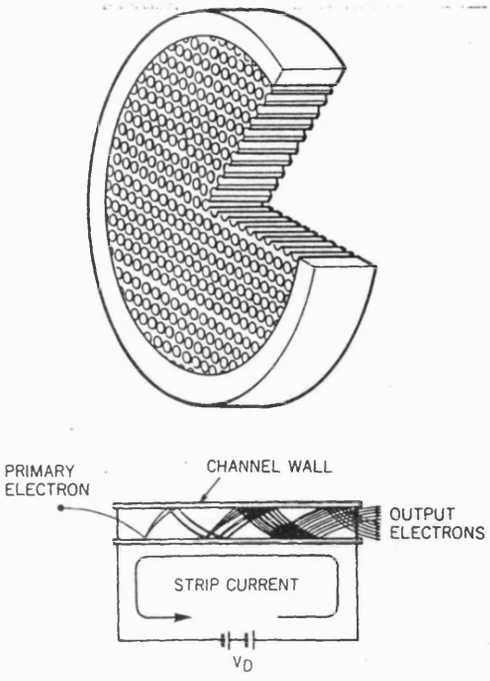

Figure 1.2: Schematic diagram of an MCP.

From Hamamatsu (1987).

Disk Diameter	A	(mm)	18		24.9			32.8			38.5		50		86.7	114								
Electrode Diameter	B	(mm)	17		23.9			31.8			37.5		49		84.7	112								
Effective Diameter	C	(mm)	14.5		20			27			32		42		77	105								
Disk Thickness	D	(mm)	0.48	0.80	0.41	0.48	0.80	0.41	0.48	0.80	0.48	0.80	0.48	0.80	1.00									
Channel Diameter		(μm)	12	20	10	12	20	10	12	20	12	20	12	20	25									
Channel Pitch		(μm)	15	25	12	15	25	12	15	25	15	25	15	25	31									
Bias Angle		θ (°)	8		5	5,8,15	8	12			8		5, 8		8									
Open Area Ratio		(%)	57																					
Electrode Material			Inconel or Ni-Cr																					

ELECTRICAL CHARACTERISTICS

(Applied Voltage: 1000V, Vacuum: 1 x 10^{-4} torr (1.3 x 10^{-4} Pa), Ambient Temperature: 25°C)

Current Gain		More than 10^4					
Plate Resistance	(MΩ)	100~1000	100~700	30~300	20~300	10~200	10~100	5~50
Dark Current	(A/cm^2)	Less than 5 x 10^{-13}						
Max. Linear Output Signal		Up to 7% of the strip current ®						

Table 1.1: Properties of various MCPs.

From Hamamatsu (1987).

Bi. This conducting layer is approximately 200 nm deep. The surface layer consists basically of silica and the resistance of this layer is approximately twice that of the conducting layer.

Figure 1.4 shows the secondary emission coefficient, δ, for the reduced glass material. The shape of the curve is characteristic for all materials. As primary electron energy increases, more energy is available to produce secondary electrons within the escape depth of the material. However, if the primary energy is increased too much, secondary electrons are produced much deeper in the material so that many do not have enough energy to escape.

Hill (1976) has calculated that the escape depth of the reduced material is approximately 3.3 nm. Therefore, the secondary electrons come from the layer that consists mainly of silica. Also, the emissive layer is separated from the conducting layer by a high resistance region several nanometers thick.

When the interior of a channel is reduced, the channel surface behaves as a continuous dynode and the channel wall contains the conducting layer, through which current flows, providing electrons to the thin emissive layer at the channel surface. The conducting layer has quite high resistance so the channel wall behaves as a dynode resistance chain.

The two faces of the MCP are coated with an evaporated layer of conductor such as Nichrome or Inconel. These conductive layers serve as the input and output electrodes and connect all of the pores in parallel. The total resistance between the two electrodes is the parallel combination of the resistance for each channel and is of the order of 100 MΩ.

MCPs are high gain devices which are physically small and require relatively small voltages, compared to first generation image intensifiers, and power, $\sim$ 10 mW. These factors make them particularly well suited for space use apart from their fragility and cleanliness requirements. Spatial resolution is limited only by pore spacing, which has been realized by some readouts (see below), and as they can be used for photon counting they have good temporal resolution. As well as electrons, MCPs are sensitive to ions, UV and X-rays. Thick MCPs, $\sim$ 5 mm, have good have good quantum efficiencies (QE) for γ-rays (Wiza, 1979), possibly up to 511 kV (McKee *et al.*, 1991). They can be provided in almost any shape in sizes up to 10 $\times$ 10 cm, with square pores (Fraser *et al.*, 1991a) and with a spherical shape (Siegmund *et al.*, 1990). MCPs have also been operated at temperatures as low as 14 K (Schecker *et al.*, 1992). This versatility has led to the extensive use of MCPs in a wide variety of applications. They have even been used as passive elements in a large aperture collimator for an X-ray spectrometer (Turner *et al.*, 1981 and Yamaguchi *et al.*, 1987) and

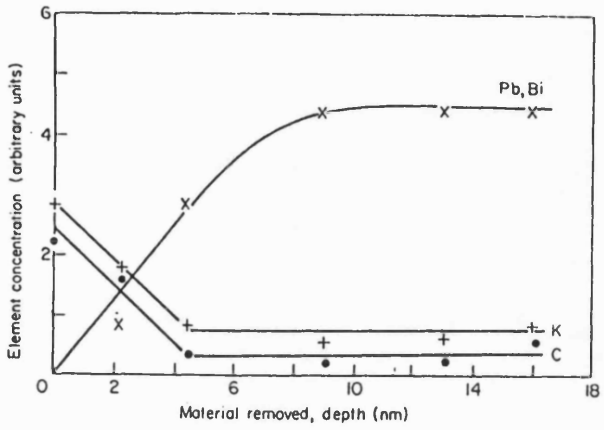

Figure 1.3: The variation of element composition with depth in the glass material after reduction.
From Hill (1976).

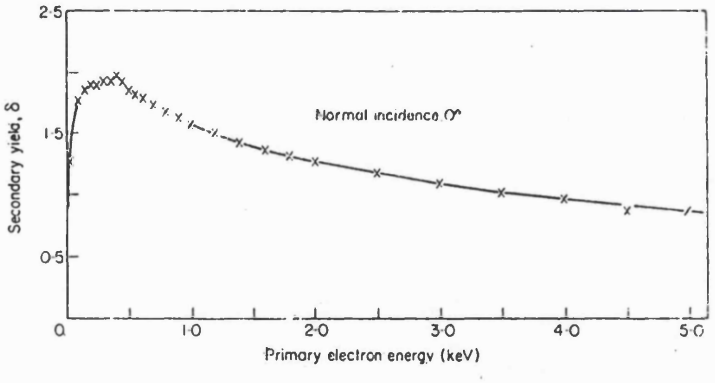

Figure 1.4: The variation in the yield of secondary electrons with varying primary electron energy for the glass after reduction.
From Hill (1976).

theoretical studies indicate that they could be used to focus hard X-rays with an efficiency of up to 48 % (Wilkins *et al.*, 1989 and Chapman *et al.*, 1991).

1.1.1 Electron Multiplication in MCPs

If we take each pore in isolation it behaves in the same manner as a Channel Electron Multiplier (CEM) (Goodrich & Wiley, 1962 and Adams & Manley, 1966). However, this is an approximation as it has been found that individual pores do interact with their neighbours. In the following discussion, only isolated channels are described. The interaction between pores will be discussed in detail in Chapter 7.

When a voltage, V_D, of the order of 1 kV, is applied to the end electrodes, an electric field, E, is established which is parallel to the pore axis. The strip current, i_s, is given by

$$i_s = V_D/R_{ch} \quad , \tag{1.1}$$

where R_{ch} is the resistance of a single channel. When an electron collides with the channel wall, secondary electrons may be produced. These electrons follow a parabolic trajectory, defined by their initial energy, eV, and E, and before colliding with the channel wall again, see Figure 1.2.

Electron gain is a complicated cascade of statistical processes, which produce a wide variation in the number of electrons in individual pulses. The magnitude of the gain also depends on the energy and angle of incidence of the incoming particle. It can only be properly described statistically, e.g. Lombard & Martin (1961) and Guest (1971). In the following discussion only the average behaviour will be considered.

The average time t and distance S between collisions for a straight channel with diameter, d, is given by

$$t = d\sqrt{\frac{m}{2eV_n}} \quad , \tag{1.2}$$

$$S = \frac{1}{2}E\frac{e}{m}t^2 \quad , \tag{1.3}$$

where we assume that the electrons have been emitted normally from the wall with energy V_n. The electrons will collide with the wall with an energy

$$V_c = ES \quad , \tag{1.4}$$

$$= \frac{V_D^2}{4V_n\alpha^2} \quad , \tag{1.5}$$

where α is the length to diameter ratio for the pore. MCPs with $\alpha = 40$ are often referred to as "single thickness plates" while if $\alpha = 80$ they are called "double thickness plates"

There will be n collisions along the length of the pore where

$$n = \frac{\alpha d}{S} \quad . \tag{1.6}$$

As there are a finite number of wall collisions with approximately constant separation, continuous dynode multipliers can be described as a conventional discrete dynode secondary electron multiplier (Goodrich & Wiley, 1961, Adams & Manley, 1966 and Eberhardt, 1979, 1981). This discrete separation is not seen in practice, due to the statistical nature of multiplication and the variable penetration depths of incident particles. One important consequence of this model is that most of the electrons in the output pulse will originate from the same region of the channel, the last dynode.

The number of secondary electrons produced in each collision is dependent on the change in voltage and δ

$$\delta = \sqrt{k\Delta V} \quad , \tag{1.7}$$

$$= \frac{Ed}{2}\sqrt{\frac{k}{V_n}} \quad , \tag{1.8}$$

where k is a constant. Guest (1988) has determined that this is a good approximation of the low energy collision typical of multiplication processes.

The increase in current along a finite length, Δl of channel is given by

$$\Delta i = i(\delta - 1)\frac{\Delta l}{S} \quad , \tag{1.9}$$

and the overall gain G is given by

$$G = \frac{i_f}{i_0} \quad , \tag{1.10}$$

$$= e^{(\frac{4V_n(\delta-1)\alpha^2}{V_D})} \quad , \tag{1.11}$$

where i_0 and i_f are the initial and final currents respectively and G is sufficiently small (Guest, 1988).

Adams & Manley (1966) and Loty (1971) have described models in which increasing E will increase the number of electrons emitted per collision by Equation 1.8 but by Equation 1.3, the number of dynodes will be reduced. Therefore, for a given length, as the

applied voltage increases, the gain will rise to a maximum and then reduce, even if saturation, see Section 1.1.3, is not taken into account. However, analysis and measurements by Gear (1971) and Eberhardt (1979) show that the gain increases monotonically with a linear relation between log G and log V_d until saturation occurs, see Figure 1.5.

Equation 1.8 can be expressed in terms of α as

$$\delta = \frac{V_D}{2\alpha}\sqrt{\frac{k}{V_n}} \quad . \tag{1.12}$$

Substituting this expression into the expression for gain, Equation 1.11, and differentiating with respect to α

$$\frac{dG}{d\alpha} = 4V_n\left(\frac{1}{2}\sqrt{\frac{k}{V_n}} - \frac{2\alpha}{V_D}\right)e^{4V_n\alpha\left(\frac{1}{2}\sqrt{\frac{k}{V_n}} - \frac{\alpha}{V_D}\right)} \quad . \tag{1.13}$$

Therefore, gain is at a maximum when

$$\frac{V_D}{\alpha} = 4\sqrt{\frac{V_n}{k}} \quad . \tag{1.14}$$

Simulations and experimental measurements by Guest (1971, 1988) show that the gain is a maximum where the normalized voltage, W, the potential difference between two points separated by an axial distance d is

$$W = \frac{V_D}{\alpha} \quad , \tag{1.15}$$

$$\approx 22 \quad . \tag{1.16}$$

Assuming that $V_n \approx 1$ eV this implies $k \approx 0.033$. Substituting these values into Equation 1.12, implies that the maximum gain occurs when approximately 2 electrons are emitted per collision. Unity gain occurs when $W \approx 11$. Figure 1.6 shows the universal gain curve for a series of channels of varying α, W and V_D derived from a simulation. The input parameters have been kept constant as a 2 KeV electron with an angle of incidence of 13°. The simulation allows for the statistical nature of the multiplication process and therefore, indicates small gains for $W \approx 11$. This figure and Equation 1.14 show that the most important parameter for describing the gain performance of a straight channel is α.

1.1.2 Ion Feedback

The probability that electron collisions with gas molecules will produce positive ions, increases with gain. These molecules may either be from residual gas or from gas

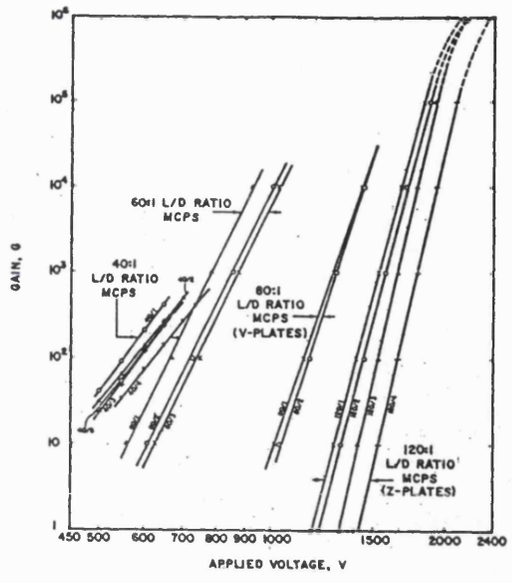

Figure 1.5: The relation between gain and V_D.
From Eberhardt (1979).

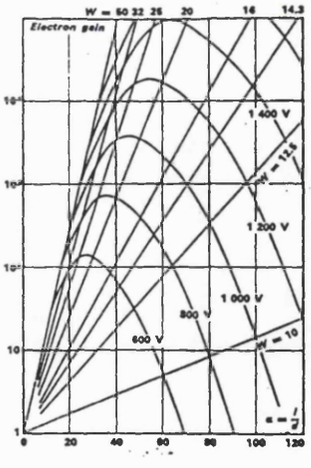

Figure 1.6: Universal gain curve of an MCP.
From Guest (1971).

desorbed from the channel wall during electron bombardment. Adams & Manley (1966) have estimated that the number of ions produced, N, is

$$N = 6n_e p \quad , \tag{1.17}$$

where n_e is the number of electrons in a region of width w at a pressure p Torr.

These ions can collide with the channel walls near the channel input producing another pulse. For sealed tubes (see below) ions can hit the photocathode, poisoning it and drastically reducing the tube lifetime (Oba & Rehak, 1981 and Norton *et al.*, 1991). They may also produce secondary electrons from the photocathode generating another event in another channel for a MCP. In this case, there will be two events occurring within nanoseconds of each other, which will be treated as simultaneous and will produce errors in position encoding in many readouts. These extra events could result in a regenerative feedback situation, which in extreme cases could lead to the destruction of some channels. The need to avoid ion feedback limits the maximum electron gain that a single straight channel can supply to $\sim 10^5$ (Wiza, 1979).

Ion feedback can be overcome in CEMs by bending or curving the tubes as the heavy ions have much longer trajectories than the secondary electrons. MCPs can also be manufactured with curved channels, a "C plate", (Timothy, 1974). The gain expression for a curved channel is different to that for a straight channel due to the effect of wall curvature on the electron trajectories (Adams & Manley, 1966). Whereas α is the parameter that determines the applied voltage/gain characteristics of a straight channel, the most important parameter for a curved channel is the included angle of the curve. There is a limit to the maximum included angle practicable for curved channels in MCPs which limits the gain to $\approx 10^6\ e^-$ for a C plate (Wiza, 1979)

Another widely used method is to use two or more plates with straight channels and with the pores inclined at an angle to the normal to the MCP face. Colson *et al.* (1973) demonstrated that if these bias angles point in opposite directions, the shape of the effective channel is bent, reducing ion feedback. They called this arrangement the Chevron Shaped Electron Multiplier (CSEM). It is sometimes called a two stage detector, "V plate" or most commonly, the "chevron pair", see Figure 1.7. The process is often extended to three MCP stages, the "Z stack". An example of a Z stack configuration can be seen in the MCP stack configuration in the drawing of the sealed tube, Figure 1.15. Often the plates are separated by a gap of approximately 100 μm. This gap allows the electron cloud from

the first MCP to expand and so fire several pores in the bottom plate, increasing the overall gain. The inter-plate gap is discussed in Section 4.4.5. Using these configurations, gains of $10^7 - 10^8$ e^- are obtainable with straight plates.

1.1.3 Saturation

Due to the statistical nature of the gain process a pulse height distribution (PHD) is produced. At low gains, the PHD has a negative exponential shape. However, as gains increase the PHD is no longer a quasi-exponential but a pseudo-Gaussian (see Figure 1.8). This effect is known as saturation.

There are two likely processes that can cause saturation.

1. The space charge of electrons in the channel is sufficient to drive secondaries back into the wall before they can acquire enough energy from the electric field to produce more secondaries (Bryant & Johnstone, 1965).

2. There is a limit on the maximum rate at which electrons can be supplied through the channel wall to the emissive layer. If more electrons are extracted than can be supplied a positive charge will build up. As the wall resistance is very high, the time constant is of the order of milliseconds while the total length of the electron pulse is of the order of 10 ps. Therefore, the positive charge cannot be neutralized during the pulse (Evans, 1965).

Experiment and simulation have determined that the dominant process in saturation is space charge for curved channels (Adams & Manley, 1966 and Schmidt & Hendee, 1966) and wall charging for straight channels (Adams & Manley, 1966, Loty, 1979 and Guest, 1988).

At low enough gains, the electric field along the pore is uniform. As gain increases and saturation begins, the potential distribution along the length of the pore changes. As most electrons are extracted from the bottom of the channel, the potential of the bottom is raised producing a low field region. This reduces the energy of the electrons colliding with the wall in this region reducing δ. As shown in Figure 1.9, E decreases near the end of the pore but increases at the start. At some point, E reaches a value that corresponds to unity incremental gain. Also, the positive charge on the surface can reduce δ directly, as some of the lower energy secondary electrons cannot escape from the surface, and a high enough charge can produce a region with close to unity gain (Hill, 1976), i.e. $\delta \approx 1$, see Figure 1.10.

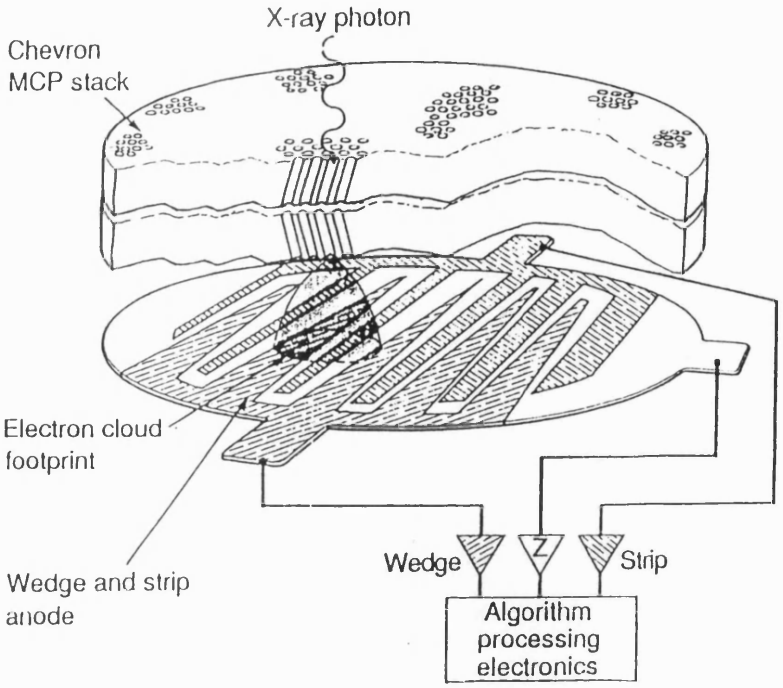

Figure 1.7: Schematic diagram of a Chevron pair MCP configuration combined with a Wedge and Strip Anode.
The Wedge and Strip Anode is discussed in Section 1.3.2.

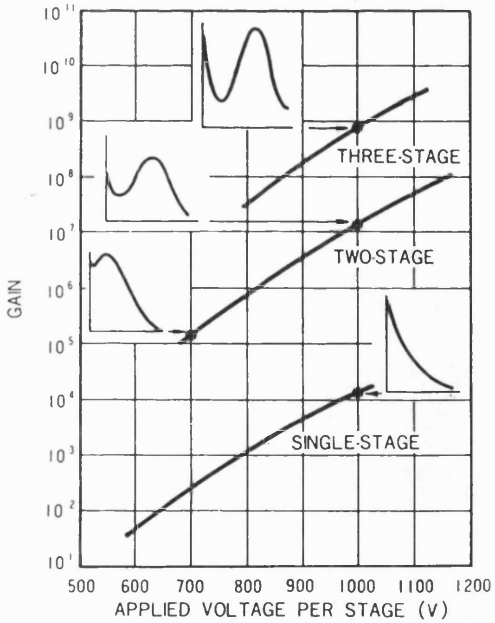

Figure 1.8: PHDs demonstrating different levels of saturation.
From Hamamatsu (1987).

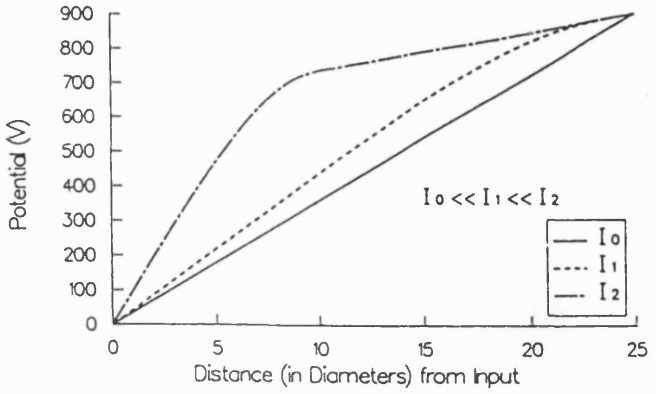

Figure 1.9: The variation of the potential within a channel with increasing saturation. The values I_0, I_1 and I_2 refer to increasing input current and distance along the channel is measured in pore diameters. From Guest (1988).

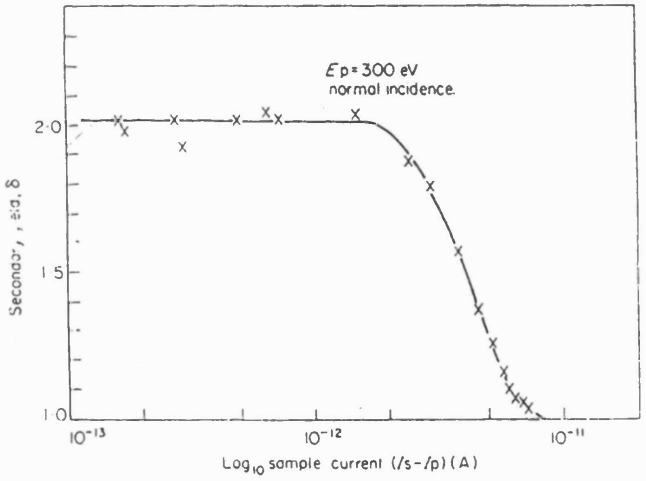

Figure 1.10: The reduction of the secondary emission coefficient, δ, with surface charging for reduced lead glass.
I_s and I_p refer to the current due to the secondary electrons and the primary electron beam, respectively. From Hill (1976).

Increasing V_D increases saturation and moves the region of unity gain further up the pore, reducing the length of pore that contributes effectively to gain. Eventually, the region of unity gain extends along most of the length of the channel. The region near the input then has a much larger E than in the unsaturated case and is the only region making an effective contribution to the gain.

Saturated PHDs are a problem for image intensifiers being used in the proportional mode, in which the output current is proportional to the input current. Saturation places an upper limit on the output current and therefore output image intensity. In order to maintain proportionality, the MCPs are operated in the low gain regime with a negative exponential PHD.

In a photon-counting detector, it is only necessary to obtain one pulse per input photon. The pulse amplitude is not important, so long as it is above a threshold defined by the signal to noise ratio (SNR) required by the position readout. In practice, a lower level discriminator (LLD) is used to reject events lying below that treshold. A PHD with the largest percentage of points lying above the LLD is necessary to ensure the best photometric linearity of the detector. It can be seen from the PHDs in Figure 1.8 that the higher the saturation, the higher the percentage of points with large amplitudes. Therefore, high saturations are desirable in photon counting detectors.

Saturated PHDs are described by two parameters, the modal gain, i.e. the gain which represents the mode of the PHD and the gain resolution or saturation, the ratio of the PHD FWHM to the modal gain.

1.1.4 Gain Depression with Count Rate

As described above, the neutralization of the positive wall charge takes a finite time, of the order of milliseconds, due to the time constant of the channel. If another cascade occurs in the channel before the wall charge is neutralized, the electric field will be still be reduced at the bottom of the channel and this region will not make an effective contribution to the gain. This depresses the modal gain (Loty, 1971, Timothy, 1981, Neischmidt *et al.*, 1982, Siegmund *et al.*, 1985), and moves the PHD to lower values. Zombeck & Fraser, (1991) have presented PHDs for various count rates, Figure 1.11.

As the local count rate increases, the counting linearity of the detector degrades as larger and larger proportions of the PHD fall below the LLD. Eventually, at a high enough

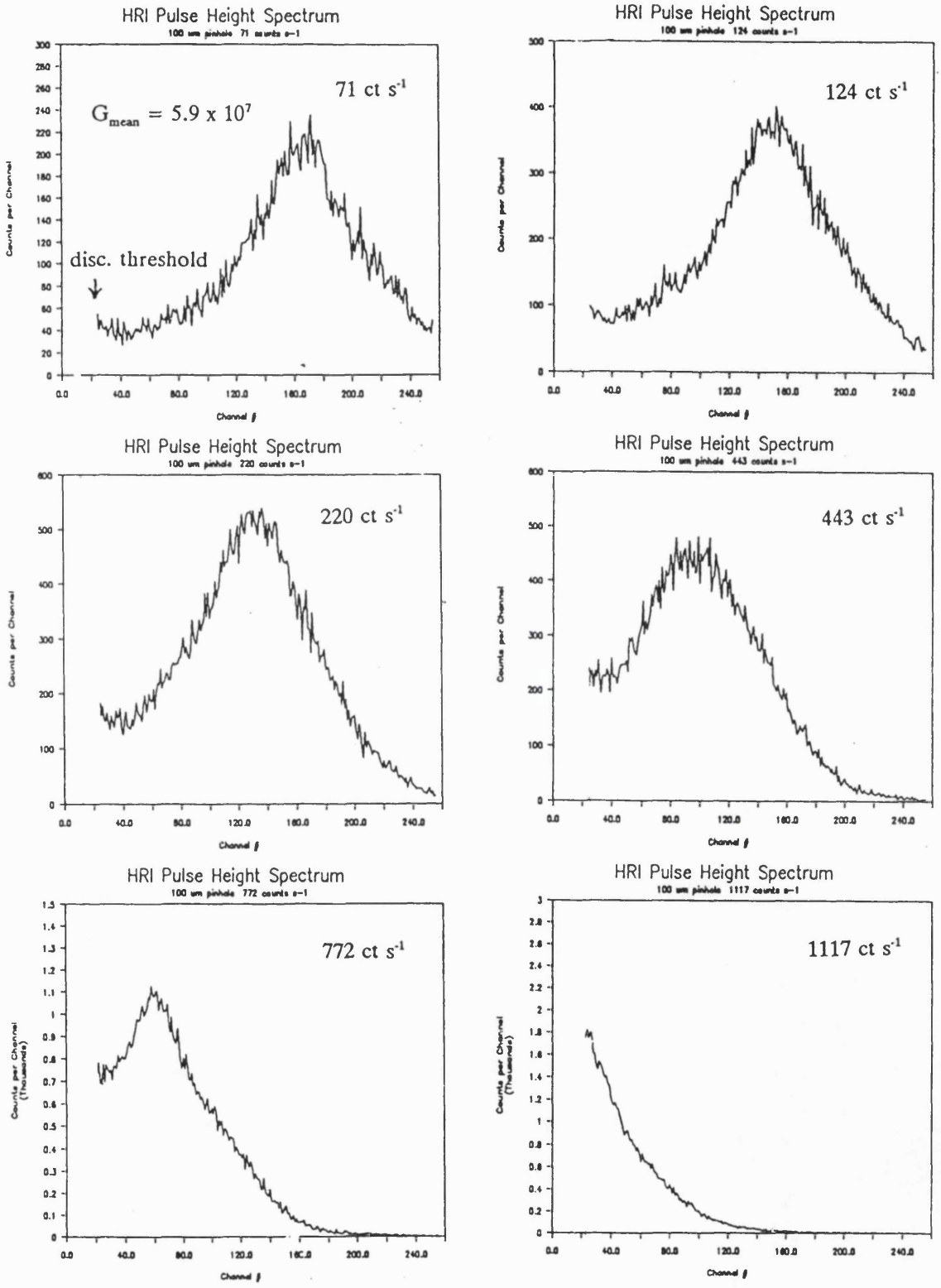

Figure 1.11: PHDs exhibiting various degrees of gain depression with variation of count rate.

From Zombeck & Fraser (1991).

local count rate, most of the PHD will fall below the LLD, effectively paralysing the pore. This process is the ultimate limit on the point source count rates for all MCP detectors. Most position readouts can achieve point source count rates at this limit. In MCPs with an individual channel resistance, R_{ch}, of $\approx 10^{15}$ Ω, significant gain depression can occur at count rates as low as ≈ 1 Hz.pore^{-1}, (Fraser *et al.*, 1991b and Nartallo Garcia, 1990), see Figure 1.12.

Note that in the Figure 1.11 the absolute width of the PHD does not vary significantly as the gain is depressed. This is also shown in the saturation graph in Figure 1.12. Saturation is a relative measurement of the PHD width with respect to the modal gain. The variation in saturation in this diagram is due in the main part to the reduction in modal gain rather than an increase in the absolute width of the PHD.

As the count rate is limited by the time constant of the pores, the photometric linearity can be increased by reducing the resistance of the pores. Evaluation of lower resistance MCPs have shown that countrates of $\approx$ 40 and 500 Hz.pore^{-1} are sustainable with minimal gain depression with $R_{ch} \approx 10^{13}$ and 10^{12} Ω, respectively, (Siegmund *et al.*, 1991 and Slater & Timothy, 1991).

However, R_{ch} cannot be made arbitrarily small and these values represent the approximate limit for conventional, stable operation of MCPs. The resistance of the channels has a negative temperature coefficient and Joule heating by the strip current running through the walls will raise temperatures. Thermal runaway will occur for power densities above 0.1 W.cm^{-2}. A 25 mm diameter plate will be unstable with a resistance less than roughly 5 MΩ. This corresponds to a limiting count rate of several times 10^8 Hz.cm^{-2} (Feller, 1991). Assuming that the plate has 12.5 μm pores on 15 μm centres, there are $\approx 5 \times 10^5$ pores.cm^{-2}. This limiting count rate corresponds to several hundred Hz.pore^{-1} for $R_{ch} \approx 10^{13}$ Ω.

In conventional MCP mounts, almost all the heat must be removed radiatively as there is poor lateral conduction through the plate edges. Feller (1991) found that by connecting one MCP face directly to a heat sink, Joule heating was removed far more efficiently by conduction and power dissipations of up to 3 W.cm^{-2} could be maintained. This allowed the continuous, stable use of a 25 mm, 750 kΩ, i.e $R_{ch} \approx 10^{12}$ Ω, plate at 1.7 kV with a maximum output rate of 12 kHz.pore^{-1}. At a voltage above 1.75 kV, the plate once more became thermally unstable.

Although conductive cooling increases the MCP point source count rate perfor-

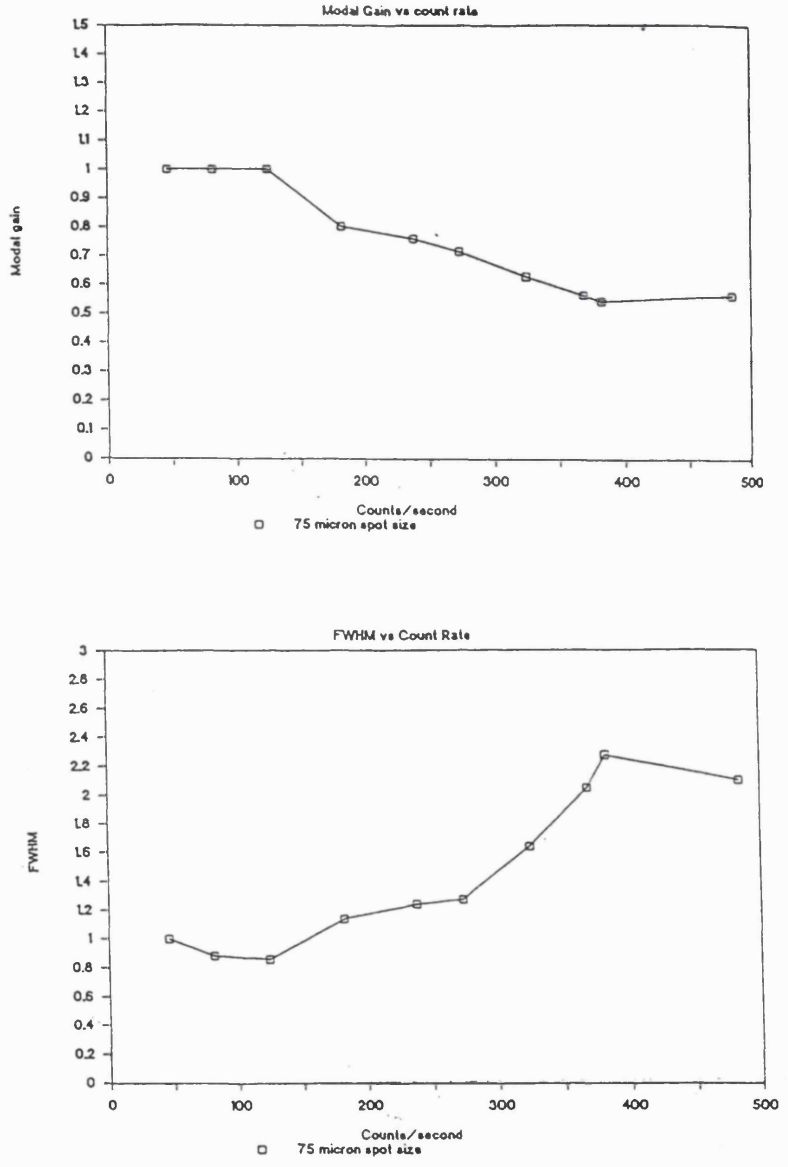

Figure 1.12: Gain depression with count rate with high resistance plates.
The top and bottom figure show the variation of relative modal gain and saturation with count rate, respectively. The MCPs used were the same as those used in Chapters 5 to 7. Data from Nartallo Garcia (1990).

mance dramatically, it requires a direct connection to the MCP face. However, it is not applicable to large format, high resolution imagers as all of the current readouts that produce this performance require a gap between the MCP and the readout of at least 100 μm and in some cases millimetres, see Section 1.3.2.

1.2 MCP Based Photomultipliers

1.2.1 EUV and X-Ray Photomultipliers

The quantum efficiency (QE) of an uncoated MCP in the UV is shown in Figure 1.13. The QE at these and soft X ray wavelengths can be enhanced by depositing a photocathode, for example CsI or MgF_2 directly onto the MCP face. The sensitivity of an MCP can also be extended into the hard X ray region by using a 100 μm Au photocathode mounted directly onto the front of an MCP. Detected quantum efficiencies of $\approx$ 0.2 % have been achieved for 1 MeV X-rays (Veaux *et al.*, 1991).

In operation, the whole MCP stack and the readout are open to vacuum, so these detectors are often called open-window detectors. These types of detectors have flown on many X-ray/EUV satellites, e.g. Einstein, EXOSAT and ROSAT (Zombeck & Fraser, 1991 and references therein) and are to be used on the Extreme Ultraviolet Explorer (Siegmund *et al.*, 1985) and Solar and Heliospheric Observatory (SOHO) (Breeveld *et al.*, 1992a) satellites.

1.2.2 Optical/UV Photomultipliers

For wavelengths from about 200 to 600 nm, the QE of a bare MCP falls off rapidly, so a photocathode is necessary. A typical photocathode for these wavelengths is the multialkali S20, see Figure 1.14.

There are a number of practical reasons why these photocathodes are not deposited directly onto the MCP surface. The photo-electrons liberated from the microchannel plate would have relatively low energies and those created other than within the channels would probably be lost. Also, during the deposition of the photocathode it might prove impossible to prevent a slight separation of photocathode constituents. These could end up deep inside the pores which could lead to "switched on channels".

Normally the photocathode is deposited on the surface of a UV/Optical transpar-

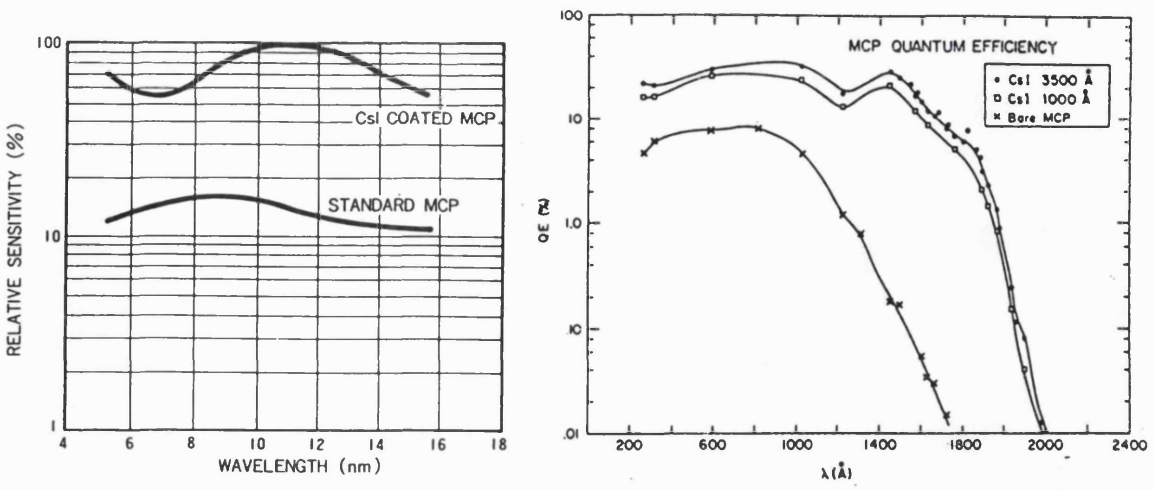

Figure 1.13: UV Quantum Efficiency of MCP material.
The left diagram is from Hamamatsu (1987) and the right figure is from Samson (1984).

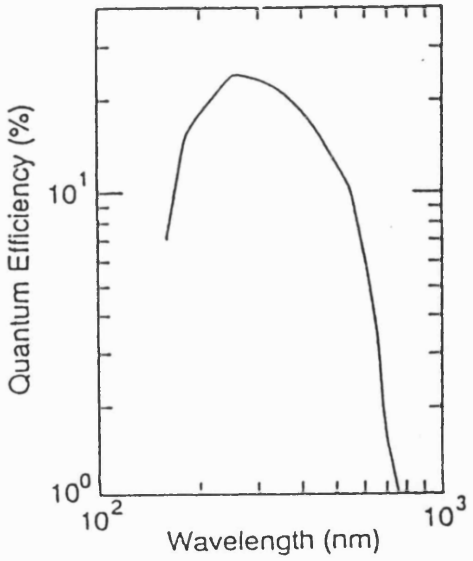

Figure 1.14: Quantum Efficiency of an S20 photocathode.

ent material, e.g. MgF_2, Sapphire or quartz, see Figure 1.15. An electric field is applied to the gap between the photocathode and the MCP, accelerating the photo-electrons towards the MCP. This process is known as proximity focussing.

The photo-electrons have a Maxwellian distribution in transverse velocities which produces a distribution of points at which the electrons are incident on the surface of the MCP. This represents the ultimate limit of resolution in a sealed tube intensifier. The point spread function (PSF) of this distribution is given by Eberhardt (1977) as

$$P(r) = P(0)e^{-r^2V/(4L^2v_r)} \quad , \tag{1.18}$$

where $P(0)$ is the peak of the PSF, r is the distance from the peak, V is the voltage applied across the gap of width L and v_r is the mean radial emission energy of the photo-electrons. As wavelength decreases, v_r increases and so the FWHM of the PSF increases. The FWHM of the PSF can be determined from this equation as

$$FWHM = 3.33L(v_r/V)^{\frac{1}{2}} \quad , \tag{1.19}$$

(Lyons, 1985).

In practice, the proximity gap is kept as small as possible and V is as large as possible to improve resolution. Figure 1.16 shows theoretical PSF FWHM curves for two gaps and various voltages over a wavelength range of 400 to 600 nm, using v_r measurements for a multi-alkali photocathode from Eberhardt (1977). The PSF for UV radiation would be higher but to date, no v_r measurements for these wavelengths have been presented in the literature. The maximum electric field strength will depend on the design of the intensifier, however, Lyons (1985) states that a maximum field strength from 1.5 to 2 $kV.mm^{-1}$ is reasonable. A proximity gap of 300 μm is the limit available in most commercial devices but a gap of 150 μm has been reported (Clampin *et al.*, 1988). Figure 1.16 shows that for a 300 μm gap, the PSF FWHM will be approximately 20 μm for all voltages. This will be value assumed for the PSF for the rest of this chapter.

Vacuums of the order of 10^{-10} torr are required to avoid poisoning of the photocathode. Therefore, the photocathode, the MCPs and often the position readout are sealed inside a leak-tight vessel. These types of detectors are referred to as "closed window" detectors or "sealed tubes".

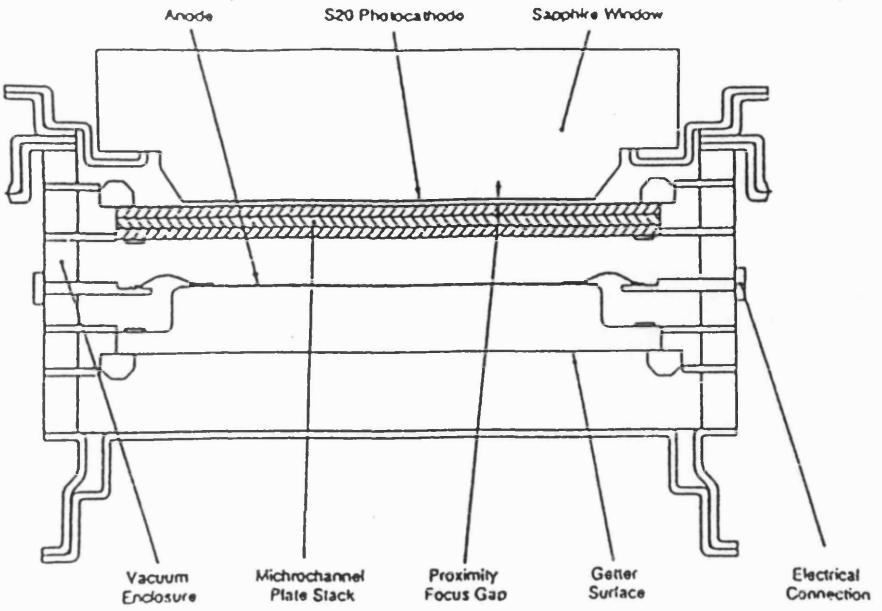

Figure 1.15: Schematic diagram of a sealed tube.

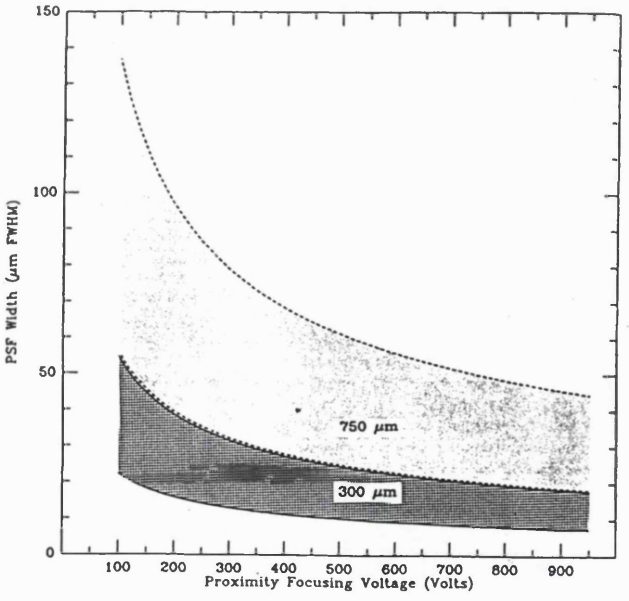

Figure 1.16: Proximity focussing PSF FWHM.

The figure represents the size of the PSF determined theoretically for gaps of 300 and 750 μm. The boundaries of the two regions are determined by the upper and lower limits on values of v_r of 0.3 and 0.05 eV. From Clampin *et al.* (1988).

1.3 MCP Position Readouts

MCP based detectors can be divided into two major types.

1. Light amplification detectors, in which the electron cloud produced by the MCP is incident upon a phosphor producing a large pulse of photons which are optically coupled to the detector, usually a CCD.

2. Charge measurement detectors, in which the centroid of the charge cloud is directly measured by a series of electrodes. The positional readouts used in these detectors can be used in MCP and gas proportional detectors.

1.3.1 Light Amplification Detectors

There are two basic types of Light Amplification Detectors.

1. Direct Readout Detectors.
   In direct readout detectors, the position of the intensified events is immediately read out and the detector performs no integration of events, e.g. PAPA.

2. Scanned Readout Detectors.
   In scanned readout detectors the event is captured and stored by a detector and read out later when the whole or part of the detector is scanned. Examples of this type of detector are the vidicon camera, the Self-scanned PhotoDiode array (SPD) and the Charge Coupled Device (CCD).

PAPA

In the Precision Analog Photon Address (PAPA) (Papaliolios *et al.*, 1985) detector the photon pulse from the phosphor is imaged by a system of lenses onto an array of Gray coded or binary masks, as shown in Figure 1.17. Light transmitted by the masks is then imaged onto a set of photomultipliers via an array of field lenses. One photomultiplier, known as the strobe channel, looks at the whole output image without a mask and determines whether an event has occurred in the field. A second photomultiplier looking through a half clear, half opaque mask determines whether the event occurred in the left or right section of the field. The light received by successive photomultipliers passes through

a set of progressively finer Gray coded masks, with the spatial frequency of the finest mask determining pixel size.

It is possible, using a set of 9 photomultipliers and their respective masks to determine the photon event position in the x direction to one of 512 positions. A similar arrangement is implemented in the y direction using another 9 photomultiplier tubes and a set of masks mounted orthogonally to the original set.

Using all 19 outputs from the above photomultipliers an 18 bit (x, y) address can be generated which represents the arrival position of each detected photon. Therefore, 19 amplifier channels each consisting of a preamp and a discriminator are required.

At present, PAPA can provide up to 512 × 512 pixels, although formats of up to 4000 × 4000 pixels have been proposed (Papaliolios *et al.*, 1985). PAPAs have been built with 25 mm active diameters (Norton, 1990). Assuming an 18 × 18 mm square, 512 pixels, 20 μm defocussing in the proximity gap and a pore spacing of 15 μm, the resolution will be approximately equal to the quadratic sum of these components, i.e.

$$\text{PSF FWHM} = \sqrt{35^2 + 20^2 + 15^2} \quad , \tag{1.20}$$

$$\approx 44\ \mu\text{m} \quad . \tag{1.21}$$

The MCP charge cloud is incident on a P47 phosphor which has an extremely short decay time of 200 ns. This implies a deadtime of 1 μs per event (Norton, 1990). In a paralysable detector, a subsequent event arriving within the initial event's deadtime, will extend the nonreceptive period of the detector by a further deadtime. In PAPA another event occurring during the phosphor decay time will lead to a wrong address being returned. The detector will not return a correct address for a third event, until after the deadtime associated with the second event has expired. PAPA can therefore be described as a paralysable detector. Given the relation for a paralysable detector (Lampton & Bixler, 1985),

$$R' = Re^{-R\tau} \quad , \tag{1.22}$$

where R is the mean rate at the input, R' is the mean rate at the output and τ is the deadtime, then there will be a 10% counting loss at a random arrival rate of 10^5 Hz. The maximum point count rate for PAPA will be ultimately set by the channel recovery time of the MCP.

In a nonparalysable detector, subsequent events do not extend the deadtime and

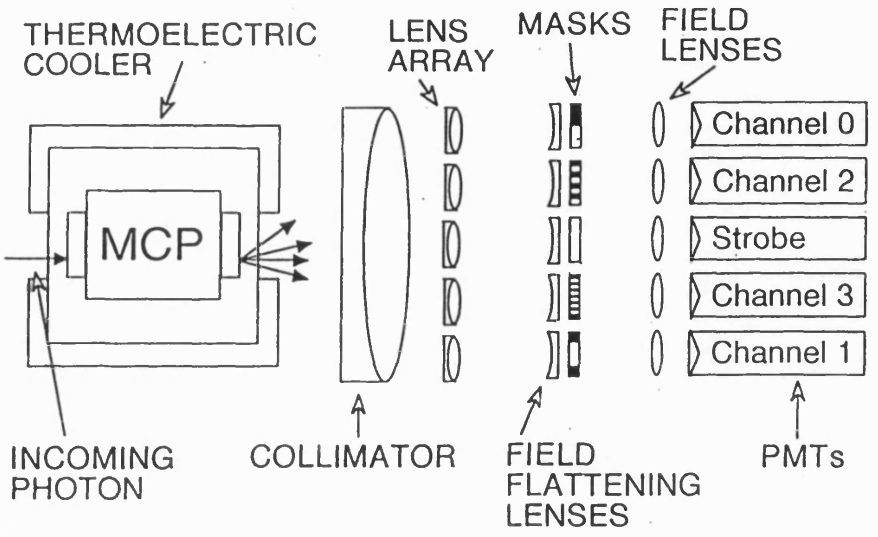

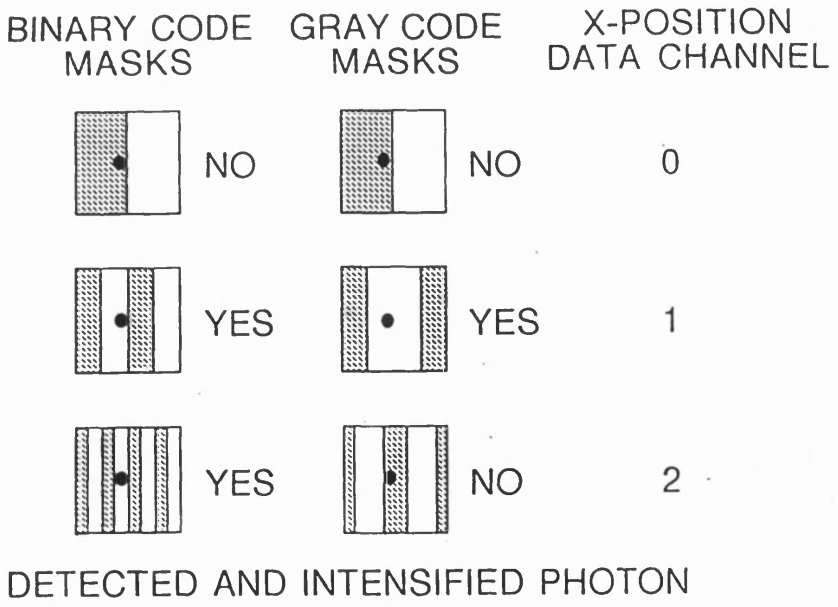

Figure 1.17: Schematic diagram of the PAPA detector.
The figure shows the arrangement of the optics, PMTs and examples of the Gray coded masks. From Sams (1991).

the reduced mean rate is given by

$$R' = \frac{R}{1 + R\tau} \quad , \tag{1.23}$$

(Lampton & Bixler, 1985). In this case, a random arrival rate of 10^5 Hz, will also cause a 10 % counting loss. All count rates quoted in this work correspond to this level of counting loss.

The PAPA detector requires that the mechanical alignment of the optics system with the coded masks be extremely precise. Sub-micron shifts in the mask position introduces serious fixed patterning noise in the final output image (Norton, 1990), i.e. some pixels detect higher intensities than others under constant illumination.

Scanned Readout Detectors

The vidicon (generic name) has a dense array of reverse biased diodes on a silicon substrate. An incident photon is converted into electron-hole pairs which locally discharge the diodes. The wafer is then raster scanned with an electron beam and the current required to recharge each diode reflects the intensity at that point. Vidicons are slow devices, intense signals can spill over into the next diode and more than one scan of the electron beam may be required to readout intense signals (Richter & Ho, 1986).

A SPD consists of an array of photodiodes connected to an output signal line via switches. A shift register sequentially recharges each diode which effectively measures the stored signal. The CCD stores signal in a similar way. The charge is transported by an analog shift register. The SPD and CCD have very similar operational characteristics. However, the CCD does have some advantages over the SPD, it is easier to construct two dimensional CCDs and the CCD's lower output capacitance means it can be clocked faster and have lower noise (Richter & Ho, 1986). The CCD is therefore the detector used in most modern scanned readout systems.

CCD Based Detectors

In CCD based detectors the pulse of photons is optically coupled to one or more CCDs through a fibre-optic bundle. The small areas of CCDs ~ 1 cm^2 compared to MCPs can be overcome by using a fibre-optic bundle to couple to several CCDs, e.g. the Photon Counting Array (PCA) which uses four (Rodgers *et al.*, 1988). The fibre-optic bundle can also be tapered, producing an optical demagnification, to couple the phosphor to a single CCD.

For example the MCP Intensified CCD (MIC) detector (Fordham *et al.*, 1989) uses a 3.8:1 fibre-optic taper.

When combined with the demagnification, CCD pixel sizes, $\sim$ 20 μm would produce pixel sizes of $\sim$ 80 μm as seen at the photocathode. This large pixel size can be overcome by spreading the photon pulse over a few pixels and centroiding which can produce sub-pixel accuracy (Carter *et al.*, 1990). Centroiding can be carried out over the pixel with the peak intensity and the intensities in the closest CCD pixels in each of the cardinal directions, 3 point centroiding, or the two closest pixels in each direction, 5 point centroiding (see Figure 1.18). Intensities are determined by digitizing the charge accumulated in each pixel by an 8 bit ADC. As the CCD can transfer charge from pixel to pixel, only one preamp and ADC are required. Three point centroiding can subdivide a CCD pixel into up to 128^2 subpixels (Carter *et al.*, 1991).

With division to 1/32 nd. of an 88 μm CCD pixel, as seen at the photocathode, the individual pores on the front MCP, 12 μm pores on 15 μm centres, can be resolved (Read *et al.*, 1990). The PSF of the centroiding has been measured as $\approx$ 2 μm using 128 subpixels (Carter *et al.*, 1991) and the overall resolution has been measured as 25 μm. This approximately represents the combination of an assumed proximity gap PSF of 20 μm and the pore spacing.

The point source countrate is limited by the decay time of the output phosphor, $\approx$ 2 μs for a P20 phosphor (Carter *et al.*, 1991) and the frame rate. The size of the region to be read out can be selected and as there are fewer pixels in a smaller region, faster frame rates are possible. The maximum linear count rate for a flat field is $\approx$ 2×10^5 Hz. The maximum point source count for a 10.6×84μm pixel is 38 Hz (Fordham, 1990) at a frame rate of about 1.5 ms.

If two photons arrive at the same position during one frame they could be counted as one photon. By operating the CCD in analog mode and measuring the amount of charge it is possible to determine if more than one event has occurred at the point. This data can be discarded or counted as two events. However, this method is very sensitive to depression of the MCP gain at high local count rates (Richter & Ho, 1986).

Great care must be also taken to ensure that overlapping events are properly identified and discarded. This places further limitations on the point source count. With 3 point centroiding, the optical pulse must cover at least an area of at least 3 × 3 CCD pixels. An overlapping event will result if a subsequent event occurs with its centre lying in

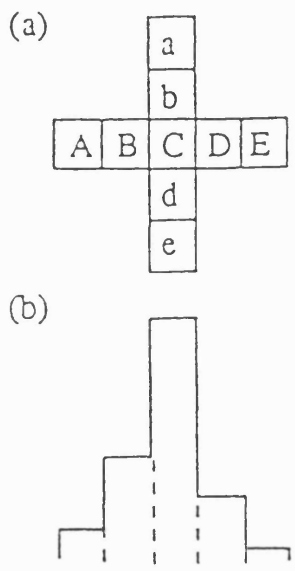

3 pt. centroiding :

$$\bar{x} = \frac{d-b}{b+c+d}$$

$$\bar{y} = \frac{D-B}{B+c+D}$$

5 pt. centroiding :

$$\bar{x} = \frac{2e+d-b-2a}{a+b+c+d+e}$$

$$\bar{y} = \frac{2E+D-B-2A}{A+B+c+D+E}$$

Figure 1.18: Three and five point centroiding for the MIC detector.
Figure a shows the centroiding window and figure b represents a typical event profile. From Carter *et al.* (1990).

one of, at the least ≈20 CCD pixels surrounding the central pixel of the first event, within one frame time (Carter, 1991a). Therefore, a single event can effectively paralyse an area containing approximately 1300 image pixels, assuming division into 8 × 8 subpixels, for the whole frame time.

The optical demagnification of a tapered fibre-optic introduces barrel distortion. The higher the taper ratio, the worse the distortion. A taper of 3.8:1 produces a distortion of ≈ 1 % of the active diameter, i.e. ≈ 300 μm (Read, 1990). It is possible that low distortion tapers may be obtained, which would reduce this effect.

Active Pixel Image Sensors

Active pixel image sensors are a family of devices recently developed for use in high definition television. These devices have not yet been used as positional readouts for MCPs, but potentially they could. Although there are several different types of device, they all consist of an array of pixels each containing a phototransistor as the light sensitive element (Yusa *et al.*, 1986, Hynecek, 1988, Tanaka *et al.*, 1990 and Nakamura & Matsumoto, 1992).

For example, in the Charge Modulation Device (CMD) (Nakamura & Matsumoto, 1992), photons incident on a photoFET produce a population of holes near the gate. During readout the magnitude of the source current is modulated by the number of holes. Readout is carried out by varying the gate voltage and is nondestructive. The gates of all pixels in a row are connected together so that a whole row is read out simultaneously. All the drains of the FETs in one column are connected together and to one capacitor. Therefore, one row at a time can be read with the source current charging capacitors in each column. The capacitors are then clocked serially to a preamp. Each row can be read out individually and in any sequence. All pixels can be reset simultaneously.

CMDs have been made with up to 2 million, ≈ 7.5 μm square pixels, *i.e.*1920×1036. Data can be read out at 75 MHz, i.e. each pixel can be read out at ≈30 Hz if the whole image is being read. The CMD has slightly better performance than the other active pixel sensors and compares favourably to that of a CCD. It would be most interesting to evaluate this chip as a MCP position readout.

1.3.2 Charge Measurement Detectors

The positional readouts in charge measurement detectors can also be divided into two broad categories:

1. Discrete Electrode Readouts, in which many anode electrodes, either pads or wires, are used. These devices produce a digital code for the centroid position and the pixel size is directly determined by the spacing of the electrodes.

2. Continuous Electrode Readouts, in which the output signal from the anode is a continuous function of the spatial position of the centroid. The continuous signal is digitized by an ADC and the pixel size is determined by the ADC quantization.

Discrete Electrode Readouts

An example of a discrete electrode readout is the Coded Anode Converter (CODACON) (Mc Clintock *et al.*, 1982). The charge from the MCP is deposited on a series of parallel strips, called charge spreaders, on one side of a dielectric substrate. These electrodes induce a charge on a set of orthogonal electrodes, called code tracks, on the other side of the dielectric. The thickness of the code tracks varies along the length so the charge induced is proportional to that area. Each charge spreader's position is then represented by a Gray code. This detector can provide 2^n pixels with n amplifier channels. Only one dimensional readouts have been constructed at this stage.

MAMA's

The most developed of the discrete electrode readouts are the Multi-Anode Microchannel Array (MAMA) readouts. There are two basic types of MAMAs; the discrete-anode array and the coincident-anode array (Timothy *et al.*, 1981).

1. The Discrete-Anode Array.
   The discrete anode array consists of of an array of $n \times m$ anodes, insulated from each other. Each channel must be read out with an individual electronic channel consisting of a preamplifier and a discriminator. Therefore, $n \times m$ channels are required.

2. The Coincidence-Anode Array.
   The simplest coincidence-anode consists of two orthogonal planes of electrodes, separated by an insulating layer, mounted on a substrate (Timothy & Bybee, 1975b). Each plane consists of a series of linear 25 μm electrodes on 50 μm centres. In operation, the MCP pulse is divided between the row and column electrodes at the point of incidence. If a pulse occurs on both the row and column electrodes within a finite

time ($\sim$ 100 ns), the position of these two electrodes is taken to be the position of the charge pulse. The coincidence anode allows an $n \times m$ array to be read out with $n+m$ discriminating channels.

The coincidence technique can be extended to further reduce the number of electronics channels (Timothy *et al.*, 1981). Figure 1.19 shows a Coincidence MAMA where 16 positions are encoded by 16 anodes and 8 amplifier channels. Every other anode, call these the even anodes for convenience, is connected to one of four fine position amplifiers. This indicates that an event is on any 4 out of 16 electrodes. Assuming that the charge cloud only covers two electrodes, by connecting the odd anodes to another set of 4 amplifiers, the coarse amplifiers, the pair of electrodes the MCP pulse straddles is determined. Comparing signal intensities on the coarse and fine channels determines if the centroid of the pulse is closer to the odd or even electrode.

All events that stimulate more than 4 electrodes or those that stimulate non-adjacent electrodes are rejected. The events that are coincident on 2 or 3 adjacent electrodes are identified and stored as addresses in the decoding electronics. This provides information from 32 pixels. Adjacent two-fold and three-fold events are then summed giving the required information for 16 pixels.

This process can be extended to more fine and coarse position channels. A 1024×1 pixel array requires 32 fine and coarse channel, i.e. 64 channels per axis. A 1024×1024 array can be manufactured by depositing another set of orthogonal electrodes, separated by an insulator, over the first set.

The deadtime associated with the analogue and the decoding electronics is 100 ns per coincidence.

resolutions of

Pixel size is determined by the size of the electrodes and 25 μm have been achieved (Timothy & Bybee, 1975a). Assuming a 20 μm FWHM defocussing in the photocathode MCP gap and 15 μm pore spacing, the overall resolution would be $\approx$ 35 μm. As MAMA only requires discrimination to determine position, they do not require as high a SNR as readouts using charge measurement, e.g. continuous electrode readouts (see below) and gains of approximately 10^6 electrons are sufficient. This can be provided by a single C plate. Also, the gain depression caused by high local count rate does not have a great affect on the resolution. However, when gain is depressed below the discriminator threshold, the

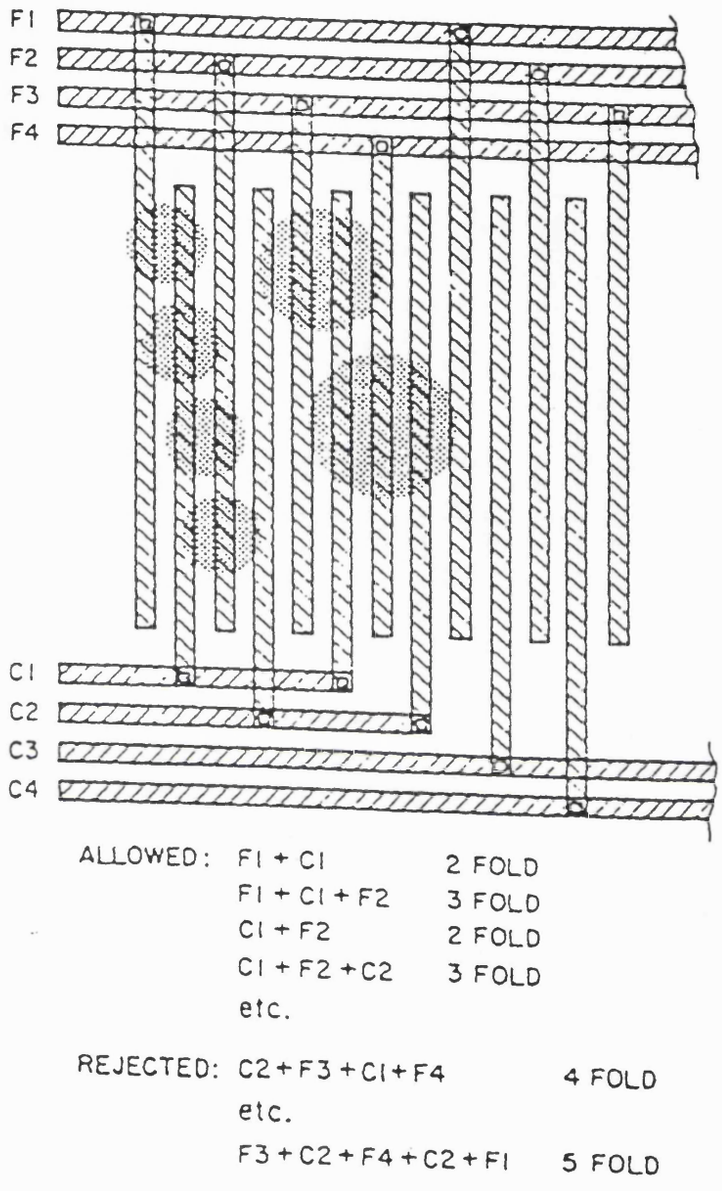

Figure 1.19: Schematic Diagram of the MAMA detector.
This example is a 16 × 1 pixel MAMA coincidence detector and shows the allowed and rejected coincidences.

photometric linearity will still be affected.

The spatial extent of the MCP charge cloud must be approximately the same size as one of the electrodes for a discrete anode. This requires that the gap between the MCP and the anode is small, $\sim$ 100 μm. Coincidence anodes require that the charge cloud is spread over at least two but not more than four electrodes, so they require similar sized anode gaps.

Continuous Electrode Readouts

In continuous electrode readouts the charge from the incident MCP pulse is partitioned between a number of amplifiers, typically 2 per axis. There are two basic types of these readouts.

1. The resistive anode, delay lines and crossed wire grid are Charge Division Readouts in which charge is divided by a resistive or capacitive network.

2. In Charge Sharing Readouts the charge is collected by a few electrodes which are insulated from each other. Ideally, the electrodes are not coupled together and the amount of charge collected on each electrode depends solely on its area. Therefore, the total charge from the MCP is shared between the electrodes according to their areas at a given point. Two well known examples of these readouts are the Backgammon and Wedge and Strip readouts.

With the exception of the Quadrant Anode and Resistive Anodes, charge division and sharing readouts consist of a repeated pattern of electrodes. The pitch of the pattern is typically of the order of 1 mm. To avoid distortion, the spatial size of the charge cloud must cover several of these pitches, see the discussion in the Wedge and Strip section and references therein. A substantial gap, typically several millimetres, is needed between the bottom of the MCP stack and the anode to ensure that the charge cloud can expand to the necessary size.

The resolution of the device depends on the accuracy of the charge measurement. Therefore, good SNR is necessary for good resolution. As the electronic noise is independent of pulse height, a larger charge pulse will have a better SNR than a smaller one. Also, these readouts are subject to partition noise. This noise is due to the quantum nature of the charge carriers and their random arrival on one of the electrodes (Martin *et al.*, 1981). Partition

noise decreases with increasing pulse height, $e_{np} \propto Q^{-\frac{1}{2}}$. Therefore, a higher gain in the MCP produces a higher SNR and better resolution. Figure 1.20 shows an example of how resolution varies with MCP gain.

As the MCP produces a PHD, the resolution of the ADCs must be at least equal to the product of the desired position resolution and the pulse height dynamic range. Practical limitations on the anode design limit the dynamic range. Gain depression caused by high local count rates will move the PHD to lower levels, reducing the digitization of the measured values and decreasing the SNR. Images must also be oversampled, i.e. the size of the pixel defined by the ADC digitization must be smaller than the desired resolution. Otherwise, a fixed patterning noise is produced (Clampin *et al.*, 1988). As a result, in practice, at least 12 bit ADCs are required to produce a 1024 $\times$ 1024 pixel array.

Resistive Anodes

The resistive anode (Stümpel *et al.*, 1973 and Lampton & Paresce, 1974) has the widest commercial availability of the MCP readout devices. It consists of an area of uniform resistance, typically $10^5 - 10^6 \Omega/\Box$. This area can have many different shapes (Fraser, 1989). The circular arc terminated resistive anode is one of the most successful designs for eliminating image distortions (Gear, 1969). Resistive anodes require two electronics channels, located on opposite sides of the resistive area, per axis.

Timing was the original method of determining the spatial position for the resistive anode (Stümpel *et al.*, 1973). The times of the signal zero crossing point in the amplifiers are measured. The electronics necessary for this method are similar to those used in delay lines, see below. In this mode, changes in the anode temperature will produce a zooming effect in the image (Allington-Smith & Schwarz, 1984 and Clampin *et al.*, 1988) and charge measurement is the most widely used method at present.

For charge measurement, each channel consists of a charge sensitive preamp, amplifier and ADC. The centroid position is determined either by measuring the magnitude of the current pulse, Q for each channel. The x and y coordinates are determined by the equations,

$$x = \frac{Q_A + Q_B}{Q_A + Q_B + Q_C + Q_D} \quad , \tag{1.24}$$

$$y = \frac{Q_B + Q_C}{Q_A + Q_B + Q_C + Q_D} \quad . \tag{1.25}$$

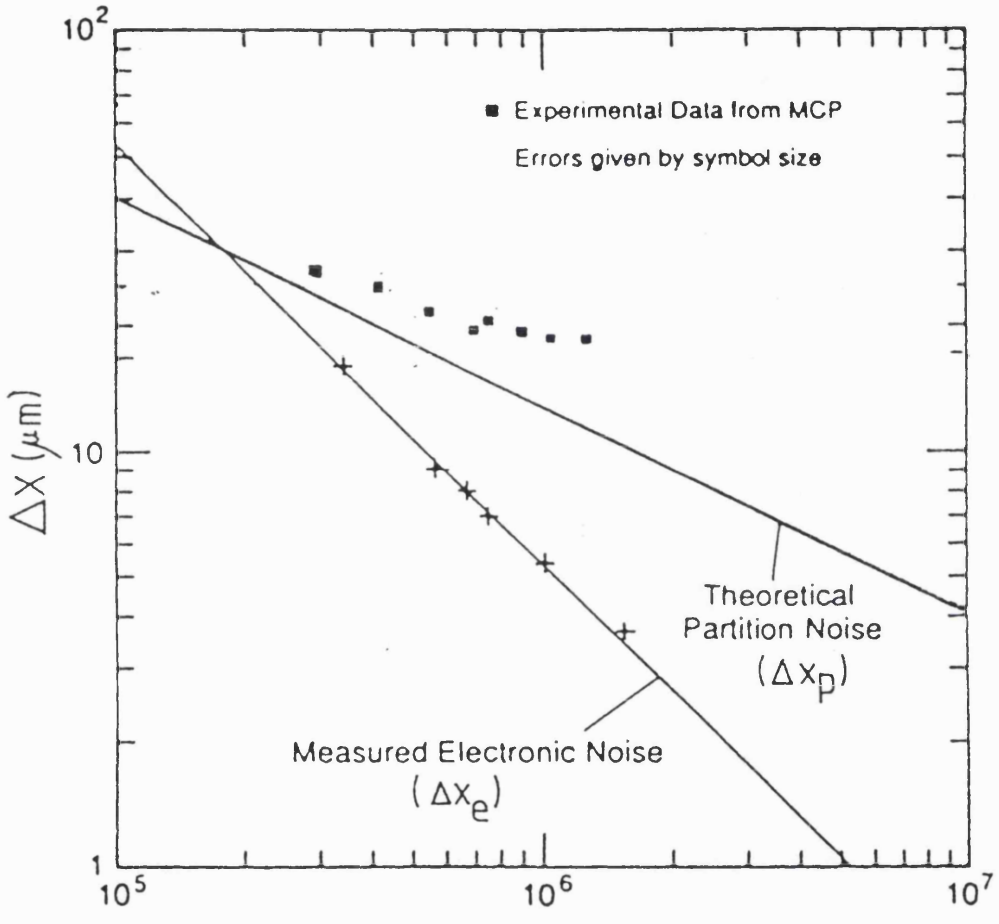

Figure 1.20: Resolution versus MCP gain for a Wedge and Strip Anode. From Lapington *et al.* (1988).

The anode will only operate linearly in the dc limit, i.e. a long filter time constant with respect to the anode time constant (Fraser & Mathieson, 1981), typically a few microseconds but as low as 0.5 μs giving a 6 μs deadtime (Clampin *et al.*, 1984).

The major limiting factor in the performance of resistive anodes is the Johnson noise associated with the resistive anode,

$$e_{nJ} = \left(\frac{4kT\tau}{R}\right)^{\frac{1}{2}} V \quad , \tag{1.26}$$

where k is Boltzman's constant, T is the temperature, τ is the time constant of the shaping time and R is the resistance of the anode.

Resistive anodes have traditionally had problems with non-uniformity of the resolution across the active area of the detector, the resolution at the edges being typically $\sqrt{2}$ worse than that at the center, $\sim$ 50μm FWHM over a 25 mm diameter, (Lampton & Paresce, 1974, Clampin & Edwin, 1987 and Floryan & Johnson, 1989). Firmani *et al.* (1984) and Clampin *et al.* (1988), however, have demonstrated a uniform resolution across the whole image of 40 μm at 650 nm at 12 bits digitization. This resolution includes the contribution of the pore spacing. The diameters of the pores are quoted as 13 μm so the spacing should be $\sim$ 15 μm. The latter group report a PSF of 22 μm FWHM from a proximity focussing gap of 300μm with an applied voltage of 300 V. If we assume that the defocussing is reduced to 20 μm, the resolution would improve marginally to $\approx$ 39 μm. Clampin *et al.* (1988) also report deviations from positional linearity of $<$ 21 μm.

Fraser *et al.* (1991a) have reported imaging 85 μm square pores on 100 μm centres, achieving a best centroiding PSF of 13.5 μm over a 5 mm image, with a resistive anode. However, they do not describe the size of the detector or the electronics.

Delay Lines

When the MCP charge pulse is incident on a delay line, it divides into two pulses that propagate in opposite directions. The centroid position is determined by measuring the difference in the arrival time of the pulses at opposite ends of the delay line. A separate delay line is required for each dimension.

There are three basic types of delay lines:

1. Solid State Delay Lines

   The charge from the MCP is collected on individual parallel strips which are connected to taps in a solid state delay line. However, this system so distorts the MCP pulse shape that the resolution is limited to 250 μm FWHM (Keller *et al.*, 1987).

2. Planar Delay Lines

   These delay lines have been produced by etching a zig-zag pattern in copper on a fibreglass substrate (Siegmund *et al.*,1989a). At present, only one dimensional delay lines can be manufactured but the authors suggest that an anode consisting of crossed delay lines may be possible. The operating characteristics are similar to those of a transmission line delay line, so most of the following discussion is relevant to planar devices as well.

3. Transmission Line Delay Lines

   Figure 1.21 shows the schematic layout of a transmission line delay line (Williams & Sobottka, 1989). Each delay line consists of two 200 μm bare Cu wires wrapped, with a 1 mm pitch, around a Cu centre. The wires are insulated from the Cu centre by ceramic spacers. One wire is wound halfway between the other wire so that the two windings form a two wire transmission line. A second set of windings is wrapped in an orthogonal direction to produce the second delay line. The two sets of windings are separated by a gap so that they are insulated from each other. Different DC voltages are applied to each of the 4 wires and the Cu centre, to ensure that 50 % of the MCP charge pulse goes to each of the delay lines and that all of the charge on one delay line is collected on only one of the wires (Sobottka & Williams, 1988).

   A schematic diagram of the electronics required for each delay line is shown in Figure 1.21. The signals from opposite ends of the two wires are fed into differential amplifiers. The outputs from these are then passed through two constant fraction timing discriminators (CFD). A delay T_d is added to one channel and then the two channels are input to a time to analogue converter (TAC). The analogue TAC output is digitized by an ADC. Therefore, only one ADC is required per axis. In practice, the TAC and ADC could be replaced by a time to digital converter (TDC). The planar delay line has a very similar electronic setup except that delay line only has one component and uses two preamps instead of two differential amplifiers.

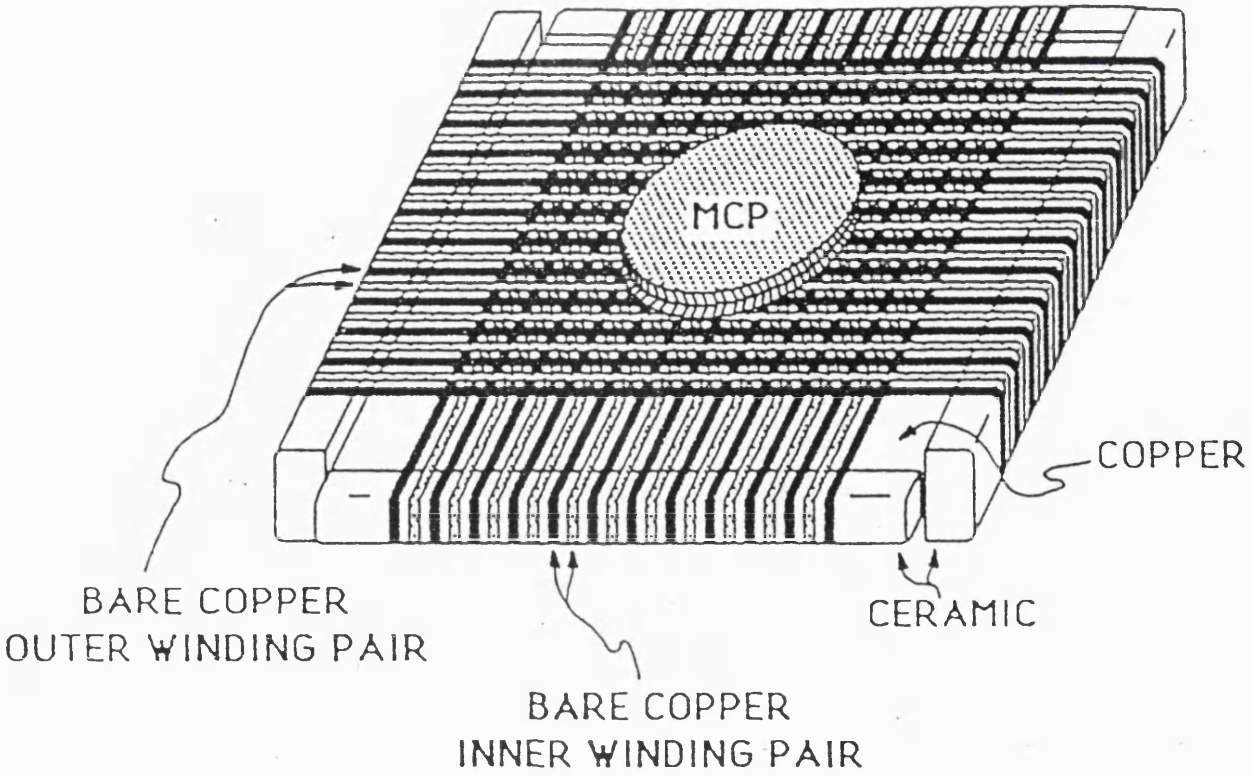

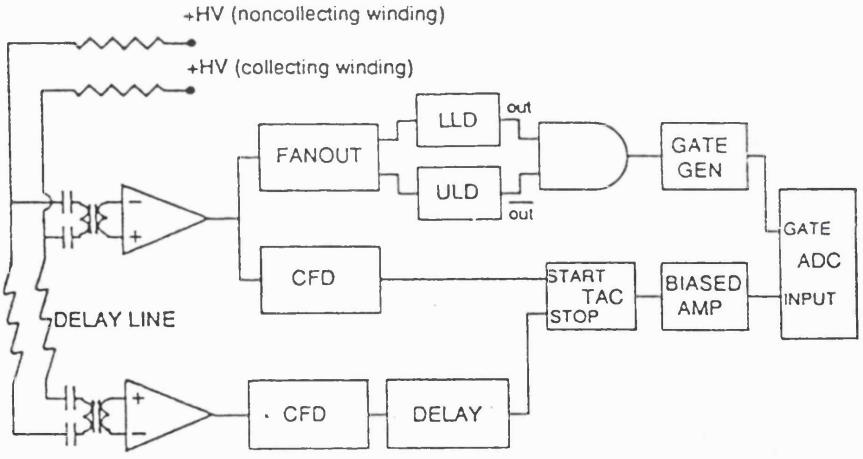

Figure 1.21: Schematic diagram and readout electronics for a transmission, line delay line readout.

The figure represents a two dimensional readout and the electronics are those required for each axis. From Williams & Sobottka (1989).

The centroid position for one axis, e.g. x_c for the x axis, is given by,

$$x_c = \frac{(T + T_d)\, v}{2} \quad , \tag{1.27}$$

where T is the difference in the time of arrival of the two pulses, as measured by the TAC and v is the characteristic velocity of signal propagation along the delay line, typically $1 - 2$ mm/ns. The delay T_d is the overall end to end delay of the anode, i.e. the time for the signal to travel from one end of the delay line to the other, $\sim 100 - 200$ ns. Adding T_d to one channel effectively normalizes x_c (Siegmund *et al.*, 1989a). The uncertainties in δx are therefore,

$$\delta x = \frac{1}{2} v \delta T \quad . \tag{1.28}$$

Resolutions of 18 μM FWHM (Williams & Sobottka, 1989) were attained with a 140 $\times$ 140mm readout imaging 50 mm diameter MCPs. This resolution corresponds to the PSF of the centroiding. Assuming a 20 μm FWHM defocussing in the photocathode-MCP gap and a 15 μm pore spacing, the resolution would be $\approx$ 31 μm. Deviations from position linearity of $< \pm 65$ μm, for both axes, over a 25 mm diameter (Sobottka & Williams, 1988) have been attained with this delay line. Siegmund *et al.* (1989a) report similar results, with 12 bit digitization, for their one dimensional delay line.

The difference in impedance between the delay line and the input to the amplifiers causes reflections along the delay line. The time that it takes the size of these reflections to reduce below the noise level determines the detector dead time. Williams & Sobottka (1989) have found that by using transformers to couple the delay line to the differential amplifiers, they could achieve a deadtime of 1 μs.

Crossed Wire Grids

In another example of charge division readouts, a series of wires or electrodes are connected in series by either a resistive or capacitive network (Richter & Ho, 1986). As in the resistive anode, position is determined by either charge measurement or pulse timing at both ends of the network.

Crossed wire grid readouts consist of two isolated, orthogonal, wire planes. Each plane is a series of parallel wires. An example of a crossed wire grid readout is the detector

used in High Resolution Imager (HRI), used on the Einstein Observatory and ROSAT (Fraser, 1989).

In the HRI readout, each of the wire planes consists of 100 μm wires on 200 μm centres. For a 25 mm diameter image, this corresponds to 125 wires per axis. The planes are held approximately at -300 V with respect to the rear of the MCP stacks. A small bias voltage between the two planes ensures that the MCP charge pulse is divided evenly between the two planes. The wires are coupled together with 10 kΩ resistors. Every eighth channel is connected to a charge sensitive preamp, called a tap. Therefore, 17 amplifier chains are required for each axis. The event position x is determined by a coarse and fine position measurement, x_c and x_f, respectively,

$$x = x_c + x_f \quad . \tag{1.29}$$

The coarse position is equal to the position, x_i, of the tap, i, that has collected the largest charge, Q_i, from the grid. The fine position is determined by a centroiding algorithm using Q_i and the charge on the adjacent taps,

$$x_f = \frac{Q_{i-1} - Q_{i+1}}{Q_{i-1} + Q_i + Q_{i+1}} \quad , \tag{1.30}$$

(Chappell & Murray, 1989).

For a 25 mm diameter image a crossed grid readout is capable of 20 μm FWHM resolution at a linear count rate of 500 Hz (Fraser, 1989). Assuming that this resolution includes the contribution from a pore spacing of 15 μm but not the proximity focussing PSF, the overall resolution would be $\approx$ 28 μm.

Wedge and Strip Anodes

In charge sharing readouts, the anode is divided into a few conductive electrodes of finite width, deposited on a substrate and insulated from each other. These types of anodes are sometimes called progressive geometry encoders. The amount of charge collected on each electrode depends on the area of that electrode. The electrodes usually have areas that vary linearly across the anode. At any one point, the ratio of the electrode areas will be unique. As a result, the ratios of the amount of charge collected on each electrode at any given point will also be unique. Examples of this type of anode are the Four Quadrant Anode (Lampton & Malina, 1976 and Purshke *et al.*, 1987), the Backgammon Anode (Allemand & Thomas, 1976) and the Sickle and Ring Anode (Knibbeler *et al.*, 1987).

Another type of charge sharing readout is the Graded-Density Anode (Mathieson *et al.*, 1980). It consists of a grid of wires for each dimension. The amount of charge collected by each amplifier depends on the number of wires connected to that amplifier at the point at which the charge cloud is incident. The ratio of the number of wires connected to one amplifier, to the number connected to the other amplifier is unique along the length of the detector. The density of wires connected to each amplifier is analogous to the electrode areas in the other types of charge sharing readouts.

The quadrant anode has good spatial readout only over a very small region of the active area while the backgammon anode is a one dimensional readout. The most highly developed and widely used of the large format, two dimensional, progressive geometry encoders is the Wedge and Strip Anode (WSA) (Martin *et al.*, 1981). The sickle and ring anode is basically a polar coordinate version of the WSA.

Figure 1.22 shows an example of a WSA. The charge pulse from the MCP is shared amongst three electrodes, the wedge (W), strip (S), and Z electrodes. Each of the electrodes requires a charge sensitive preamp, a shaping amplifier and an ADC. Two dimensional information is determined by the ratios of the magnitude of charge collected on each electrode, Q_i, i.e.

$$x = \frac{2Q_S}{Q_W + Q_S + Q_Z} \quad , \tag{1.31}$$

$$y = \frac{2Q_W}{Q_W + Q_S + Q_Z} \quad . \tag{1.32}$$

The Z electrode is required so that the position (x, y) can be normalized with respect to the height of the MCP pulse.

The absolute resolution limiting factor intrinsic to a WSA is the partition noise. Care must also be taken in the layout of the WSA, as a large coupling capacitance between electrodes, combined with the input noise of the preamp can become the dominant noise source.

Resolutions of 35 μm FWHM have been obtained with 20 mm (Siegmund *et al.*, 1989b) and 23 mm (Rasmussen & Martin, 1989) diameter WSA's, at 14 and 12 bit digitization, respectively. Resolution is almost constant in the central region of the WSA and degrades slightly at the edges. The pore spacing was 15 μm in both cases.

The highest resolution obtained for a single 50 mm diameter WSA was 80 μm FWHM (Siegmund *et al.*,1986a). Rasmussen & Martin (1989) have proposed the Mosaic

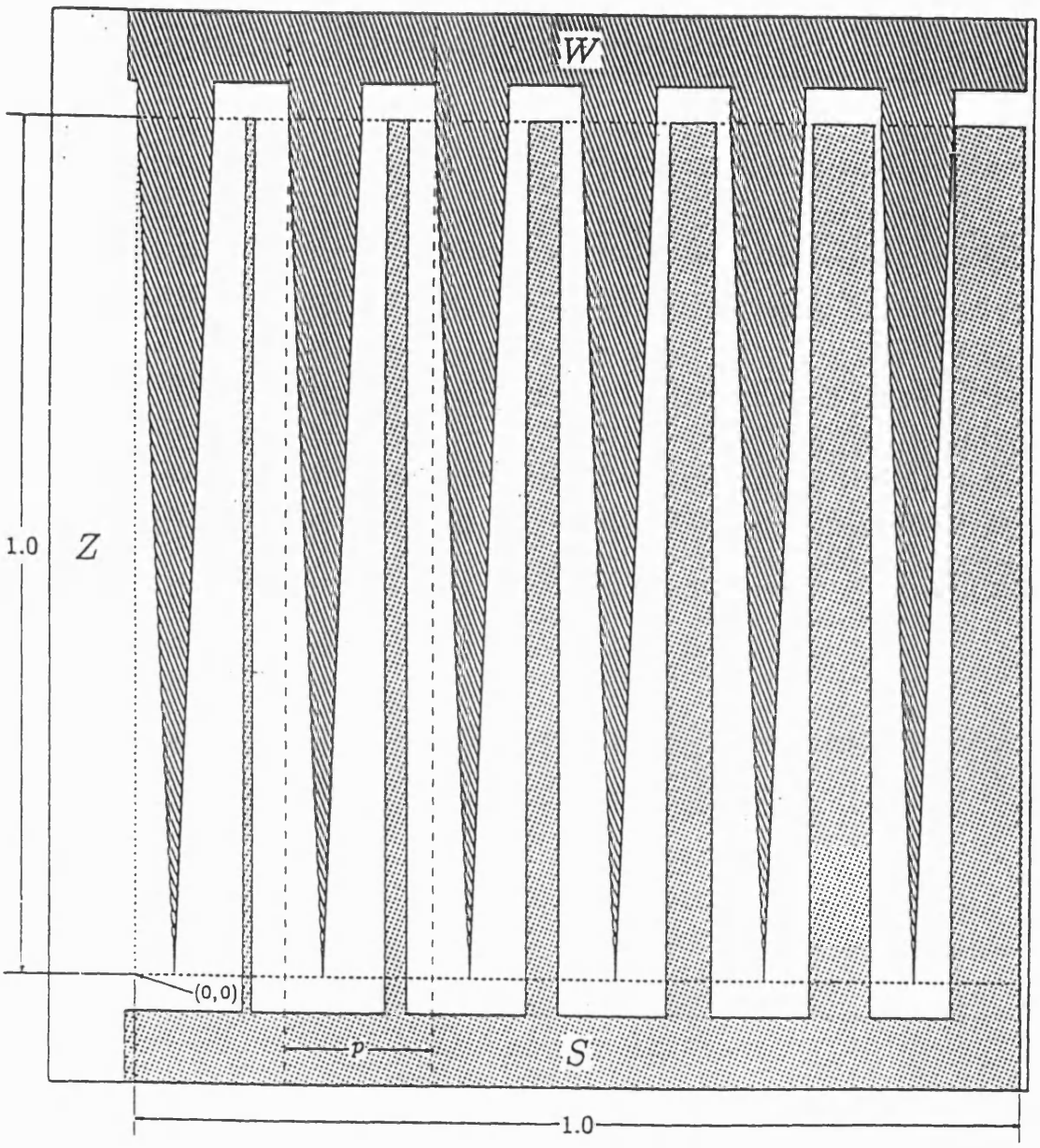

Figure 1.22: Schematic diagram of a WSA.
The length p represents the repeat pitch of the pattern. From Smith *et al.* (1989).

Wedge and Strip readout. Basically, nine 23 mm square, WSAs would be butted together, requiring 29 channels of electronics, 9 × 3 plus 2 extra channels for border sampling electrodes. They estimate this would produce < 30 μm resolution over a 50 mm diameter. They have demonstrated that it is possible to butt two WSAs together with positional linearities of 50-100 μm across the boundaries.

Assuming a 20 μm FWHM defocussing in the photocathode-MCP gap, a resolution of 35 μm without defocussing would correspond to an overall resolution of $\approx$ 41 μm.

Variations in the size of the MCP charge cloud can introduce severe distortions in WSA images (Smith *et al.*, 1989 and Vallerga *et al.*, 1989). These distortions are discussed in Chapter 3. The spatial distribution of the charge cloud and its size have been measured for various operating conditions and are discussed in Chapter 4.1. The distortion of the position linearity for a WSA can be < 0.5 % of a 50 mm diameter image, i.e., 125 μm (Siegmund *et al.*, 1986b). Using a correction map generated by image calibration, the distortion could be reduced to approximately 25 μm (Vallerga *et al.*, 1989).

The limiting factor on the speed of a WSA is usually the time constant of the shaping amp. Rasmussen & Martin (1989) used 5 μs shaping times while obtaining 35 μm resolution.

Cyclic Continuous Electrode Readouts

These types of readout include a novel form of MCP readout being developed at MSSL and are analyzed in detail in the next chapter. The operation of one example is discussed in Chapter 5.

1.4 An Optical Monitor for the XMM Satellite

In order to best understand the nature of high energy sources it is necessary that correlated observations are made over many wavelengths. During the operation of previous X-ray astronomy satellites such as EXOSAT, large amounts of ground based and IUE (International Ultraviolet Explorer) observing time were devoted to correlated observations of approximately 60% of the X-ray targets (Briel et al., 1987).

As most X-ray sources exhibit high variability over very short timescales, it is also important that the multi-frequency observations be carried out simultaneously. It is difficult to coordinate ground based observations with those of a satellite, given the vagaries

of time allocation and the weather.

Including an optical/UV telescope on an X-ray satellite would facilitate correlated multi-frequency observations and would guarantee their simultaneity. This capability would be very important in the study of important astronomical subjects, e.g. the relationship between X-ray and optical variability in AGN, X-ray bursters and transient outbursts.

Interstellar extinction in the direction of X-ray sources can be determined by carrying out broadband photometry in the U,B,V bands and bands not observable by ground based telescopes, such as in the UV at 2500 $\AA$ and the far UV at 1500 $\AA$. Narrow band photometry can also be carried out in lines common to X-ray objects, e.g. the Hβ line is typically in emission from cataclysmic variables (CV) and QSO nuclei; the [OIII] $\lambda = 5007\ \AA$ line, characteristic of AGN, QSO and nebulae; and He II $\lambda = 4686\ \AA$, found in almost all X-ray binaries, is particularly strong in CV and WR stars.

Due to the obvious versatility of such a system, the European Space Agency has decided to include a small Optical/UV telescope, the Optical Monitor, on its X-ray Multi Mirror (XMM) satellite. This will be the first time that an X-ray satellite has carried an optical telescope.

1.4.1 Detectors.

The optical monitor will have two detectors. The blue detector will be a photon counting, sealed tube MCP intensifier with a S20 photocathode to cover the approximate wavelength range 150 to 650 nm. The red detector consists of a CCD for the range 550 to 10000 nm.

The main performance requirements for the blue detector are:

1. Active Area: 18 ×18 mm square, which corresponds to a 16 × 16 arcmin field of view.
2. Number of pixels: 2048, i.e. $\approx 9\ \mu$m pixels.
3. Maximum countrate over the entire active area, defined by the Zodiacal Light: 2×10^5 Hz.
4. Point Spread Function: 18 μm
5. Maximum Point Source Countrate: 10^3Hz
6. Maximum Point Source Countrate with defocussing to twice the PSF: 10^4 Hz.

These are demanding requirements especially when combined with a proposed ten year lifetime and a total radiation dose of more than 100 krad.

Table 1.2 summarizes the performance of existing two dimensional detectors reviewed in the previous section. None of the detectors actually meet the specification. As MIC is limited only by the pore spacing and the proximity focussing PSF, it would appear that the resolution requirement is optimistic. Only MIC, the crossed wire grid, the delay line and MAMA have resolutions within a factor of two of the requirement. It should also be remembered that 30 μm represents the Nyquist limit of an image sampled by pores with 15 μm pore spacing. The proximity focussing PSF probably cannot be significantly reduced, especially at wavelengths shorter than 400 nm. Using a smaller pore spacing would produce some improvement in resolution. For example, using a 8 μm pore diameter could reduce the overall resolution of MIC to 22 μm. The resolutions of the other detectors would improve by a similar amount.

The crossed wire grid is too slow to meet the full field countrate The delay line is a factor of two slower than required but this probably could be overcome. MIC just meets the requirement while MAMA satisfies it easily.

The delay line's and MAMA's point source count rate is limited by the dynamic performance of the MCP while MIC is limited by the frame rate of the CCD and the need to avoid of overlapping events. Therefore, it is unlikely that MIC could attain the high point source countrates that low resistance MCPs would allow.

In Chapters 2 and 5, I discuss a novel type of charge division readout developed at MSSL and evaluate its performance with respect to the Optical Monitor's blue detector requirements.

Detector	Active Area mm	Resolution * μm	Positional Nonlinearity μm	Count Rate Hz	No. of Amps	ADC Bits
MIC	40 ⊘	25	300	2×10^5	1	8
PAPA	18 x 18	44	Neg.	10^5	19	
Discrete MAMA	25 x 25	35	Neg.	10^6	10^6	-
Coincidence MAMA	25 x 25	35	Neg.	10^6	128	-
Resistive Anode	25⊘	39	< 21	2×10^4	4	12
Delay Line	50 ⊘	31	$< \pm 65$	10^5	4	12
Crossed Wire Grid	25 ⊘	28 †		500	34	
WSA	23 x 23	41	25	2×10^4	3	12

Table 1.2: Performance characteristics of two dimensional MCP readouts.

* FWHM, assuming a 20 μm FWHM PSF for proximity focussing and 15 μm pore spacing.

† Assuming value in literature was obtained with 15μm pore spacing and no contribution from proximity focussing PSF.

Chapter 2

Cyclic Continuous Electrode Charge Measurement Devices

An idealized example of a cyclic continuous electrode is shown in Figure 2.1. It consists of three electrodes, the sum of whose widths is constant, w. The widths of the electrodes at a given point p is given by

$$x = r\cos p + c \quad , \tag{2.1}$$

$$z = r\cos(p+\phi) + c \quad , \tag{2.2}$$

$$y = w - (x+z) \quad . \tag{2.3}$$

The offset c must be greater than the amplitude r to ensure that the electrodes are continuous and it is typically $w/3$. The phase shift ϕ is constant along the whole anode.

The position p of an event is determined by a combination of two parts, a coarse and fine position. The fine position is determined by the value of the phase angle θ within a cycle of the repeated pattern, that satisfies Equations 2.1 and 2.2 The coarse position is found by determining in which cycle an event occurs. If n is the number of the cycle, then

$$p \propto 2n\pi + \theta \quad . \tag{2.4}$$

The advantage of cyclic electrodes is that the full dynamic range of the ADCs is used in determining the fine position within a single cycle which is repeated several times across the pattern. In other types of charge measuring readouts, e.g. the WSA and delay lines, the ADC dynamic range can be used only once across the whole active area of

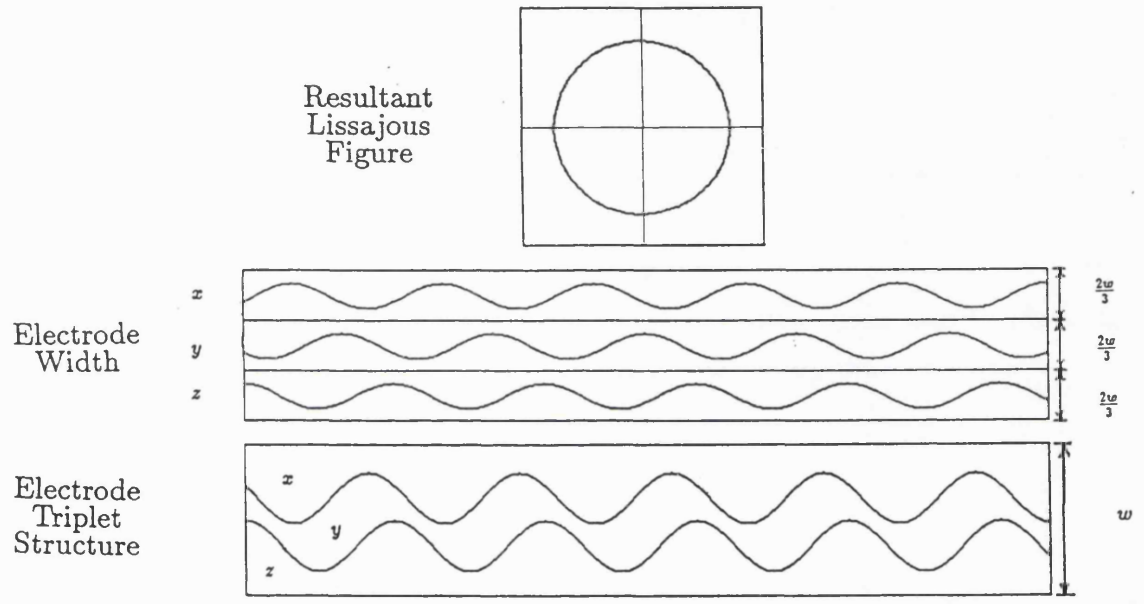

Figure 2.1: Schematic diagram of sinusoidal, continuous, cyclic electrodes and the resultant Lissajous figure.

the detector. Therefore, for a given digitization level, continuous readouts offer, to a first order approximation, an improvement in resolution by a factor directly proportional to the number of cycles.

2.1 Fine Position

2.1.1 Analysis of Sinusoidal Electrodes

Let us represent the electrodes as oscillators, exhibiting simple harmonic motion, with the same frequency and unit amplitude such that

$$x(t) = \cos(\omega t) \quad , \tag{2.5}$$

$$z(t) = \cos(\omega t + \phi) \quad , \tag{2.6}$$

$$y(t) = w - (x(t) + z(t)) \quad . \tag{2.7}$$

where $0 < t < \infty$.

By treating the electrodes as orthogonal oscillators we can describe their output in terms of Lissajous figures.

For convenience I shall change the notation to the form

$$x = x(t) \quad , \tag{2.8}$$

$$\theta = \theta(t) = \omega t \quad . \tag{2.9}$$

Expanding Equation 2.6 and substituting for x

$$z = \cos\theta\cos\phi - \sin\theta\sin\phi \quad , \tag{2.10}$$

$$= x\cos\phi + \sqrt{1-x^2}\sin\phi \quad , \tag{2.11}$$

regrouping the term and squaring we obtain

$$z^2 + x^2 - 2zx\cos\phi - \sin^2\phi = 0 \quad . \tag{2.12}$$

Including the condition that the sum of of the three oscillators is constant Equation 2.7 gives the polynomial $f(x,y,z)$ such that

$$f(x,y,z) = z^2 + x^2 - 2zx\cos\phi - \left(\frac{sin2\phi(x+y+z)}{w}\right)^2 \quad , \tag{2.13}$$

$$= 0 \quad . \tag{2.14}$$

As $f(x,y,z)$ satisfies

$$x\frac{df}{dx} + y\frac{df}{dy} + z\frac{df}{dz} = 2f(x,y,z) \quad , \tag{2.15}$$

by Euler's theorem, it is a homogeneous polynomial of order 2 in x, y, z (Massey & Kestelman, 1964). As $f(x,y,z)$ is homogeneous and by Equation 2.14, $f(x,y,z) = 0$, Equation 2.13 describes a cone with its vertex at the origin (Massey & Kestelman, 1964). Figure 2.2 illustrates why this is the case. If a function $f(x,y,z)$ is homogeneous and $f(x,y,z) = 0$ for a point $P(\xi,\eta,\zeta)$, then $f(x,y,z) = 0$ for all points $P(t\xi,t\eta,t\zeta)$, for all numbers t. Therefore, all points on the line joining P to the origin also lie on the surface of the cone.

Therefore, for oscillators with a constant amplitude, the resulting locus is a conic section. Continuously varying the amplitude of the oscillations would produce the cone.

2.1.2 The Effect of the Phase Angle

As the cone surface is sectioned by various planes, a family of conic sections is produced. Two sets of planes are of particular interest.

Firstly the planes in which y is a constant, i.e. the planes parallel to the xz plane. The equation of this section is given by Equation 2.12. This equation is the general form of equation for Lissajous figures obtained from two orthogonal oscillators with equal amplitudes and frequencies (Massey & Kestelman, 1964). If the condition that the phase difference $\phi = 90°$ is imposed, this equation reduces to

$$x^2 + z^2 = 1 \quad , \tag{2.16}$$

the unit circle centred on the origin. For successive cycles of the oscillators, the same locus will be produced, so with only this information, it is impossible to determine during which cycle an event occurred. Therefore, the time t at which a given event occurred is unknown, only its phase.

The unit circle is produced by the ideal simple harmonic oscillators. Replacing these by the equations for the actual electrodes, Equations 2.1-2.3 we obtain by the same process

$$(x-c)^2 + (z-c)^2 = r^2 \quad , \tag{2.17}$$

a circle of radius r centred at (c,c). The fine position, θ, is determined in a straight forward

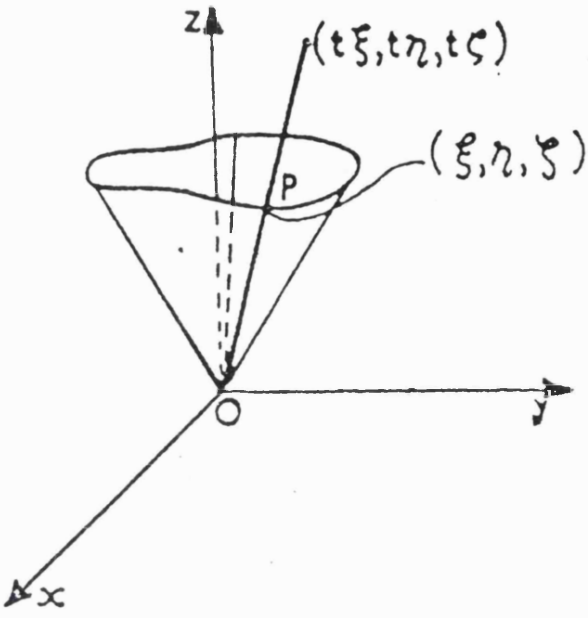

Figure 2.2: Demonstration that a homogeneous polynomial $f(x, y, z)$ describes a cone with an apex at the origin.
The symbols are explained in the accompanying text. From Massey & Kestleman (1964).

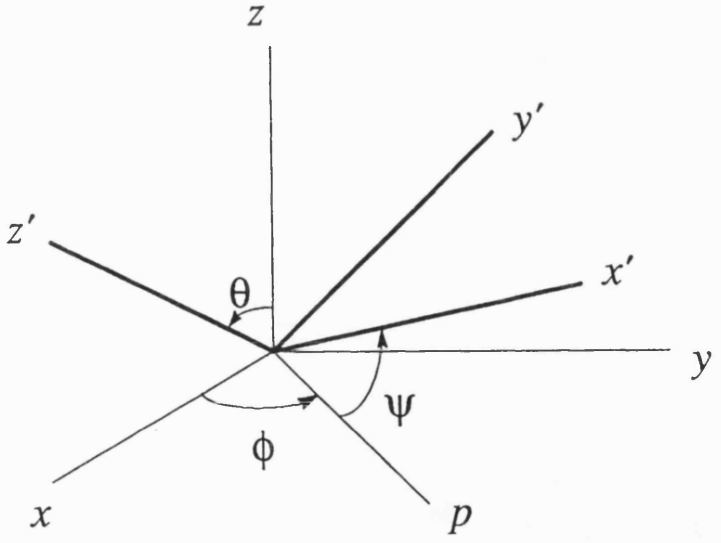

Figure 2.3: The Euler angles for a rotation through three dimensions.

manner by

$$\theta = \arctan \frac{x-c}{z-c} \quad . \tag{2.18}$$

The other conic section of particular interest is defined by the condition that the sum of amplitudes be a constant, i.e. the section defined by the plane $x + y + z = w$. The equation of this section is given by Equation 2.13. It is on this plane that the locus described by the three oscillators lies. The image in the xz plane is the projection of this locus into two dimensions.

A coordinate system where one of the coordinates will be a constant, simplifying the equation of the locus, can be obtained by changing the axes. Let this new constant coordinate be z', the obvious vector to use for the z' axis is the vector normal to the plane and running through the origin, i.e. (1,1,1). This is achieved by rotating the axes.

A rotation can be completely described as a series of three rotations through the Euler angles ϕ, θ and ψ (Corben & Stehle, 1974).

1. A rotation through an angle of ϕ about the z axis. The matrix for this rotation is

$$S_\phi = \begin{pmatrix} \cos\phi & \sin\phi & 0 \\ -\sin\phi & \cos\phi & 0 \\ 0 & 0 & 1 \end{pmatrix} \quad . \tag{2.19}$$

2. A rotation through an angle of θ about the new y axis, the line $\overline{OP}$,

$$S_\theta = \begin{pmatrix} 1 & 0 & 0 \\ 0 & \cos\theta & \sin\theta \\ 0 & -\sin\theta & \cos\theta \end{pmatrix} \quad . \tag{2.20}$$

3. A rotation through an angle of ψ about the new z axis, z',

$$S_\psi = \begin{pmatrix} \cos\psi & \sin\psi & 0 \\ -\sin\psi & \cos\psi & 0 \\ 0 & 0 & 1 \end{pmatrix} \quad . \tag{2.21}$$

These rotations are shown in Figure 2.3.

The rotation matrix, S, such that

$$\begin{pmatrix} x' \\ y' \\ z' \end{pmatrix} = \mathbf{S} \begin{pmatrix} x \\ y \\ z \end{pmatrix} \quad , \tag{2.22}$$

is given by

$$S = S_\psi S_\theta S_\phi \quad . \tag{2.23}$$

Only the first two rotations are required to carry out the transformation such that the z' axis lies along the vector (1,1,1). For convenience, at this stage, we can impose the condition $\psi = 0$. The rotation matrix reduces to

$$\mathbf{S} = \begin{pmatrix} \cos\phi & \sin\phi & 0 \\ -\cos\theta\sin\phi & \cos\phi\cos\theta & \sin\theta \\ \sin\theta\sin\phi & -\sin\theta\cos\phi & \cos\theta \end{pmatrix} \quad . \tag{2.24}$$

Therefore, the equations for the transformation are

$$x' = \cos\phi\, x + \sin\phi\, y \tag{2.25}$$

$$y' = -\cos\theta\sin\phi\, x + \cos\theta\cos\phi\, y + \sin\theta\, z \tag{2.26}$$

$$z' = \sin\theta\sin\phi\, x - \sin\theta\cos\phi + \cos\theta\, z \quad . \tag{2.27}$$

As the z' axis lies along the vector (1,1,1) then

$$x' = y' = 0 \quad , \tag{2.28}$$

when $x = y = z$. From this result and Equation 2.25

$$\begin{aligned} \cos\phi &= -\sin\phi \\ \Rightarrow \phi &= -45^\circ \quad . \end{aligned} \tag{2.29}$$

Substituting ϕ into Equation 2.26 and applying the condition of Equation 2.28 gives

$$\sqrt{2}\cos\theta = -\sin\theta \quad , \tag{2.30}$$

$\cos^2\theta + \sin^2\theta = 1$, so

$$3\cos^2\theta = 1 \quad . \tag{2.31}$$

with reference to Equation 2.30

$$\Rightarrow \theta = -54^\circ 44' 8.2'' \quad , \tag{2.32}$$

This is the so called "magic angle", which is the angle between the body diagonal of a cube and each of its faces (Klinowski, 1990). Substituting θ and ϕ into Equations 2.25-2.27 gives the equations of the transformation

$$x' = \frac{1}{\sqrt{2}}(x - y) \tag{2.33}$$

$$y' = \frac{1}{\sqrt{6}}(x + y - 2z) \tag{2.34}$$

$$z' = \frac{1}{\sqrt{3}}(x + y + z) \quad . \tag{2.35}$$

Combining the electrode equations with the rotation equations and applying the condition that $a = \frac{w}{3}$ we obtain

$$x' = \frac{1}{\sqrt{2}}(2z + x - 3c) \quad , \tag{2.36}$$

$$= \frac{1}{\sqrt{2}}(r\cos\theta + 2r\cos(\theta + \phi)) \quad , \tag{2.37}$$

$$y' = \frac{1}{\sqrt{6}}(3x - 3c) \quad , \tag{2.38}$$

$$= \sqrt{\frac{3}{2}}(r\cos\theta) \quad . \tag{2.39}$$

Substituting y' into Equation 2.37 and expanding we obtain

$$x' = \sqrt{2}(r\cos\theta\cos\phi - r\sin\theta\sin\phi) + \frac{1}{\sqrt{3}}y' \quad , \tag{2.40}$$

$$= \sqrt{2}r\cos\theta\cos\phi - \sqrt{2r^2(1 - \cos^2\theta)}\sin\phi + \frac{1}{\sqrt{3}}y' \quad . \tag{2.41}$$

Substituting y' and regrouping

$$x' - \frac{y'}{\sqrt{3}}(2\cos\theta + 1) = -r\sqrt{1 - \frac{2x^2}{3}}\sin\phi \quad , \tag{2.42}$$

by squaring both sides it can be shown that

$$x'^2 + \frac{y'^2}{3}(4r\cos\phi + 5) - \frac{x'y'}{\sqrt{3}}(4r\cos\phi + 2) = 2r^2\sin^2\phi \quad . \tag{2.43}$$

If $\cos\phi = -\frac{1}{2}$ i.e. $\phi = -60^\circ$ or 120°

$$x'^2 + y'^2 = 3r \quad , \tag{2.44}$$

a circle centred on the z' axis is produced. The fine position, θ is determined by

$$\theta = \arctan \frac{x'}{y'} \quad , \tag{2.45}$$

Therefore, the phase shift determines what type of coordinate transform is necessary and in which plane the conic section will be a circle. This is far the most convenient curve to use, and it has important implications for the Spiral Anode, which is discussed in the Section 2.2.3.

2.2 Coarse Position

Various methods have been proposed for determining in which cycle an event has occurred.

2.2.1 The Double Diamond Cathode

This readout has not been used in a MCP based detector but in large, metre scale, drift chambers for particle physics detectors such as OPAL (OPAL Collaboration, 1991). However, it represents an example of a cyclic, continuous electrode readout that could in principle be used for MCPs.

Figure 2.4 shows the basic form of this readout (Allison *et al.*, 1985). The electrodes above the wire in the drift chamber are 90° out of phase with those below. Although the waveform is triangular, the analysis described in the previous section will be true for all of its Fourier components, and a square rather than circular locus would be produced (Allison *et al.*, 1991).

Fine position is determined with a triangular pattern of wavelength 171 mm and is proportional to arctan $\frac{epsilon_s}{\epsilon_c}$, where ϵ_s and ϵ_c are values returned the cathodes above and below the wire, respectively. The method for calculating the ϵ values is shown in Figure 2.4.

The coarse position is determined in a similar way with a triangular waveform with a wavelength 10 times longer. Allison *et al.* (1991), call this the medium position. Determining on which of the 1710 mm wavelengths an events occurs is determined by arrival time of events at either end of the wire or an extra series of electrodes. Resolutions of 1.5 mm have been achieved for a wire 10.4 m long, using 8 bit ADCs.

For an MCP based system, 4 channels would be required per dimension, each consisting of a preamp and an ADC.

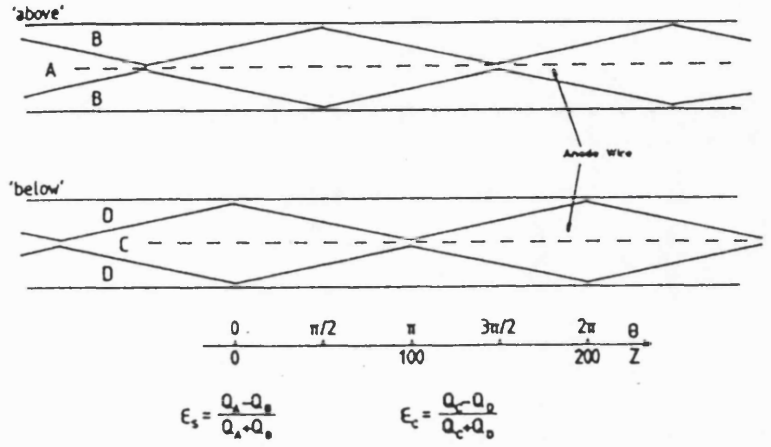

Figure 2.4: Schematic diagram of the Double Diamond readout.
The fine position is proportional to arctan $\frac{\epsilon_s}{\epsilon_c}$. From Allison *et al.* (1985).

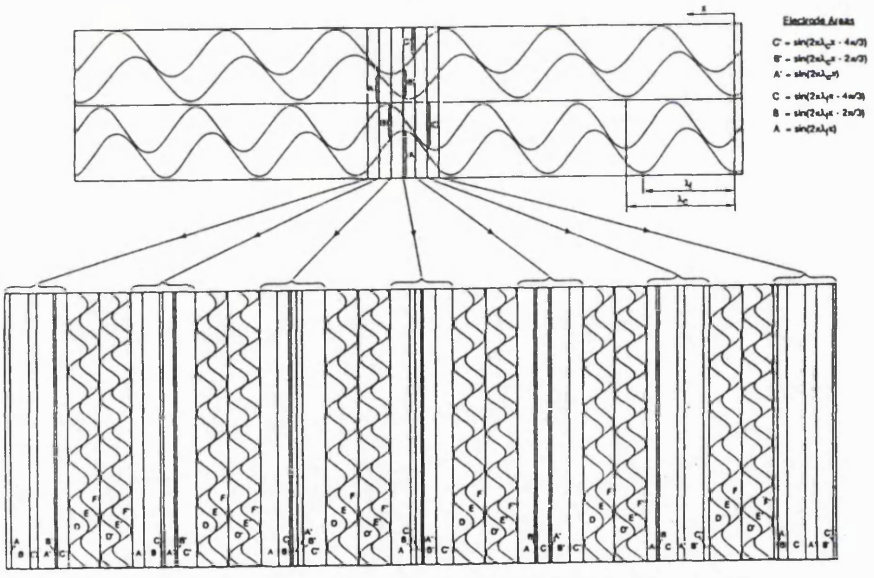

Figure 2.5: Schematic diagram of the Vernier anode.
As in Figure 2.4, the labels A, B and C correspond to the terms x, y and z in the analysis in the accompanying text. The Figure also shows a proposal for producing a two dimensional readout, which is discussed in the text. From Lapington *et al.* (1991).

2.2.2 The Vernier Anode

An example of the Vernier Anode is shown in Figure 2.5. The vernier anode uses two triplets of sinusoidal electrodes similar to those in Figure 2.1 and so would require six charge measuring channels per dimension. Both triplets have the same phase difference between the x and z electrodes but the two triplets have slightly different wavelengths (Lapington *et al.*, 1990, Lapington *et al.*, 1991). The coarse position is the difference between the phase angles returned from the two triplets.

Figure 2.5 also shows a proposal for producing a two dimensional readout. The position in the vertical direction is encoded by the six continuous sinusoidal electrodes in that direction. Horizontal position is determined by the other set of electrodes whose widths vary from pitch to pitch so as to represent the width ratios determined by sinusoidal electrodes at discrete intervals. These discrete and continuous axes represent an early proposal for producing a two dimensional detector but in practice a method similar to that described in Section 2.2.3 would probably be used.

2.2.3 The Spiral Anode (SPAN)

Unlike the other two examples, SPAN does not require any extra electrodes to determine the coarse position but achieves this by modulating the amplitude of the sinusoidal component of the electrode widths. Therefore, it requires only three channels of charge measuring electronics per axis.

If the amplitude of the sinusoidal electrode is directly proportional to the position along the length of the anode p then the widths of the electrodes are

$$x = c + kp\cos p \quad , \tag{2.46}$$

$$z = c + kp\cos(p+\phi) \quad , \tag{2.47}$$

$$y = 3c - (x+z) \quad , \tag{2.48}$$

assuming a phase difference of 120°, although it would be equally true for 90°, and following the procedure described in Equations 2.36-2.44

$$x'^2 + y'^2 = 3(kp)^2 \quad , \tag{2.49}$$

or converting into polar coordinates

$$r = \sqrt{3}kp \quad , \tag{2.50}$$

which is the equation for an Archimedean Spiral. Figure 2.6 shows the evolution of the spiral as the position moves along the electrodes.

The fine position is determined by by the phase angle θ in the usual manner and the coarse position is determined by calculating which spiral arm an event lies on. The position is therefore,

$$p \propto \theta' = 2n\pi + \theta \quad , \tag{2.51}$$

where n is the spiral arm number.

If p is made directly proportional to θ' the resolution of the detector will vary as the spiral evolves, i.e. along the length of the anode. As shown in Figure 2.6, the wavelength decreases as the amplitude decreases. This is to ensure the change of spiral arc length is approximately constant for equal lengths along the anode. If the spiral arc length is chosen as the measure of position, rather than θ', varying the wavelength can keep the resolution constant across the width of the detector (Lapington *et al.*, 1990 and Lapington *et al.*,1991).

Figure 2.7 shows an increment in the arc length of the spiral, S for a small increment of the angle θ. From this figure we can see that

$$\delta S^2 = (r\delta\theta)^2 + \delta r^2 \quad . \tag{2.52}$$

Given the general equation of a spiral in polar coordinates

$$r = k\theta \quad , \tag{2.53}$$

we can express δS^2 as

$$\begin{aligned} \delta S^2 &= (k\theta\delta\theta)^2 + (k\delta\theta)^2 \quad , \\ &= k^2(\theta^2+1)\delta\theta^2 \quad , & (2.54) \\ \Rightarrow \frac{dS}{d\theta} &= k(\theta^2+1)^{\frac{1}{2}} \quad . & (2.55) \end{aligned}$$

The general solution to an integral of the form

$$y = \int (x+a)^{\frac{1}{2}} dx \quad , \tag{2.56}$$

is

$$y = \frac{1}{2}\left[x\sqrt{x^2+a} + a^2 \log\left(x + \sqrt{x^2+a}\right)\right] \quad , \tag{2.57}$$

(Weast, 1966). Therefore,

$$S = \frac{k}{2}\left[\theta\sqrt{\theta^2+1} + \log\left(\theta + \sqrt{\theta^2+1}\right)\right] \quad . \tag{2.58}$$

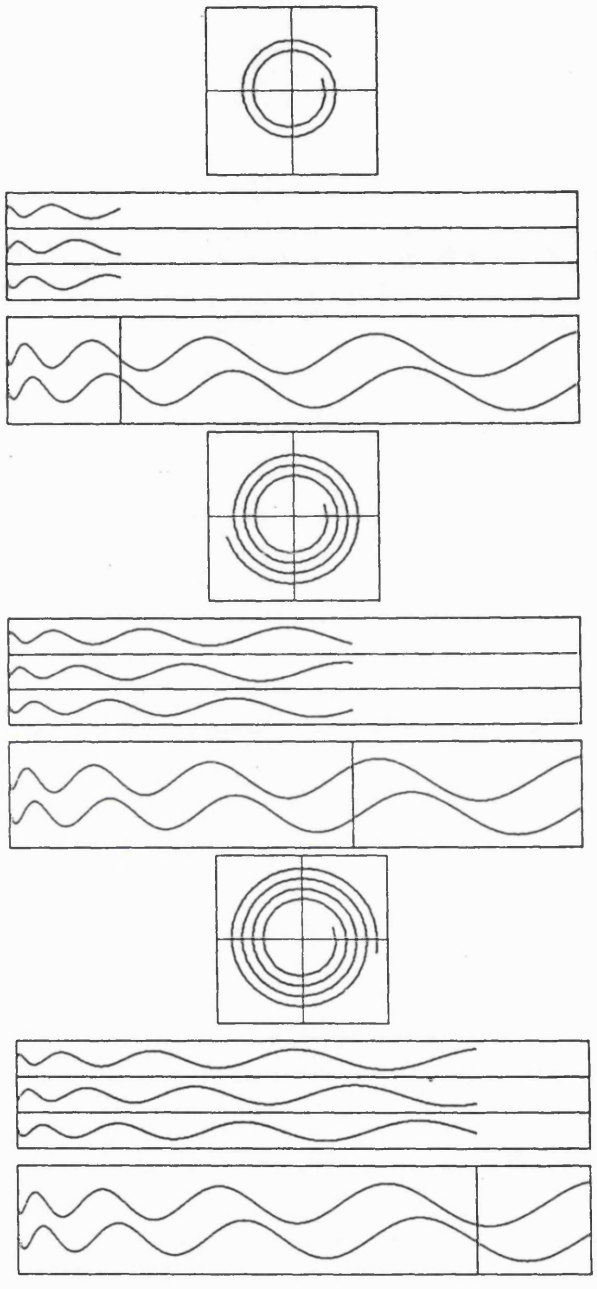

Figure 2.6: The evolution of the spiral with movement along the anode. The various parts of the three figures correspond to those in Figure 2.1.

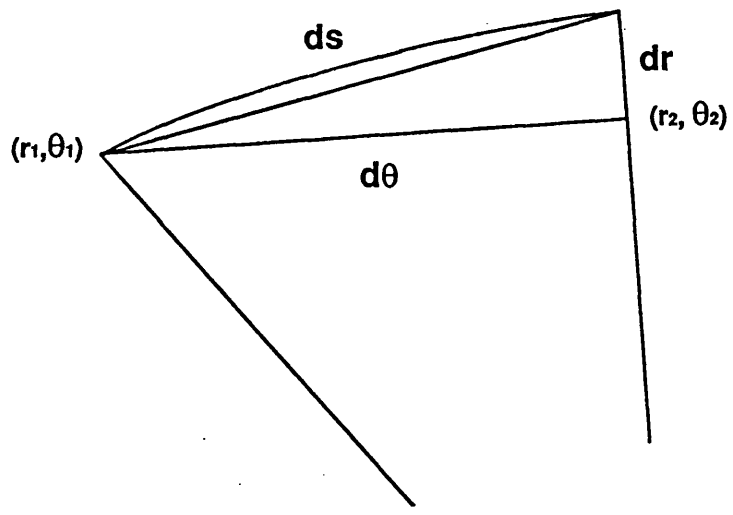

Figure 2.7: The differential increase of arc length for a curve.

If we substitute Equation 2.55 with

$$\frac{dS}{d\theta} \sim k\theta \quad , \tag{2.59}$$

then we can express the condition that the rate of change of S with position p as

$$\frac{dS}{dp} = \frac{dS}{d\theta}\frac{d\theta}{dp} \quad , \tag{2.60}$$

$$\sim k\theta\frac{d\theta}{dp} \quad , \tag{2.61}$$

therefore to keep the rate of change of arc length with position approximately constant requires that

$$\frac{d\theta}{dp} = \frac{c}{\theta} \quad . \tag{2.62}$$

2.3 Practical Anodes

So far, only SPAN has been used as a MCP readout. However the techniques used in constructing a SPAN readout could be also used for the double diamond and the vernier.

Figure 2.8 shows a portion of the a one dimensional SPAN readout which is currently being developed for the Coronal Diagnostic Spectrograph (CDS) on ESA's SOHO mission (Breeveld *et al.*, 1992a). The anode consists of a periodic repetition of the triplet of

sinusoidal electrodes. This figure shows 5 such triplets while the actual detector would consist of approximately 50 sets. The x electrodes for all the triplets are connected together in parallel, usually by wire bonding, at the ends of each triplet. All the y and z electrodes are also connected in the same manner.

The triplets must be repeated, placed side by side, to ensure that each set of sinusoidal electrodes samples the charge cloud accurately. The repeat pitch of the triplets is typically 600 μm. Like most continuous electrode readouts (Section 1.3.2), SPAN requires a gap of several millimetres between the MCP stack and the anode, to ensure that the charge cloud is large enough to cover several pitches. The size and spatial distribution of the MCP charge cloud and their interaction with readouts are discussed in the next chapter.

Figure 2.9 shows how a two dimensional SPAN readout can be made. The triplets for each of the axes are interleaved but the sinusoids have been projected through 45° and drawn at 45° to the axes, so that the projections onto the axes are normal sinusoids (Lapington *et al.*, 1991).

The two dimensional SPAN is discussed in detail in Chapter 5.

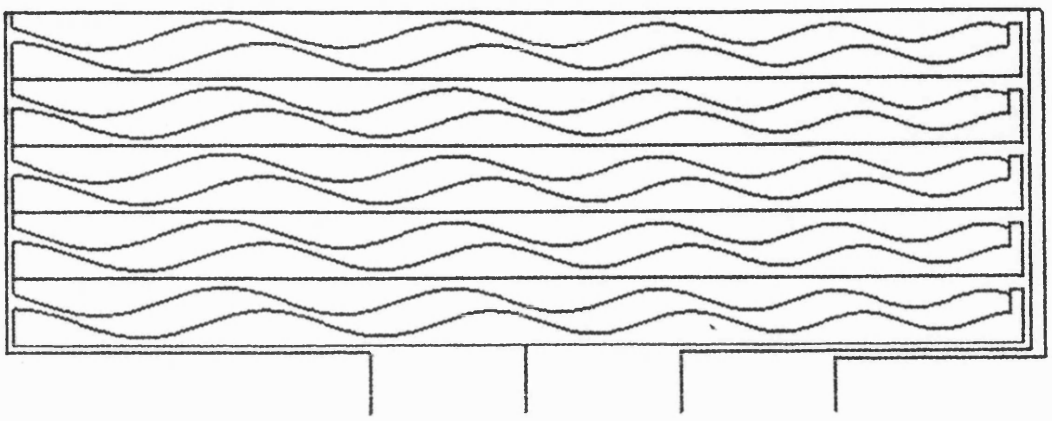

Figure 2.8: Schematic diagram of the one dimensional SPAN readout for the SOHO satellite. The width of the electrode triplets has been expanded by a factor of 10 for clarity. From Breeveld *et al.* (1992b).

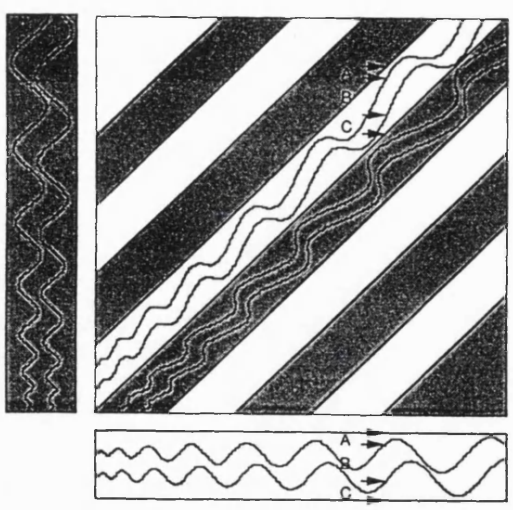

Figure 2.9: Schematic diagram of a two dimensional SPAN.
The labels A, B and C correspond to the terms x, y and z in the analysis in the text. From Lapington *et al.* (1992).

Chapter 3

Techniques for Measuring the Size and Spatial Distribution of Electron Clouds From Microchannel Plates

3.1 Introduction. The Interaction of MCP Charge Clouds with Readouts

In all MCP readouts with a repeat pitch, it is necessary that the pitches oversample the charge cloud. If the charge cloud is too small with respect to the pitch, the charge cloud is undersampled and an effect analogous to aliasing, called modulation or differential nonlinearity, is introduced. This effect has been studied experimentally and by computer simulation for the WSA (Smith *et al.*, 1989, Vallerga *et al.*, 1989). Figure 3.1 shows an example of modulation.

Modulation can be overcome by allowing the charge cloud to spread over a larger area. However, if the cloud is too large, charge will be lost off the edge of the anode introducing another distortion. For the WSA, this is known as "S distortion", see Figure 3.2. Therefore, the anode design places constraints on the charge cloud size or a given cloud size will place constraints on the anode design.

The spatial distribution of the charge cloud also affects the continuous cyclic elec-

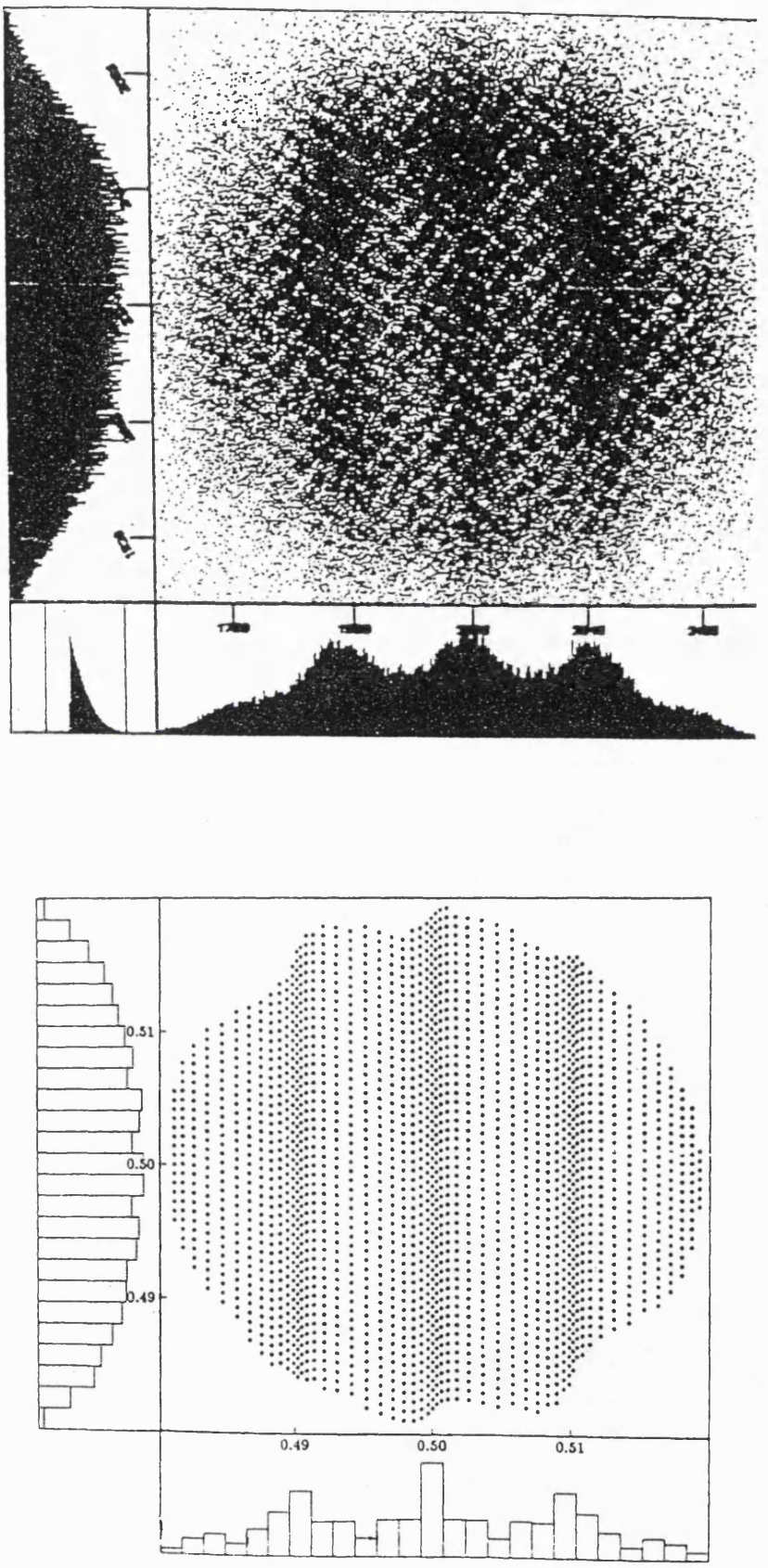

Figure 3.1: An example of measured and simulated modulation for a WSA. The histograms at the edges of the the central image are the intensity distributions integrated across each dimension. From Smith *et al.*, 1989.

trodes discussed in the previous chapter as the charge cloud will behave as a spatial, band pass filter. Convolution with the charge cloud will reduce the magnitude of any spatial frequency component. Any continuous, cyclic detector which contains more than one spatial frequency component in its electrode structure , i.e. any type that produces an ideal Lissajous figure other than a circle, will have the magnitudes of those components reduced by varying amounts depending on their frequency. Therefore the resultant Lissajous figure will be distorted. Such effects have been observed in the double diamond cathode, see Figure 3.3. The extent of this distortion will be dependent on the size and distribution of the charge cloud as this defines the filter response.

Carter *et al.* (1990) have modelled the affect of varying event width on the centroiding for the MIC detector, see Section 1.3.1. They find positional shifts of the order of 10 μm due to undersampling for too small an event and a loss of signal outside the 5 or 9 pixels used in centroiding if the event is too wide. They suggest that a detailed knowledge of the spatial distribution of the charge cloud would enable these shifts to be removed during calibration.

All of these studies assumed a charge cloud distribution, usually a Gaussian as was suggested by the group at Berkeley (Martin *et al.*,1981). However, the same group found that the charge cloud was not quite Gaussian but the core was sharper and the wings more extended (Jelinsky, 1979). Both of the WSA studies (Smith *et al.*, 1989, Vallerga *et al.*, 1989) found that a quantitative prediction of a charge division readout's performance depends sensitively on the assumed charge cloud distribution. A detailed knowledge of the charge cloud for a given set of MCP operating conditions allows the simulation of the operation of an anode and characterization of the effects of modulation. It should also allow selection of anode designs that will minimize the effects of modulation for that set of operating conditions.

3.2 The Split Strip Anode

Lapington *et al.* (1988) developed the Split Strip Anode specifically to measure the spatial distribution of the charge cloud. Figure 3.4 shows a simplified version of the anode. The anode is a Strip and Strip detector with an insulating gap down the middle, i.e. a split. The position, along the x axis, of the centroid of the charge cloud and the fraction of charge falling on one side of the split can be measured simultaneously, for each event.

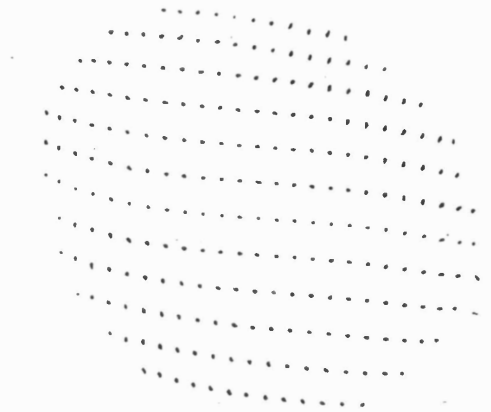

Figure 3.2: Measured S-distortion for a WSA.
From Vallerga *et al.*, 1989.

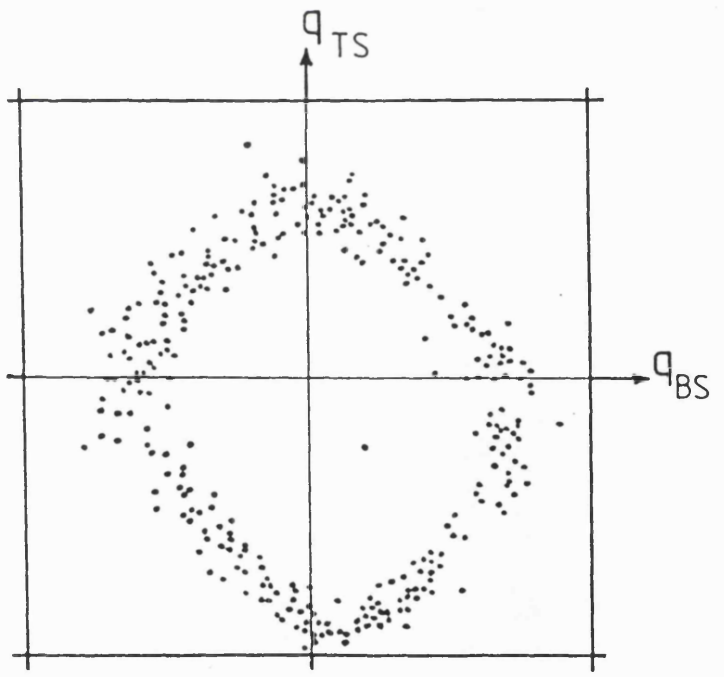

Figure 3.3: Output from the double diamond cathode showing the effects of the convolution of the charge cloud with the geometry of the electrodes.
An ideal detector would produce a square image. The values q_{TS} and q_{BS} correspond to the values ϵ_s and ϵ_c in Figure 2.4. From Allison *et al.*, 1991.

The centroid position, cp, and the fractional charge, fc, are given by

$$cp = \frac{Q_A + Q_D}{Q_A + Q_B + Q_C + Q_D} \quad , \tag{3.1}$$

$$fc = \frac{Q_C + Q_D}{Q_A + Q_B + Q_C + Q_D} \quad . \tag{3.2}$$

Two different sized anodes were used due to the large variation in sizes of charge clouds encountered during the experiment. The first anode had a pattern repeat pitch of 630 μm, was 27 mm across with a scale of 9.54 μm/pixel, which was defined by the use of 12 bit ADCs. The second anode was a half scale version of the first, *i.e.* a pattern repeat pitch of 315 μm, 4.77μm/pixel and 13.5 mm active width.

3.3 The Experimental Setup

Figure 3.5 shows a schematic diagram of the general layout of the detector, demonstrating the various parameters that describe the operating conditions for which the charge cloud was measured. The detector consists of a pair of 36 mm, Phillips, resistance matched, double thickness microchannel plates in a chevron configuration. The MCPs have a pore diameter of 12.5 μm, an end-spoiling of a half a pore diameter, a pore bias angle of 13° and the pores have a length to diameter ratio of 80:1.

During the experiment, the MCPs were illuminated by Al-K X-rays, $\sim$ 1.5 keV, through a slot orientated parallel to the x axis of the anode. The length of the slot is approximately equal to the active width of the anode. The pores spread along the length of this slot provide the variation in cp; no mechanical scanning takes place. Pores at either end of the slot deposit most of their charge on one side of the anode; whereas pores in the middle deposit approximately equal amounts of charge on either side of the split.

The actual output from the experiment is the function of fc against cp. An example of a typical result is shown in Figure 3.6 representing the output from 45000 events, which is number of events acquired for almost all of the measurements. For obvious reasons we call the function the S curve. In all the cases described in the next chapter, the same number of events were acquired at a count rate of approximately 500 to 600 counts s^{-1} with a background event rate less than 10 counts s^{-1}.

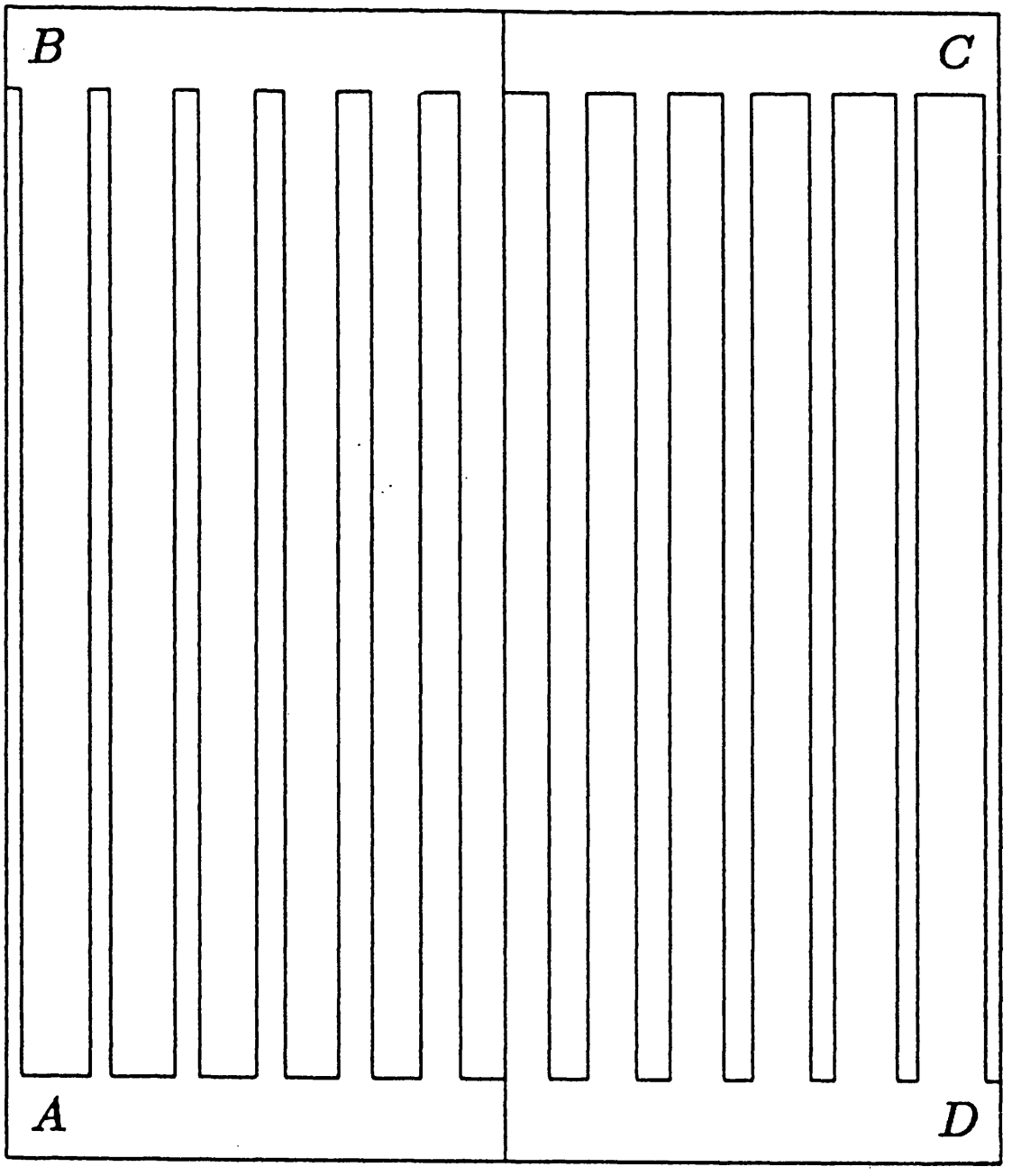

Figure 3.4: Schematic diagram of the Split Strip anode.
From Edgar *et al.* (1989).

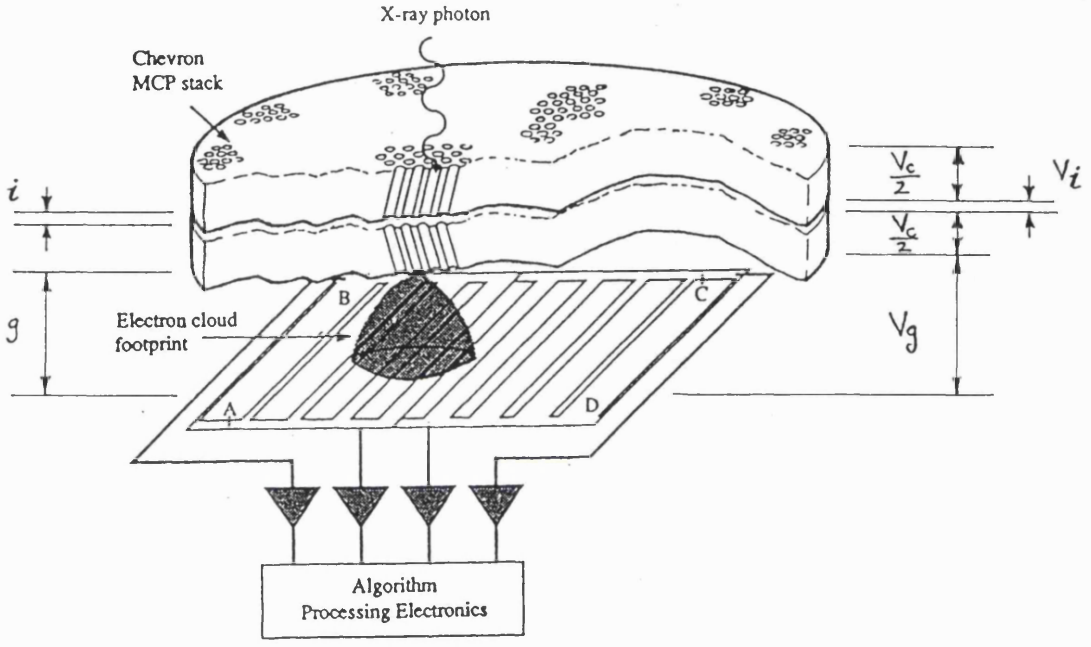

Figure 3.5: Schematic diagram of the general layout of the detector.

The notation is as follows:

- V_c: The voltage applied across the chevron pair. Approximately equal voltages were applied to each of the MCPs in all cases.
- i: The inter-plate gap.
- V_i: Voltage applied across the inter-plate gap.
- g: The width of MCP-anode gap.
- V_g: The voltage applied across the anode gap.

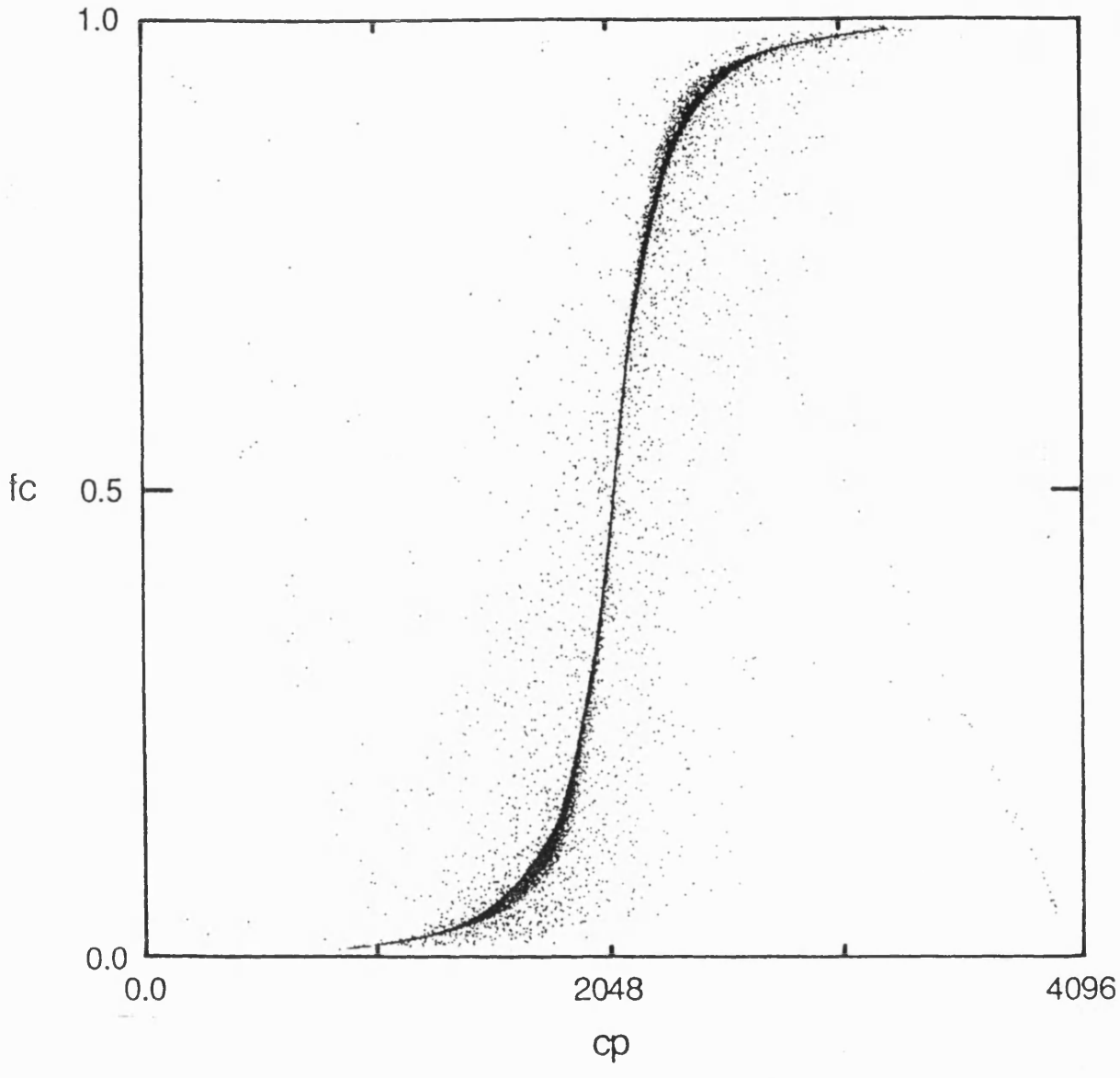

Figure 3.6: The S curve returned by the Split Strip anode.
This curve was obtained at $V_c = 2.65$ kV, $V_g = 100$ V and $g = 6.2$ mm. Centroid position is given in screen pixels, where, in this case, one screen pixel corresponds to 9.54 μm. The points far from the S curve are single events while those on the curve represent typically 50 to 100 events. The straight line visible in lower right corner of the figure, is an artefact produced by clipping. From Edgar *et al.* (1989).

3.3.1 Electronics and Data Acquisition

The electronics and data acquisition for this experiment are the same as used by Lapington *et al.* (1986). The signals from the Split Strip anode are processed by four parallel channels of electronics, each consisting of a low noise, charge-sensitive preamplifier, followed by a shaping amplifier and finally a peak-detecting, 12 bit Wilkinson ADC. The data from the four ADCs are multiplexed on to a parallel bus controlled by a personal computer (PC). The PC continuously examines the status of the data ready line from each ADC. When one data ready line goes high to indicate that one ADC has digitized a pulse, the PC begins a timing loop, and looks for data from the remaining ADCs within the ADC conversion time. If all four ADCs digitize data within that time, the PC accepts this as a valid event and addresses each ADC in turn to read the digitized data. If one or more ADCs do not fire, the PC rejects the data and resets the ADCs to await the next event.

In order to both simplify and make more systematic the process of calibrating the gains and DC offsets of the four parallel processing channels, a closed loop calibration technique is employed. The PC outputs a digital magnitude to a high precision DAC, the output of which is used as the reference voltage for a reference pulse generator. The pulses are fed to the test inputs of the four preamplifiers. The PC then acquires data in the normal way for a range of digitally defined pulse amplitudes and performs a least squares fit of the ADC data versus the data output to the DAC. The gains and DC offsets are displayed on the screen, allowing them to be trimmed iteratively. Fine tuning of the gains is performed by connecting the pulse generator output through an external test capacitor to the input of each preamplifier in turn, to by-pass the affect of the small differences in values of the internal test capacitances.

3.4 Analysis of the S curve

3.4.1 The Probability Density Distribution of the One Dimensional Integrated Charge Cloud

The S curve, $S(cp)$, corresponds to the cumulative probability distribution function of the charge cloud, $P(cp)$. This function gives the probability that any instantaneous value of $cp(t)$, will be less than or equal to cp', as $P(cp')$, *i.e.*

$$P(cp') \;=\; \text{Prob}\,[cp(t) \leq cp']$$

$$= \int_{-\infty}^{cp'} p(cp)d(cp) \quad , \tag{3.3}$$

where $p(cp)$ is the probability density function (Brendat and Piersol, 1966). Therefore, $p(cp)$ can be determined by

$$p(cp) = \frac{dP(cp)}{dcp} \quad . \tag{3.4}$$

As the Split Strip anode has translational symmetry parallel to the split, *i.e.* the y axis, it can only produce one dimensional information about the charge cloud. The function $S(cp)$ represents the charge distribution integrated along the y axis. Therefore, the function $p(cp)$ corresponds to the probability density distribution of the one dimensional integrated charge cloud. It represents the percentage of the charge cloud lying within a window of cp with a constant, finite width. Figure 3.7 shows an example of $p(cp)$.

It must be stressed that the Split Strip anode measures the probability distribution of the charge cloud. It does not represent the number of electrons collected at any one point but the fraction of the total charge cloud. The number of electrons can be determined if the gain is known. In this and the next chapter, when I discuss the size of the charge cloud, I am always referring to the width of the probability distribution. This allows direct comparisons between the radial distributions of charge clouds containing a large variation in the total number of electrons.

3.4.2 The Structure and Reduction of the S curve

The S curve is reduced to a curve consisting of the average fc for a given cp. The mean is determined over the whole range of fc for bins of cp 30 pixels wide, i.e. the sections along which $\overline{fc}$ is determined, are always parallel to the fc axis.

The S curve consists of contributions from the charge clouds of tens of thousands of events with pulse heights spread across the entire PHD. Figure 3.8 shows how the variation in pulse height affects the shape of the S curve. In the linear region and at the edge of the curve, there is no appreciable variation. However in the region of high curvature there is a marked spectrum produced by the varying pulse height. It appears that this region is most sensitive to a variation of charge cloud size with pulse height.

Figure 3.9 shows cross sections through the S curve, parallel to the fc axis at a selection of points. In the central, linear region the cross sections are approximately Gaussian. The cross sections through the regions of high curvature have the same general

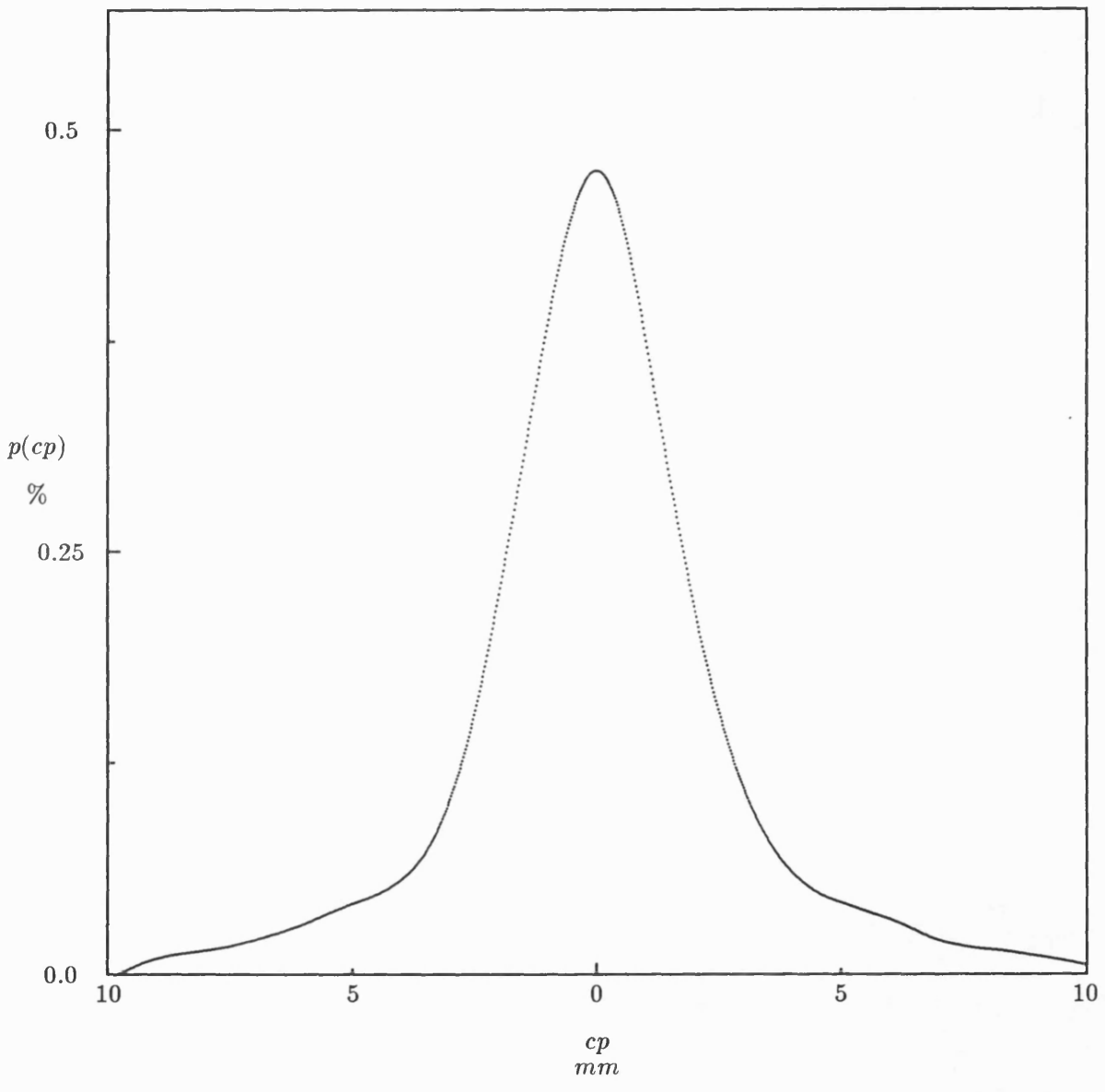

Figure 3.7: The probability density distribution of the integrated one dimensional distribution, $p(cp)$ of the charge cloud obtained from the data represented in Figure 3.6.
The values of $p(cp)$ represent the fraction of the charge cloud lying within a 20 μm segment of cp. The values of $p(cp)$ quoted in all the appropriate curves in this chapter correspond to this width. The points in the curve indicate the values for which the cubic spline is tabulated. The derivative of this curve, i.e. the second derivative of $S(cp)$, is used to estimate the centre of the charge cloud which is then set to be the point at which $cp = 0$.

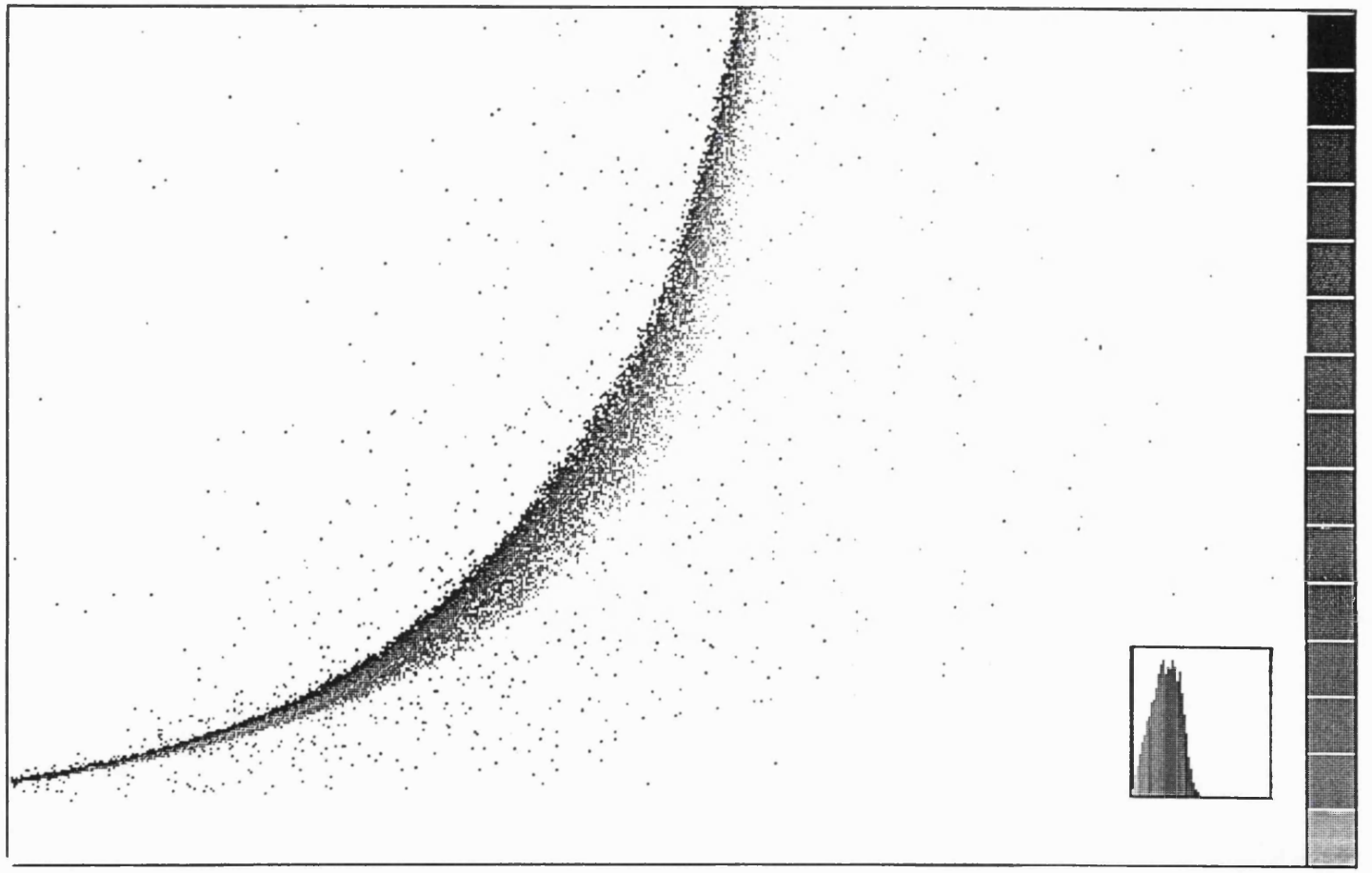

Figure 3.8: The variation in the S curve with varying pulse height.
This figure is the bottom half of Figure 3.6. The grey scale is proportional to the pulse height of the event. The PHD is shown in the inset.

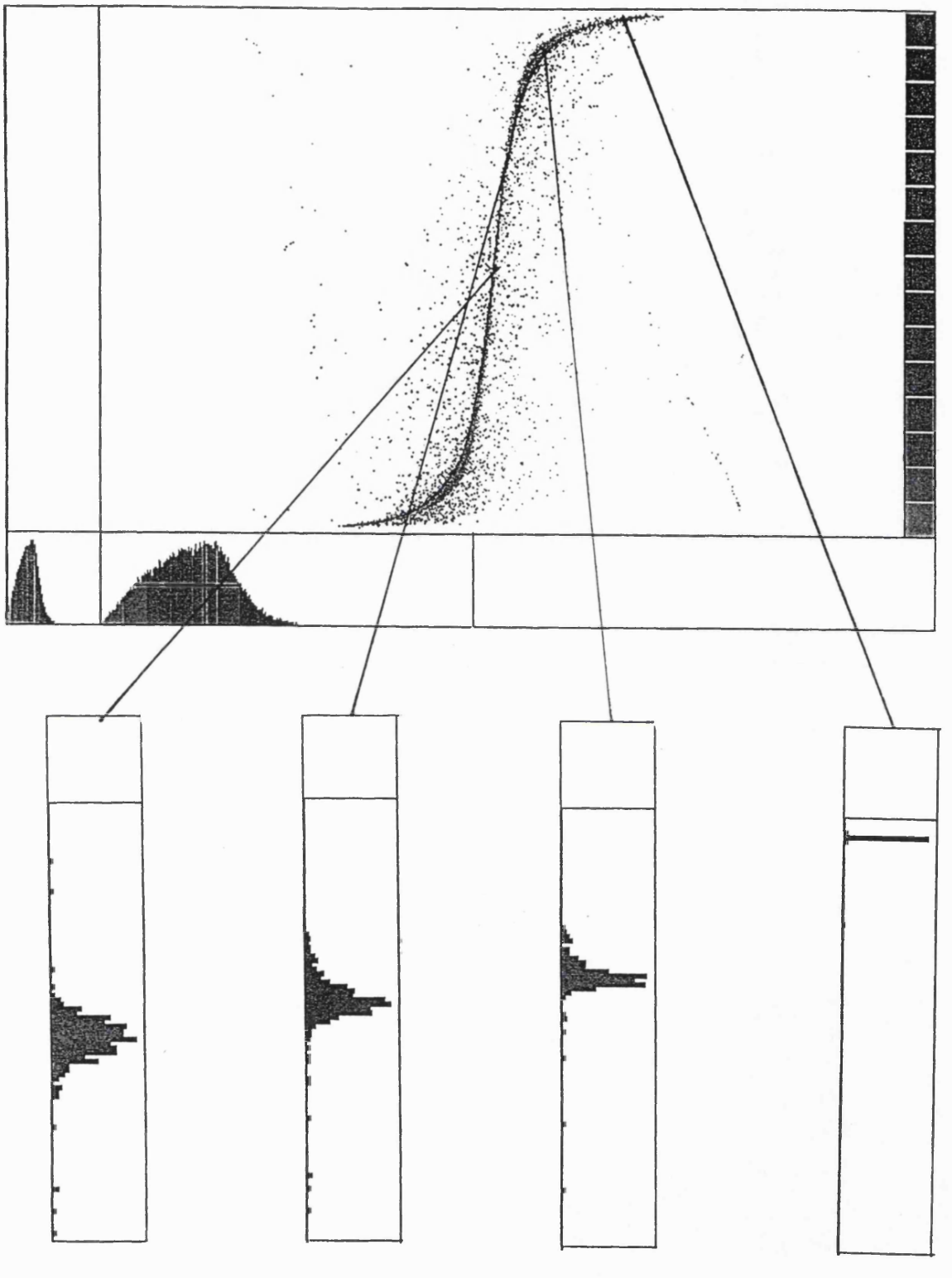

Figure 3.9: Selected cross sections through the S curve.
The width of the sections is approximately equal to the width of the *cp* bins used during the reduction to $S(cp)$. The greyscale in the central window represents a linear intensity scale with unit steps.

shape as the PHD. So in these regions it is reasonable to assume that the cross sections normal to the S curve are proportional to the PHD, and the cross sections in Figure 3.9 are the projections of these normal sections onto a line parallel to the fc axis. As the PHDs are approximately Gaussian, so are the cross sections parallel to the fc axis. Therefore, the data points are approximately normally distributed about the mean S curve.

These cross sections are symmetric about the centre of the curve. The lower pulse height events are always on the outside of the curve, i.e. further from the centre indicating a tighter S curve. This behaviour was observed in every S curve obtained during the experiment. This suggests that charge cloud size is a function of gain, with lower gain events producing smaller charge clouds.

After reduction, the mean S curve, $S(cp)$, consists of on average 80 points with coordinates $(cp_i, \overline{fc_i} \pm \sigma_i)$, where σ_i is one standard deviation for the ith. bin.

In practice, $p(cp)$ is determined from the derivative of $S(cp)$. As differentiation enhances noise, a smoothing, cubic spline (Mc Kinley, 1986) was used to produce the $p(cp)$ curves. The spline contains 2000 data points across the width of $S(cp)$.

3.4.3 Qualitative Discussion of the Charge Cloud Using $p(cp)$

The distribution $p(cp)$ is useful in describing the gross behaviour of the charge cloud (Edgar *et al.* 1989, Chappel & Murray, 1989, Rasmussen & Martin, 1989). Figure 3.10 shows an example of the effects of varying the electric field strength in the MCP anode gap. Both curves show indications of at least two components. At low electric fields there is a broad central core with extensive wings. At high electric fields, most of the charge cloud is concentrated in a small, well defined peak with only small wings.

Figure 3.11 shows the affect of the voltage across the chevron, V_c, on the charge cloud. There is little difference in the behaviour of the edges of the distribution but the lower V_c produces a more well defined peak with a larger percentage of charge concentrated in it.

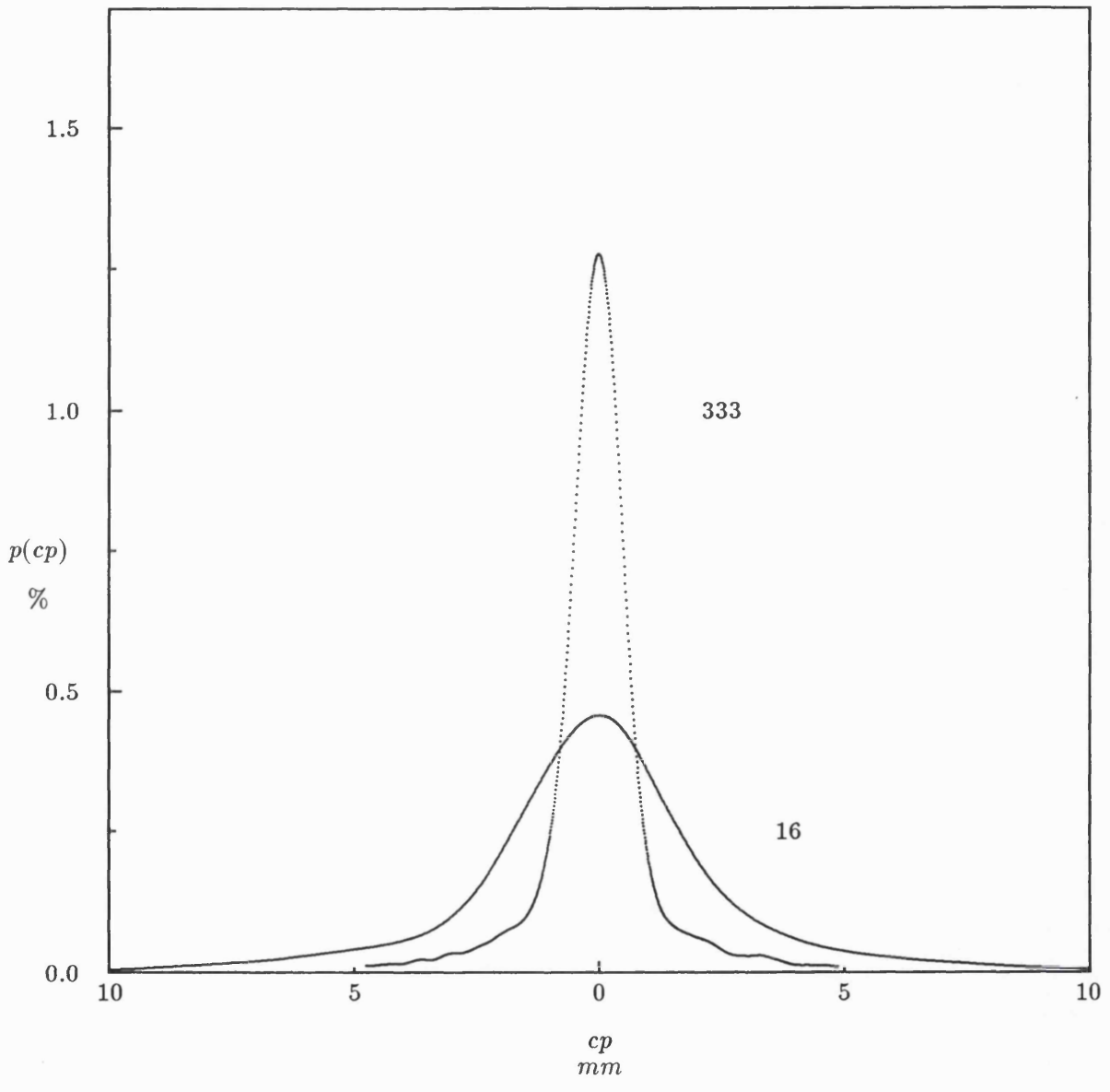

Figure 3.10: The effect of electric field strength in the anode gap on the charge cloud. Both curves were obtained at $V_c = 2.8$ kV. The field strengths are as indicated in kV.m^{-1}. The two centres of the charge cloud have been aligned during analysis, in this and the next diagram.

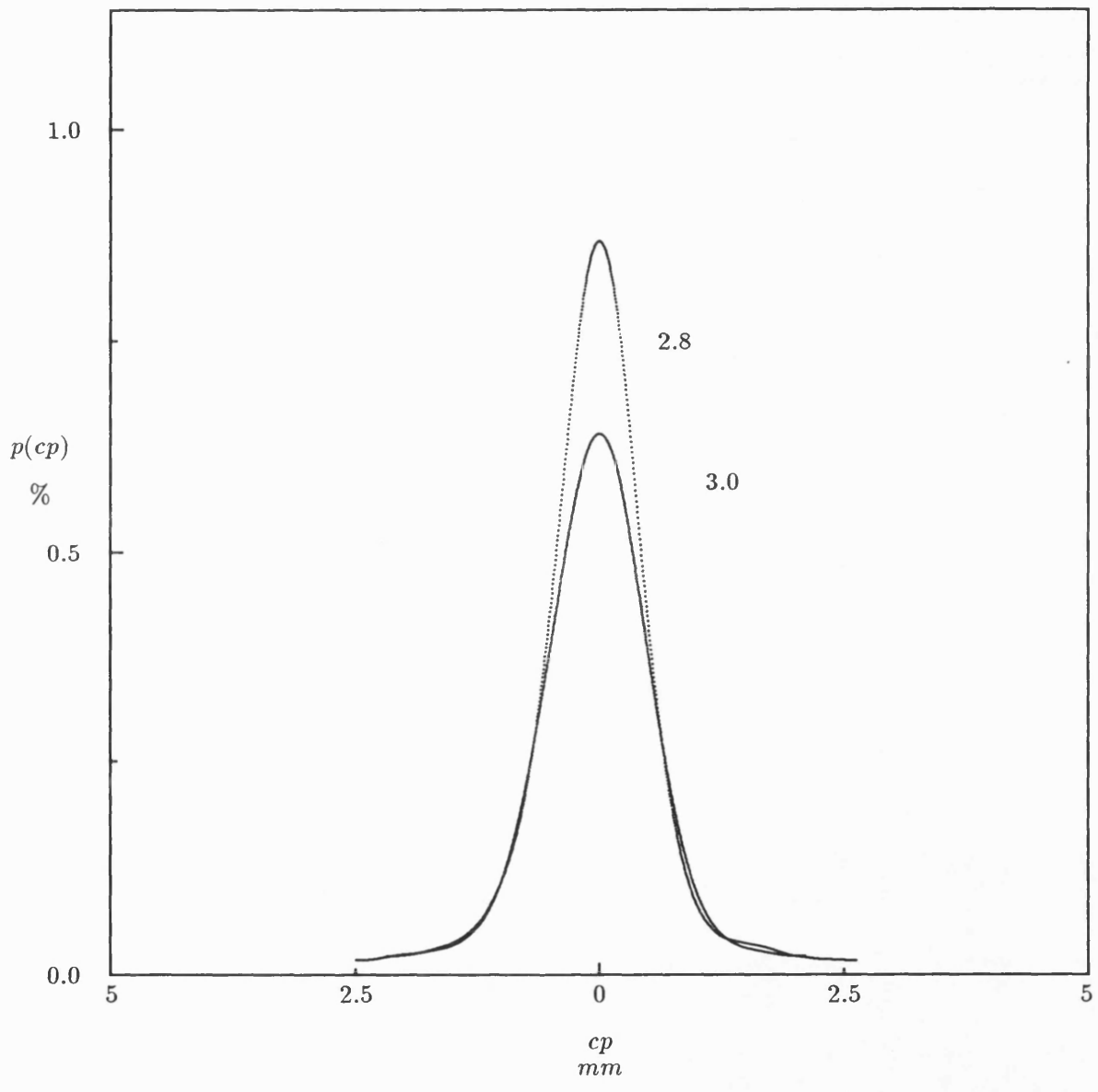

Figure 3.11: The effect of plate bias voltage on the charge cloud.
Both curves were obtained with 200 V applied across a 3 mm anode gap, i.e. 67 $kV.m^{-1}$.

3.5 Determining The Radial Distribution of the Charge Cloud

The models developed to study modulation both require the radial distribution of the charge cloud, rather than just the integrated distribution. (Smith *et al.*, 1989, Vallerga *et al.*, 1989). The radial distribution also presents a simpler, more general description of the charge cloud and would overcome any ambiguity introduced by integration, inherent in $p(cp)$.

In order to discuss the data quantitatively, it is necessary to obtain a best fit to the data. We chose to fit directly to the mean S curve, $S(cp)$ rather than $p(cp)$ in which the data has already undergone significant manipulation.

3.5.1 Necessary Conditions for Determining the Radial Distribution of the Charge Cloud

As no mechanical scanning takes place, the S curve does not represent the charge cloud from one group of pores in the bottom MCP. It is the aggregate of all of the charge clouds distributed across the anode. The spatial distribution can be determined without mechanical scanning only if the form of the charge cloud remains constant along the length of the slot. Figure 3.12 demonstrates that regions equi-distant from the approximate centre of the slot have similar charge cloud distributions. Therefore, it is a reasonable assumption that the general form of the charge cloud is constant along the length of the slot.

As the S curve represents the charge cloud integrated along the fc axis, determining the radial distribution from the S curve requires the assumption that the charge cloud has azimuthal symmetry. A possible source of asymmetry is the orientation of the pore bias angle with respect to the anode split. Figure 3.13 compares the distributions from the two orientations. The similarity between the two indicates only a small degree of asymmetry in the distribution and so, to a first order approximation, the charge cloud is radially symmetric. The topic of charge cloud symmetry is discussed further in Section 4.5.

3.5.2 The Inversion

The methods for carrying out the inversion and determining the linear least squares solution, see Section 3.5.4, described here, in Edgar *et al.* (1989) and Lapington & Edgar

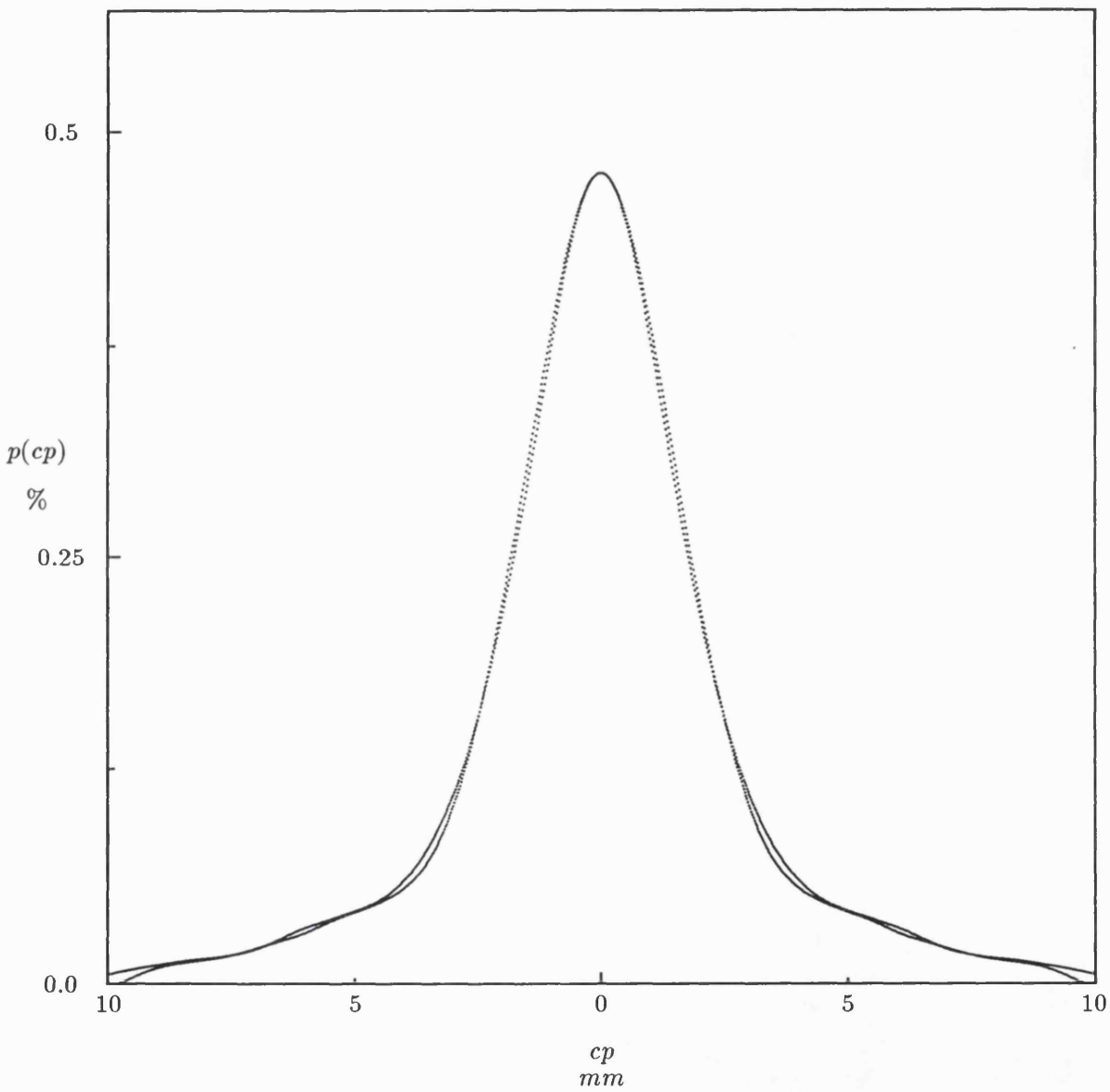

Figure 3.12: The $p(cp)$ curve displayed in Figure 3.7, overlayed with its reflection about its centre.

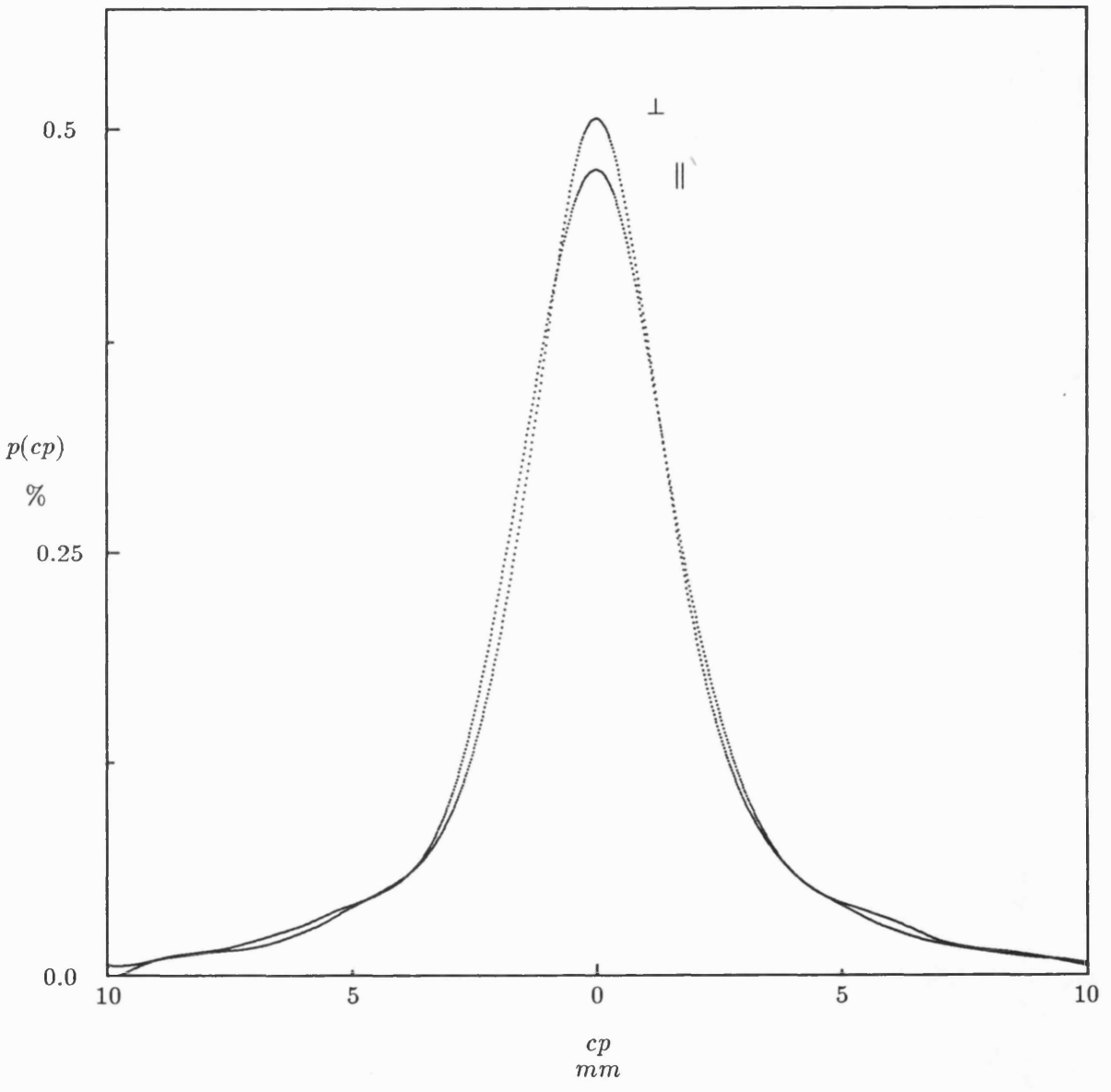

Figure 3.13: Two overlayed $p(cp)$ curves obtained with the pore bias angle aligned normal and parallel to the split.

The curve obtained with the bias angle normal to the split is the same as is shown in Figure 3.7.

(1989) follows that determined by Kessel (1988).

Let the spatial distribution be represented by a radial distribution, $N(r)$; the measured S curve, $S(cp)$, is produced by the convolution of $N(r)$ with the Split Strip. The radial distribution can be determined by carrying out an inversion, *i.e.* find an expression for $N(r)$ that generates $S(cp)$. The S curve is expressed as a function of $N(r)$ by

$$S(cp) = \frac{2\pi\int_0^{cp} rN(r)dr + 2\int_{cp}^{r_{limit}}[\pi - \arccos(\frac{cp}{r})]rN(r)dr}{2\pi\int_0^{r_{limit}} rN(r)dr} \quad , \tag{3.5}$$

where r_{limit} is the radius containing all of the charge. In the analysis, this radius is taken to be equal to the half-width of the anode. Figure 3.14 shows the areas of the charge cloud corresponding to each of the three terms.

The second term in the numerator of Equation 3.5 is

$$2\int_{cp}^{r_{limit}}[\pi - \arccos(\frac{cp}{r})]rN(r)dr \quad . \tag{3.6}$$

As only one of the limits of this integral is fixed, inverting this expression for $N(r)$ is a Volterra problem of the first kind (Arfken, 1970), *i.e.*

$$f(x) = \int_a^x K(x,t)\phi(t)dt \quad , \tag{3.7}$$

where $K(x,t)$ is a known function called the kernel and $\phi(t)$ is the unknown function. Expressions such as Equation 3.7 can be sometimes solved for the unknown function $\phi(x)$ as a function of $f(x)$ and $K(x,t)$. In this case the kernel is

$$K(cp,r) = r(\pi - \arccos(\frac{cp}{r})) \tag{3.8}$$

and the unknown function is the radial distribution $N(r)$.

If the kernel is separable, *i.e.* $K(x,t)$ can be expressed as a sum of of n terms

$$K(x,t) = \sum_{j=1}^{n} M_j(x)N_j(t) \quad , \tag{3.9}$$

where n is a finite number, the integral can be replaced by a finite series of simultaneous algebraic equations. Then the unknown function $\phi(x)$ can be expressed as the sum of a finite number of terms. However, in this case the kernel

$$\begin{aligned} K(cp,r) &= r(\pi - \arccos(\frac{cp}{r})) \quad , \\ &= r(\pi - \int_{\frac{cp}{r}}^{1} \frac{dt}{\sqrt{1-t^2}}) \quad . \end{aligned} \tag{3.10}$$

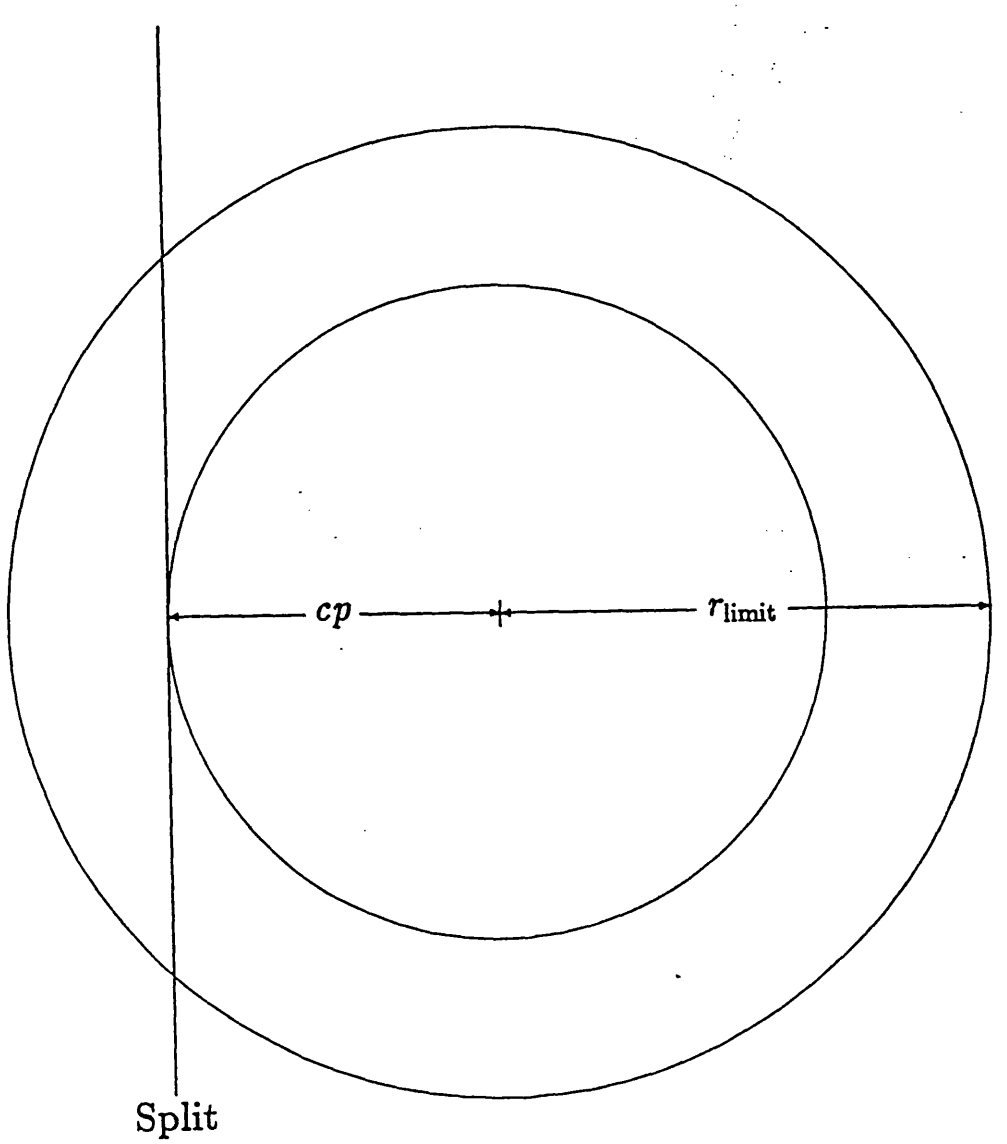

Figure 3.14: The annular regions of the charge cloud corresponding to the three terms in Equation 3.5.

The first integral in the numerator is the charge inside the circle of radius *cp*. The second integral in the numerator is the charge within the backwards 'C' shaped region outside the first region and to the right of the split. The denominator is the total charge within the circle of radius r_{limit}. From Edgar *et al.* (1989).

This cannot be expressed as a finite sum of terms of the form of Equation 3.9. Therefore, the unknown function, $N(r)$, would have to be expanded as an infinite Neuman series and this would only be successful if that series converged. This method is not practical as it would have to be carried out for each different S curve and there is no guarantee that an analytical solution exists in every case. As a result, we decided to carry out a numerical procedure based on the Least Squares Fit to determine $N(r)$.

3.5.3 The Least Squares Problem

The radial charge distribution can be modelled as the sum of n terms

$$N(r) = a_1 N_1(r) + a_2 N_2(r) + \cdots + a_n N_n(r) \quad , \tag{3.11}$$

where a_1, a_2,...,a_n are the weights of the components which make up the radial charge distribution. For computational ease we impose the normalization condition, $a_1 + a_2 + \cdots + a_n = 1$. An S curve is generated by substituting each of the terms in Equation 3.11 into Equation 3.5, producing a series of basis functions. The integrals in this expression are evaluated by a numerical method based on cautious Romberg integration (de Boor 1970, 1971).

The generated S curve is the sum of these basis functions,

$$S(cp) = a_1' S_1(cp) + a_2' S_2(cp) + \cdots + a_n' S_n(cp) \quad . \tag{3.12}$$

This S curve is then compared to the measured, mean S curve, which is expressed by the coordinates $(cp_i, fc_i \pm \sigma_i)$. We use the weighted χ^2 as a figure of merit for the fit which is computed in the standard way as

$$\chi^2 = \sum_i^m \left[\frac{fc_i - S(cp_i)}{\sigma_i} \right]^2 \quad , \tag{3.13}$$

where m is the number of points in the measured S curve, typically $m \sim 80$. Substituting Equation 3.12 into this equation gives

$$\chi^2 = \sum_i^m \left[\frac{fc_i - \sum_j^n \left(a_j' S_j(cp_i) \right)}{\sigma_i} \right]^2 \quad . \tag{3.14}$$

If we define a $m \times n$ matrix containing the set of basis functions such that

$$\mathbf{A_{ij}} = \frac{\mathbf{S_j}(cp_i)}{\sigma_i} \quad , \tag{3.15}$$

this is known as the design matrix (Press *et al.* 1986), and we also define vectors $\mathbf{a}'$ and $\mathbf{b}$, such that $\mathbf{a}'$ is the vector containing the set of a'_i and

$$\mathbf{b_i} = \frac{fc_i}{\sigma_i} \quad , \tag{3.16}$$

$$\mathbf{a'_i} = \frac{\mathbf{a'_j}}{\sigma_i} \quad , \tag{3.17}$$

then we can rewrite Equation 3.14 as

$$\chi^2 = (\mathbf{b} - \mathbf{A}\mathbf{a}')^2 \quad . \tag{3.18}$$

The Least Squares problem is two fold:

1. The Linear Least Squares Problem.
   Find the vector $\mathbf{a}'$ that minimizes χ^2 for a given matrix.

2. The Nonlinear Least Squares Problem.
   Find the design matrix $\mathbf{A}$ that minimizes χ^2.

3.5.4 The Linear Least Squares Solution

If a function has a quadratic form such as

$$f(\mathbf{x}) = a + \mathbf{b}^T + \frac{1}{2}\mathbf{x}^T \quad , \tag{3.19}$$

we can use the singular value decomposition method (Press *et al.*, 1986) to find a solution to the Linear Least Squares Problem. There is also a normalization condition on the basis function weights of the form $a'_1 + a'_2 + \cdots + a'_n = 1$. If this condition is not satisfied, then the fitted S curve is not symmetric about its centre and cannot be obtained from Equation 3.5. Hence, the sum of $a'_1, a'_2, \ldots, a'_n$ provides a test of the least squares fitting program. In practice, the sum of the weights was always within 0.1 % of 1.

For the weights determined with the least squares fit to be useful, a relationship between the coefficients of Equation 3.11 and Equation 3.12 is needed. There is a specific normalization condition on the $N_j(r)$ of Equation 3.11 which yields $a'_1 = a_1$, $a'_2 = a_2, \ldots$. Substitution of Equation 3.12 into Equation 3.5 yields

$$\begin{aligned} S(fc) \;=\; & a_1 \left\{ \frac{2\pi \int_0^{fc} r N_1(r)dr + 2\int_{fc}^{r_{\rm limit}} [\pi - \arccos(\frac{fc}{r})] r N_1(r)dr}{2\pi \int_0^{r_{\rm limit}} r N_1(r)dr + 2\pi \int_0^{r_{\rm limit}} r N_2(r)dr + \cdots} \right\} \\ & + a_2 \left\{ \frac{2\pi \int_0^{fc} r N_2(r)dr + 2\int_{fc}^{r_{\rm limit}} [\pi - \arccos(\frac{fc}{r})] r N_2(r)dr}{2\pi \int_0^{r_{\rm limit}} r N_1(r)dr + 2\pi \int_0^{r_{\rm limit}} r N_2(r)dr + \cdots} \right\} + \cdots \quad . \end{aligned} \tag{3.20}$$

Notice that if

$$2\pi \int_0^{r_{\text{limit}}} r N_j(r) dr = 1 \tag{3.21}$$

for all j, then the denominator in each term on the right hand side of Equation 3.20 is 1. This results in the required equality between the coefficients.

The radial distribution which satisfies this normalization condition for an exponential is

$$N_{exp}(r, r_o) = \frac{1}{2\pi r_o^2} e^{-\frac{r}{r_o}} \quad ,$$

or for a Gaussian it is

$$N_{gau}(r, \sigma) = \frac{1}{2\pi\sigma^2} e^{-\frac{1}{2}(\frac{r}{\sigma})^2} \quad .$$

3.5.5 The Radial Probability Distribution

If a radial distribution $N(r)$ satisfies the normalization condition, Equation 3.21, the radial cumulative probability distribution, $P(r)$, is

$$P(r) = 2\pi \int_0^r r N(r) dr \quad , \tag{3.22}$$

and so the radial probability density distribution, $p(r)$ is

$$p(r) = 2\pi r N(r) \quad , \tag{3.23}$$

which represents the fraction of the total charge lying on the circumference of a circle with radius r.

The general form of the radial charge distribution consisting of, for example, an exponential core and a Gaussian wing, that satisfies the normalization condition is given by

$$N(r) = \frac{a_c}{2\pi r_{oc}^2} e^{-\frac{r}{r_{oc}}} + \frac{a_w}{2\pi\sigma^2} e^{-\frac{1}{2}(\frac{r}{\sigma})^2} \quad , \tag{3.24}$$

where a_c is the weight in the centre component, a_w is the weight in the outer or wing component, $a_w = 1 - a_c$.

The program developed to carry out the linear least squares solution, requires the values for r_{oc} and r_{ow} for the two components. It takes approximately 2 minutes of Vax 11-780 equivalent CPU time to evaluate the two basis functions, calculate the weights that produce a minimum χ^2 for those functions and return the weights and the minimum χ^2 of the fit.

3.6 The Nonlinear Least Squares Problem

The Nonlinear Least Squares Problem requires an iterative solution. A search is made for the set of radial functions that produces the minimum χ^2.

As the inversion program assumes azimuthal symmetry, the S curve is taken to be symmetric about the point at which the fractional charge is equal to 0.5. The centroid position of this point, *i.e.* the centre channel (*cc*), should be located at channel 2048 but, in practice, the actual centre channel for any given S curve, is randomly distributed about channel 2047, with $\sigma = 6$. The minimum χ^2 and the basis functions obtained for any fit are very sensitive to the chosen *cc* and, therefore, a search must be made to find this value.

As at least two terms were always found necessary to successfully model the radial distribution of the charge cloud (see Section 4.2.1), a search for the minimum χ^2 must take place through, at least, a three dimensional space.

3.6.1 A Manual Search In Three Dimensions

A minimum exists for a two term fit for any value of *cc*. The minimum value of χ^2 is very sensitive to *cc* and an uncertainty of less than 1 % in the centre channel can produce an uncertainty in the scale parameters of approximately 5 %. Therefore, the first stage in a search is to determine a good estimate of *cc*.

A standard set of basis functions was chosen with 5 exponential terms, each with a r_o that is kept constant and 2 Gaussian terms of constant σ. Only *cc* is varied on successive runs of the inversion program, until a minimum of the reduced χ^2 (i.e. $\chi^2_\nu = \chi^2/\nu$, where ν is the number of degrees of freedom) is found. This value of χ^2_ν also represents a useful first order approximation of the absolute minimum χ^2_ν obtainable for a given data set.

In the next stage of data reduction, the estimate of the centre channel is kept constant, a new set of basis functions is chosen and their parameters varied until a new χ^2_ν minimum is found. Then, keeping the basis function parameters constant, the adjacent values of the centre channel are inserted into the fit to verify that the present χ^2_ν minimum is the true minimum. If it is not, a further search is necessary. The function of χ^2_ν against centre channel does not have any localized minima and the centre channel that produces the true minimum is usually located within 3-4 channels of the seven element estimate. Although small adjustments may be necessary to the basis function parameters when varying the centre channel, a search over such a small scale is reasonably straight forward.

In order to fit a combination of two basis functions, for example an exponential and a Gaussian, as in Equation 3.24, I first selected a constant value for one parameter (e.g. $r_o = r_{ok}$) and minimize χ^2_ν along that line by varying σ. The function $\chi^2_\nu(r_{ok}, \sigma)$ was found to contain no localized minima and was basically parabolic. The search for the value of σ ($\sigma = \sigma_k$) that produces the minimum χ^2_ν for a given r_{ok} ($\chi^2_\nu = \chi^2_{\nu k}$) is, therefore, straight forward and can be carried out by a Golden Ratio Search (Press *et al.*, 1986). The end result is the three dimensional co-ordinate $(r_{ok}, \sigma_k, \chi^2_{\nu k})$.

The above process should be repeated several times for a spread of values of r_{oi}, until the minimum is bracketted, i.e. there are three points, j, k and l, such that;

$$\chi^2_{\nu k} < \chi^2_{\nu j} \quad , \tag{3.25}$$

and

$$\chi^2_{\nu k} < \chi^2_{\nu l} \quad , \tag{3.26}$$

where

$$r_{oj} < r_{ok} < r_{ol} \quad . \tag{3.27}$$

The plot of $\chi^2_{\nu k}$ against r_{ok} also has a parabolic nature without any localized minima.

The plot of r_{ok} against σ_k is a monotonically increasing curve for increasing r_{ok}. It is, therefore, possible to interpolate between any two known values, e.g. r_{oj} and r_{ol}, and obtain a good estimate of σ_k for any given r_{ok} lying between them. This significantly reduces the number of iterations required. The search procedure then is almost reduced to a normal minimum search in a well defined, two dimensional "valley".

The total fitting procedure, including finding the centre channel and basis function parameters, typically required 70 to 80 iterations, with approximately 2 minutes of Vax 11-780 equivalent CPU time required per iteration.

Given the amount of time necessary to find the point that produces the minimum χ^2_ν, a program that carried out an automated search was obviously desirable especially if more than two terms are included in the fit. Also, carrying out the manual search for charge clouds obtained over a range of MCP operating conditions, approximately 30 data sets, showed that the χ^2_ν surface was continuous and contained no localized minima above levels of 0.1%. Therefore, an automatic search routine is a suitable method for finding the global minimum.

3.6.2 Methods for Minimizing a Variable

Most methods of minimizing an N dimensional function rely on the existence of an algorithm to minimize along a given vector. If we start at the point $\mathbf{P}$ in an N dimensional space, then the function of N-variables, $f(\mathbf{x})$, can be minimized along a vector $\mathbf{n}$ by one dimensional methods. These vector minimization routines require the input vectors $\mathbf{x}$ and $\mathbf{n}$, and find the scalar λ such that $f(\mathbf{x} + \lambda\mathbf{n})$ is a minimum. The routine then replaces $\mathbf{x}$ with $\mathbf{x} + \lambda\mathbf{n}$ and $\mathbf{n}$ with λ $\mathbf{n}$. The N dimensional methods only vary in the manner in which they choose the vector $\mathbf{n}$ to be minimized along.

Most general purpose minimization routines depend on the function behaving as a quadratic, at least within the neighbourhood of the minimum. During the manual search, it was found that the χ^2_ν function was approximately quadratic, so these methods are applicable. A quadratic expression can be expanded in the form

$$f(\mathbf{x}) = a + \mathbf{b}^T\mathbf{x} + \frac{1}{2}\mathbf{x}^T\mathbf{M}\mathbf{x} \quad , \tag{3.28}$$

where $\mathbf{x}$ and $\mathbf{b}$ are vectors and $\mathbf{M}$ is a $n \times n$ positive definite matrix. The gradient of the function is therefore

$$\nabla f = \mathbf{b} + \mathbf{M}\mathbf{x} \quad , \tag{3.29}$$

and the condition for a minimum along a vector $\mathbf{v}$ is

$$\mathbf{v}^T(\mathbf{b} + \mathbf{M}\mathbf{x}) = 0 \quad , \tag{3.30}$$

(Kowalik & Osborne, 1968).

Many methods for minimizing a function depend on evaluating ∇f for each step in the iterative procedure, in order to determine the next direction to minimize along. Widely used examples of these methods are the conjugate gradient, variable metric and the Marquadt methods. The last example is the usual method used in nonlinear least squares problems (Press *et al.*, 1986). However, the non-separable kernel in the second term in the expression for the S curve, Equation 3.5, will also be non-separable in the derivative. Therefore, determining the partial derivatives of the χ^2 function, Equation 3.14, would also require a numerical approximation for each partial derivative. Each approximation would be expected to take as long as evaluating Equation 3.5, i.e. approximately 2 minutes. These methods would take too long.

There are methods which can minimize a function without determining ∇f. The most widely used of these is Powell's Method of conjugate directions which is discussed in detail in the next section.

3.6.3 Powell's Method of Conjugate Directions

Two vectors, $\mathbf{u}$ and $\mathbf{v}$ are said to be conjugate with respect to a positive definite matrix $\mathbf{M}$ if

$$\mathbf{u}^T\mathbf{M}\mathbf{v} = 0 \quad . \tag{3.31}$$

If $\mathbf{d}_1, \mathbf{d}_2, \ldots \mathbf{d}_n$ are a set of vectors mutually conjugate with respect to the positive definite matrix $\mathbf{M}$ then the minimum of the quadratic form

$$f(\mathbf{x}) = a + \mathbf{b}^T\mathbf{x} + \frac{1}{2}\mathbf{x}^T\mathbf{M}\mathbf{x} \quad , \tag{3.32}$$

can be found from any arbitrary initial point $\mathbf{x}_0$ by minimizing along each each of the vectors $\mathbf{d}_i$, only once (Kowalik & Osborne, 1968). The order in which the vectors are used is unimportant.

Powell's method attempts to find the set of mutually conjugate vectors. It is based on the observation that if the minimum is determined along the vector $\mathbf{v}$ from two different initial points then the vector joining the minima, $\mathbf{x}_1$ and $\mathbf{x}_2$ (see Figure 3.15), is conjugate to $\mathbf{v}$. This can be demonstrated by

$$\mathbf{v}^T(\mathbf{M}\mathbf{x}_1 + \mathbf{b}) = 0 \quad , \tag{3.33}$$

$$\mathbf{v}^T(\mathbf{M}\mathbf{x}_2 + \mathbf{b}) = 0 \quad , \tag{3.34}$$

by the definition of a minimum along a vector, Equation 3.30; subtracting these two equations gives

$$\mathbf{v}^T\mathbf{M}(\mathbf{x}_1 - \mathbf{x}_2) = 0 \quad , \tag{3.35}$$

which by Equation 3.31 shows the vector $(\mathbf{x}_1 - \mathbf{x}_2)$ is conjugate to $\mathbf{v}$.

Powell's method extends this result. If the search for each minimum is made along p conjugate directions then the join of these minima is conjugate to all of those vectors.

The basic algorithm (Kowalik & Osborne, 1968), who also include a proof, for n independent vectors $\mathbf{d}_1, \ldots, \mathbf{d}_n$

1. Let λ_0 minimize $f(\mathbf{x}^{(0)} + \lambda\mathbf{d}_n)$ and set

$$\mathbf{x}^{(1)} = \mathbf{x}^{(0)} + \lambda_0\mathbf{d}_n \quad . \tag{3.36}$$

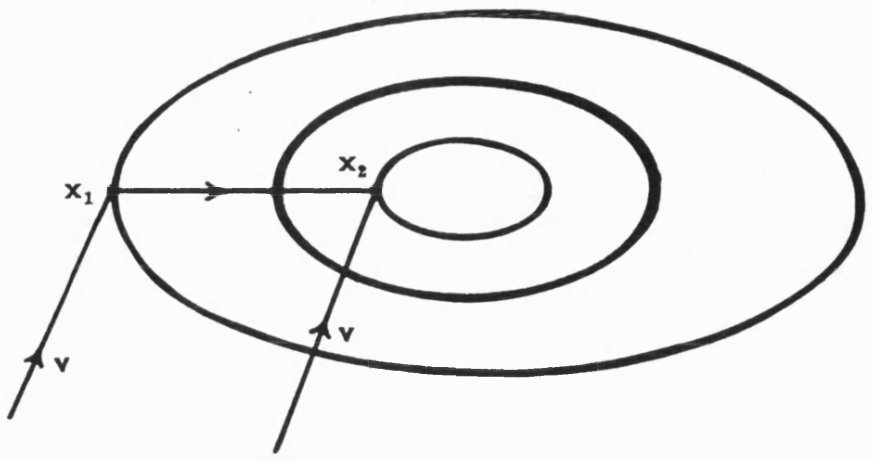

Figure 3.15: The vector between two minima $\mathbf{x}_1$ and $\mathbf{x}_2$ obtained by minimizing along the vector $\mathbf{v}$ from two initial points, is conjugate to $\mathbf{v}$.
From Kowalik & Osborne (1968).

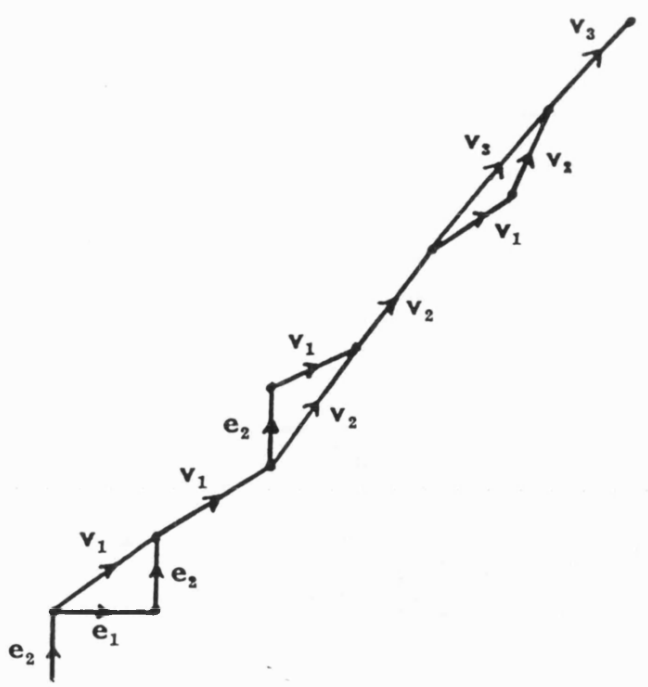

Figure 3.16: Example of Powell's method for finding the minimum by using conjugate directions.
From Kowalik & Osborne (1968).

2. For $i = 1, \ldots, n$ compute λ_i, to minimize $f(\mathbf{x}^{(i)} + \lambda \mathbf{d}_i)$ and set

$$\mathbf{x}^{(i+1)} = \mathbf{x}^{(i)} + \lambda_i \mathbf{d}_i \quad . \tag{3.37}$$

3. Set $\mathbf{d}_i = \mathbf{d}_{i+1}, i = 1, \ldots, n-1$.

4. Set $\mathbf{d}_n = \mathbf{x}^{n+1} - \mathbf{x}^{(i)}$, $\mathbf{x}^{(0)} = \mathbf{x}^{(n+1)}$.

5. Repeat (1).

Figure 3.16 shows an example of Powell's method in two dimensions using the basis vectors as the initial vector set, i.e. $n = 2$ and $\mathbf{d}_i = \mathbf{e}_i$. At the end of the first sweep the vector

$$\mathbf{v}_1 = \mathbf{x}^{(n+1)} - \mathbf{x}^{(1)} \tag{3.38}$$

is conjugate to $\mathbf{d}_n$, i.e. the vector $\mathbf{e}_2$. After the second iteration the vector

$$\mathbf{v}_2 = \mathbf{x}^{(n+1)} - \mathbf{x}^{(1)} \tag{3.39}$$

is conjugate to the vectors $\mathbf{d}_n$ and $\mathbf{d}_{n-1}$, i.e. $\mathbf{v}_1$ and $\mathbf{e}_2$. And so the process continues.

Powell (1964) showed that for a quadratic function such as Equation 3.28, after k iterations a set of vectors is produced such that the last k members are mutually conjugate. Therefore, n iterations will exactly minimize a n dimensional function of quadratic form.

The coordinates of the minimum describe the basis functions and will generate the elements of the design matrix **A** for least squares problem, Equation 3.15. This represents the solution to the nonlinear least squares problem, i.e. the matrix that minimizes χ^2 in Equation 3.18.

3.7 Practical Considerations

The automated search routine (ASR) that was developed was based on Powell's method as described by Press *et al.* (1986). However, the line minimization routines they use were replaced by routines written by the author which minimize along vectors and not the cardinal directions. These routines are based on those described by Press *et al.* (1986) for Brent's method and bracketting a minimum. Also when a minimum along a vector is determined, the four closest neighbours are examined, to determine if the search has

converged to a local minimum because of the noisy nature of the χ^2 surface. If one of the neighbours is smaller the search then walks in that direction until a new minimum is found.

The whole width of the anode is 4096 pixels, defined by the digitization level of the ADCs. All units of the ASR are defined in these pixels. The ASR is constrained so that the components of the distribution are kept within a reasonable range of sizes. These constraints are determined by the anode, all components must have a scale parameter, i.e. σ or r_0, less than half the anode width and must be larger than 10 pixels. If the central peak of a charge cloud was so small that it was sampled by such a small number of pixels, the transitional region in the S curve would appear as a very steep straight line and the curve would be better described as a step function rather than an S curve.

The ASR is written in FORTRAN and is approximately 3000 lines long, 2000 lines are devoted to the nonlinear least squares problem and the rest deals with the linear least squares and the inversion. The ASR takes from 2 to 4 Vax 11-780 equivalent CPU hours to determine a centre channel estimate and a two component fit.

Table 3.1 shows the information returned from the ASR. The uncertainties on the weights are those returned by the Single Value Decomposition. The probability quoted is probability that a random sample of n values, where n is the number of data points, would have a larger χ^2 than that returned by the fit.

If further information is needed, all of the vectors, the coordinates and χ^2 for every point for which χ^2 was evaluated are included in a log file.

3.7.1 Accuracy and Stability

The smallest step of the ASR is 0.5 pixels. The small uncertainties this produces in the centre channel, affect the values of the scale parameters and can introduce an uncertainty of less than 1 % in the centre term but up to 5 % in the wing term. When using the ASR, measurements of several data sets taken with the same operating conditions showed that the uncertainties associated with the central components are 3 %, 5 % for the wing components and 2 % for the weight of the central component.

The value of χ^2_ν returned by a nine element fit used for estimating cc and the result from the two element fit provide two independent values of χ^2_ν. The χ^2 value is a measure of discrepancy between the estimated function and the parent function as well as the deviations between the data and the parent function. By carrying out an F test with

```
filename:   a100p265.als
no. of valid data pts.:          95
          2  exponentials           0  gaussians.

I.P.:
 2060.36   100.00   300.00
Nine element reduced chisq:   1.258037
At centre channel:   2060.360

         19  vectors (total)           6   non basis vectors.
          6 powel iterations

min pt: pixels
cen. chan    ro       ro

 2060.16   108.90   372.47
min pt: mm
             1.04     3.55
weights and their uncertainties:
             0.69     0.31
             0.00     0.00

Reduced Chi Sq.:   1.187718
Probability     :  0.1045723
```

Table 3.1: Example of the information returned by the automatic search routine. This example is for a two exponential fit to the data shown in Figure 3.6, the actual fit itself is shown in Figure 4.1. This value of the reduced χ^2 is approximately the average of those returned for all of the data sets.

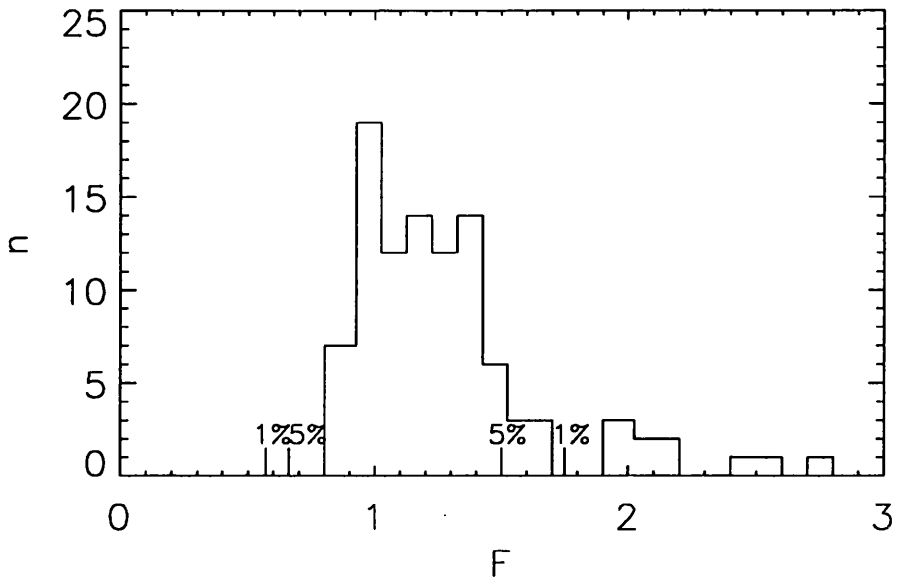

Figure 3.17: The distribution of F obtained with the automatic search routine. The values of F correspond to the ratios of χ^2_ν obtained for the best two term fit against the nine term fit for each of 100 measured data sets. The 1 and 5% confidence limits for a set containing 80 data points, are also displayed.

the ratios of the two χ^2_ν values, we can determine whether the fit of the estimated function to the parent function is reasonable (Bevington, 1969). For 80 data points, which is typical for the data sets, the ratio of the two χ^2_ν, F, should be between approximately 0.66 and 1.5 to have confidence in the fit at the 5 % level, i.e. the probability of observing such a large F, or $1/F$ if $F < 1$, from a random set of data compared with the correct fitting function, is less than 5%. At this level, we can have confidence in the fit. As shown in Figure 3.17, most of the two term fits did lie within this region. A two term fit for which $F > 1.75$, corresponding to the approximate 1 % level, should be treated with suspicion.

The ASR has been tested on approximately 40 sets of simulated noisy S curves to determine reliability and accuracy. It was found that in most instances the routine would find a minima within the accuracies described above. The χ^2 for a successful two term fit was always within ± 20 % of the χ^2 determined when estimating the centre channel with a nine term fit.

The ASR did prove to be unreliable when the ratio of the two components was too

small, i.e. less than a factor of about 2, and most of the power was in the wings. In this instance the search routine would attribute almost all of the power to a component whose scale parameter was approximately half way between the two components.

Care must be taken in the selecting the initial point of the search. In some instances the search will not converge to a minimum. The search routine will halt if a minimum has not been found along vector after 25 iterations of the Brent method, or after four times as many Powell iterations as needed for a n dimensional search. Another problem is that the search may converge to a local minimum very quickly. This usually occurs when the Powell algorithm does not select a new set of vectors but keeps using the original set of basis functions, i.e. the orthogonal vectors in the direction of centre channel and the charge cloud component scale parameters. In this instance, the search "folds up" on itself and converges to a minima quite quickly as it can only search along the original vector set. Another problem, similar to the resolution problem discussed above, is that if the scale parameters come too close together in size, the ASR will begin to treat them as one term, either assigning equal weights to both terms or all the weight to one term.

If any of these problems occur, they can usually be overcome by selecting a new initial point and starting again. I have found that the best selection for an initial point is to choose the two scale parameters at the outside of the available set, i.e. 50 and 500 pixels. If problems persist, the centre channel value can be set at a value a long way from the best estimate. This is almost guaranteed to move the search around and ensure that non-basis vectors are used.

Chapter 4

Measurements of the Radial Distribution of the Charge Cloud.

4.1 Range of Measurements

The radial distribution of the charge cloud was determined for over 80 different operating conditions. The parameters describing the operating parameters in this chapter are the same as those displayed in Figure 3.5. The measurements were made at 4 different chevron voltages, V_c, at 11 anode gap voltages, V_g, across two anode gaps, g, corresponding to 15 electric field strengths, E_g, two orientations of the pore bias angle and with varying inter-plate gap voltage, V_i.

4.1.1 Range of Measurements at an MCP Anode Gap of 6.2 mm

Table 4.1 shows a summary of the operating voltages for which the charge cloud was determined with $g = 6.2$ mm. Severe modulation prevented obtaining a measurement for $V_g = 800$ V and $V_c = 2.9$ kV. In each case, the two MCPs were separated by a 100μm thick conducting spacer, therefore V_i was always zero.

Measurements were taken for all of the voltage combinations with the MCP pore bias angle aligned both perpendicular and parallel to the split in the anode. These results were presented by Edgar *et al.* (1989).

V_g (V)	E_g (kV.m^{-1})	$\log E_g$	V_c (kV) 2.65	2.8	2.9
50	8	3.91	•	•	•
100	16	4.21	•	•	•
200	32	4.51	•	•	•
400	64	4.81	•	•	•
800	129	5.11	•	•	
Gain @V_g = 100 V					
G_m	(10^7 e^-)		1.0	2.9	4.6
Sat.	(%)		130	64	44

Table 4.1: Summary of operating voltages and typical gains for measurements with an anode gap of 6.2 mm.

The presence of a dot indicates a measurement was made at these voltages. The titles G_m and Sat. refer to the modal gain and saturation of the PHD, repsectively, as measured at that V_c.

4.1.2 Range of Measurements at an Anode Gap 3.0 mm

Table 4.2 summarizes the voltages at which measurements of the charge cloud were made with $g = 3.0$ mm. The maximum values for V_g for $V_c = 3.0$ and 3.1 kV is due to the rather prosaic condition that the high voltage supply I used could not supply 4 kV. Measurements were not made for $V_g > 600$ V at $V_c = 3.2$ kV because of severe modulation, see Figure 4.5. The small variation in the minimum value of V_g with V_c is due to the high voltage pulling up V_g.

Some of these measurements were described by Lapington & Edgar (1989). In this set of measurements, the two MCPs were separated by an 80 μm thick insulator. Therefore, a potential difference could be applied across the inter-plate gap. In all the measurements described in Table 4.2, $V_i = 0$. The pore bias angle was always aligned perpendicular to the anode split.

At a single, fixed combination of V_g and V_c, V_i was varied through a range of ± 30 V. These measurements are discussed in Section 4.4.5.

4.2 The General Form of the Radial Distribution of the Charge Cloud

Only Gaussian, exponential and constant offset basis functions were examined during the experiment.

4.2.1 The Two Component Nature of The Radial Distribution

Figure 4.1 compares the best fit to a typical S curve obtained with a single exponential a single Gaussian and two exponential terms. Clearly a single function is unsatisfactory. In all cases, two terms were required to successfully fit the data. The general form of these components is a narrow central peak containing the majority of the charge and a broad diffuse wing component typically three times larger than the peak.

As shown in Figure 3.17, of the 100 two term fits, 16 lie outside the 5% confidence limits when compared to the nine term fits. The addition of a third term in these cases, does reduce their χ^2_ν significantly, so that the corresponding values of F lie within that confidence region. However, in all but six cases at least one of the terms has a negative weight. Negative weights imply that the third term was mainly cancelling contributions

V_g (V)	E_g (kV.m^{-1})	log E_g	V_c (kV) 2.8	2.9	3.0	3.1	3.2
110	37	4.56	•	•			
115	38	4.58			•		
120	40	4.60				•	•
200	67	4.82	•	•	•	•	•
300	100	5.00	•	•	•	•	•
400	133	5.12	•	•	•	•	•
500	167	5.22	•	•	•	•	•
600	200	5.30	•	•	•	•	
700	233	5.37	•	•	•	•	
800	267	5.43	•	•	•	•	
900	300	5.48	•	•	•		
1000	333	5.52	•	•			
Gain @ V_g = 200 V							
G_m	(10^7 e^-)		1.4	4.8	11	17	21

Table 4.2: Summary of operating voltages and typical gains for measurements with an anode gap of 3.0 mm.
The symbols are the same as in Table 4.1.

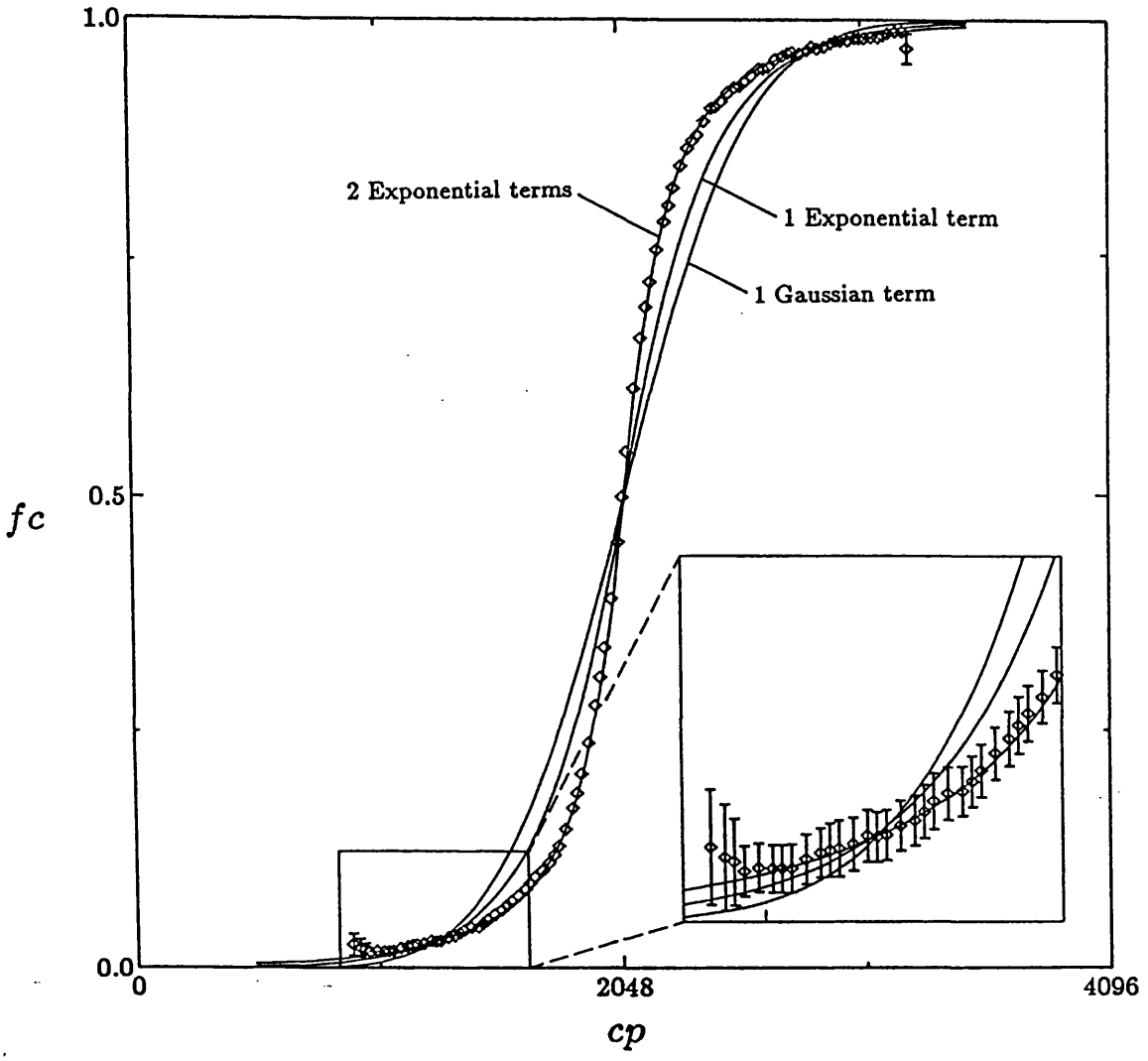

Figure 4.1: Comparison of typical fits to a mean S curve, $S(cp)$.
The data points are the vertically binned averages of the S curve shown in Figure 3.6. The error bars are are only plotted when they exceed the size of the diamond and are $\pm 3\sigma$ for each bin. Note that the inset is plotted on a finer scale so the error bars are shown for all of the points. The solid curves represent the best fits obtained using a single Gaussian, a single exponential and two exponential terms. From Edgar *et al.* (1989).

Fit Parameters	Term 1	2	3	F
r_0 (mm)	0.83	4.8		1.99
a	0.93	0.7		
r_0 (mm)	0.51	0.51	2.0	0.92
a	142 ± 3	-141 ± 3	0.23	

Table 4.3: Comparison of two exponential and three exponential fits.
The data set is the data obtained at $V_c = 3.0$ kV, $V_a = 115$ V and $d = 3.0$ mm. The value of F represents the ratio of χ^2_ν for the respective fits to the χ^2_ν for the nine term fit, 0.4711.

from the first two terms.

Table 4.3 shows the fit parameters for a typical example of these cases. In the three term case, two of the terms have the same size and almost cancel each other. The values of a returned by the single value decomposition when determining the Linear least Squares solution, as discussed in Section 3.5.4, are not constrained such that $0 \leq a \leq 1$. The negative and large magnitude weights are possible mathematically, but clearly have no physical significance.

Of the 100 cases examined, every one required at least two terms in the fit. Only for six cases do three term fits produce a significant improvement over the best two term fit, where the weights associated with all of the components are physically plausible. Therefore, I conclude that only two terms are required to successfully fit the charge cloud in the majority of cases.

4.2.2 The Form of the Central Component

Figure 4.2 compares the χ^2_ν of fits with an exponential central component to those with a Gaussian core. Only the data for $V_c = 2.8$ and 2.9 kV is shown as these are the only

two voltages for which measurements were made at all of the electric field strengths.

The figure demonstrates that there is a trend in the difference between the quality of the fits obtained with the two types of cores with varying E_g. At low electric fields, the two exponential fits are superior to the Gaussian and exponential combinations, the value of F decreases progressively with E_g and the Gaussian core fits are superior at high fields.

From the F test for 80 data points for two fits with the same number of degrees of freedom, as discussed in Section 3.7.1, the boundary for the 5 % and 1 % confidence limits are $|\log F| \approx 0.16$ and $|\log F| \approx 0.23$, respectively. Only at the extremes of the ranges of E_g, do a significant proportion lie outside of these confidence limits. Figure 4.2 also shows the large scatter in F obtained for the six data sets measured at $V_c = 2.8$ kV where $E_g \approx 16$ kV.m^{-1}. These two factors, taken in conjunction, indicate there is not a significant difference between the success of the fits with the two different forms of core for the majority of values of E_g.

4.2.3 The Form of the Wing Component

In some instances, there is a slight variation in the quality of the fit between fits with Gaussian and exponential wing terms. The exponential fit usually produced the better fit but the differences in χ^2_ν are much less than those obtained by changing the form of the core term. When the weight associated with the wing was less than 20%, there was no significant difference in the quality of the fit for the two types of terms.

Flat Terms and Modulation

In other instances unreasonably large sizes of the wing were returned by the search routine, for example 12 mm at $V_c = 2.9$ kV, $V_g = 400$ V, $g = 6.2$ mm and the chevron plane parallel to the split. Figure 4.3 shows the charge cloud does not have a component this large. A fit consisting of a single exponential and a constant term is as successful as the two exponential case for both chevron plane orientations. This suggests that the large r_{ow} is not a physical result, but is instead an artefact of the fitting procedure trying to fit to an essentially flat term.

These large terms appear at the onset of modulation, as shown in the behaviour of wings in Figure 4.3. I tried to investigate the flat terms and the onset of modulation with measurements at $g = 3.0$ mm. Figure 4.4 and 4.5 show examples of an essentially flat wing

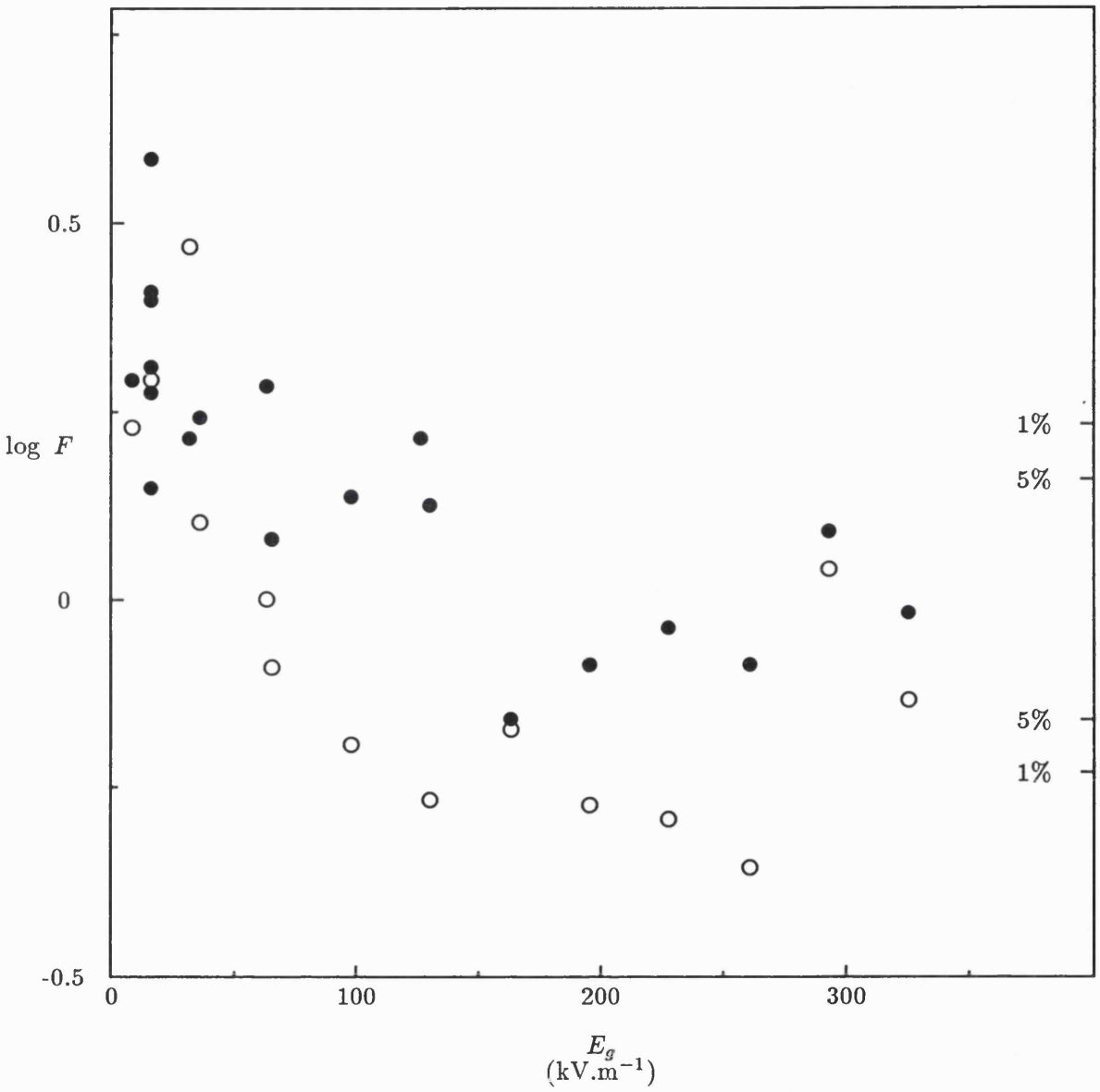

Figure 4.2: Comparison of the success of fits with exponential and Gaussian central components.

The values of F correspond to the ratios of the minimum χ^2_ν returned by fits with a Gaussian centre component to those with an exponential core, i.e. $\log F$ is positive when the exponential fit returns a χ^2_ν less than that returned with a Gaussian term. The wing component in each case was an exponential. The filled and empty circles represent data acquired at $V_c = 2.8$ and 2.9 kV, respectively.

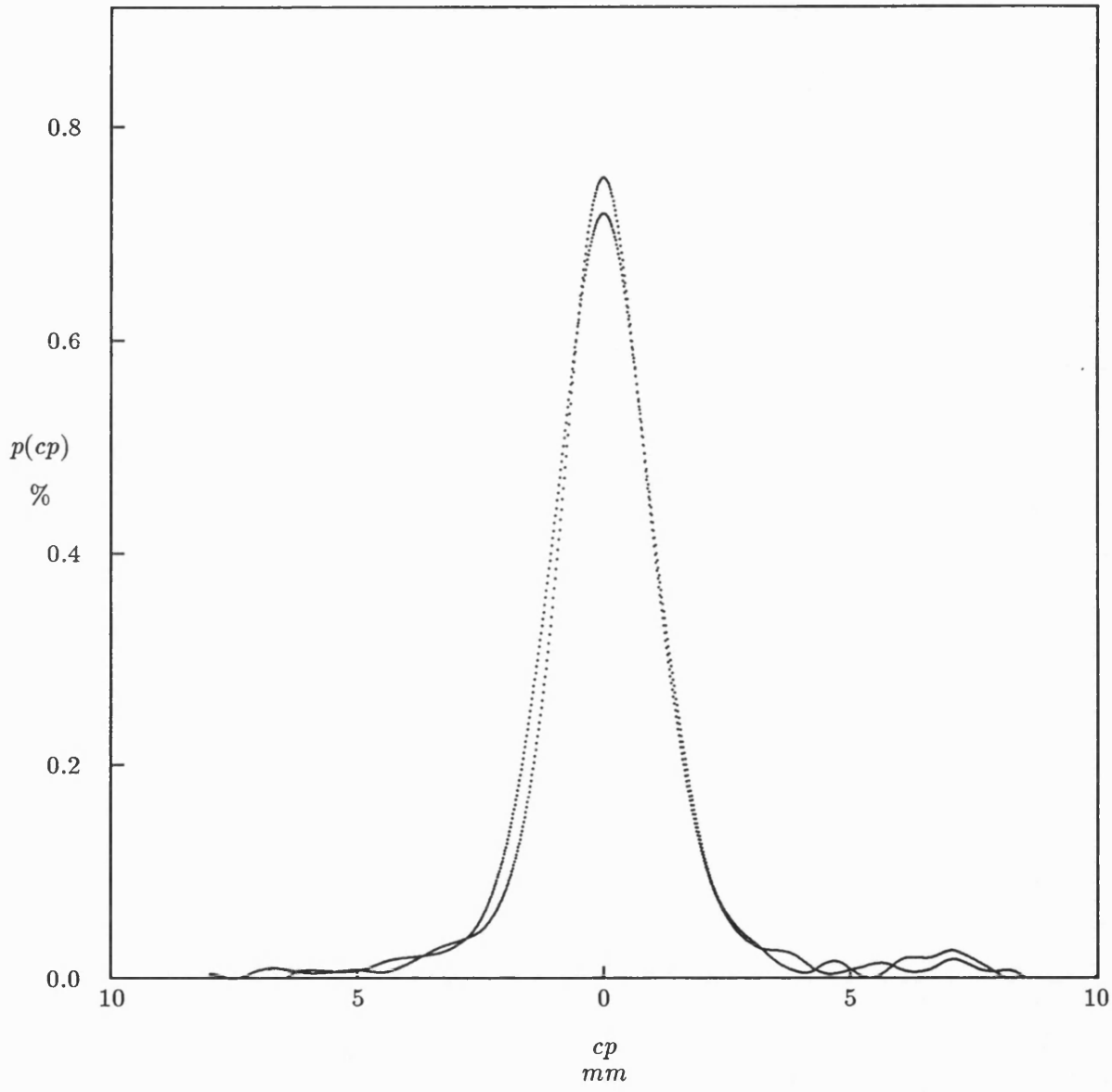

Figure 4.3: The one dimensional integrated probability density distributions obtained for $g = 6.2$ mm, $V_g = 400$ V, $V_c = 2.9$ kV for both chevron bias angle/split orientations.

component and an example of severe modulation obtained at the smaller gap.

The $p(cp)$ plot in Figure 4.4 was obtained just before the onset of modulation; when V_g was increased by 100 V, modulation similar in magnitude to that seen in Figure 4.3 was evident. As for $g = 6.2$ mm, the presence of the flat term and modulation appeared only at for the highest plate voltages, for $g = 3.0$ mm $V_c = 3.1$ and 3.2 kV. Fits to these S curves would only converge if a constant offset wing was used and not with an exponential wing term. The search would converge with Gaussian terms more often, but these were always unfeasibley large.

The modulation increased in severity as V_g increased. Significant modulation was not present in any of the 3.0 kV data sets but it becomes evident for $V_g \geq 500$ V and $V_g \geq 300$ V for 3.1 and 3.2 kV, respectively. Figure 4.5 suggests that the 3.2 kV charge cloud is larger than the corresponding 2.8 kV case. The values of r_{oc} returned by the search routine for 3.1 kV were on average, 20% larger than those returned for the corresponding values of V_g at 3.0 kV, and 25% larger for 3.2 kV.

This data shows that modulation occurs in larger charge clouds before it appears in smaller ones. Therefore, the modulation is not purely a function of the charge cloud size. It is possible that the flat term is responsible for this as it could introduce high spatial frequency components in to the charge cloud distribution. However, the flat term may itself be an artefact of modulation, as it only appears on the verge of modulation.

Unfortunately at 3.1 kV and 3.2 kV, there was significant ion-feedback and clipping of the front-end of the preamp, which makes data obtained at these voltages extremely unreliable. This data is not discussed further in this chapter, but the onset of modulation and the presence of the flat wings and their association with higher values of V_c warrants further detailed study.

It would be very interesting to carry out a large series of measurements on a finely spaced mesh of V_c and V_g values, in the transitional region between no modulation and severe modulation. In order that modulation can be induced without requiring that V_c should be so large that ion-feedback occurs, the anode should have a larger repeat pitch, g should be larger or higher values of V_g should be used.

As the Split-Strip anode consists of a repetitive structure, it is susceptible to modulation but it can simultaneously return information about the charge cloud size. It therefore provides a unique capability to study modulation *in situ*.

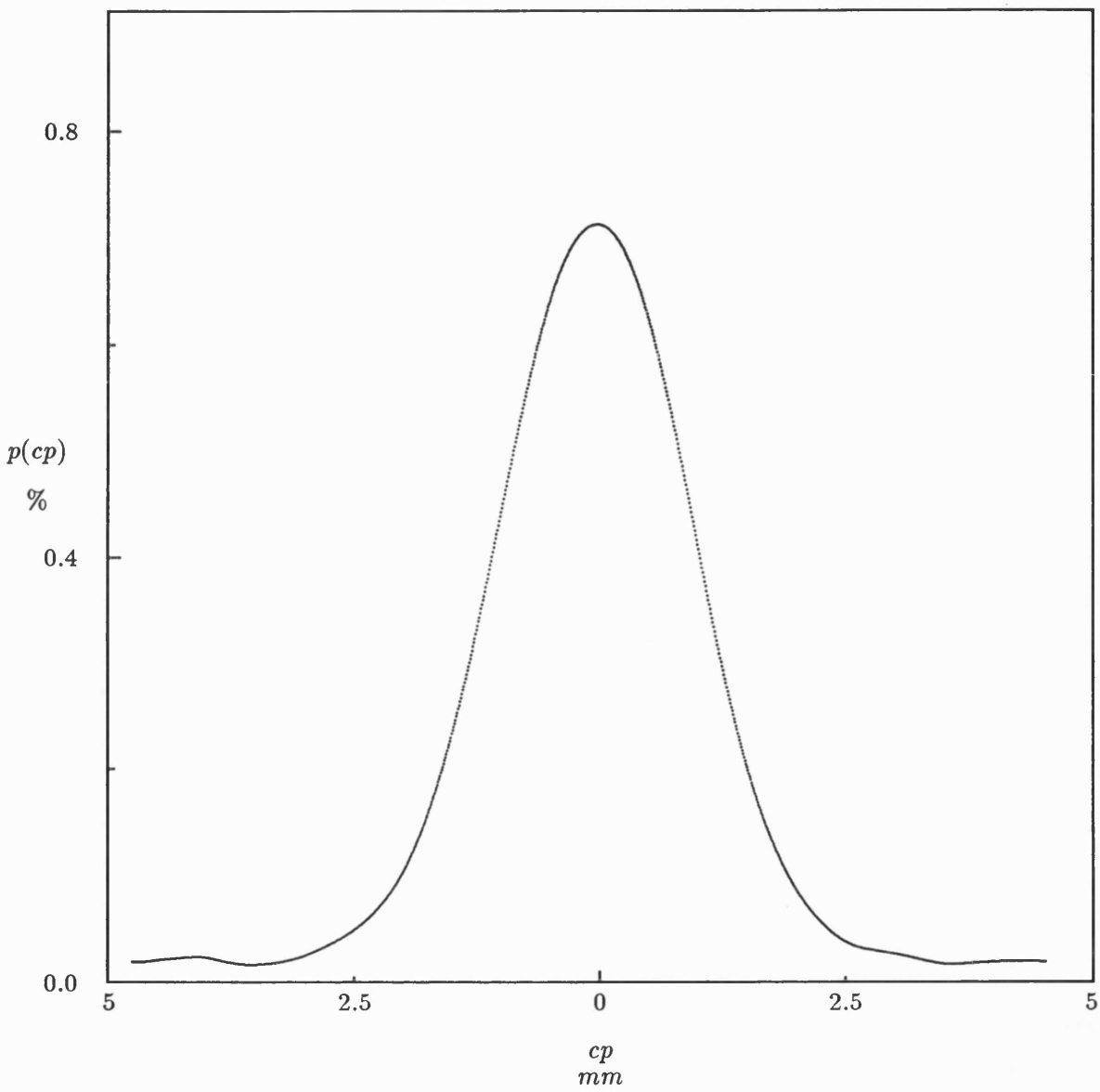

Figure 4.4: An example of a flat wing.

The $p(cp)$ distributions obtained for $g = 3.0$ mm, $V_g = 400$ V and $V_c = 3.1$ kV. In this case the fitting routine would only converge if a constant offset wing term was used rather than an exponential or Gaussian.

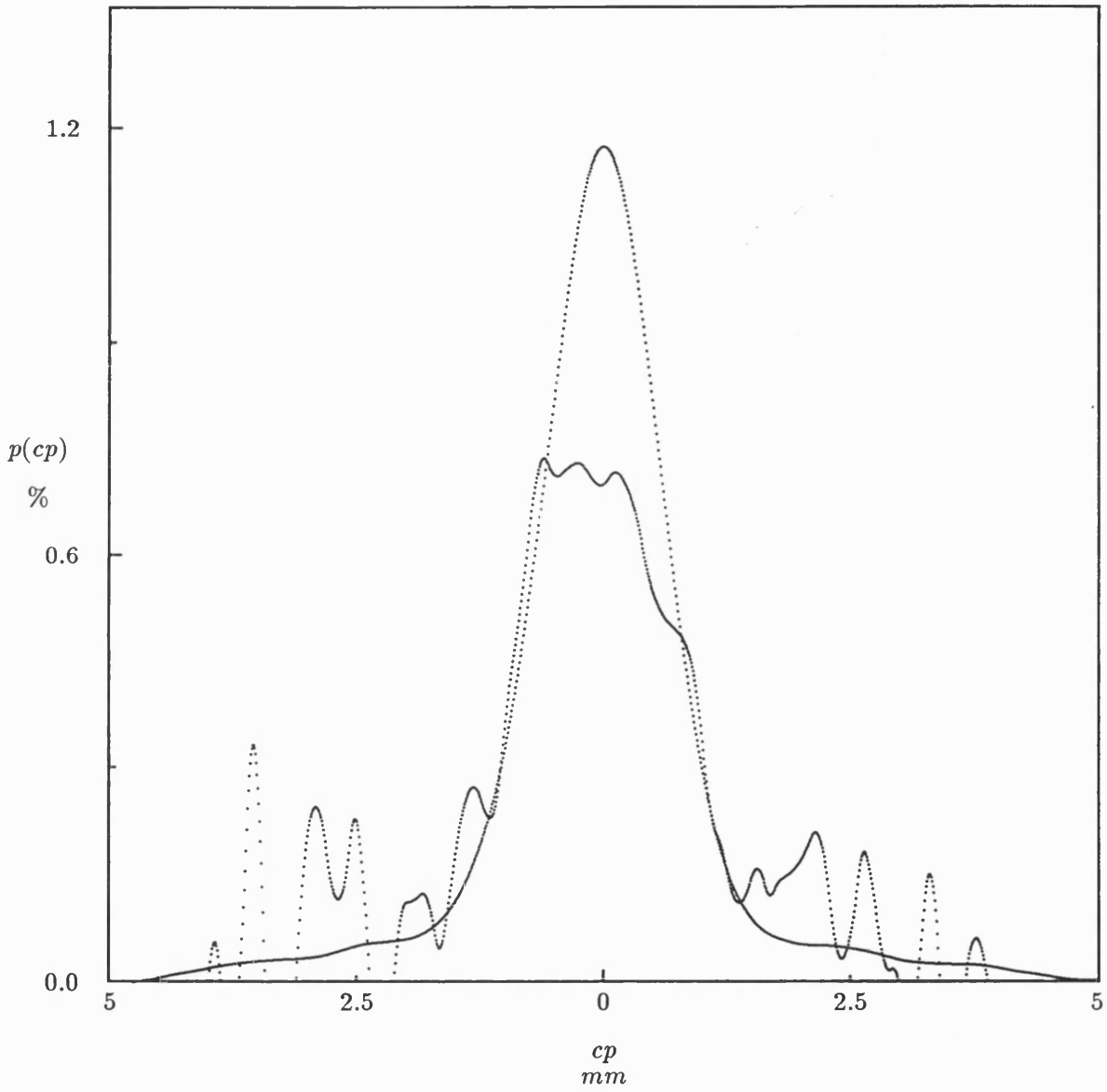

Figure 4.5: An example of severe modulation.
The $p(cp)$ distributions were obtained at $g = 3.0$ mm and $V_g = 600$ V. The badly affected curve was obtained at $V_c = 3.2$ kV and the other at 2.8 kV. The centre channels have been aligned during analysis, the 3.2 kV centre was estimated as the midpoint at FWHM.

4.3 The Size of the Radial Distribution

4.3.1 The Fit Parameters and the Radial Distribution

The radial distributions presented in this chapter are the best fits to the mean charge cloud obtained with either two exponential terms, as presented in Edgar *et al.* (1989) and Lapington & Edgar (1989), or, as in approximately a dozen cases, a combination of an exponential and a constant basis function.

The three fit parameters provide a convenient method of describing the form of the charge cloud but do not provide a direct measure of the amplitude of the charge cloud at given radius. It is necessary to use the radial probability distributions to describe the fraction of charge present at a given radius or contained within an annulus.

The general form of the probability density function for the radial distribution for the charge cloud is derived similarly to the example in Section 3.5.5 and is given by Equations 3.24 and 3.23

$$p(r) = r\left(\frac{a_c}{r_{oc}^2}e^{-\frac{r}{r_{oc}}} + \frac{(1-a_c)}{r_{ow}^2}e^{-\frac{r}{r_{ow}}}\right) \quad , \tag{4.1}$$

where a_c is the weight associated with the central component, r_o is the scale parameter and the subscripts c and w refer to the core and wing components, respectively.

In the two exponential case, the total fraction of charge lying within a finite annulus bounded by r_1 and r_2 is given by

$$\begin{aligned} P(\Delta r) &= a_c\left[e^{-\frac{r_1}{r_{oc}}}\left(1+\frac{r_1}{r_{oc}}\right) - e^{-\frac{r_2}{r_{oc}}}\left(1+\frac{r_2}{r_{oc}}\right)\right] \\ &\quad +(1-a_c)\left[e^{-\frac{r_1}{r_{ow}}}\left(1+\frac{r_1}{r_{ow}}\right) - e^{-\frac{r_2}{r_{ow}}}\left(1+\frac{r_2}{r_{ow}}\right)\right] \quad , \end{aligned} \tag{4.2}$$

where $r_2 > r_1$. The fraction of of charge lying within a limiting radius, r_l is given by

$$P(r_l) = a_c\left[1-e^{-\frac{r_l}{r_{oc}}}\left(1+\frac{r_l}{r_{oc}}\right)\right] + (1-a_c)\left[1-e^{-\frac{r_l}{r_{ow}}}\left(1+\frac{r_l}{r_{ow}}\right)\right] \quad . \tag{4.3}$$

I shall use the quantities r_l and P to describe the size of the charge cloud as determined from the fit parameters.

Figure 4.6 shows the radial probability density and cumulative distributions obtained from a set of fit parameters. Also shown is the uncertainty on $P(r)$, σ_P, which assuming the errors are not correlated, are determined by

$$\sigma_P^2 = \left(\sigma_{r_{oc}}\frac{\delta P}{\delta r_{oc}}\right)^2 + \left(\sigma_{r_{ow}}\frac{\delta P}{\delta r_{ow}}\right)^2 + \left(\sigma_{a_c}\frac{\delta P}{\delta a}\right)^2 \quad , \tag{4.4}$$

where $\sigma_{r_{oc}}, \sigma_{r_{ow}}$ and σ_{a_c} are the uncertainties on the fit parameters. Multiple data sets were taken at the same operating conditions as the data presented in this figure, for both pore bias/split orientations and the fractional uncertainties were found to be

$$\sigma_{r_{oc}} = 3\% \ , \tag{4.5}$$

$$\sigma_{r_{ow}} = 5\% \ , \tag{4.6}$$

$$\sigma_{a_c} = 2\% \ . \tag{4.7}$$

These were the only operating conditions for which the uncertainties were determined and I have assumed that they are also true for the other operating conditions when calculating errors.

The three partial derivatives for the two exponential case are

$$\frac{\delta P}{\delta r_{oc}} = \frac{-a_c r_l^2}{r_{oc}^3} e^{\frac{-r_l}{r_{oc}}} \ , \tag{4.8}$$

$$\frac{\delta P}{\delta r_{ow}} = \frac{(a_c - 1) r_l^2}{r_{ow}^3} e^{\frac{-r_l}{r_{ow}}} \ , \tag{4.9}$$

$$\frac{\delta P}{\delta a_c} = e^{\frac{-r_l}{r_{ow}}} \left(1 + \frac{r_l}{r_{ow}}\right) - e^{\frac{-r_l}{r_{oc}}} \left(1 + \frac{r_l}{r_{oc}}\right) \ . \tag{4.10}$$

The uncertainty in P produces an uncertainty in r_l which is also shown in Figure 4.6

$$\sigma_{r_l} = \frac{dr_l}{dP} \sigma_P \ , \tag{4.11}$$

$$= \frac{\sigma_P}{p} \ . \tag{4.12}$$

4.3.2 The Fit Parameters at an Anode Gap of 6.2 mm.

The fit parameters obtained at $g = 6.2$ mm are listed in Table 4.4 and are shown in Figures 4.7 and 4.8 as a function of E_g and V_c. These figures show that the size of the charge cloud decreases with increasing E_g. The gap voltage is the predominant factor in determining the size of the charge cloud. As E_g increases and the size of the charge cloud decreases, more charge is concentrated in the central component. At $V_g = 50$ V, the distributions have r_{oc} values of 0.9 to 1.4 mm and r_{ow} values of typically 4.0 mm, with approximately equal weights. At 800 V, r_{oc} has reduced to approximately 0.5 mm while r_{ow} has dropped to approximately 3 mm.

There is relatively little difference between the charge clouds obtained at $V_c = 2.65$ and 2.80 kV across the range in V_g. However, at $V_c = 2.90$ kV there is a marked difference.

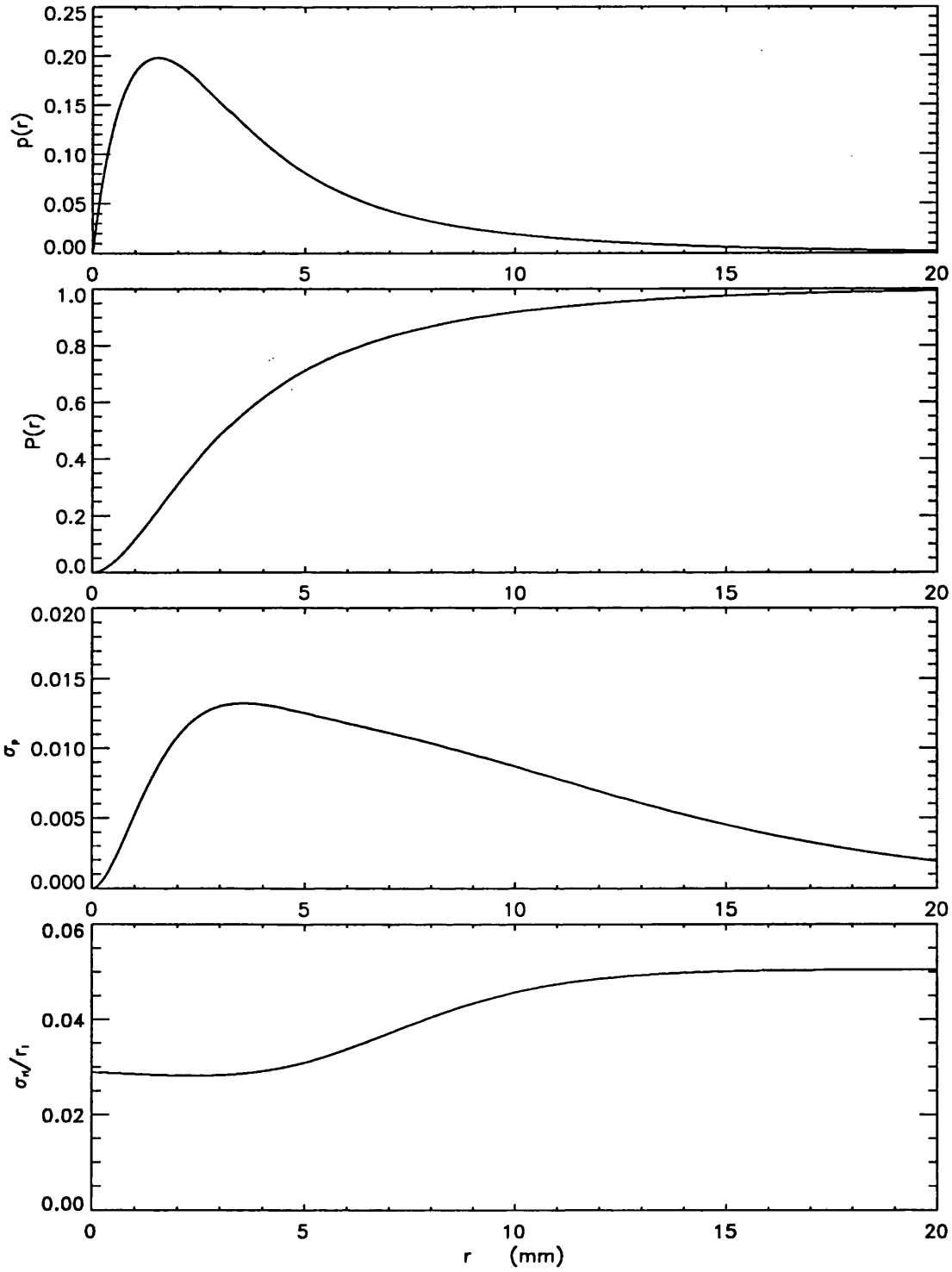

Figure 4.6: Radial probability distributions and associated uncertainties as determined from the fit parameters.

These curves are generated from the fit parameters obtained for g = 6.2 mm, V_g=100 V and V_c=2.8 kV and with a perpendicular pore bias angle/split orientation. The terminology is explained in the text.

V_g (V)	V_c (kV)	Bias Angle Alignment	r_{oc} (mm)	r_{ow} (mm)	a_c
50	2.65	$\perp$	1.32	3.8	0.59
50	2.80	$\perp$	1.28	3.9	0.56
50	2.90	$\perp$	0.86	3.3	0.44
100	2.65	$\perp$	0.96	3.5	0.69
100	2.80	$\perp$	0.95	3.3	0.66
100	2.90	$\perp$	0.76	2.9	0.57
200	2.65	$\perp$	0.69	3.1	0.75
200	2.80	$\perp$	0.78	3.4	0.78
200	2.90	$\perp$	0.72	3.5	0.78
400	2.65	$\perp$	0.54	3.1	0.82
400	2.80	$\perp$	0.59	3.0	0.81
400	2.90	$\perp$	0.62	4.3	0.87
800	2.65	$\perp$	0.42	3.1	0.85
800	2.80	$\perp$	0.47	3.0	0.84
50	2.65	$\parallel$	1.41	4.3	0.64
50	2.80	$\parallel$	1.34	4.1	0.60
50	2.90	$\parallel$	1.04	3.8	0.52
100	2.65	$\parallel$	1.04	3.6	0.70
100	2.80	$\parallel$	1.04	3.5	0.69
100	2.90	$\parallel$	0.90	3.2	0.65
200	2.65	$\parallel$	0.78	3.6	0.80
200	2.80	$\parallel$	0.82	3.4	0.79
200	2.90	$\parallel$	0.82	3.5	0.79
400	2.65	$\parallel$	0.59	3.5	0.85
400	2.90	$\parallel$	0.73	12	0.93
800	2.65	$\parallel$	0.43	3.1	0.85
800	2.80	$\parallel$	0.50	3.5	0.87

Table 4.4: The fit parameters for the radial distribution as measured at 6.2 mm for both anode orientations.

The parameters are defined in Equation 4.1. The alignment column refers to the alignment of the channel pore bias angle with respect to the split on the anode.

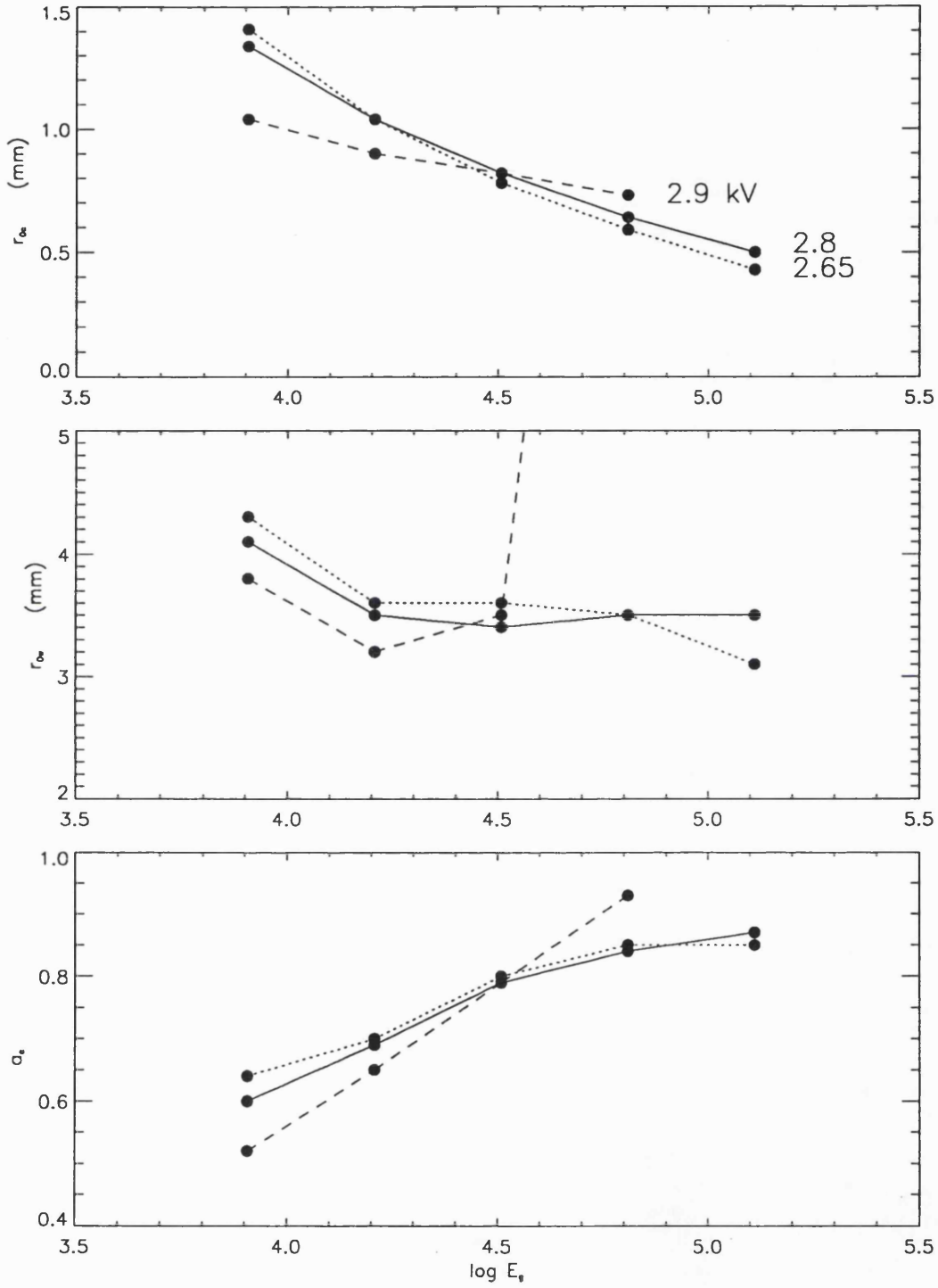

Figure 4.7: The fit parameters obtained with $g = 6.2$mm and the chevron bias angle aligned parallel to the anode split.

The line types in each graph correspond to the value of V_c as indicated in the r_{oc} plot. The parameters are defined in Equation 4.1.

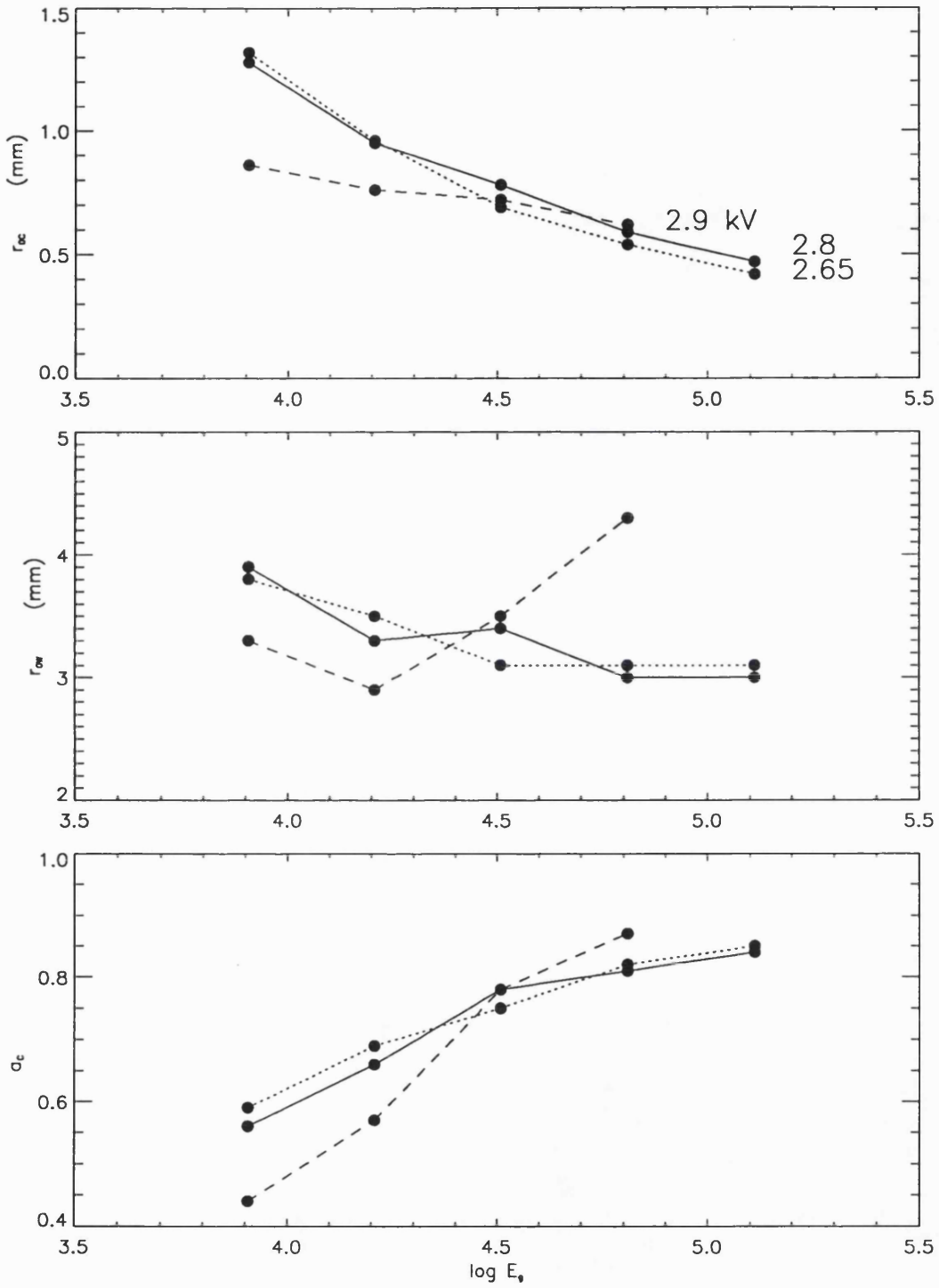

Figure 4.8: The fit parameters obtained with $g = 6.2$mm and the chevron bias angle aligned perpendicular to the anode split.

The line types in each graph correspond to the value of V_c as indicated in the r_{oc} plot. The parameters are defined in Equation 4.1.

Both components of the charge cloud are significantly smaller for V_g = 100 V, i.e. E_g = 160 kV.mm^{-1}. At V_g = 200 V, the three values of V_c produce similar charge clouds. At 400 V, the values of r_{oc} are larger at V_c = 2.9 kV than for the other two. This behaviour is present to a much smaller extent for V_c=2.8 kV. This behaviour is present for both pore bias angle orientations and is also present to a lesser extent in the size of the wing component.

For the data taken at this anode gap, the amount of charge concentrated in the central component increases with increasing V_g, from approximately 50% at 50V, to 85 % at 800 V. Therefore, at high gap voltages the central peak is the dominant component of the spatial distribution.

The variation of a_c with E_g and V_c is analogous to that observed with the scale parameters of the two terms. A larger fraction of the charge is concentrated in the core for lower values of V_c at low E_g and the situation is reversed at high E_g. The concentration of more charge in the wings with increasing gain has also been seen by Rasmussen & Martin (1989) at g = 15 mm and V_g=400 V, corresponding to E_g=2.67 kVm^{-1}.

4.3.3 The Fit Parameters at an Anode Gap of 3.0 mm.

The fit parameters obtained for g = 3.0 mm are listed in Table 4.5 and are shown in Figure 4.9. At a gap of 3 mm, the sizes of the scale parameters decrease with increasing V_g for all values of V_c.

The fit parameters appear to vary monotonically with V_c for this gap. The difference between the values r_{oc} obtained for each V_c remain fairly constant for various values of V_g. The difference between the size of the wing components, those that could be measured, reduces significantly with increasing V_g. At least 75% of the charge is always present in the core component. Hence, the central peak is always the dominant component at this gap width. As opposed to the measurements made at g = 6.2 mm, the amount of charge concentrated within the core reduces with increasing V_g.

4.3.4 A Simple Ballistic Model

Assuming no interaction between the electrons, the horizontal distance, d, an electron will travel from the pore while traversing the MCP-anode gap is,

$$d = \frac{2g\sqrt{T}\sin\theta}{\sqrt{T}\cos\theta + \sqrt{T\cos^2\theta + V_g}} \quad , \tag{4.13}$$

V_c (kV)	V_g (V)	r_{oc} (mm)	r_{ow} (mm)	a_c
2.8	110	0.68	2.45	0.81
	200	0.55	2.04	0.81
	300	0.47	1.83	0.79
	400	0.42	1.63	0.77
	500	0.38	1.49	0.75
	600	0.37	1.59	0.77
	700	0.35	1.47	0.75
	800	0.33	1.34	0.73
	900	0.32	1.41	0.73
	1000	0.30	1.33	0.70
2.9	110	0.77	3.27	0.88
	200	0.61	2.35	0.86
	300	0.53	2.03	0.84
	400	0.47	1.59	0.78
	500	0.45	1.63	0.80
	600	0.42	1.49	0.77
	700	0.41	1.52	0.77
	800	0.39	1.43	0.74
	900	0.39	1.40	0.75
	1000	0.39	1.50	0.76
3.0	115	0.83	4.87	0.93
	200	0.69	3.20	0.91
	300	0.63	2.91	0.91
	400	0.56	1.73	0.83
	500	0.57	2.39	0.88
	600	0.54	1.76	0.82
	700	0.53	1.94	0.83
	800	0.52	1.82	0.81
	900	0.51	1.80	0.77

Table 4.5: The fit parameters for the radial distribution obtained at a gap of 3.0 mm. The parameters are defined in Equation 4.1

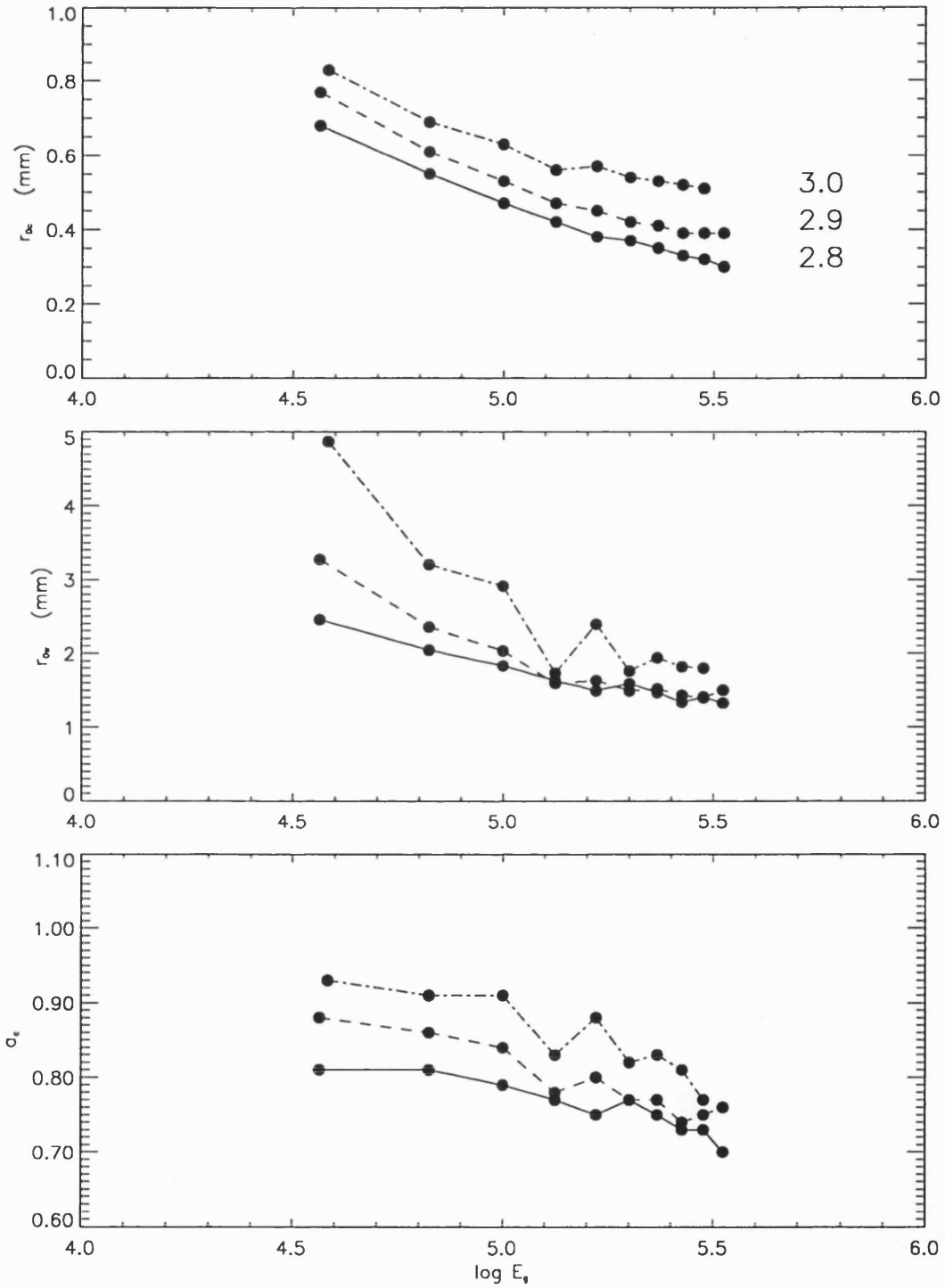

Figure 4.9: The fit parameters obtained at an anode gap of 3.0 mm. The parameters are defined in Equation 4.1.

where T is the output kinetic energy of the electron and θ is the angle between the MCP velocity vector and the normal to MCP face. A ballistic model requires knowledge of the angle and energy distributions.

Energy and Angular Distribution of the Output Electrons

The energy distribution of output electrons for a single, single thickness MCP has been measured by Koshida & Hosobuchi (1985) and Koshida (1986). They find that the energy distribution has a peak at about 5 eV and a long exponential tail with energies exceeding 100 eV, see Figure 4.10. As shown in this diagram, in unsaturated mode the majority of electrons have an energy > 50 eV. As saturation increases the number of high energy electrons decrease. Approximately 80% of the electrons lie equally distributed between the two lower energy ranges. They determine that the low energy peak is caused by electrons produced in the region of constant potential caused by the end-spoiling while the high energy tail originates from regions further up the pore. The authors attribute the shift to low energy electrons with increasing saturation to the charging of the channel wall producing a nonlinear electric field inside the pore, as discussed in Section 1.1.3.

As electrons with different output energies appear to originate from different regions within the channel, the energy and angle distributions of the electrons cannot be treated independently. Low energy electrons originating on the end-spoiling should have a broader output angle distribution than the high energy electrons originating further up the channel.

Bronshteyn *et al.* (1980) have measured the angular distribution of the electrons from a single MCP. They found that the distribution is approximately Gaussian with a half-width of $10 - 20°$ and a peak at an inclination to the MCP normal equal to the bias angle. They also measured the energy distribution of electrons at a given output angle and found that the range of energies is much larger for electrons with low inclination angles than for those with relatively high inclinations, see Figure 4.11. However, the authors do not discuss saturation. Given that they measured increasing electron energy with increasing plate bias voltage, as opposed to what Koshida & Hosobuchi (1985) described for increasing saturation, it is most likely that the MCPs are operated in the linear mode.

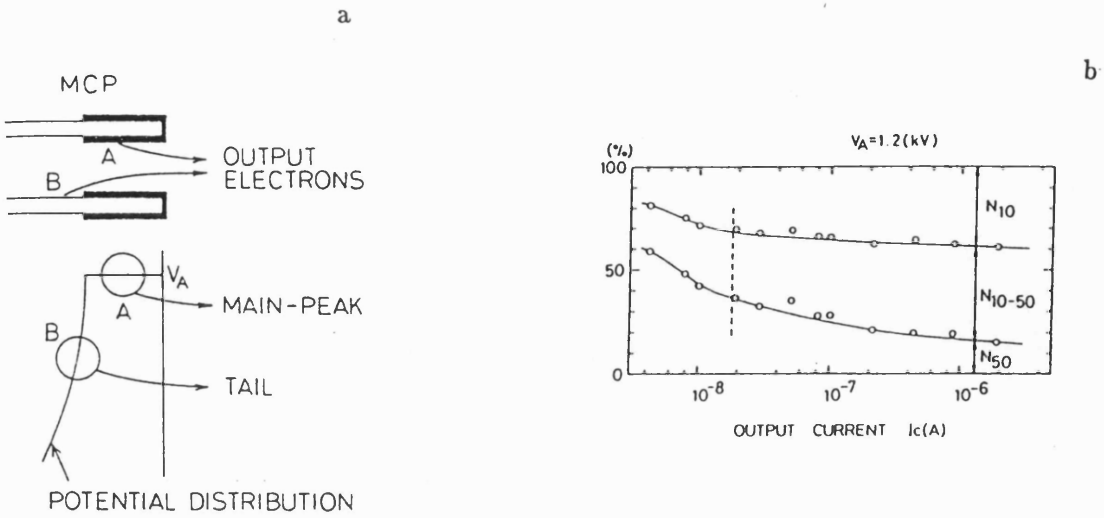

Figure 4.10: The output energy distribution from one single thickness MCP.
Figure a) shows the energy distribution of output electrons for both saturated and unsaturated modes and the probable regions from which the various energy output electrons originate. Figure b shows the cumulative distribution of the output energies with varying levels of saturation. The variables V_A and I_c refer to the plate voltage across the single plate and the amount of current collected on the anode, respectively. Approximately 45000 pores were illuminated so $10^{-}8$ A corresponds to $\approx 1.4 \times 10^6$ e^-.pore^{-1}.s^{-1}. The dashed line represents the onset of saturation. Both figures are from Koshida & Hosobuchi (1985).

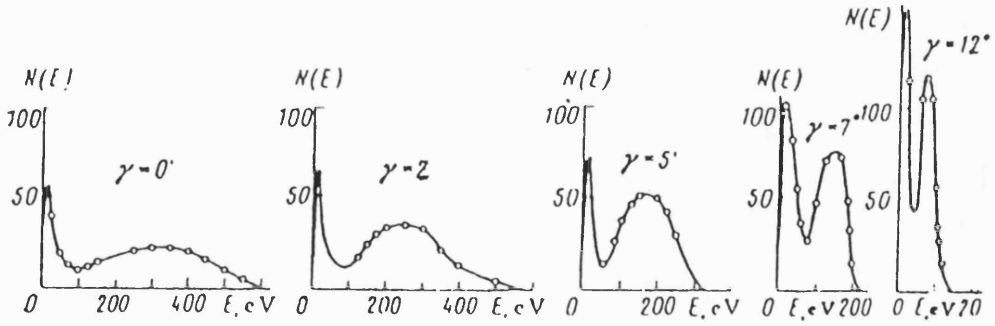

Figure 4.11: Energy distribution of output electrons at various output angles for a single MCP.
The angle γ refers to the inclination of the output electrons velocity vector to the pore axis. From Bronshteyn *et al* (1980).

The Maximum Size of the Charge Cloud Due Solely to Ballistic Effects

Figure 4.12 shows the horizontal distance an electron can travel while traversing the MCP-anode gap for various combinations of output angles and energies, as determined by using Equation 4.13. Electrons with energies less than 10 eV are assumed to be emitted from the end-spoiling, undergo no acceleration in the channel and have no constraints on their output angles.

Electrons with higher energies are assumed to come from the wall of the channel beyond the end-spoiling. They are assumed to be emitted from the wall with no energy so that all the kinetic energy comes from acceleration within the channel. The electric field within the pore is assumed to be linear, i.e. the gradient of the potential along the channel is linear until the end-spoiling is reached. The constraint on the angles is determined by the straight line between the point from which the electron is assumed to be emitted and the opposite edge of the channel. As the output angles of these electrons are assumed to be constrained but those with low energies are not, there is a discontinuity in the model at 10 eV.

These constraints represent the upper limit of the possible output angles as the electric field within the channel will cause the electrons to follow parabolic trajectories, and so inclinations to the pore axis will be less than in the straight line case. The presence of an electrostatic lens at the pore output will tend to further collimate the electrons (Guest, 1978).

Figure 4.12 shows that relatively low energy electrons at high inclinations to the pore axis travel the greatest horizontal distance. Although the output angle is the most important variable for determining the horizontal distance, the variation of electron energy for a given angle can produce differences in the distance travelled, particularly for low energy electrons.

Given that the peak of the angular distribution occurs at the pore bias angle and almost all the electrons have an energy less than 50 eV, the peak of the charge cloud would be expected to lie within 1 mm of the pore. I shall take it to be located at a distance of 0.5 mm.

Even though the maximum value for the output angle for a given energy is almost certainly overestimated, those electrons that have travelled the furthest from the pore have not reached a distance of 4.0 mm, i.e. a radius of 3.5 mm. The average values of the fit

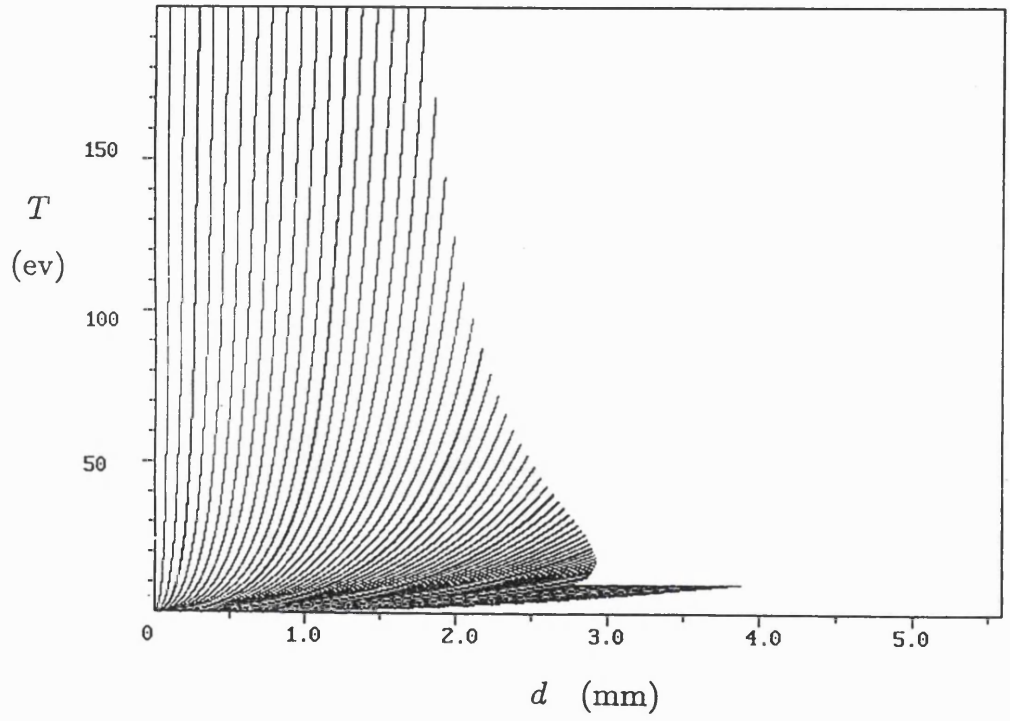

Figure 4.12: Horizontal distance travelled by output electrons while traversing the MCP-anode gap for a simple ballistic model with various combinations of angles and output kinetic energies.

This diagram represents the case where $V_g = 100$ V, $g = 6.2$ mm and a plate voltage of 1.4 kV. The channel is assumed to be azimuthally symmetric and the electrons all come from one azimuth angle. The physical dimensions of the channel and the end-spoiling are set to be the same as the MCPs used in the experiment, see Section 3.3. In this model, the electrons do not interact. The various curves represent different angles between an electron's velocity vector and the normal to the MCP. The angles increase in a clockwise direction about the origin and the step between each of the curves is 1°. The dark curves are separated by 10° and correspond to inclinations to the MCP normal of 3°, 13° (the pore bias angle), 23° and so on. The limits on the combinations of angle and kinetic energy are discussed in the text.

parameters for $V_g = 100\ V$ from Table 4.4 are; $r_{oc} = 0.94$ mm, $r_{ow} = 3.4$ mm and $a_c = 0.66$. Combining these values with Equation 4.3, I estimate over 30% of the total charge cloud lies outside a radius of 3.5 mm. With a limit on the combination of angle and energy comparable to that measured by Bronshteyn *et al.* (1980), i.e. 10° and 20 eV, the limiting radius is approximately 1.0 mm which contains only about 20% of the charge cloud. Also, as seen in Figure 3.7, a significant number of electrons have been collected at radii of up to 10 mm. Even if an electron was emitted parallel to the MCP face, it would require an initial energy of approximately 65 eV to travel 10 mm horizontally while traversing the gap.

Although a simple ballistic model can produce distributions with sizes comparable to the size of the core, it is totally inadequate for describing the size of the wing component.

4.3.5 Space Charge

Figure 4.13 shows the horizontal distance travelled by an electron due to the coulomb repulsion between it and a single particle with a massive negative charge for typical output electron time of flights. At $g = 6.2$ mm and $V_g = 100\ V$, it would take approximately 2.0 ns for an electron with zero initial velocity to cross the MCP-anode gap. The diagram shows that a charge of only a few percent of the total charge within the electron cloud, $\approx\ 6.4 \times 10^5\ q$, is needed to accelerate the electrons to the horizontal velocity needed to reach a distance of 10 mm. Therefore, space charge effects can explain the relatively large size of charge cloud.

The large variation in electron velocities will make a detailed model of the interaction between electrons extremely complex. Only a detailed Monte-Carlo simulation could produce realistic predictions. Detailed knowledge of the electric fields at the pore exit would also be necessary to determine an initial distribution of charge.

4.4 The Variation of Charge Cloud Size with MCP Operating Conditions.

4.4.1 The Effects of Gain on Charge Cloud Size

As discussed in Section 3.7.1, multiple data sets were acquired at constant operating conditions. Some of these data sets were concatenated to produce a data set containing 3.6×10^5 events. The data were binned into 10 intervals of gain each containing approxi-

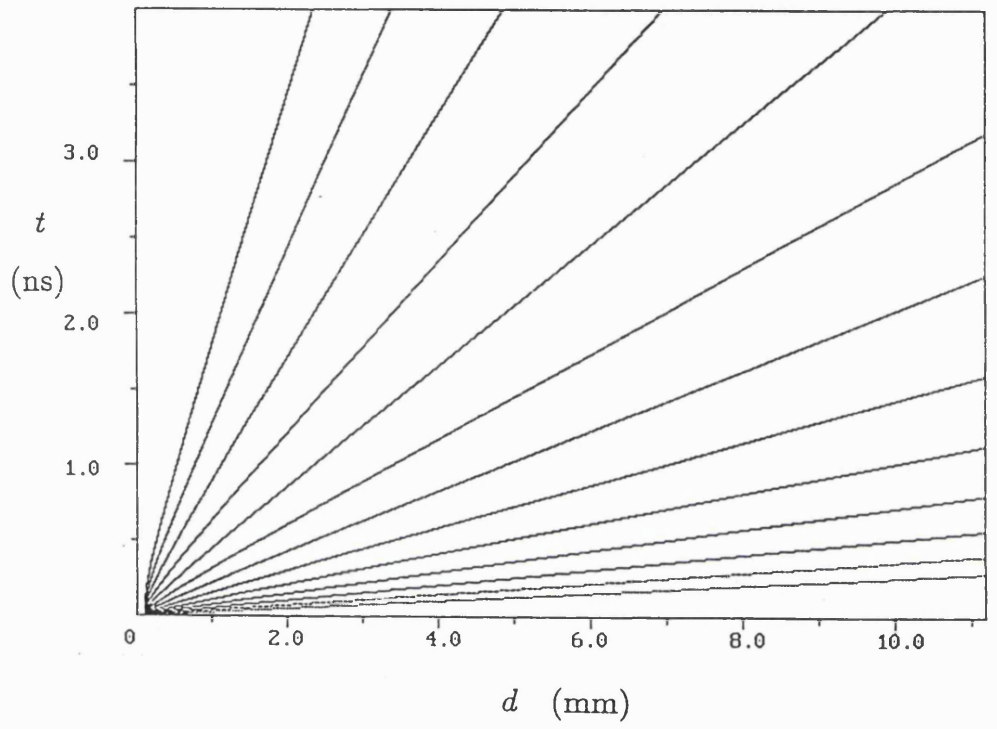

Figure 4.13: Horizontal distance travelled by a single electron in a given time due to Coulomb repulsion.

The various curves represent the distance travelled in a given time due to the repulsion between an electron and a single, massive particle with varying large negative charges. The particle with the large charge is taken to be massive so that only the electron moves due to repulsion. The charge on the massive particle increases in a clockwise direction about the origin and doubles for each successive curve. The range of the magnitude of the charge represented by the 13 curves is from 10^4 to 4.096×10^7 q, where q is the unit charge. The initial separation between the two particles for each of the curves is 50 μm and they are assumed to be moving with zero relative velocity.

G (Channel)	G ($\times 10^7\ e^-$)	r_{oc} (mm)	r_{ow} (mm)	a_c
65	1.7	0.86	3.4	0.64
82	2.2	0.94	3.6	0.68
94	2.5	0.99	3.9	0.70
105	2.8	1.04	4.0	0.72
115	3.0	1.06	3.9	0.71
125	3.3	1.24	4.3	0.77
136	3.6	1.29	4.4	0.78
147	3.9	1.29	4.2	0.75

Table 4.6: Fit parameters determined for the gain intervals as indicated in Figure 4.14. The channel numbers and gains correspond to the centre points of the intervals.

mately 3.6×10^4 events. The two extreme intervals were discarded as they cover a much wider range of pulse height than the other eight. An average S curve was produced and the best two exponential fit was determined for each of the eight remaining intervals. Figure 4.14 shows the PHD for this data set and the edges of the pulse height intervals. Table 4.6 shows the fit parameters obtained for these intervals.

Figure 4.15 shows the radii containing fixed percentages of the total charge cloud for the 8 different gain intervals. The plots show that below $P(r_l) < 0.8$ the relationship between gain and r_l is monotonic. The variation is small with respect to the uncertainties but it is clearly systematic as was suggested by the pulse height related structure within the S curve, see Section 3.4.2.

Similar results were obtained for both bias angle/split orientations. When I subdivided the 45000 event data sets, I did not obtain a systematic relationship between r_l and gain at any probability level. This is probably due an insufficient number of events in the gain intervals to obtain reliable estimates of the mean S curve. Therefore, the monotonic relationship between size and gain has been only unambiguously demonstrated at this set of operating voltages, which is the only set at which hundreds of thousands of events were

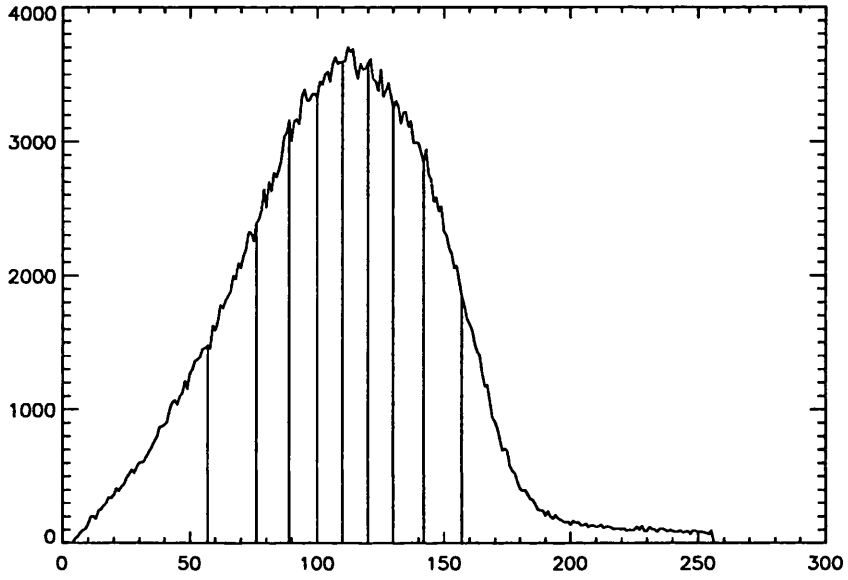

Figure 4.14: The PHD of the large data set showing the edges of the multiple gain intervals. The data was obtained at $g = 6.2$ mm, $V_g = 100$ V, $V_c = 2.8$ kV with a perpendicular pore bias/split orientation. The units on the abscissa are the channel numbers as determined directly from the ADC readings. The conversion factor is 2.6×10^5 e^-/channel and the modal gain is 2.9×10^7 e^-.

acquired during the experiment. However, as Figure 4.15 confirms the existence of a systematic relationship, suggested by the pulse height related structure within the S curve and this structure was observed in all data sets, the gain/size relationship must be expected to exist under all operating conditions.

The fits obtained for S curves consisting of the whole PHD, as displayed in Figure 4.15 and Table 4.6, describe smaller charge clouds than those obtained for the gain intervals containing the mode, mean or median of the PHD. This is most probably caused by bias towards the low gain events when determining the average S curve. Figure 3.8 shows that in some regions of the measured S curve, there is a much larger variation in the curve for low gain events than for the larger events. This larger variation might provide a larger "moment" when determining the mean, biasing the average to a lower level.

Therefore, the affect of varying charge cloud size on the Split Strip Anode itself is of importance as the fitting procedure returns smaller charge clouds than would be expected, when the whole PHD is used. Although in this instance, the biasing and the variation of radius with gains are comparable to the uncertainties produced by the fit parameters, it is not known how significant it would be under other operating conditions. Both of these effects should be examined in detail in future experiments to determine how significant they are and how they vary with operating conditions. This would require data sets containing several hundred thousand events as 45,000 event data sets have proved inadequate to achieve reliable fits for determining the variation of the S curve with gain. The gain intervals that I used had sharp edges, so the cross sections through the S curve could not be approximated by Gaussians. The χ^2 statistic assumes implicitly that the errors in a distribution are normally distributed. Ideally, a few million events should be acquired and subdivided into a series of gain intervals with a Gaussian intensity distribution.

All of the other fits described in this chapter were made using the full PHD. As nothing is known about the biasing of the mean S curve for the other operating conditions, there is inevitably some degree of ambiguity when comparing data obtained under different conditions. For the rest of the chapter I have assumed that this biasing always behaves in a similar manner and that any variation is only comparable to the uncertainties observed for this set of operating conditions.

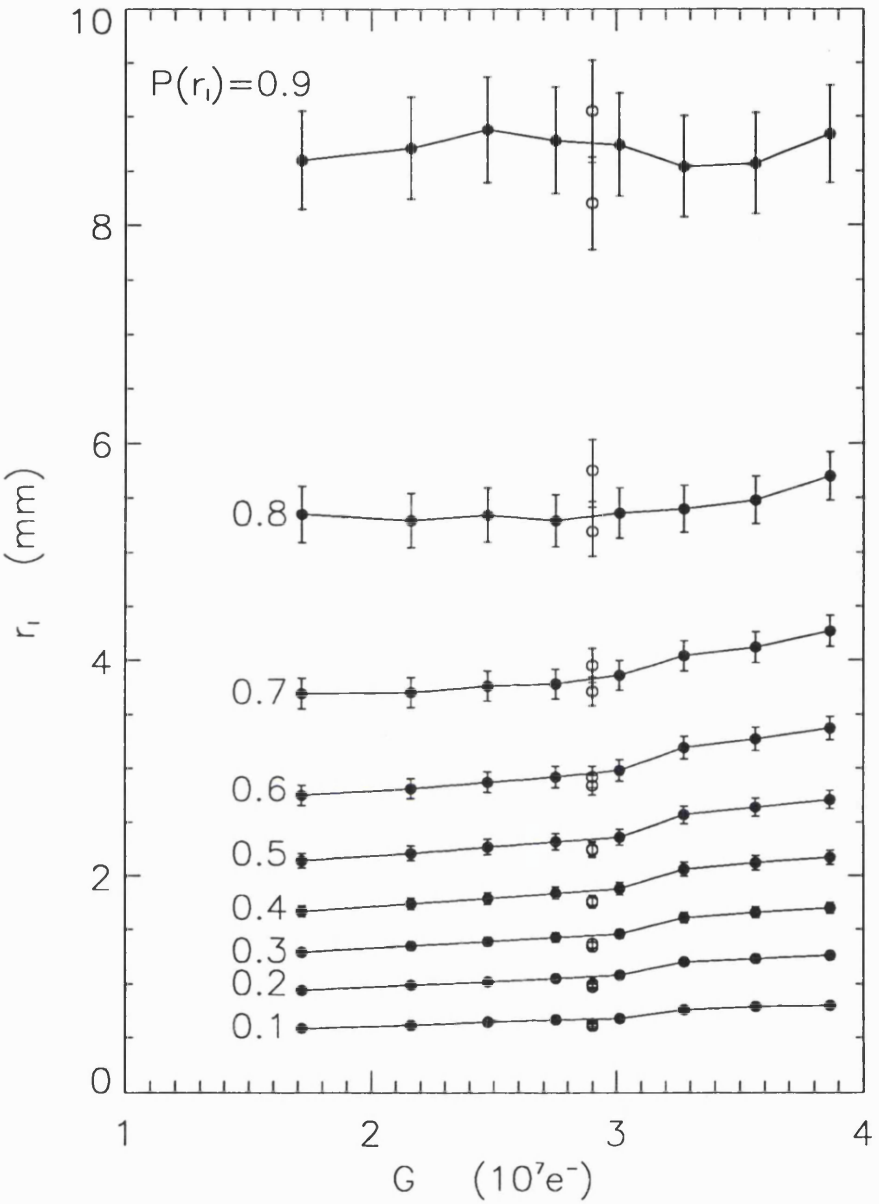

Figure 4.15: The variation of the size of the charge cloud with varying gain.
The filled circles represent the data obtained from the fits to the S curves derived from the subdivision of the PHD, as shown in Figure 4.14 The values of $P(r_l)$ for each of the curves are indicated in the figure. The values for r_l are determined from the fit parameters listed in Table 4.6. The open circles indicate the fit to the S curve consisting of contributions from events throughout the entire PHD for both the 45,000 and 360,000 event data sets. These fit parameters are listed in Table 4.4. The gain at which these data are plotted correspond to the modal gains of the PHDs. The mean and median gains are located within only a few channels of the mode.

4.4.2 The Effects of E_g on Charge Cloud Size

Figure 4.16 shows the variation of r_l for various levels of $P(r_l)$ with increasing E_g. As the plot is log/log, a power law between radius and electric field strength would appear as a straight line. As all the curves show significant curvature, there is no straight forward power law relationship. There is also very little variation between the form of the curves for the different $P(r_l)$ levels of the charge cloud from the 10% to the 90% levels.

Approximating the data at $E_g < 100$ kV.m^{-1} to a straight line, the approximate index of the power law is -0.3. The time of flight, t_f, for an electron with zero initial kinetic energy, across the MCP-anode gap can be determined from Equation 4.13,

$$t_f = g\sqrt{\frac{2m_e}{qV_g}} \quad , \tag{4.14}$$

where m_e is the electron mass. A charge cloud in which the size evolved ballistically would follow a power law with an index of -0.5 and one in which the electrons continuously underwent a constant acceleration would have an index of -0.25.

Figure 4.17 shows the variation of r_l with t_f and gives some indication of the expansion rate of the charge cloud. It is clear that the cloud expands at different rates at different levels and that it is not expanding at a constant velocity but being continuously accelerated. The acceleration is highest at the radii containing the most charge which is as expected for Coulomb repulsion.

4.4.3 Plate Bias Voltage

Figure 4.18 shows the variation of r_l with E_g for three separate values of V_c at four probability levels for $g = 3.0$ mm. They indicate a monotonic relationship between r_l and V_c for $P(r_l) < 0.9$. However, as shown in Figure 4.19, this situation does not hold for $g = 6.2$ mm in which at low field strengths and at up to the 50% probability level the 2.9 kV charge cloud is significantly smaller than the 2.8 kV case. The data obtained at the two gaps are compared in the next section.

Therefore, V_c does affect the size of the charge cloud but not in an easily predictable manner and the size of the charge cloud is not driven solely by the gain. Therefore, space charge alone is insufficient to explain the variation of the charge cloud with V_c.

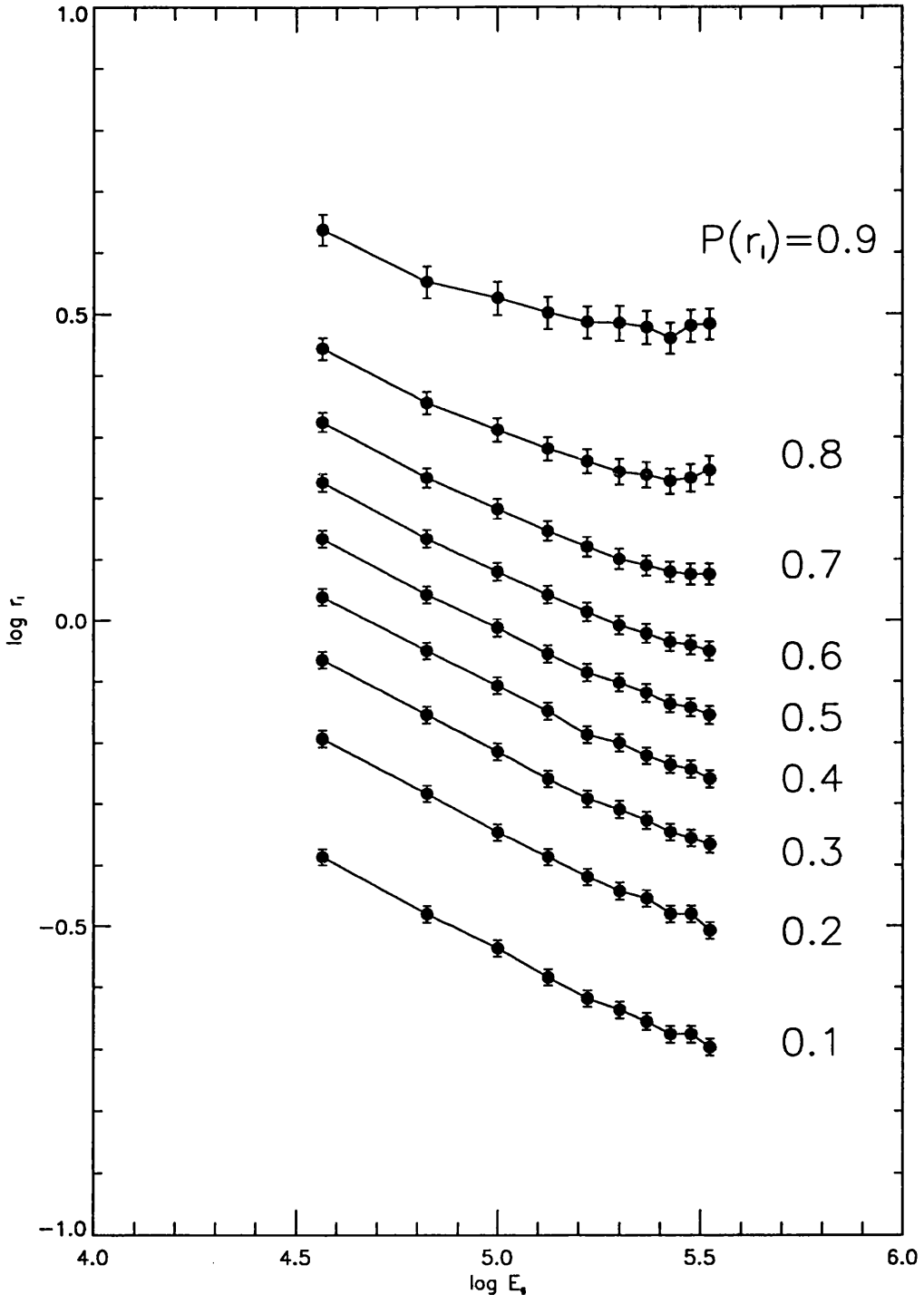

Figure 4.16: The variation of radii containing fixed fractions of the charge cloud with E_g. The data were obtained with $g = 3$ mm and $V_c = 2.8$ kV. The units of the radii are quoted in millimetres and E_g in V.m^{-1}. These are the same units used for all the logarithmic values displayed in all of the figures in this chapter.

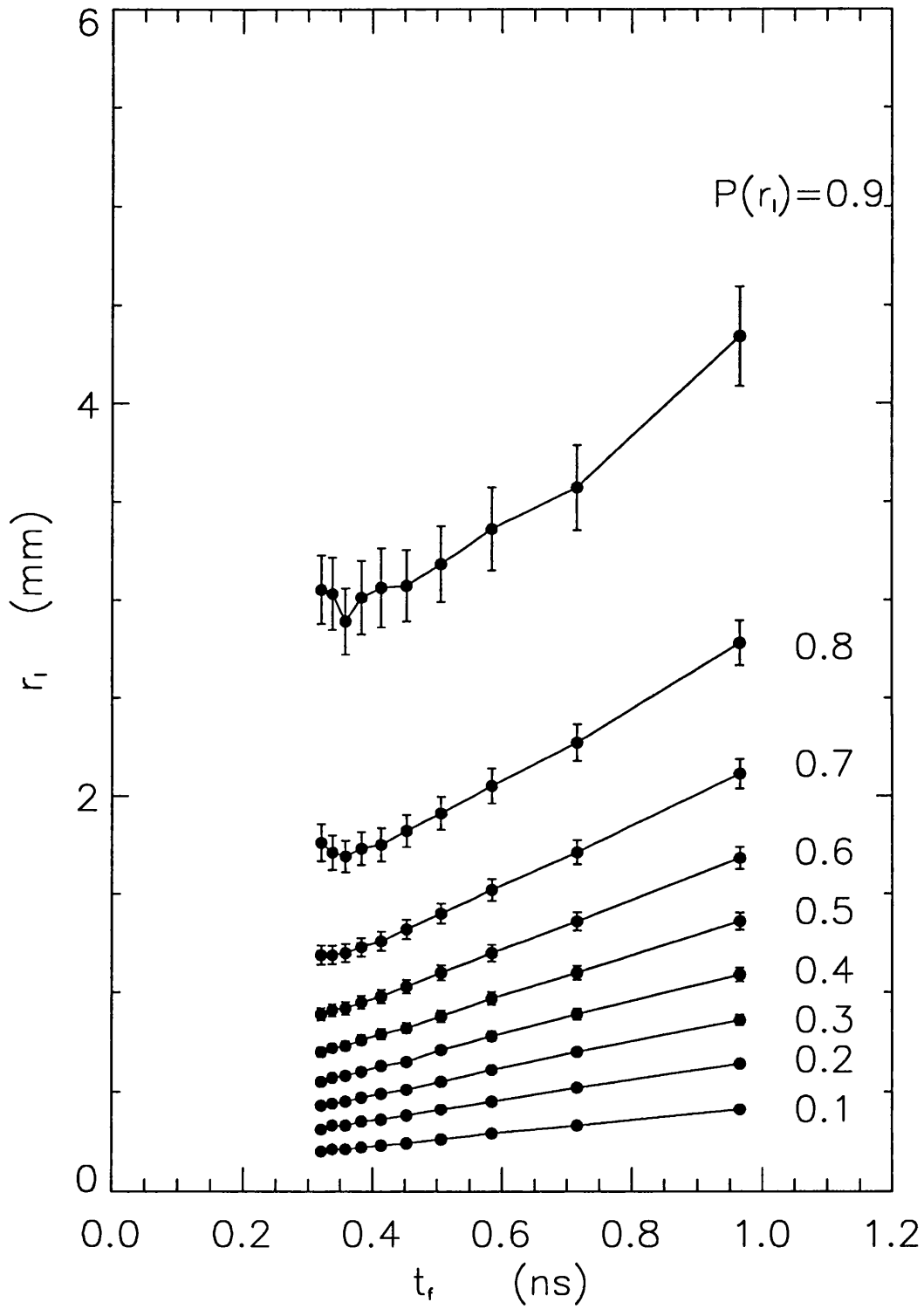

Figure 4.17: The variation of radii containing fixed fractions of the charge cloud with approximate electron time of flight.

The data are the same as in Figure 4.16. Time of flight for an electron with zero initial kinetic energy, t_f, is determined as in Equation 4.14.

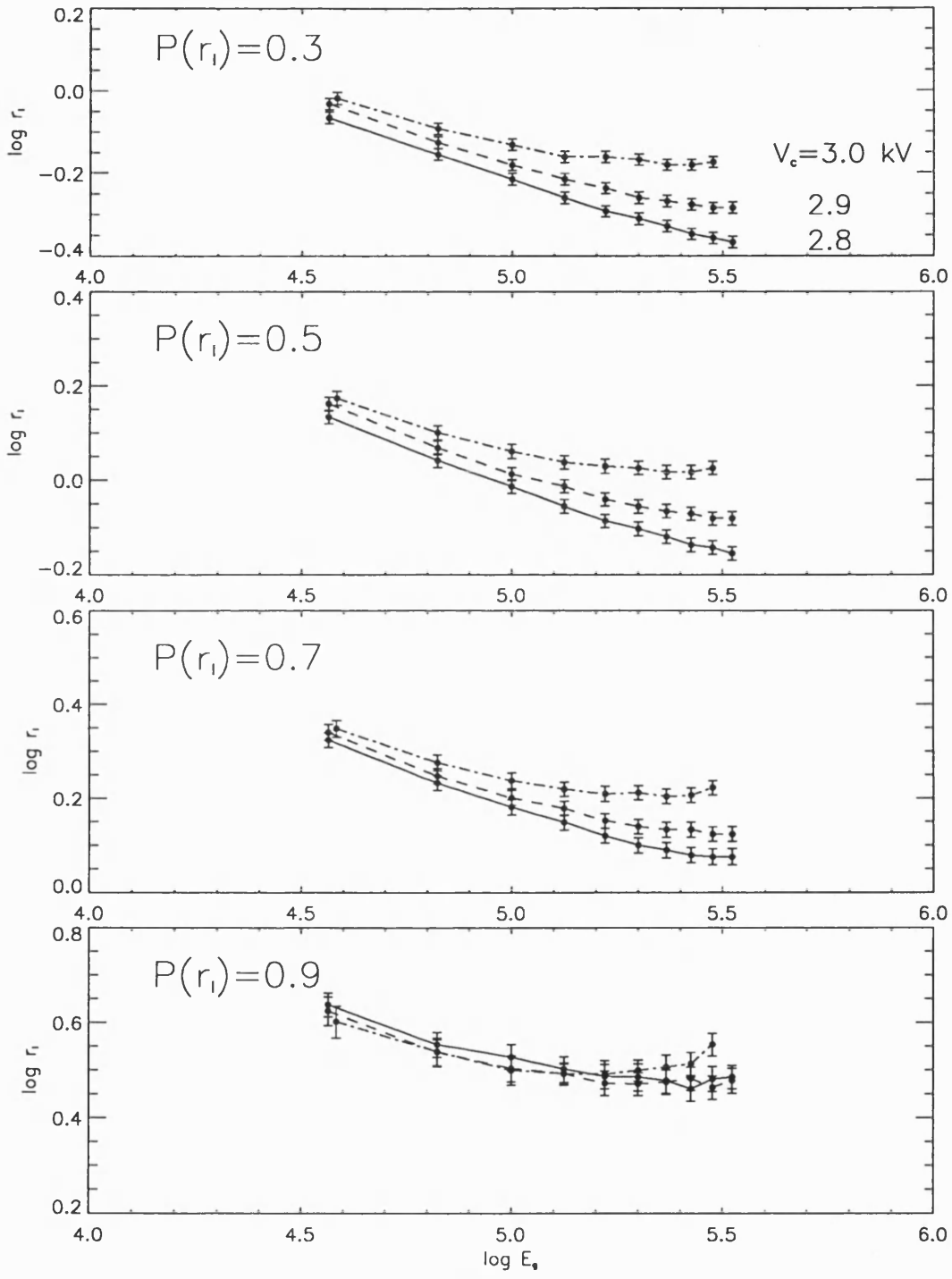

Figure 4.18: The variation of radii containing fixed fractions of the charge cloud with varying V_c for $g = 3.0$ mm.

The fraction of the charge cloud contained within r_l are indicated in each of the plots. The line types in the four diagrams correspond to the V_c values as indicated in the top graph.

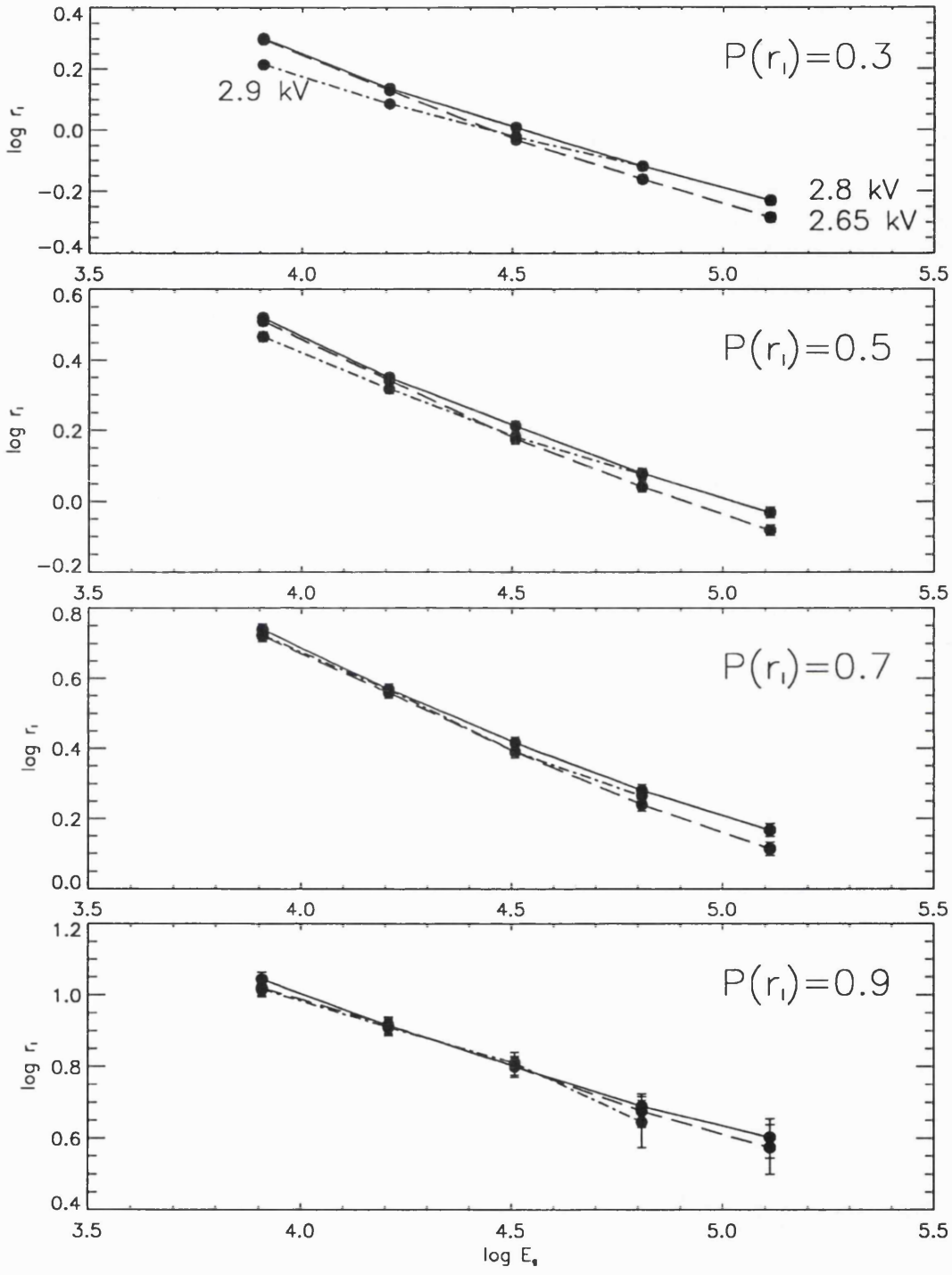

Figure 4.19: The variation of radii containing fixed fractions of the charge cloud with varying V_c for $g = 6.2$ mm.

This data was taken with the pore bias angle aligned perpendicular to the anode split. The plot for the parallel case is similar. The fraction of the charge cloud contained within the radii are indicated in each of the plots. The line types in the four diagrams correspond to the V_c values as indicated in the top graph.

4.4.4 Comparison of the Measurements for the Two Gaps.

Figure 4.20 directly compares r_l for the 2.8 and 2.9 kV data obtained for the two MCP-anode gaps with respect to E_g. Of the 14 different combinations of V_g and g, 8 correspond to values of E_g lying within a region in which the data sets for the two gaps overlap. The figure shows that at $P(r_l) < 0.9$ the two curves fall on top of each other, within errors, for most of the values of E_g in the overlapping region. For $P(r_l) > 0.9$ the discontinuity observed at the 90% level becomes larger.

Figure 4.21 compares the data obtained at the two gaps with respect to t_f. Unfortunately, there is a smaller degree of overlap between the two data sets for t_f than for E_g. The curves show a clear discontinuity between the two gaps for $P(r_l) < 0.9$. The intersection of the curves at the 90% level is probably coincidental as at higher levels the discontinuity is present again, but in the opposite sense to that observed at lower levels, i.e. the radii for $g = 3.0$ mm are less than those for $g = 6.2$ mm.

Figures 4.20 and 4.21 indicate that the size of the majority of the charge cloud most probably scales with the anode gap electric field strength rather than with the electron time of flight.

An interesting feature in Figure 4.20 is that at the 30% level, the 2.9 kV radii are significantly smaller than those for 2.8 kV for $\log E_g < 4.5$, approximately equal for $4.5 < \log E_g < 5.2$ and significantly larger where $E_g > 5.2$. This does not appear to be a function of the gap as the radii at these chevron voltages can be seen to be approximately equal within the intermediate range of E_g in Figures 4.18 and 4.19 but it appears to be a function of E_g.

As described in the previous section, the relationship between r_l and V_c is not a straightforward function of the increased gain due to increased V_c. However, the gain related structure within the S curves indicates that there is probably a direct relationship between gain and charge cloud size for a constant set of operating conditions. Therefore, the varying ratio of r_l at 2.9 kV to r_l at 2.8 kV is probably due to the variation of the applied voltage itself and the interaction with E_g, not the associated gain variation. The most likely mechanism for this behaviour involves the electrostatic lens present at the end of the pore formed by the electric field within the channel due to V_c and its interaction with E_g which penetrates into the channel. As E_g increases it will penetrate further into the channel, changing the electrostatic lensing.

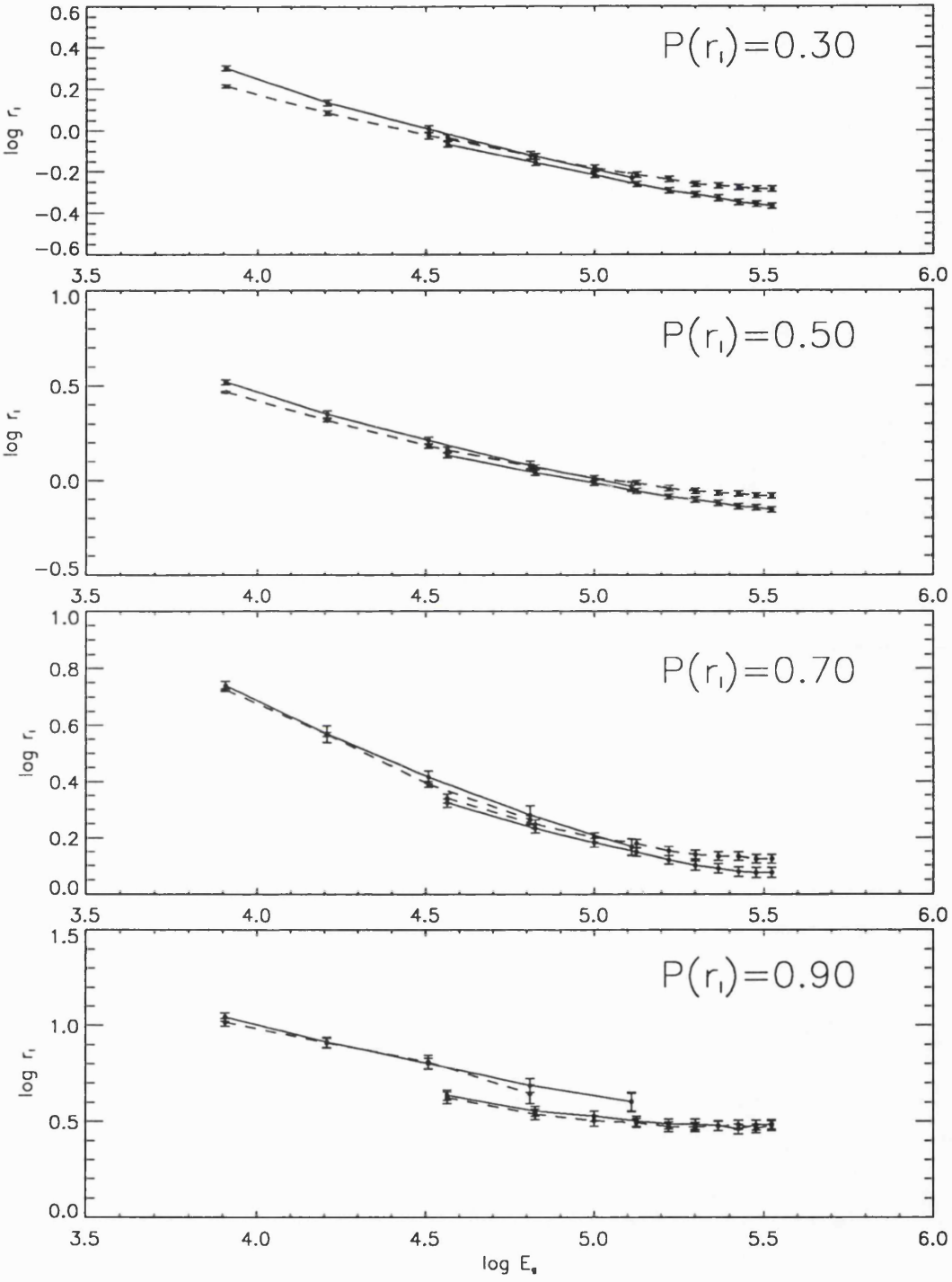

Figure 4.20: Comparison of r_l for the two anode gaps versus E_g.
The solid and broken lines represent the 2.8 and 2.9 kV data, respectively. The curves starting on the left side of the diagram represent the 6.2 mm data.

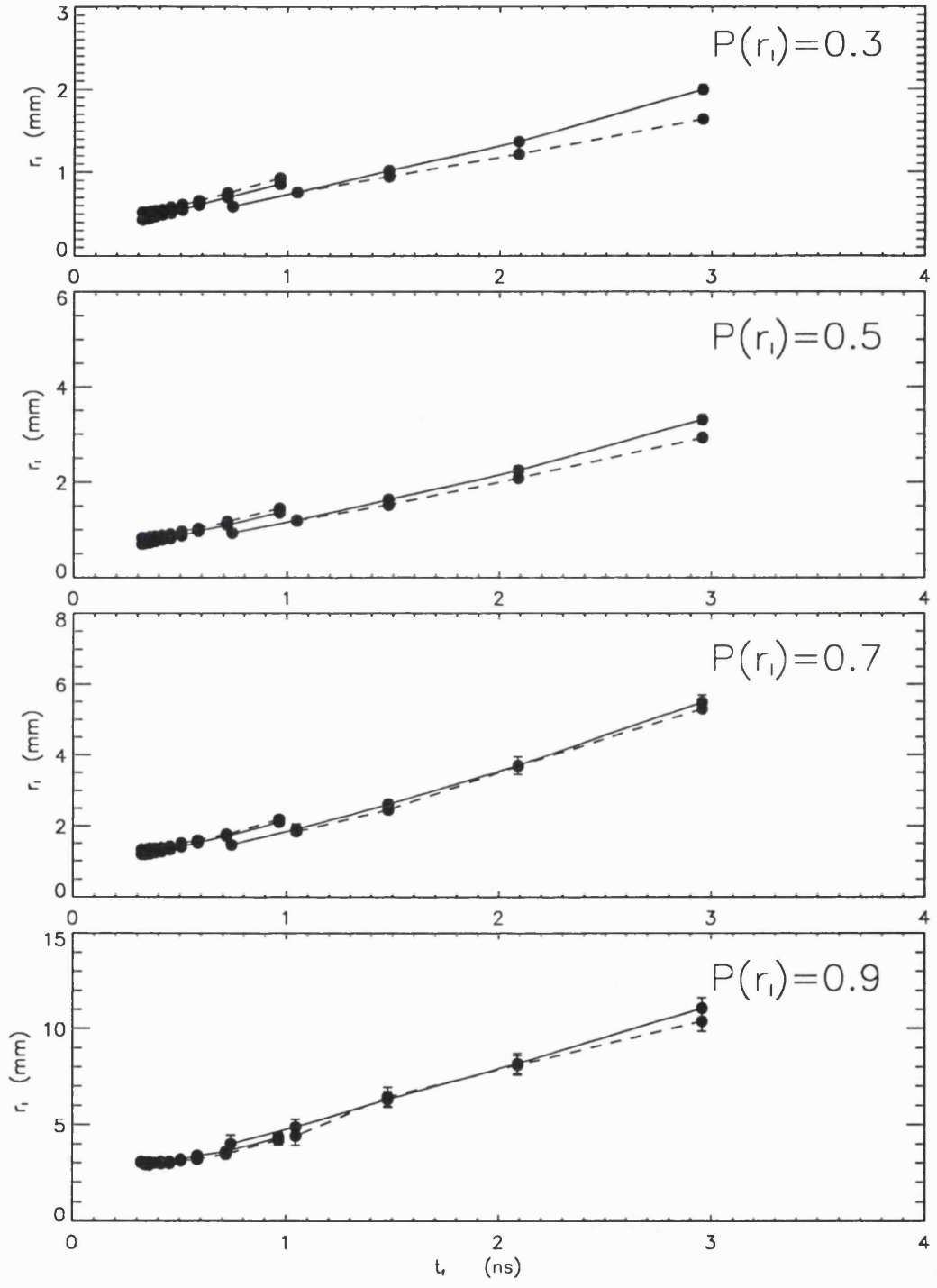

Figure 4.21: Comparison of r_l for the two anode gaps with respect to t_f. The solid and broken lines represent the 2.8 and 2.9 kV data, respectively. The curves starting on the left side of the diagram represent the 3.0 mm data.

Guest (1978) has modelled the electrostatic lens at the pore exit, with an estimated initial electron velocity distribution. However, the model does not take into account saturation or interaction between electrons as he modelled the situation for linear operation of a single plate illuminating a phosphor. A model of the affect of V_c in the present situation in which a chevron pair is being used in the saturated mode with a charge division readout, would have to take into account lensing as well as the variation of initial energy/angle distributions due to saturation and the effects of space charge. It would also probably need to take into account the time variation of the electric field inside the pore while firing including the influence of the electric field rotation (Gatti *et al.*, 1983). Such a model is far beyond the scope of this discussion.

4.4.5 The Effect of the Inter-plate Gap Voltage

The Effect on Gain

The effect of V_i on the gain of a chevron pair has been studied by Wiza *et al.* (1977), Fraser *et al.* (1983) and Smith & Allington-Smith, (1986). They find that the variation of gain with V_i, where $V_i > 0$, can be explained by considering the varying number of pores illuminated in the bottom MCP by a single pore in the top MCP. The last authors used the same set of MCPs as those used in this experiment and the discussion that follows is based on their analysis.

The number of pores illuminated in the bottom plate is calculated using a simple ballistic model. As the number of electrons leaving the first plate is much less than those exiting the rear plate, interaction between electrons is disregarded. Adding the radius of the pore to Equation 4.13, produces a equation similar to that presented in Fraser *et. al.* (1983) which can be used to calculate the illuminated area.

The maximum angle between the velocity vector and the MCP normal was determined, for this set of MCPs, to be $10 \pm 5°$ and the average energy was assumed to be 3 eV (Smith & Allington-Smith, 1986). Using these values, the gain would be a maximum for $V_i = 0$ when approximately 7 pores are illuminated in the bottom plate and reduce as V_i increases: at +30 V only 3 pores would be illuminated.

A negative V_i applies a retarding potential and so the low energy electrons are collected on the front MCP electrode. As low energy electrons represent a large proportion of the output from the first plate, the gain is significantly reduced.

The Effect on Charge Cloud Size

Figure 4.22 shows the variation of the fit parameters with V_i and is compared to the variation of gain. The saturation reduced by about 25 % at the extremes of the V_i range from the maximum at $V_i = 0$ and, given the large systematic error on saturation estimates of 10%, no significant difference between the positive and negative voltages was observed. Note that the maximum size of r_{ow} and a_c are offset by approximately +5 V from the maximum value of r_{oc} at $V_i = 0$.

Figure 4.23 shows the variation of r_l with modal gain. It shows that the size of the charge cloud is fairly insensitive to the variation in gain for $V_i > 0$ at all probability levels but is very sensitive to gain variations when $V_i \leq 0$. This again demonstrates that variation in gain alone is insufficient to explain variations in charge cloud sizes.

4.5 Charge Cloud Symmetry

4.5.1 Ellipticity

The values of r_o returned by the fitting procedure for the two chevron plane orientations indicate that the charge cloud is not azimuthally symmetric. In all cases, the values r_{oc} and r_{ow} obtained with the pore bias angle parallel to the split are greater than, or equal to those obtained with the bias angle and split orthogonal. Table 4.7 shows the ratios of the fit parameters obtained for the two bias angle orientations. Excluding the case where $V_c = 2.9$ kV and $V_g = 400$ V, in which anomalously large wing components were obtained, the average difference in the size of the fit parameters over all the cases is 9%. Figure 4.24 shows that on average, the charge clouds obtained with the parallel alignment are significantly larger at almost all $P(r_l)$.

From the MCP pore geometry, it is reasonable to expect that the charge cloud will exhibit either azimuthal or elliptical symmetry depending on the influence of the pore bias angle. Our experiments show that, to a first order approximation, the charge cloud can be regarded as being azimuthally symmetric. The variations between r_o values for the two chevron plane orientations show that a function with elliptical symmetry presents a more accurate description of the charge cloud. The fitting procedure we have described returns a radial distribution. However, the translational symmetry of the anode also allows it to measure an elliptical charge cloud. The fitting procedure returns the charge distribution

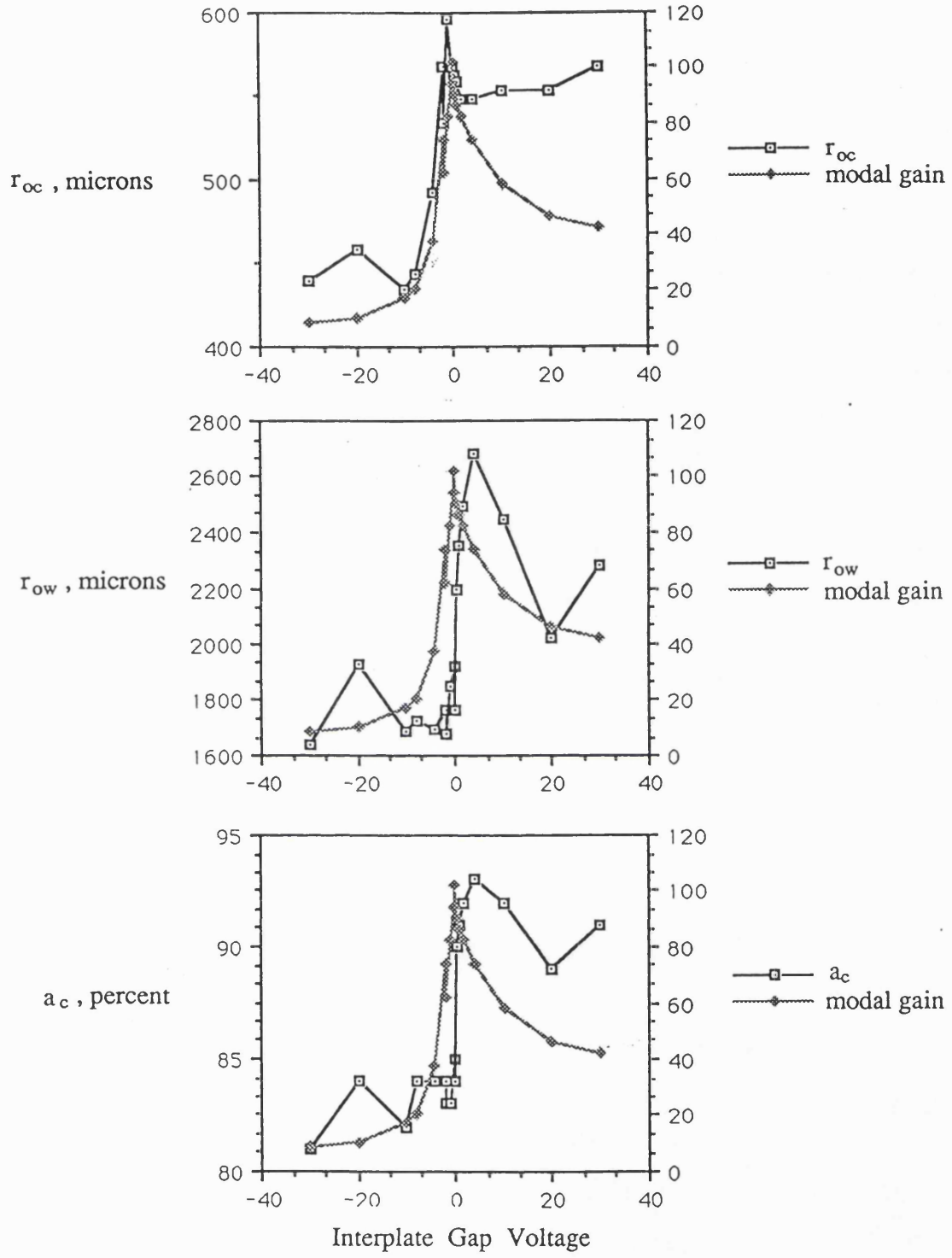

Figure 4.22: The affect of the inter-plate voltage on the fit parameters.
The voltages V_g and V_c were held at constant values of 400 V and 3.0 kV, respectively. The modal gain is plotted in units such that 100 corresponds to 1.5×10^8 e^-. The fit parameters are defined in Equation 4.1. From Lapington & Edgar, (1989).

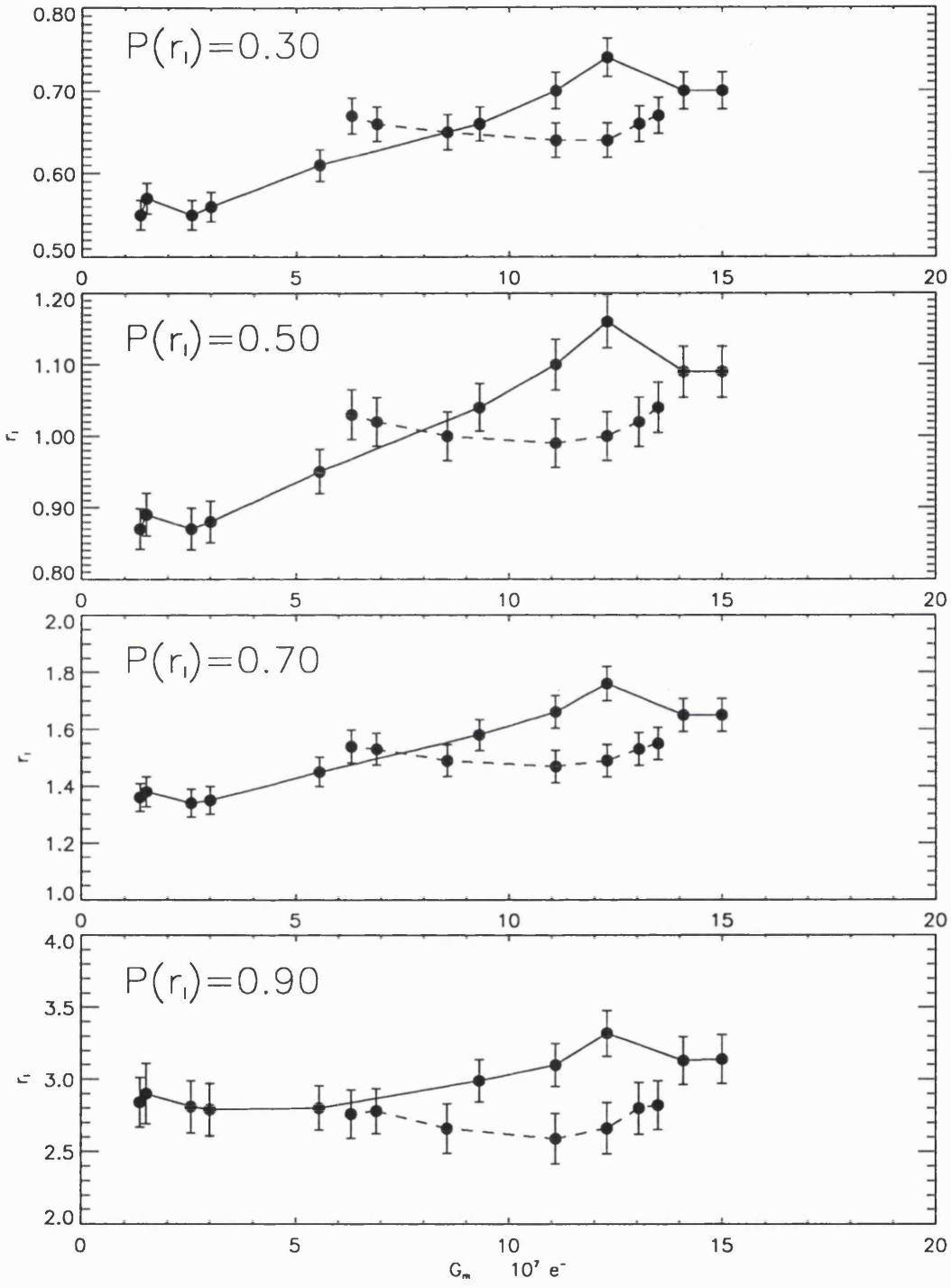

Figure 4.23: The variation of r_l with gain due to the variation of the inter-plate gap voltage. The data in this figure is determined from the parameters presented in Figure 4.22. The broken and solid lines correspond to $V_i > 0$ and $V_i \leq 0$, respectively.

V_g (V)	V_c (kV)	$\frac{r_{oc\parallel}}{r_{oc\perp}}$	$\frac{r_{ow\parallel}}{r_{ow\perp}}$	$\frac{a_{c\parallel}}{a_{w\perp}}$	Δ_{cc} $\perp$ (pixels)	Δ_{cc} $\parallel$ (pixels)
50	2.65	1.07	1.13	1.08	2	-1
50	2.80	1.05	1.05	1.07	2	-3
50	2.90	1.21	1.15	1.18	-2	-4
100	2.65	1.08	1.03	1.01	2	1
100	2.80	1.09	1.06	1.05	4	-5
100	2.90	1.18	1.10	1.14	0	-3
200	2.65	1.13	1.16	1.07	9	-1
200	2.80	1.05	1.00	1.01	6	-2
200	2.90	1.14	1.00	1.01	1	-2
400	2.65	1.09	1.13	1.04	10	-2
400	2.80	1.08	1.17	1.04	10	0
400	2.90	1.17	2.79	1.07	5	0
800	2.65	1.02	1.00	1.00	9	-7
800	2.80	1.06	1.17	1.04	7	8

Table 4.7: The ratio of the fit parameters for the two pore bias angle/anode split orientations and the difference between the two estimates of the centre channel.
The parameter Δ_{cc} is discussed in Section 4.5.2.

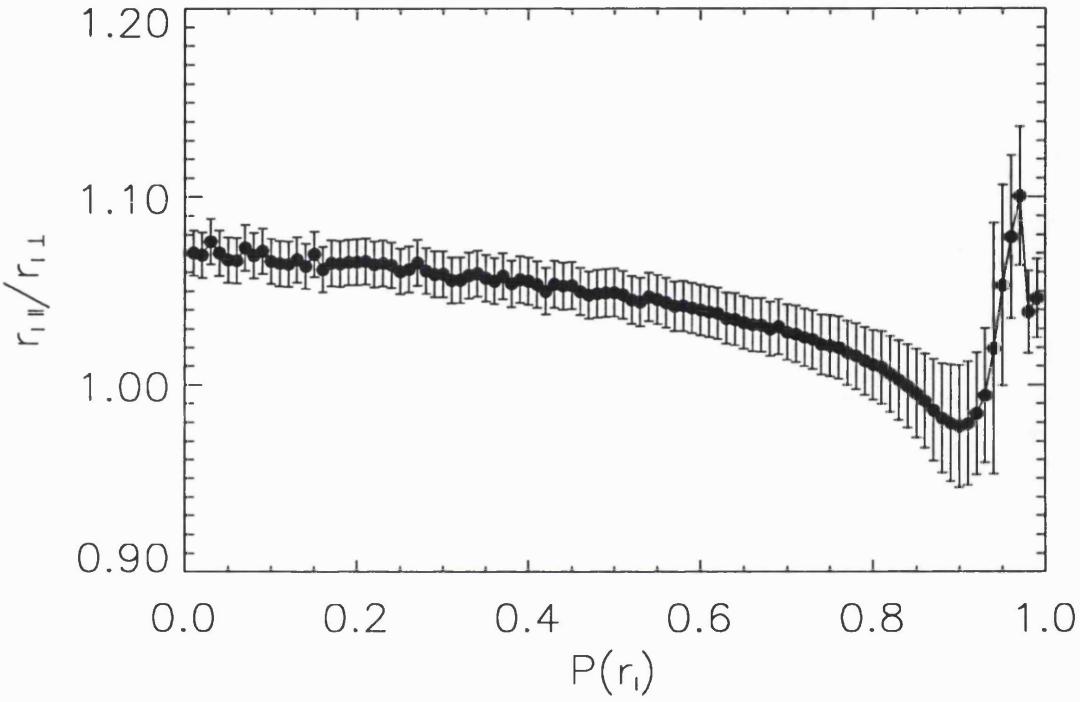

Figure 4.24: The ratio of the average limiting radii for both the bias angle/split orientations. The r_l values represent the average limiting radii for 13 data sets, i.e. all the operating conditions as described in Table 4.7, excluding $V_g = 400$ V and $V_c = 2.9$ kV.

for a section along the major or minor axis provided that axis is perpendicular to the split direction. In the experiments, the chevron plane was aligned with an anode axis to within 10°. Assuming one of the axes is aligned with this plane, the distributions returned represent the major and minor axes of the charge cloud.

As we are fitting to the charge cloud integrated across one axis, we would expect that the values of ellipticity we measured to represent the lower limit. The ellipticity has been measured for MIC type detectors, as described in Section 1.3.1 by direct imaging of the light output from the phosphor. The major axis was on average 25% larger than the minor axis for measurements over a wide range of operating conditions (Kawakami, 1992).

If the charge cloud is elliptical, the major axis should be in the direction of the pore bias angle, assuming that the energy and angle distributions of the output are constant with azimuthal angle around the pore and using a purely ballistic model. Therefore, broader one dimensional integrated distributions should be observed when the pore bias angle is aligned normal to the anode split. However, we observe precisely the opposite, indicating that the major axis is perpendicular to the pore bias angle.

Bronshteyn *et al* (1980) report that the angular distribution of the output electrons varies with the channel azimuth angle and that the distribution can be twice as wide for electrons emitted normally to the plane of the channels as that for electrons emitted within the plane. They also find that all the electrons have energies < 50 eV, independent of the emission angle.

If the anode split is aligned parallel to the pore bias angle and assuming purely ballistic behaviour, the angular spread of electrons emitted within the plane of the channels will be preferentially spread across the *cp* axis. Those emitted normally to the channel plane will be distributed along the *fc* axis. As shown in Figure 4.12, if the maximum emission angle relative to the channel axis is doubled from $\approx 10°$ to 20°, even if the energy is < 50 eV, the electrons will travel a significantly larger distance than higher energy electrons emitted at smaller angles. Therefore, even though the electron velocity distribution is not azimuthally symmetric, a ballistic model would still predict that the major axis of the charge be aligned along the pore bias axis.

However, I have already shown that the ballistic model is inadequate for predicting the size of the charge cloud. Space charge, the initial electron distribution on exiting the pore, the complex electric fields at the pore exit or a combination of any of these factors, are all plausible mechanisms for the counter-intuitive orientation of the axes.

4.5.2 Skewness

The centre channel of the S curve is the centroid position of the curve's inflexion point, which corresponds to the position of the peak of the integrated charge cloud distribution. Its value (cc_{sd}) can be obtained from the zero intercept of the second derivative of the S curve. This measurement is independent of any symmetry assumptions. The fitting procedure also returns a value for the centre channel (cc_{fit}). This represents the best estimate of the point about which the experimental S curve is rotationally symmetric.

The centre point should be located at 2048.0, but cc_{fit} is randomly distributed about channel 2048, $\sigma = 6$, and cc_{sd} about channel 2046, $\sigma = 7$. The similarity between the two distributions indicates that, as a group, there are no obvious differences between the two centre channel estimates. However, for each individual S curve, differences between cc_{fit} and cc_{sd} are evident. The values of this difference ($\Delta_{cc} = cc_{fit} - cc_{sd}$) for the 28 data sets are listed in Table 4.7 and are shown in Figure 4.25. When the chevron plane is aligned parallel to the split, Δ_{cc} is negative for 10 of the 14 cases and when the chevron plane is aligned perpendicular to the split, 12 of the values of Δ_{cc} are positive. The average values of Δ_{cc} for the five data sets taken for each chevron plane orientation, at a constant combination of voltages, $V_g = 100$ V and $V_c = 2.80$ kV, are; with chevron plane perpendicular to split, $\Delta_{cc} = 4$, $\sigma = 1$, and with chevron plane parallel to split, $\Delta_{cc} = -3$, $\sigma = 1$. As the values of Δ_{cc} are small, less than 0.5 % of the centre channel, and the uncertainties are large, the differences appear to be just on the edge of detection. However, the systematic nature of the differences and their opposite signs for the two chevron plane orientations suggest strongly that the previous symmetry assumptions are invalid at scales of the order of 1%.

The assumption of azimuthal symmetry appears to be valid for a first order approximation of the charge cloud. Variations between measurements of r_o show that, to second order, a more accurate representation assuming elliptical symmetry is valid. At even higher orders of accuracy, the systematic differences between the centre channel estimates, Δ_{cc}, imply that the charge cloud distribution is skew. At this level, the charge cloud can only be characterized by taking data at many orientations of the chevron plane with respect to the anode split.

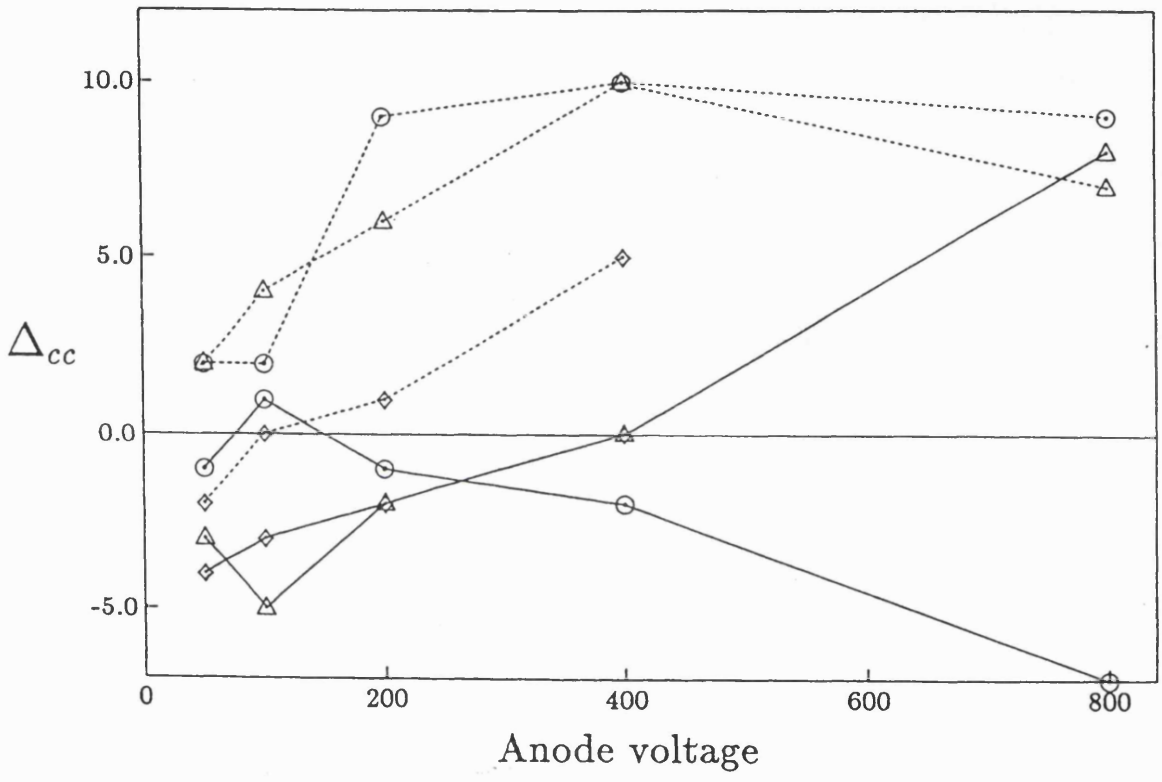

Figure 4.25: The difference between the two estimates for the centre channel, Δ_{cc} for the 28 data sets.

Units are in screen pixels. The solid and dotted lines represent data acquired with the split aligned parallel and perpendicular to the pore bias angle, respectively. The circles, triangles and diamonds represent data acquired with values of V_c of 2.65, 2.8 and 2.9 kV, respectively. From Edgar *et al.* (1989).

Chapter 5

Operating the Spiral Anode

All the data presented in this chapter was acquired with a similar experimental setup to that described in Section 3.3, except there were six channels of electronics instead of four. New software was required to implement the decoding algorithm for SPAN, and this is discussed briefly in Section 5.6.

The MCPs are similar to those used in the charge cloud experiments, as described in that section but they are not the same set. The MCPs and configuration used in this chapter are discussed in detail in Section 7.2.1.

5.1 Spiral Transform

Figure 5.1 summarizes the five steps necessary to transform the digitized measurements of the charge deposited on each of the three electrodes, into a one dimensional coordinate.

In a two dimensional detector, the two coordinates are determined independently so we can limit our discussion to one dimension.

5.1.1 Coordinate Rotation

The geometries of the three electrodes, for any given anode, define two conditions on the coordinate transformation specific to that anode. For the anodes developed at MSSL so far these conditions are:

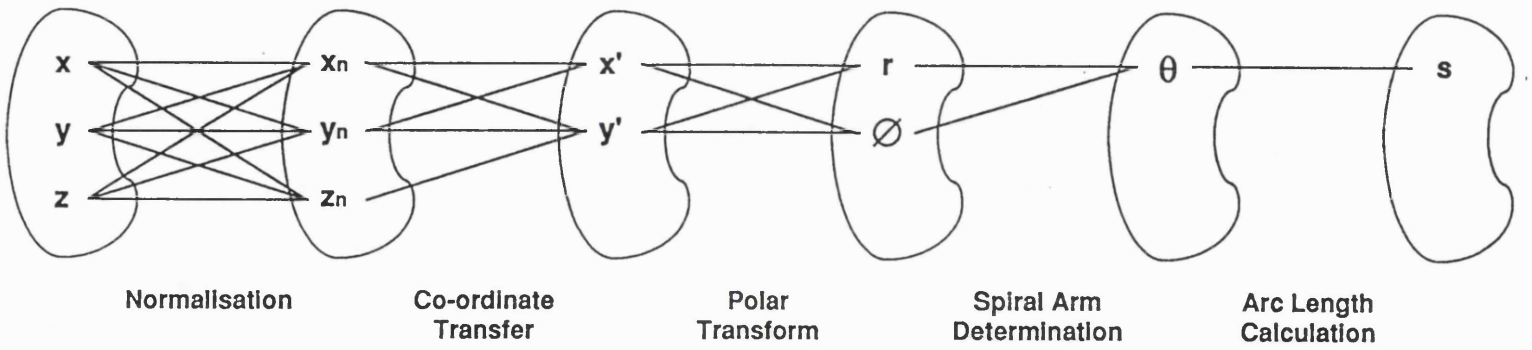

Figure 5.1: Summary of the five steps necessary to transform the three ADC values into the one dimensional output.

1. The radius of the angle, θ, increases as the spiral rotates about the three axes in the order xzy, i.e. clockwise in Figure 5.2.

2. In polar coordinates, the line $\theta = 0$ must intercept the x axis.

The first condition is imposed for convenience in the decoding, as a spiral evolving in an anti-clockwise direction can be transformed into one evolving clockwise simply by interchanging the x and z electrodes. In order to satisfy this condition, it can be shown from the equations of the coordinate transform as derived in Chapter 2, i.e. Equations 2.33 and 2.34,that

$$\theta = \arctan \frac{x'}{y'} \quad . \tag{5.1}$$

Using this equation the $\theta = 0$ line intercepts the $-z$ axis. After a rotation through $-60°$ about the z' axis, this line will intercept the x axis. Therefore, the third Euler angle is

$$\psi = -60° \quad . \tag{5.2}$$

The three Euler angles have now been determined and the full rotation matrix, **S**, is,

$$\mathbf{S} = \begin{pmatrix} 0 & \frac{-1}{\sqrt{2}} & \frac{1}{\sqrt{2}} \\ \frac{2}{\sqrt{6}} & \frac{-1}{\sqrt{6}} & \frac{-1}{\sqrt{6}} \\ \frac{1}{\sqrt{3}} & \frac{1}{\sqrt{3}} & \frac{1}{\sqrt{3}} \end{pmatrix} \quad . \tag{5.3}$$

The set of equations for the transformation is now

$$x' = \frac{1}{\sqrt{2}} (z - y) \quad , \tag{5.4}$$

$$y' = \frac{1}{\sqrt{6}} (2x - (y + z)) \quad , \tag{5.5}$$

$$z' = \frac{1}{\sqrt{3}} (x + y + z) \quad . \tag{5.6}$$

Figure 5.2 shows an example of data that has undergone this coordinate rotation.

5.1.2 Transformation to Cylindrical Polar Coordinates

The transformation to cylindrical polar coordinates (r, ϕ, h) is straight forward after the coordinates have been rotated.

$$r = \left(x'^2 + y'^2\right)^{\frac{1}{2}} \quad , \tag{5.7}$$

$$\phi = \arctan \frac{x'}{y'} \quad , \tag{5.8}$$

$$h = z' \quad . \tag{5.9}$$

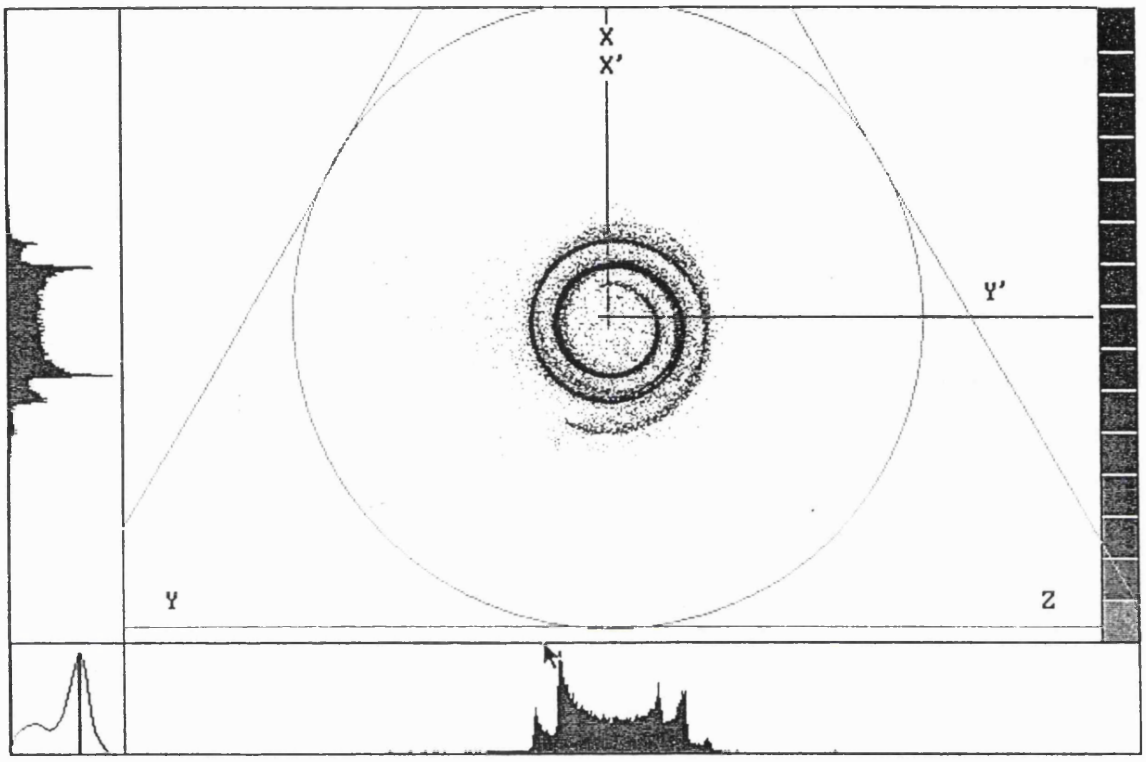

Figure 5.2: An example of data that has undergone the coordinate rotation.
The figure represents data from only one pulse height channel so that all data lies in the plane $x + y + z = c$, where c is a constant. The original and the new coordinate frames are shown. The z' axis is normal to the page. The bounding equilateral triangle, defined by the requirement that all the values of x, y and z are positive, and the largest radius, continuous circle that can be drawn within this triangle are also shown, see Section 5.1.3 for discussion. The small peak at the low end of the PHD, shown in the bottom left corner, is due to a hot spot on the edge of the active area of the detector.

By far the most convenient way to display the spiral is in r/ϕ space, i.e. plotting the radius and the phase angle as Cartesian coordinates. As $r = k\theta$, we would expect a straight line relationship in this space. However, as arctan will only return angles between 0 and 2π a series of parallel lines representing each of the spiral arms, will be produced. Figure 5.3 shows an example of this space for an ideal spiral. Any departure from the ideal spiral, e.g. due to eccentricity or offset of the centre, will be apparent as a deviation from a straight line. It is much easier to spot such deviations if the data is plotted in this manner rather than as a spiral.

5.1.3 Normalization With Respect to Pulse Height

The cylindrical polar coordinate h is directly proportional to the amount of charge collected on the three electrodes x, y and z. For convenience let us define a new variable h' such that

$$h' = \sqrt{3}h \quad , \tag{5.10}$$

$$= \sqrt{3}z' \quad , \tag{5.11}$$

$$= x + y + z \quad . \tag{5.12}$$

If the integers x, y and z are constrained to be positive, as is the case for ADC outputs, then all the points that lie on a plane such that h' is a constant, will be bound by an equilateral triangle with vertices at $(0, 0, h'), (0, h', 0)$ and $(0, 0, h')$. Also, the maximum radius of a continuous circle that can be drawn within this triangle is

$$r_{lim} = \frac{h'}{\sqrt{6}} \quad . \tag{5.13}$$

An example of the limiting triangle and a circle with radius r_{lim} are shown in Figure 5.2. In order for an anode to produce points lying on this circle, would require that the amplitude of the sinusoid would have to be equal to the whole width of the electrode, see Section 2.1.1, i.e. at some point the width of the electrode would go to 0 and the electrode would not be continuous. A continuous spiral must always have $r < r_{lim}$.

A series of spirals exist on parallel planes defined by the pulse height of the event. Figure 5.4 shows a section through a family of ideal spirals on a continuous series of planes. It is apparent that the spiral constant k and therefore the radius are functions of pulse height, $r(h') = k(h')\theta$. Normalizing with respect to pulse height, will project the spirals in

all of the planes into one plane, thereby reducing the spiral to a two dimensional object. Ideally, by similar triangles, one normalized spiral

$$r_n = k_n\theta \quad , \tag{5.14}$$

where

$$r_n = \frac{r(h')}{h'} \quad , \tag{5.15}$$

$$k_n = \frac{k(h')}{h'} \quad , \tag{5.16}$$

will correctly represent the spirals from all of those planes.

As any common factor in x' and y' will cancel when ϕ is determined, normalization is only necessary for r, i.e. for the coarse position and not the fine. Also, normalization can be carried out at any stage during the coordinate transforms.

From Equations 5.7, 5.4 and 5.5 it can be seen that the origin for each spiral, i.e. $r = 0$, occurs when $x = y = z$, i.e. along the h' axis. Therefore, the spiral origin does not vary with pulse height when using this coordinate system.

In all other coordinate frames the origin must be translated when normalizing with respect to pulse height. For example, as discussed in Section 2.1.2 a spiral with a phase difference of 90° produces an Archimedean spiral in the xy plane. If a spiral is projected into this plane, it's origin will lie at the point $\frac{1}{3}(h, h)$. The position of the origin is therefore dependent on the pulse height and lies along the line $x = y$. The translation would have to be carried out before conversion to polar coordinates, i.e. Equation 5.4 and 5.5 would be replaced by

$$x' = x - \frac{h'}{3} \quad , \tag{5.17}$$

$$y' = y - \frac{h'}{3} \quad , \tag{5.18}$$

respectively.

5.1.4 Spiral Arm Assignment by Linear Discriminant Analysis

As discussed in Chapter 2, r is used to determine the spiral arm on which an event lies, giving its coarse position. Therefore, spiral arm assignment is crucial for operating the SPAN readout.

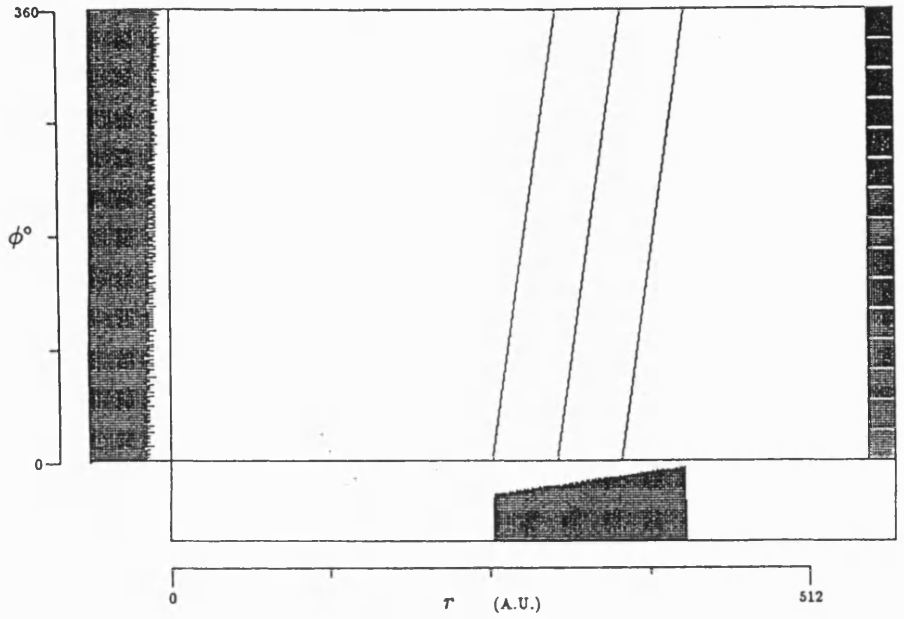

Figure 5.3: Ideal, three arm spiral represented in r/ϕ space.
In this figure, and all others in this chapter, the radius is measured in arbitrary units (A.U.).

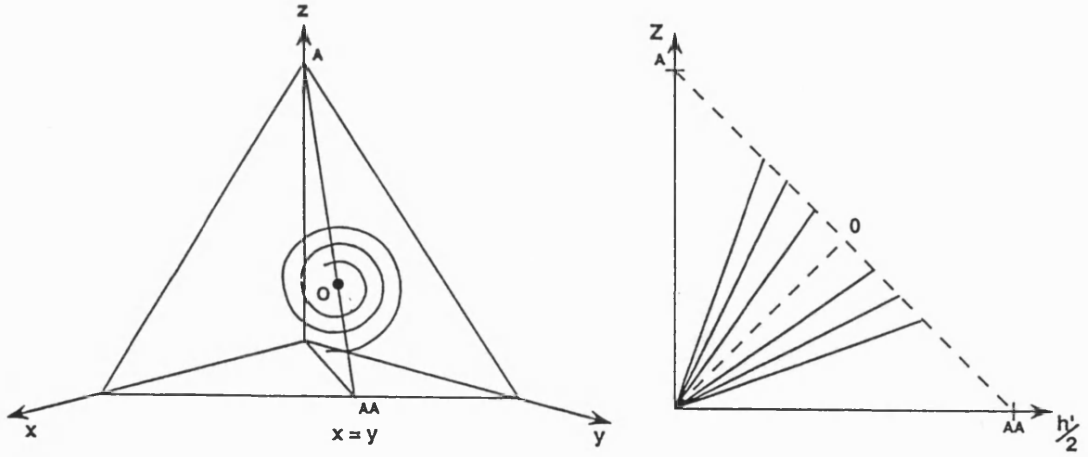

Figure 5.4: A family of ideal spirals on a continuous series of planes, sectioned by the plane $x = y$.

In the ideal case represented by Figure 5.3, it is a straight forward procedure to determine the true angle, i.e.

$$\theta = 2n\pi + \phi \quad , \tag{5.19}$$

where n is the spiral number. For any point, provided the spiral constant k is known,

$$\theta = \frac{r}{k} \quad . \tag{5.20}$$

If the lines in Figure 5.3 had a finite width, the problem would be more involved. A spread in r, for any given k, will return an incorrect value of θ.

However, if Equations 5.19 and 5.20 are combined,

$$n = \frac{1}{2\pi}\left(\frac{r}{k} - \phi\right) \quad , \tag{5.21}$$

the quotient of n, n_{quot}, is the number of the inner arm of the two arms that bracket the point. The remainder, n_{rem}, is the fractional distance of the point from the inner arm relative to the separation of two spiral arms. We use n_{rem} to determine which of the two bracketting arms the point will be mapped to. The true angle θ is given by

$$\theta = \begin{cases} 2n_{quot}\pi + \phi & \text{if } n_{rem} < 0.5 \\ 2(n_{quot}+1)\pi + \phi & \text{if } n_{rem} > 0.5 \\ 0 & \text{if } n_{rem} = 0.5 \end{cases} \quad . \tag{5.22}$$

Setting θ to 0, effectively discards the point as this is the spiral origin. This would require that the areas of the three electrodes would be equal, which never occurs in practice. Therefore, any data at this point is spurious.

In practice, there is an interval of finite width, $2w$, in which all points are discarded, as it is assumed that points lying in this region cannot be confidently assigned to either of the bracketting arms. Therefore, the previous equation becomes

$$\theta = \begin{cases} 2n_{quot}\pi + \phi & \text{if } n_{rem} < w \\ 2(n_{quot}+1)\pi + \phi & \text{if } n_{rem} > 1 - w \\ 0 & \text{if } w \leq n_{rem} \leq 1 - w \end{cases} \quad . \tag{5.23}$$

Once the point has been assigned to a spiral arm, conversion to the arc length S is a straight forward process as $S \approx \frac{k}{2}\theta^2$ as described in Section 2.2.3.

5.1.5 Ghosts

If the spiral arms are wide with respect to their separation, events associated with one of the bracketting spiral arms may be mistakenly mapped onto the other arm. If events are assigned to the incorrect arm there will be an error in their coarse position of one cycle. Therefore there will be an error in S of $2k\pi^2$, producing a spurious image or a "ghost". As an example of what can occur, Figure 5.5, shows the result of spiral arm assignment failing in both axes for a two dimensional image, compared to Figures 5.6 and 5.7 which are corrected images.

Therefore, every effort must be made to minimize deviations from the ideal spiral arms and ensure that the width of the arms is small with respect to their spacing.

5.2 Radius as a Function of Pulse Height

Figure 5.8 shows an example of the r_n/ϕ plot for actual data that has been normalized with respect to pulse height. This clearly indicates that the width of the spiral arms cannot be ignored and that Equation 5.20 is invalid. The arms are so wide that severe ghosting is produced, Figure 5.5 is the image produced from this data. The situation is worse than the diagram suggests. The two bright spots in the image are from a "hot spot" on the MCP and are actually associated with the centre spiral arm. Also the brighter central regions of the arms are due to the convolution of the pulse height distribution (PHD) with the radial variation. The severity of the problem can be better appreciated if a flat PHD is used.

Figure 5.9 shows a subset of the data in Figure 5.8. The 256 channel PHD has been subdivided into 16 channel windows with approximately equal numbers of events in each window. The region containing the hot spots has been masked out as the hot spots' PHDs consist almost entirely of low pulse height events and so these points would be over-represented in a flat PHD image of the whole MCP.

Figure 5.10 shows a section through the continuous sets of non-normalized spirals, similar to the ideal case in Figure 5.4 for a 30° wide slice in ϕ for the data displayed in Figure 5.8. The wide slice is needed to provide enough data for a reasonable graph. As the radius varies continuously with the phase angle, the width of the three curves is exaggerated and is not the cause of the wide spiral arms in Figures 5.8 and 5.9. The wide linear arms are

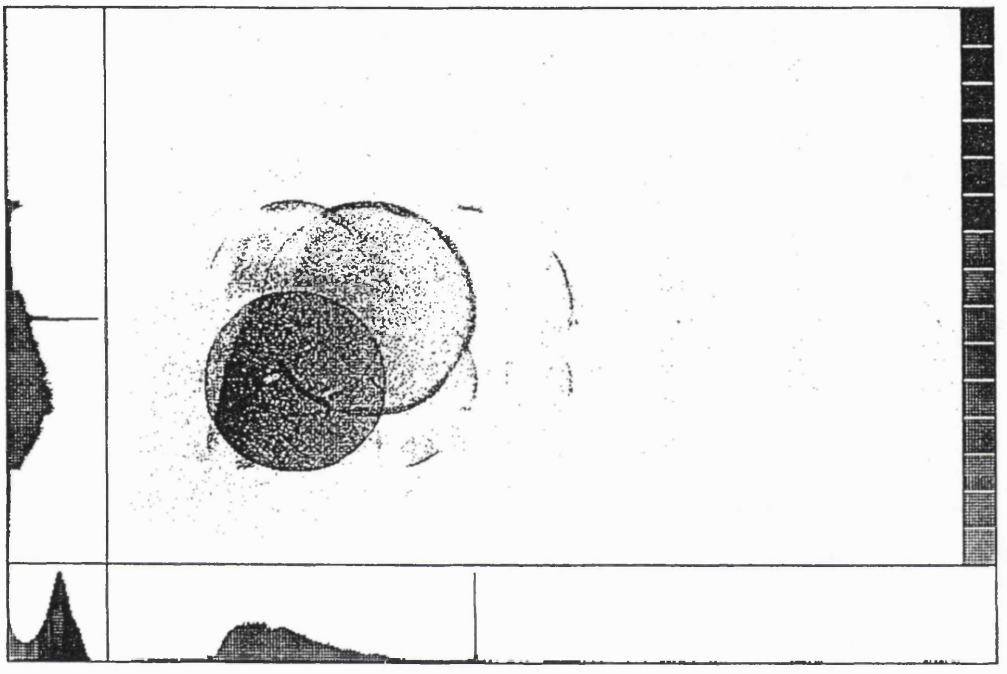

Figure 5.5: An example of ghosting.
The image represents the full 25 mm diameter, active area. The greyscale, as shown on the right edge of the figure, is proportional to the intensity at each pixel. In this case, the scale is linear with a step of 1. The spike present in the side histograms is due to a hot spot at the edge of the MCP. The image contains approximately 10^5 events, which is the typical size of data sets acquired to determine the spiral constants.

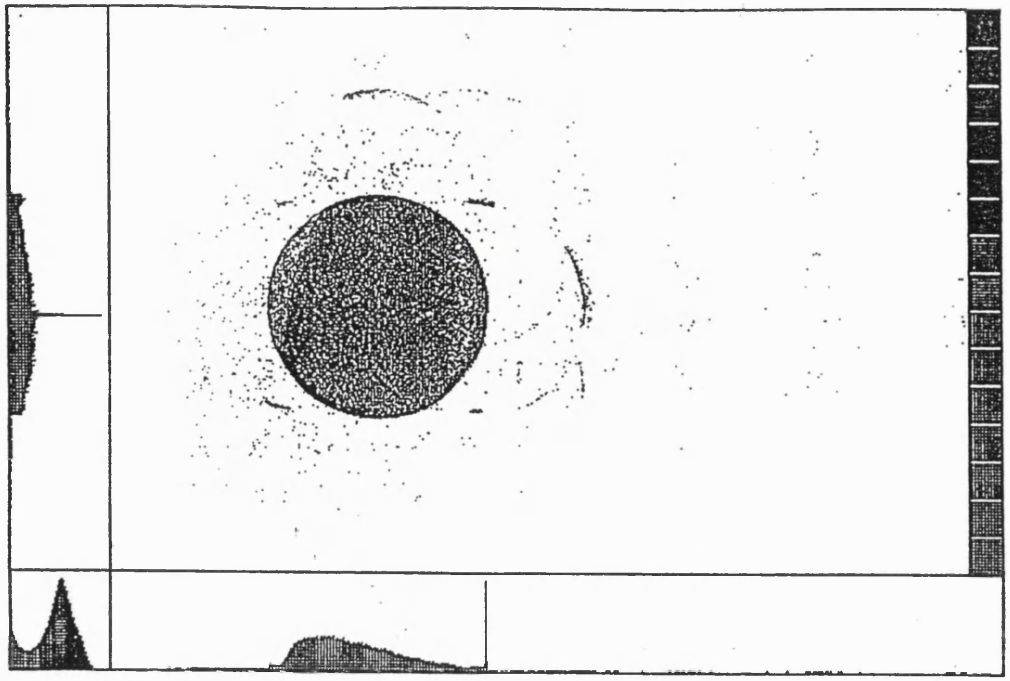

Figure 5.6: A corrected version of Figure 5.5.
The extent of ghosting has been reduced significantly but has not been eliminated.

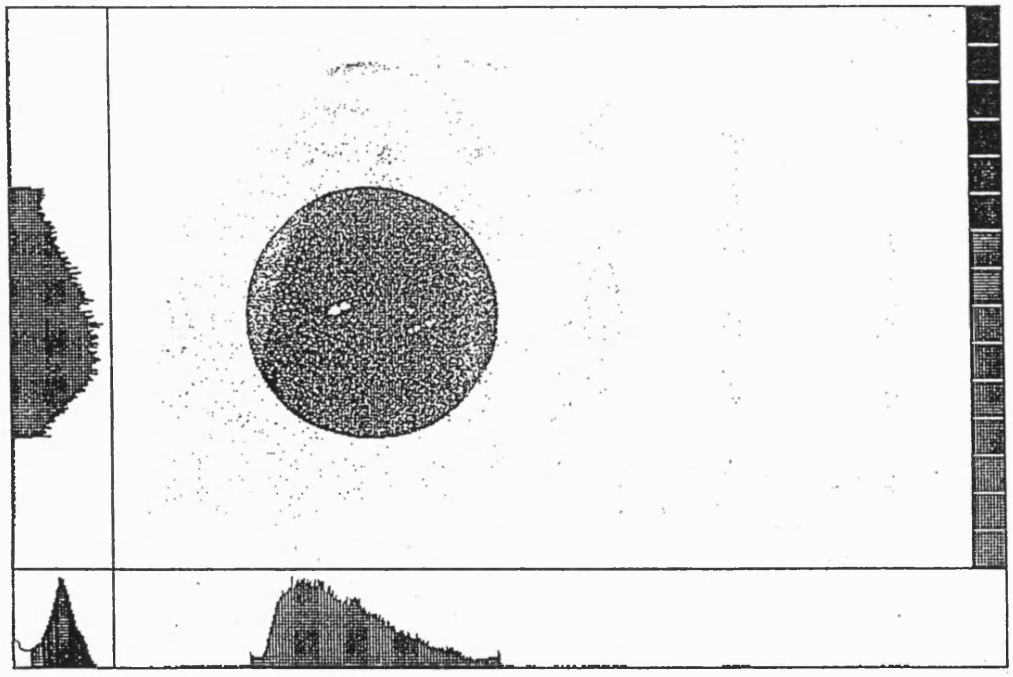

Figure 5.7: The same as Figure 5.6 except that the LLD has been set to a higher value, as shown by the PHD in the bottom left corner.
This shows that most of the ghosting left after correction is due to low pulse height events.

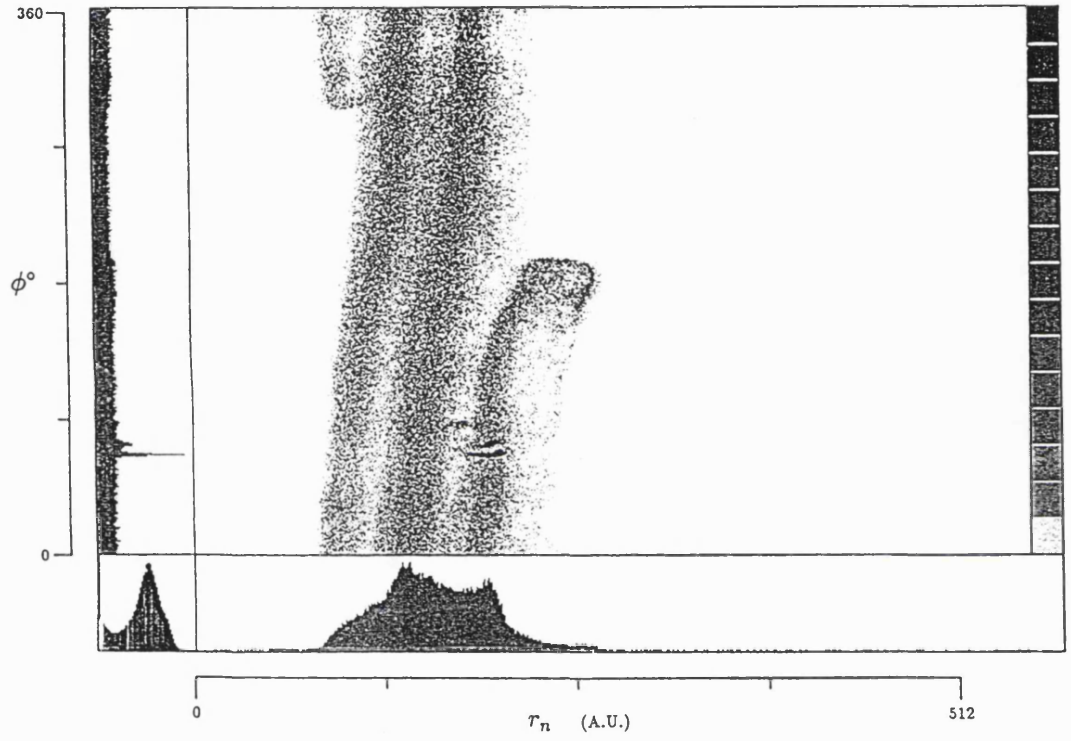

Figure 5.8: Radius that has been normalized with respect to pulse height, r_n plotted against ϕ.

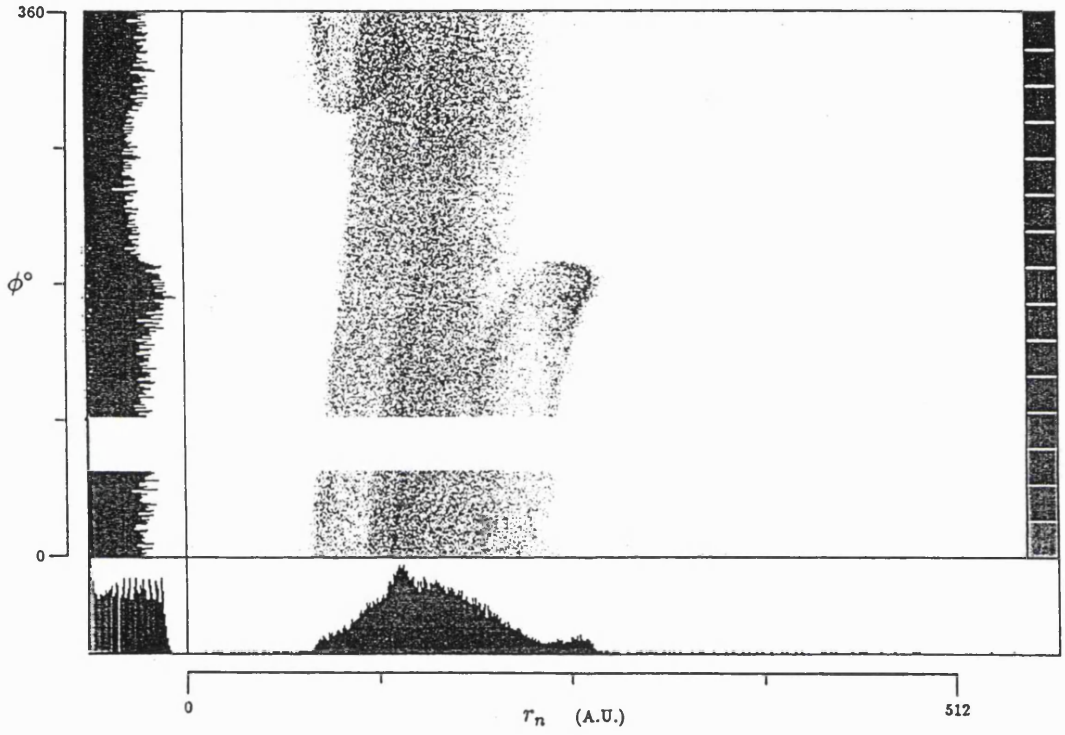

Figure 5.9: A similar diagram to Figure 5.8 except that it represents the subset of that data that has a flat PHD.

produced by the deviation of the radius/pulse height function, $r(h')$ from the ideal linear behaviour as illustrated in Figure 5.4. This is more clearly illustrated by the r_n/h' curve in Figure 5.11, which shows the variation of the normalized radius plotted against pulse height for a section of Figure 5.8. The lines would be horizontal if there was no variation of the radius with h'. The side histogram on the r_n axis shows the intensity distribution along the r_n axis for a 30° wide section of ϕ in Figure 5.8

5.2.1 The Cause of Variation of Radius with Respect to Pulse Height

Simulated charge cloud distributions, based on the measurements from the previous chapter, have been convolved with a triplet of sinusoidal electrodes, see Section 2.1.1, by Breeveld (Breeveld *et al.*, 1992b). The amplitudes of the electrodes were not damped but were constant so that the resultant Lissajous figure was a circle. As shown in Figure 5.12, the radius of the Lissajous figure is a function of charge cloud size. The best fit to the relationship between the two is

$$R_r \approx 3.9 - \frac{R_{cc}}{4} \text{ mm}, \tag{5.24}$$

where R_r is the radius of the Lissajous figure and $R_(cc)$ is the limiting radius that contains 99% of the total charge in the cloud. In terms of the values described in Chapter 4.1, R_{cc} corresponds to r_l where as $P(r_l) = 0.99$. The relationship is also linear for the radii containing 68% and 95% of the total charge.

As discussed in Section 4.4.1, for a given set of operating voltages there is significant variation of the size of the charge cloud with the gain of the event. This is probably the case for all operating conditions. Variation of the charge cloud size with gain is a probable mechanism for the variation of radius with pulse height. However, nonlinearities in the electronics or cross talk are also plausible mechanisms.

Figure 5.13 shows that α, the gradient of $r_n(h')$ as determined from the lines in Figure 5.11, is not correlated with the phase angle of the spiral. The method for determining this gradient is discussed in Section 5.3.3. This method is statistical in nature, the error bar in the figure corresponds the bin size in the distribution used to determine α. The FWHM of these distributions are 10 to 20 bins wide, i.e. the same size as α. The scatter of data in this figure is typical of that observed for all the other data sets, so the bin width is a better indicator of the uncertainty associated with a given measurement of α than the FWHM. The same size bins were used for all measurements of α.

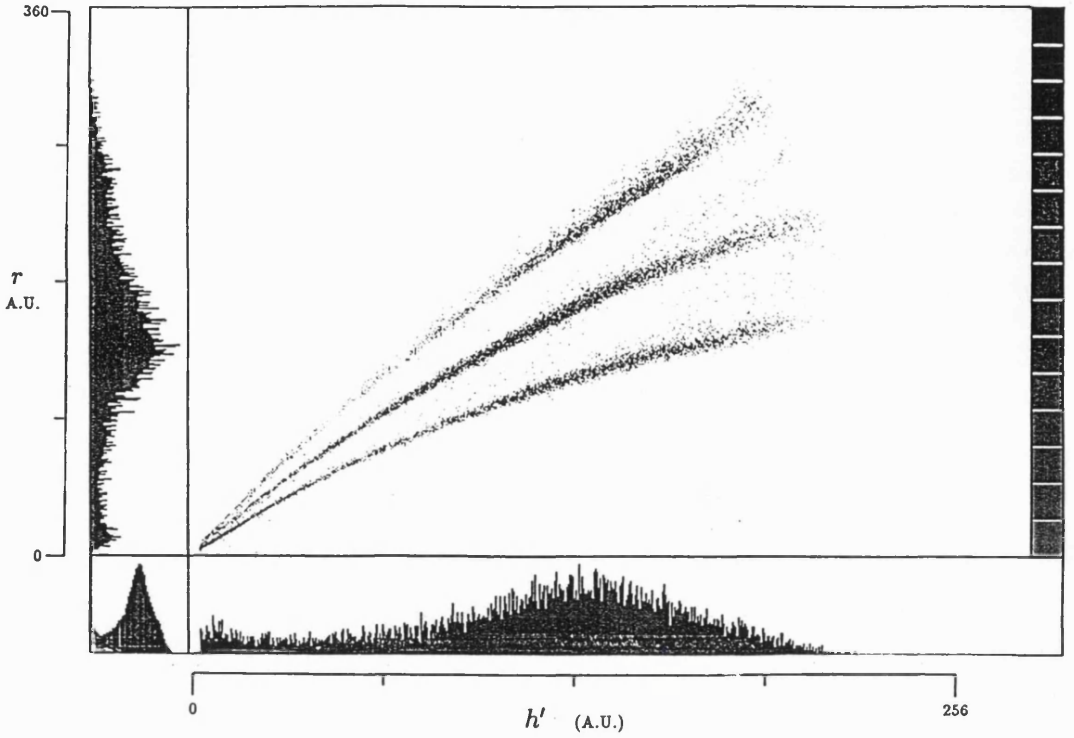

Figure 5.10: The non normalized radius r plotted against the pulse height h'. This figure represents approximately 7500 events lying within the interval $0° < \phi < 30°$. The three curves represent the three spiral arms.

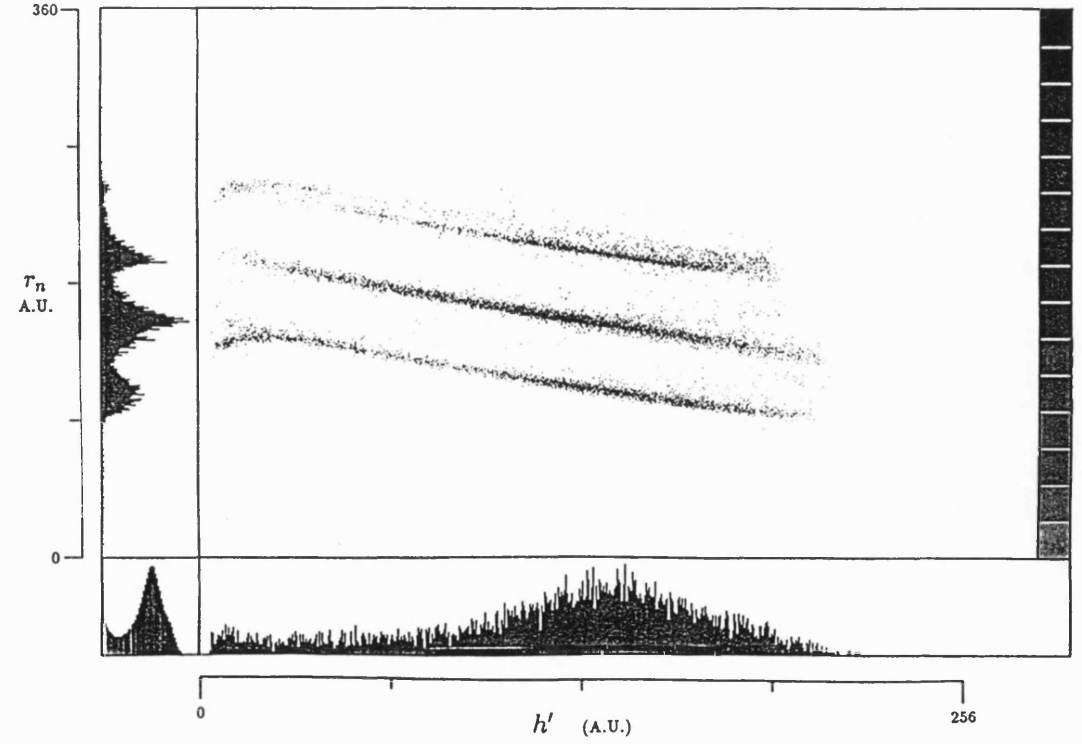

Figure 5.11: The same data as in Figure 5.10, but plotting the normalized radius against pulse height.

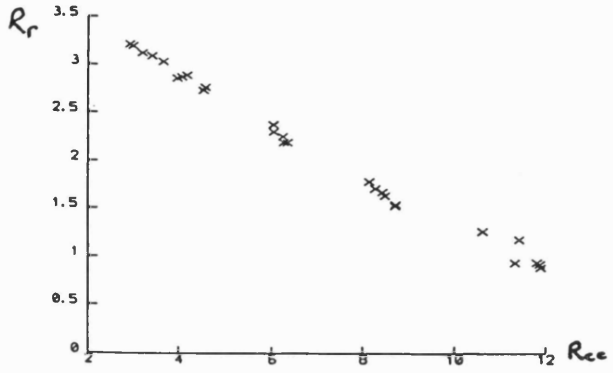

Figure 5.12: The simulated variation of the radius of a Lissajous circle with respect to charge cloud size.
The variables are defined in Equation 5.24. From Breeveld *et al.* (1992b).

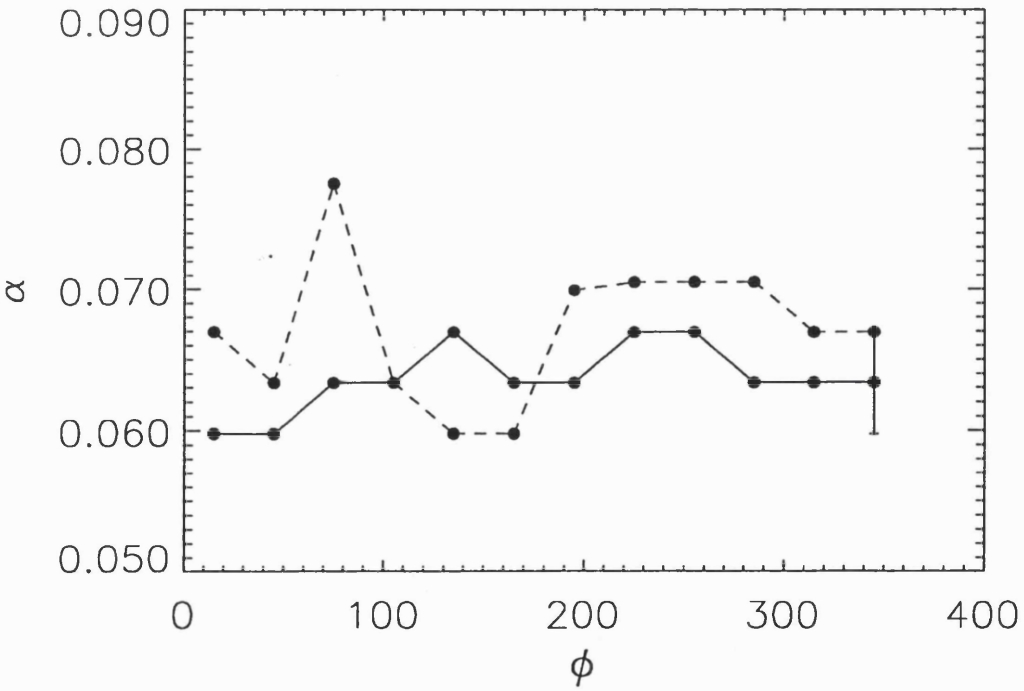

Figure 5.13: The gradient of $r_n(h')$, α, as a function of ϕ.
Measurements of α were made over 30° wide bins in ϕ. The error bar is discussed in the accompanying text.

Figure 5.14 shows the variation of α with V_g and shows significant reduction with increasing voltage. The PHD also varies with increasing V_g. However, at high voltages, α still varies significantly while the PHD parameters remain approximately constant. This suggests that α depends on the electric field strength rather than varying PHD.

Figure 5.15 shows the variation of α with G_m obtained at different V_c values at constant E_g. It shows that α is insensitive to G_m at high field strengths. As was observed with the charge cloud size, the electric field strength appears to be the critical factor in determining α rather than the gain.

As V_g increases, the charge cloud size decreases and so does α. It is interesting that at a low E_g, there is a large variation in α with V_c, with the largest α at the lowest V_c. This is the general behaviour of the charge cloud size observed at $g = 6.0$ mm, see Section 4.4.3, although in Figure 5.15 the electric field strengths are significantly higher. The strongest fields are comparable to those obtained with $g = 3$ mm in which the charge cloud increased with increasing V_c, while in this case there is no significant variation.

As α is insensitive to PHD variations, it is unlikely to be due to nonlinearities or offsets in the electronics. Cross talk is also unlikely, due to this PHD insensitivity and the insignificant variation with ϕ. The electric field strength is the dominant factor in determining the size of α. It also appears that α is correlated with the average charge cloud size and behaves in a similar manner with respect to gain variations due to varying operating voltages. The most probable cause for the variation of radius with pulse height is the variation in charge cloud size with gain, for a constant set of operating voltages.

Irrespective of the cause, the magnitude of the r_n/h' variation can be varied by the operating voltages. It also depends on the actual anode. Breeveld (1992) has measured α for the one dimensional SPAN detector for the SOHO CDS. She finds the values of α also vary with V_g and are smaller than those displayed in Figure 5.14. The maximum value of α was 0.05 and the minimum was -0.02. By tuning V_g and plate voltage, data sets with $\alpha = 0$ could be reliably achieved.

Therefore, on some detectors the effect can be removed totally but this may not be possible for all detectors. Generally, the highest E_g practicable should be used to minimize this effect. However, there will have to be a compromise between obtaining narrow spiral arms and imaging performance.

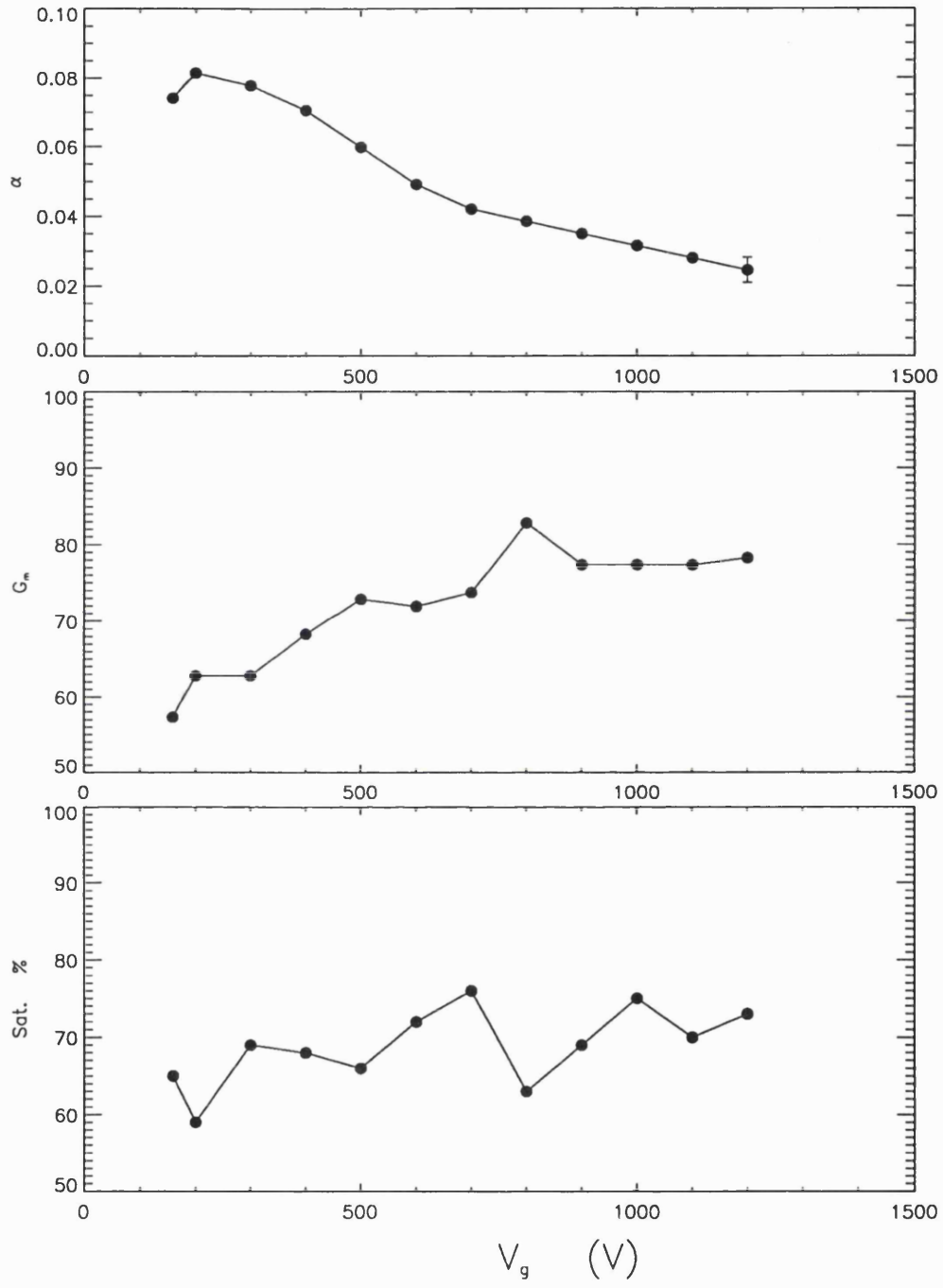

Figure 5.14: The Variation of α with anode gap voltage.

As V_g was varied, V_c was held constant at 2.9 kV. The modal gain and saturation of the PHDs for each measurement are also shown. The MCP-anode gap was 4.7 mm. The modal gain is quoted in units of millions of electrons. In this and the next figure, α was determined over the range $0° < \phi < 30°$.

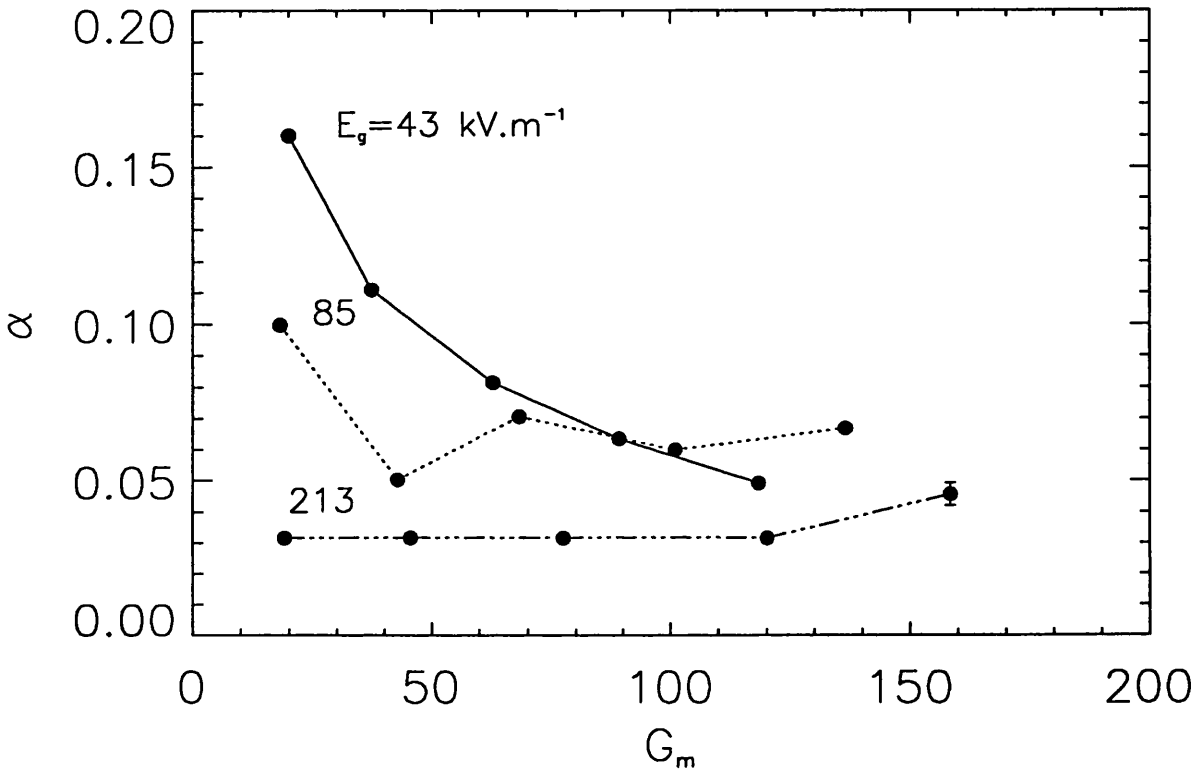

Figure 5.15: The variation of α with plate voltage and anode gap electric field strength. The three curves correspond to the indicated constant E_g. The five different gains for each curve correspond to chevron voltages in the range 2.7 to 3.1 kV with 100 V steps and the units are in millions of electrons.

5.2.2 Correction of Radius With Respect to Pulse Height

When correcting for pulse height effects, a flat PHD should be used. The correction is based on a best fit to the gradient of the $r(h)$ function. A correction for a peaked PHD will be biased towards the modal gain and will only be the best fit for that particular PHD. This does not represent a problem for low count rates but at higher rates, gain depression will occur reducing the modal gain. A correction optimized for the original PHD will no longer be ideal for the new PHD. Given that an astronomical detector will probably observe some relatively bright point sources, there is little point in optimizing the detector for a diffuse, low level illumination. If the best fit is determined for a flat PHD it should be equally applicable for all likely PHDs.

Radius Dependent Correction by Quadratic Normalization

The nonlinear behaviour of $r(h')$, as shown in Figure 5.10 strongly suggests that the normalization should include second or higher order terms of the pulse height. Figure 5.16 and Figure 5.17 show the r_n/ϕ and r_n/h' plots for the flat PHD data in Figure 5.9, respectively, where

$$r_n = \frac{r}{h'(1+\alpha h')} \quad . \tag{5.25}$$

This technique has the advantage that as it consists solely of a division, it can be carried out, like normalization, at any stage during the coordinate transform. However, the divergence of the r_n/h lines, as shown in Figure 5.17, gives rise to the variation in the widths of the spiral arms in Figure 5.16. This shows that this radius correction is of limited efficiency.

Radius Independent Correction

Figures 5.18 and 5.19 are similar to Figures 5.16 and 5.17, respectively except that

$$r_n = \frac{r}{h'} + \alpha h' \quad , \tag{5.26}$$

where α once again is constant and the gradient in Figure 5.11.

The fact that the lines in Figure 5.19 are parallel and with approximately zero gradient gives rise to the narrow spiral arms in Figure 5.18 and indicates that this method is superior to the radius dependent correction. The parallel lines also indicate that the normalized spiral constant k_n is independent of pulse height but that the effect of pulse

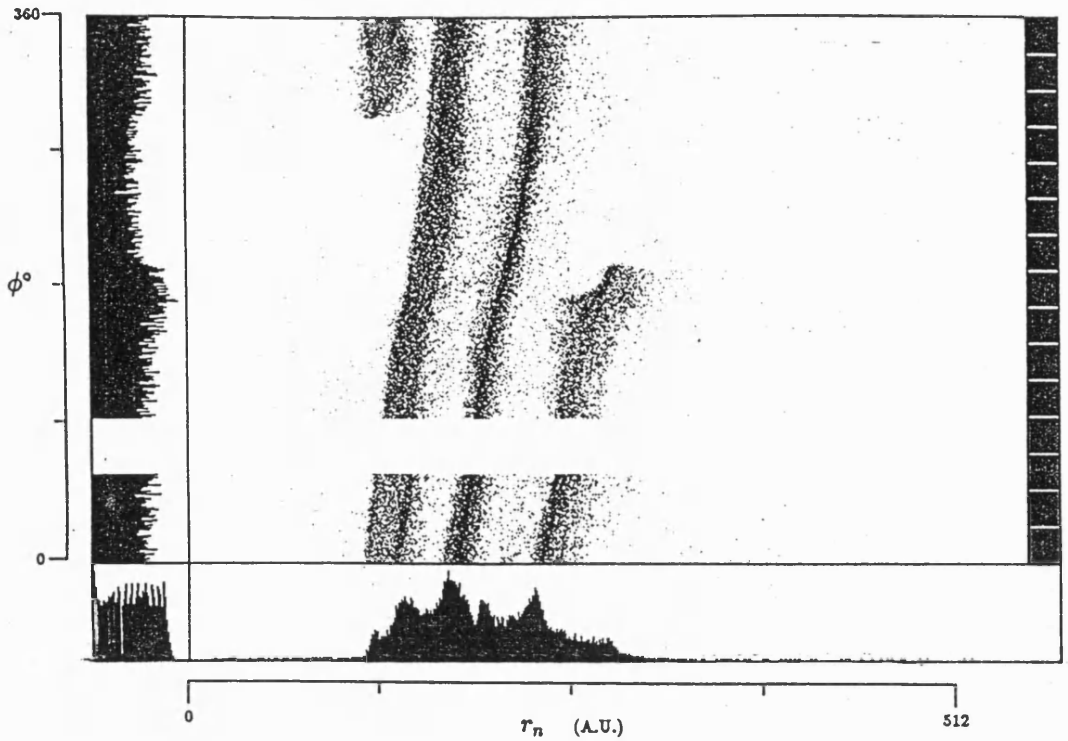

Figure 5.16: As for Figure 5.9 after radius dependent correction.

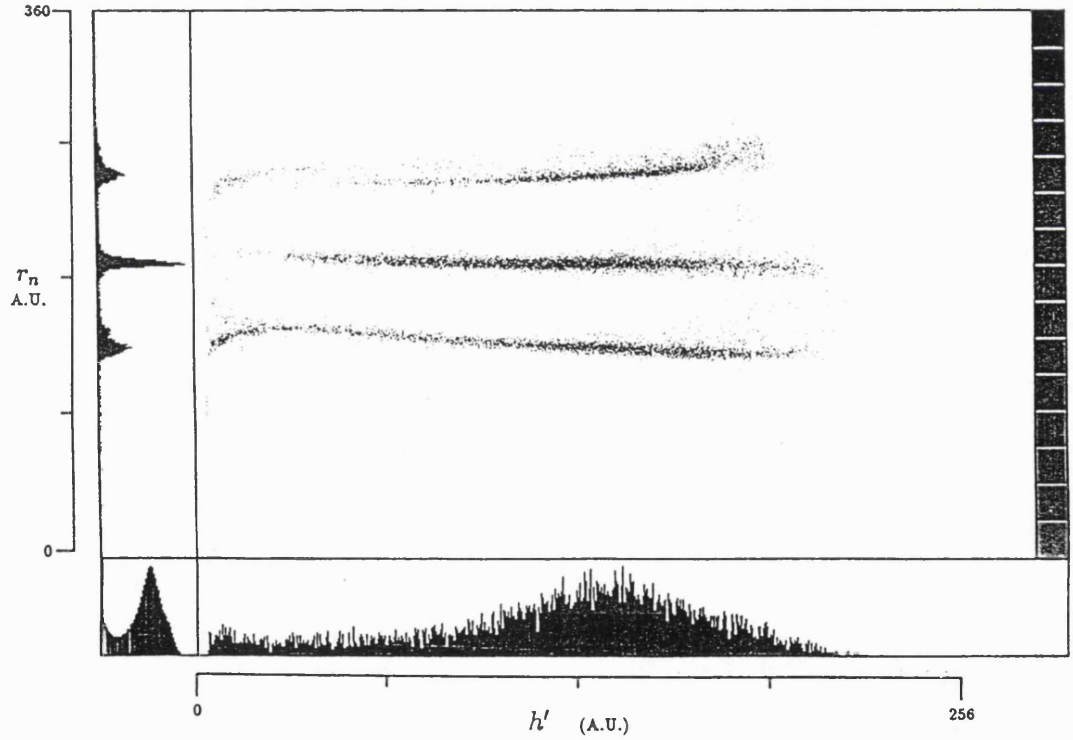

Figure 5.17: As for Figure 5.11 after radius dependent correction.

height is a constant reduction in r_n with increasing pulse height. However, as the correction consists of an addition to r_n, it can only be carried out after conversion to polar coordinates.

5.2.3 Limitations on the Correction

The methods described for correcting the r_n/h' variation assume that the function is a simple linear relationship. As shown in Figure 5.20, this is not always the case. At low pulse heights the relationship is clearly nonlinear and the curves actually intersect. Although the lower digitization of these smaller events tends to produce wider arms when normalized with respect to pulse height, it does not produce such significant broadening nor can it explain the phenomenon in which the events tends to concentrate in one or two relatively narrow bands. No simple method will be able to reliably resolve the spiral arms below a pulse height, in this diagram, of channel 16. Above this level the charge relationship can be reasonably approximated as a linear relationship.

The linearity of the r_n/h' relationship defines the point at which the LLD should be set. Gain depression will produce events in the nonlinear region of the relationship, where the corrections are not accurate and there is a significant chance that ghosting will occur. In practice a compromise would have to be set between reduced photometric linearity and an increased risk of ghosting.

5.3 Determining Spiral Constants

In the linear discriminant analysis as described by Equation 5.23, the sole criterion for assigning a point to either bracketting spiral is which of the arms is closer. It is therefore absolutely essential to have good estimates of the positions of the arms and determining the spiral constants is an integral part of spiral arm assignment.

In r_n/ϕ space, assuming that the arms are parallel, the position of the arms can be described by k_n, the gradient, and the intercept of the first arm with the r_n axis. By the equation of an Archimedean spiral, this offset can be represented by an angle ψ, so that for any phase angle ϕ the positions of the ith. spiral arm (r_{ni}, ϕ) can be determined from the two spiral constants,

$$r_{ni} = k_n(2i\pi + \psi) \quad , \tag{5.27}$$

For the same reasons as discussed above for the radius/pulse height correction, a

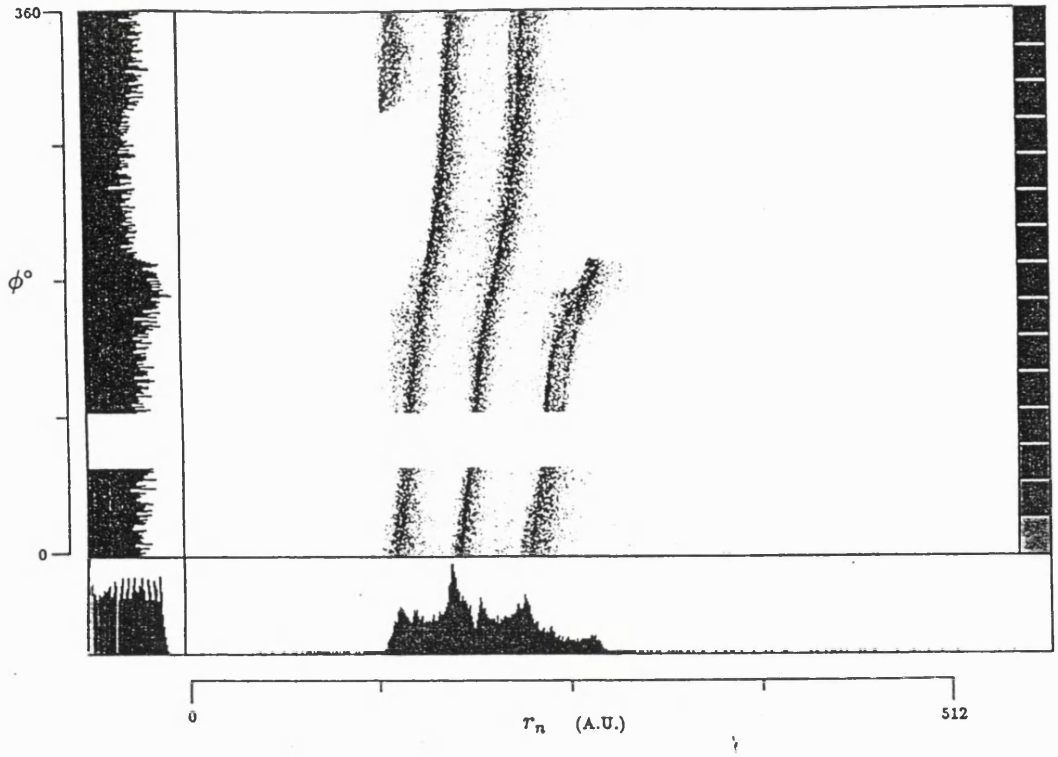

Figure 5.18: As for Figure 5.9 after radius independent correction.

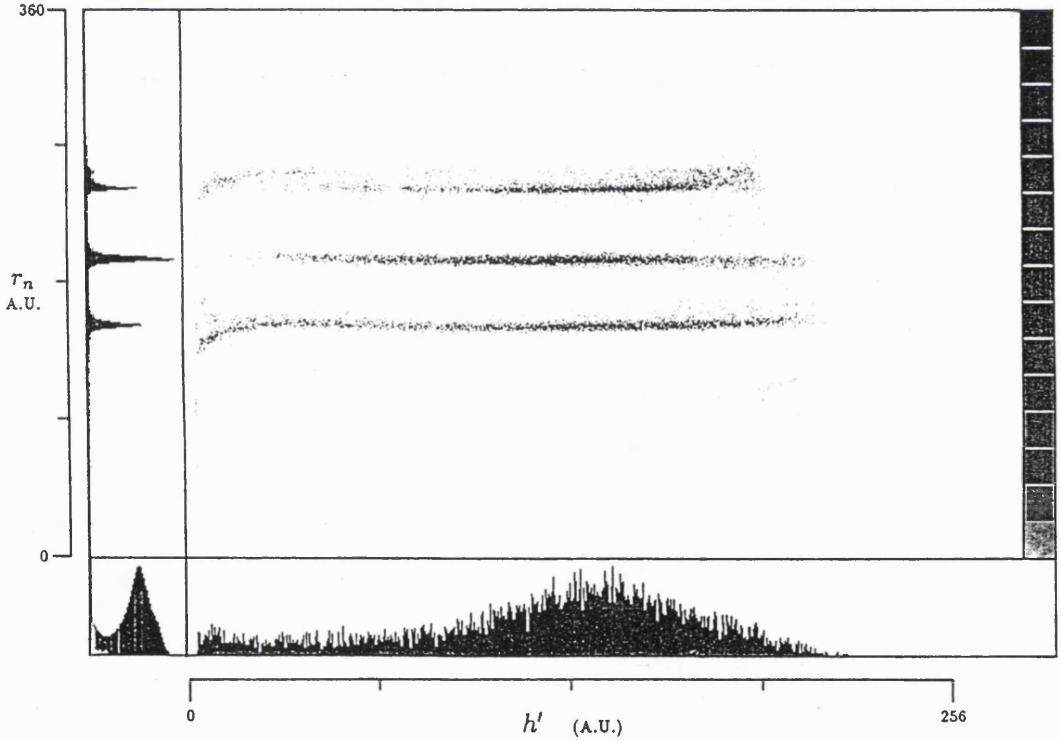

Figure 5.19: As for Figure 5.11 after radius independent correction.

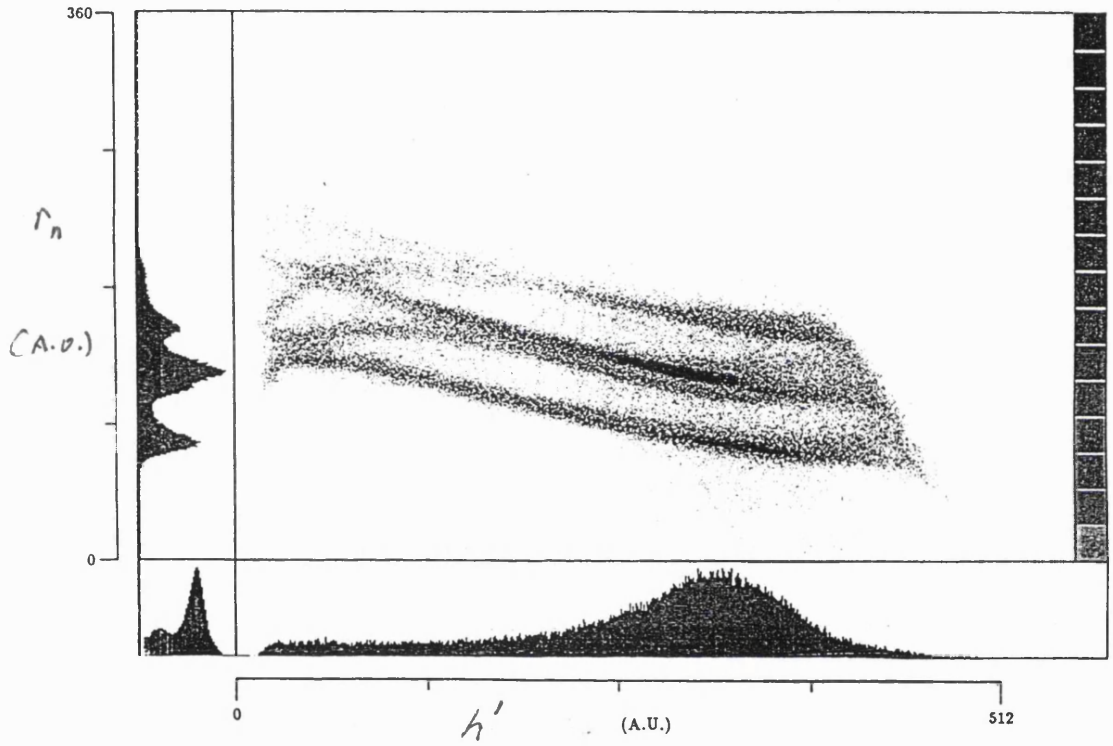

Figure 5.20: The nonlinearity of the radius/pulse height relationship.
This data is similar to that displayed in Figure 5.11 except that it represents approximately 10^5 events. The gains on the electronics channels have also been altered to enhance the low pulse tail. The pronounced diagonal, sharp edge apparent at the high pulse height end of the diagram is a geometrical effect caused by the finite volume of three dimensional space addressable by the ADCs. This effect is discussed in detail in Section 6.2.

flat PHD should be used for determining the spiral constants so that the constants have the most general applicability and have not been optimized for a narrow range of PHDs.

While evaluating methods of determining the spiral constants I have concentrated on procedures that could be highly automated and require a minimal supervision by the operator.

5.3.1 Line Finding by Edge Detection

In this method, I try to determine which points are associated with each of the spiral arms, without making any assumptions about the spiral constants. When the spiral arms have been identified, they are connected together to form one continuous line. The gradient and offset are then determined for this line.

The first stage is to determine which points are connected to the spiral arms and discard those that are not. I evaluated several edge detection algorithms for this purpose. The edge detector (ED) algorithm returns a value for each point. In most image processing applications this value is retained rather than the original intensity distribution, $I(r_n, \phi)$. However, in this application I only wish to determine which points are associated with the spiral arms and retain as much of the original distribution as possible. If the value returned by the ED lies above a threshold, the intensity at that point, $I(r_n, \phi)$ is retained, if not the intensity is set to zero. Ideally, isolated points will return a result below the threshold and be discriminated against.

Compass Masks

Figure 5.21 shows the result of a northeast compass mask ED (Pratt, 1978) when applied to the r_n/ϕ data produced by the radius dependent pulse height correction shown in Figure 5.16. This is a good example to use as the wide arms represent a worst case for EDs which are more suited to narrow lines such as the central arm. The results obtained for radius independent correction are similar to those obtained for the central arm.

The northeast compass mask is the 3×3 matrix

$$\begin{pmatrix} 1 & 1 & 1 \\ -1 & -2 & 1 \\ -1 & -1 & 1 \end{pmatrix}. \tag{5.28}$$

It is called the northeast mask because when convolved with $I(r_n, \phi)$ edges with inclinations to the y axis of $\approx$ 45° will return the highest values. As the gradients in Figure 5.16 are quite steep, a north compass mask was used as well. The matrix for this mask is

$$\begin{pmatrix} 1 & 1 & 1 \\ 1 & -2 & 1 \\ -1 & -1 & -1 \end{pmatrix}. \tag{5.29}$$

The results obtained with the north mask were almost indistinguishable from those for the northeast mask.

For all of the compass masks, the maximum value an isolated point will return is $I(r_n, \phi)$, however, the point will be represented at five connected points after convolution. Also, the sum of the elements is zero, so that regions of constant intensity will return zero. This is a problem with the wide spiral arms when using a flat PHD, as $I(r_n, \phi)$ varies slowly over the 3 pixel width of the mask. This leads to the fragmentation of the arms and suppression of the centres. Fragmentation is exacerbated if $I(r_n, \phi)$ has been smoothed with a filter. If the spiral arm is fragmented, it severely complicates assignment of points to individual arms.

A pseudo-compass mask of my own devising is

$$\begin{pmatrix} 0 & 1 & 0 \\ 1 & 0 & 1 \\ 0 & 1 & 0 \end{pmatrix}. \tag{5.30}$$

This mask retains the edge enhancing feature but as the sum of the elements is non-zero it does not return zero in regions of constant intensity and so reduces fragmentation. The behaviour for isolated points is similar to compass masks producing a characteristic diamond shape as seen in Figure 5.22.

Nonlinear Edge Detection

Nonlinear EDs use a nonlinear combination of pixels to enhance edges before thresholding the returned value (Pratt, 1978) An example of such a method is the Sobel ED, in which the value returned for each point (i, j) is given by

$$S(i,j) = \sqrt{X^2 + Y^2}\ , \tag{5.31}$$

where

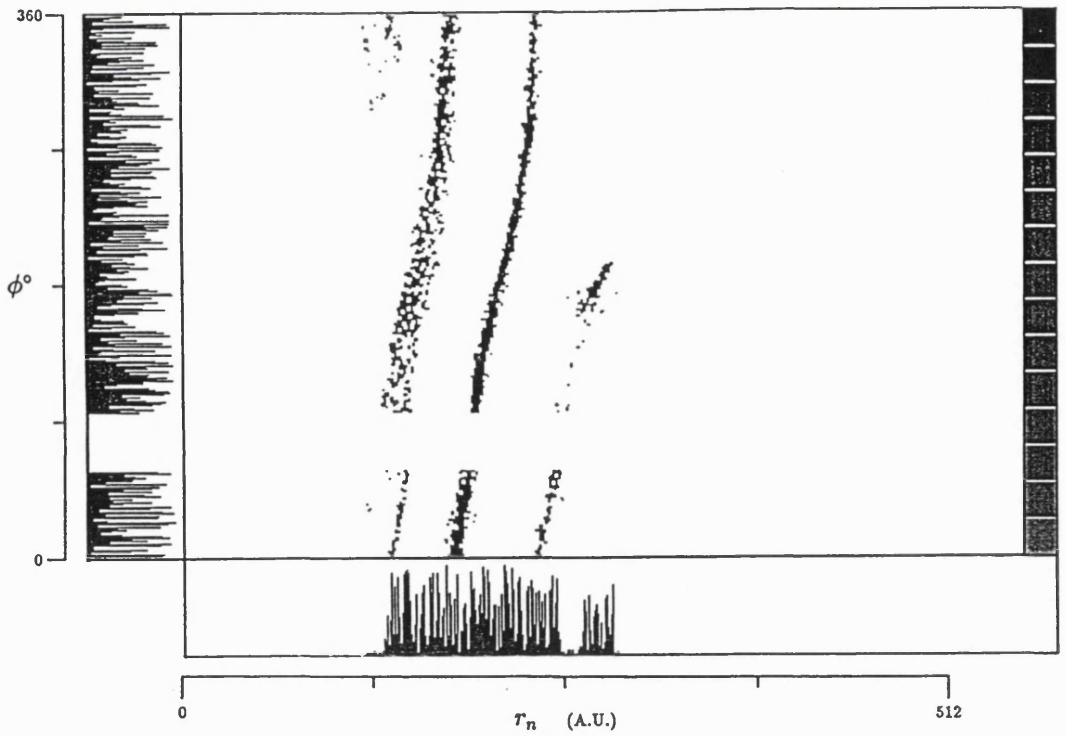

Figure 5.21: As for Figure 5.16 after use of a northeast compass mask ED, as described by Equation 5.28.

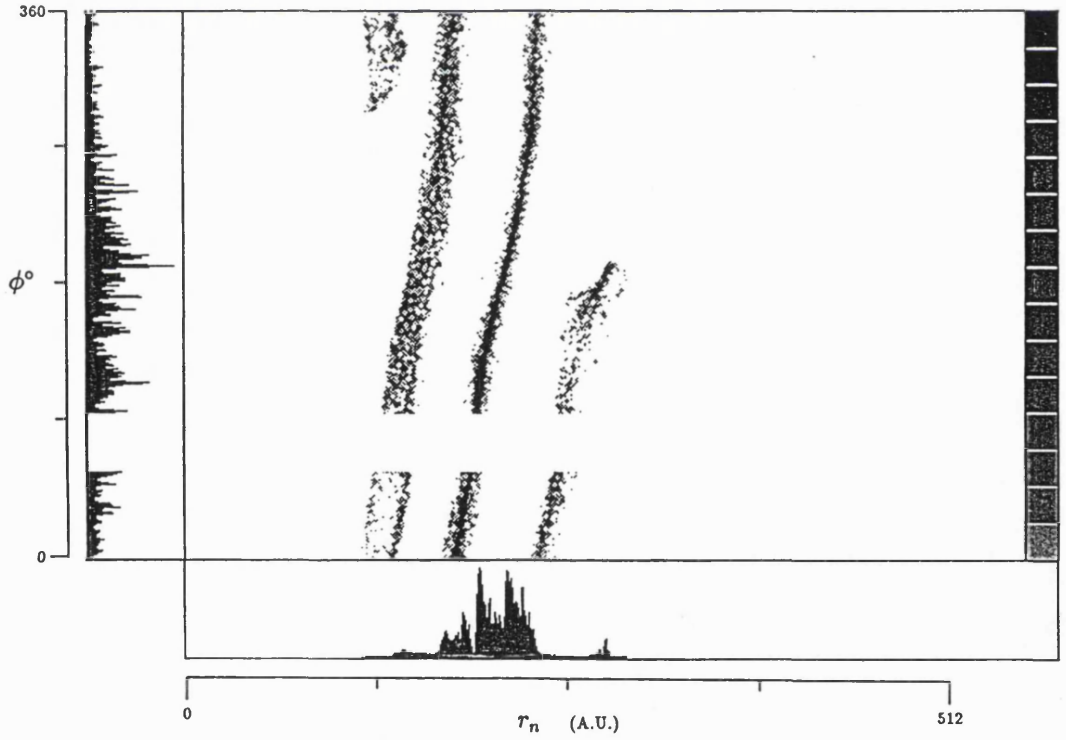

Figure 5.22: As for Figure 5.16 after use of a pseudo-compass mask ED, as described by Equation 5.30.

$$X = (A_2 + 2A_3 + A_4) - (A_0 + 2A_7 + A_6) \quad , \tag{5.32}$$

$$Y = (A_0 + 2A_1 + A_2) - (A_6 + 2A_5 + A_4) \quad , \tag{5.33}$$

where the pixels are numbered as

$$\begin{pmatrix} A_0 & A_1 & A_2 \\ A_7 & I(i,j) & A_3 \\ A_6 & A_5 & A_4 \end{pmatrix} . \tag{5.34}$$

As is the case with most nonlinear EDs, $S(i,j)$ must be thresholded. As is shown in Figure 5.23, if the threshold is set too low, the isolated points are not discriminated against, and if the threshold is set too high, the spiral arms are fragmented.

Arm Identification

After the ED has discriminated against the isolated points, it is necessary to determine with which spiral arm the remaining points are associated. I carry this out by moving along each line of constant phase angle ϕ_c and assigning each point of non-zero intensity to the nearest intensity distribution above a certain threshold, $I_a(r_n, \phi_c) = I(r_n, \phi_c)$. If a group of points have intensity above that threshold and are a given distance from the previous distribution, $I_a(r_n, \phi_c)$, the software designates them as a new distribution, $I_{a+1}(r_n, \phi_c)$. The separation required for designation is determined empirically and is equal to the average expected spiral arm separation. The intensity threshold is also determined empirically.

This is why it is so important to discard events between the arms. If there is a group of points between two arms, a and $a+1$, with sufficient separation then those points will be assigned to $I_{a+1}(r_n, \phi_c)$ and the points actually associated with spiral arm $a+1$ will be assigned to $I_{a+2}(r_n, \phi_c)$. All subsequent events along the line will have an error in their assignment of at least one arm.

Also, if there are no points associated with spiral arm a then those points associated with spiral arm $a+1$ will be assigned to distribution $I_a(r_n, \phi_c)$. Once more, all subsequent events along the line will have an error in their assignment. This is the reason that fragmentation of the spiral arms must be avoided. Figure 5.24, shows examples of errors in arm assignment due to fragmentation of the arm.

When all the points have been assigned to a distribution, the distributions $I_a(r_n, \phi_c)$, are combined for all values of ϕ_c to produce a series of parallel curves, $I_a(r_n, \phi)$. As shown in

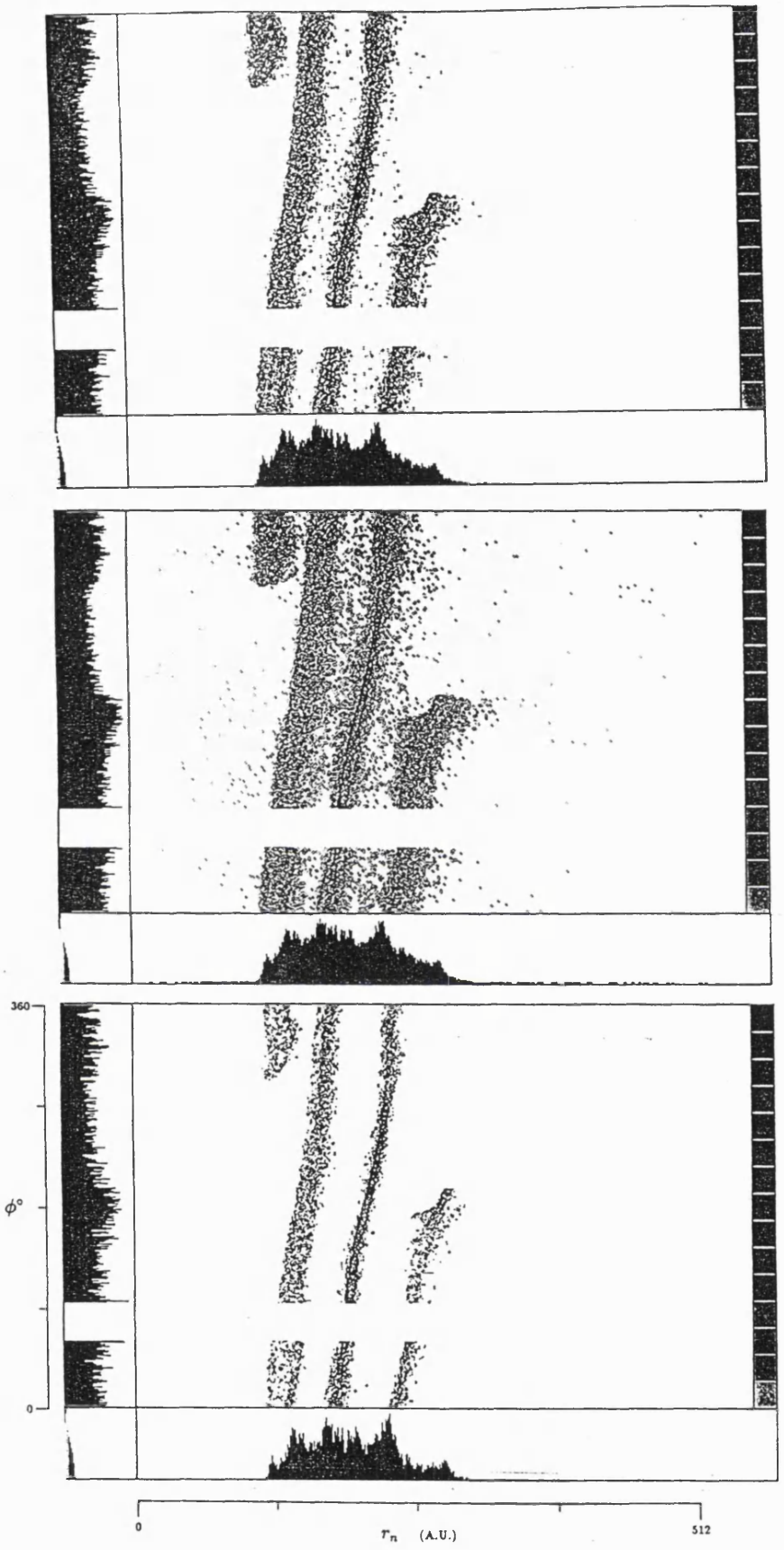

Figure 5.23: As for Figure 5.16 after use of a Sobel ED. The three figures show the effect of varying the threshold level.

The thresholds are set at 0, 6 and 12 db, increasing from top to bottom. The greyscale corresponds to a logarithmic intensity scale with 6 dB steps. The distribution in the bottom left corner represents the logarithmic distribution of the intensity levels returned by the ED.

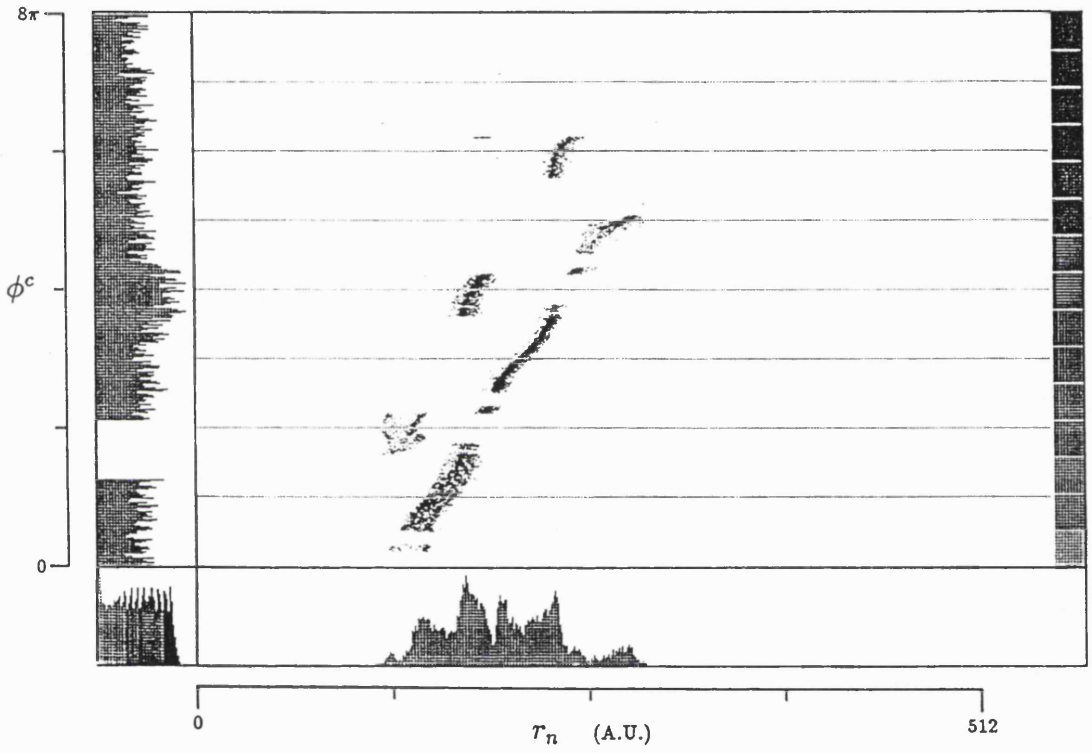

Figure 5.24: Fragmentation of the spiral due to errors in spiral arm assignment.

the r_n/ϕ plots, the start and end of the spiral do not correspond to the line $\phi = 0$. Therefore, the distribution numbers assigned by the software, even when the errors described above don't occur, will not correspond exactly to the spiral arm number for all values of ϕ. The discontinuity in the distribution caused by the presence of a partial spiral arm, is found by evaluating $\frac{d\overline{r_n}}{d\phi}$ where

$$\overline{r_n} = \frac{\sum_{i=1}^{m} r_i I_a(r_{ni}, \phi)}{\sum_{i=1}^{m} I_a(r_{ni}, \phi)} \quad , \tag{5.35}$$

where m is the number of pixels with non-zero intensity in the $I_a(r_n, \phi)$ distribution for a constant value of ϕ. Points with values of ϕ greater than the discontinuity are assigned the same spiral arm number as the distribution number a, while those points below the discontinuity are deemed to belong to spiral arm $a - 1$.

It is necessary to use this discontinuity method because if the length of the first spiral arm is small, as is the case with this dataset, the values of r for the end of the first arm will overlap with the beginning second arm. So the $I(r)$ distribution cannot be relied on to detect the start of the spiral. Also, as the phase angle at which the spiral starts is not correlated with the angle at which the spiral ends, any sudden variation in $I(\phi)$, even assuming that the spiral is continuous, cannot be used as an indicator of the start of the spiral. By a similar argument, any sudden variation in $\overline{r_n}$ over the full width of the detector does not indicate the start of the spiral. Therefore, the one dimensional and the full two dimensional intensity distributions cannot be guaranteed to correctly detect the start of the spiral.

Determining the location of the discontinuity is the stage of the procedure that is most susceptible to errors in the assignment of points to distributions. If errors have occurred, discontinuities in the distributions will be present, comparable in magnitude to those produced by the partial spiral arm. The software will reject any discontinuity that is not present in all of the intensity distributions, excluding the last distribution. However, if the first spiral arm is fragmented, no data may be present in the first distribution for a finite range of ϕ. This missing data will also produce a discontinuity in all distributions. The data can be smoothed if too many discontinuities occur. However, as the operator has to inspect the data to determine if the correct discontinuity was found, the procedure is not wholly automatic and the operator should probably just choose the start point of the spiral by eye.

When the spiral arms have been identified, they are all joined at their ends, making

one continuous line, Figure 5.25. This figure is the data from the flat PHD with radius independent correction, Figure 5.18, as an ED causes too much fragmentation of the arms with the radius dependent correction. The spiral constants are then estimated by taking the line of best fit to the continuous line.

Line Fitting by Robust Estimation

Given that errors can occur in in the assignment of points to spiral arms and that the continuous line has significant deviations from the ideal straight line particularly at the ends, a line fitting routine is necessary that is robust, i.e. insensitive to outlying points. Press *et al.* (1986) provide a more robust routine than the linear least squares which fits a line by minimizing the absolute deviation, i.e.

$$\sum_{i=1}^{N} |y_i - a - bx_i| \quad , \tag{5.36}$$

where

$$y = a + bx \quad , \tag{5.37}$$

is the equation of the line. The algorithm carries out an iterative search by bracketting and bisection to find the minimum. The initial point for the search the line fit parameters are returned by a linear least square algorithm. In my software both the linear least squares and the robust estimates are returned so that the operator can compare and choose the best fit.

At present this method of determining the spiral constants takes approximately 5.5 minutes on our PC, described below in Section 5.6, the time being approximately equally divided between the ED and the line fitting.

5.3.2 The Hough Transform

The Hough transform (HT) is a well known method for line-finding in image analysis (Pratt, 1978 and references therein). It involves the transformation of a line in Cartesian coordinates into polar coordinates. As shown in Figure 5.26, a straight line may be parametrically described as

$$\rho = x \cos\theta + y \sin\theta \quad , \tag{5.38}$$

where ρ is the normal distance of the line from the origin and θ is the inclination of the normal to the x axis. **N.B.** This θ bears no relation to the spiral angle, but I have called it

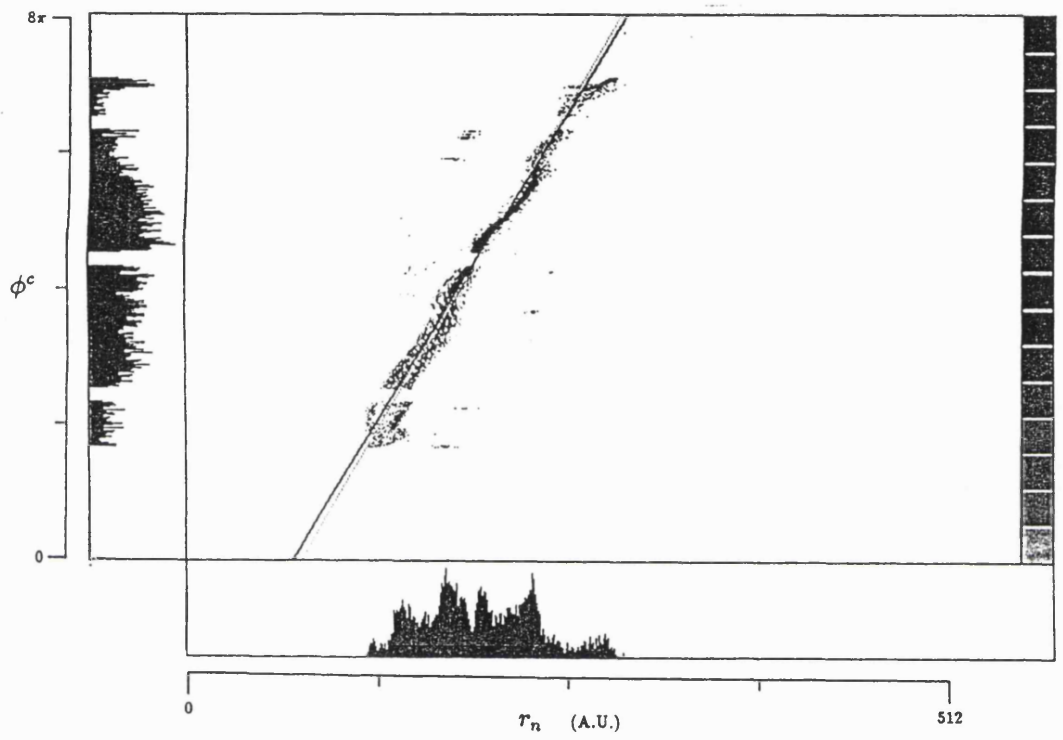

Figure 5.25: Fits to the whole spiral.
The dark line represents the linear least squares fit and the light line represents the robust estimate.

θ to be consistent with the literature on the HT. The transform maps the line onto a single point in Hough space with coordinates, (ρ, θ).

The family of all lines passing through a given point (x, y), maps onto a continuous sinusoidal curve in Hough space, as shown in Figure 5.26. This curve consists of the values of ρ and θ that satisfies Equation 5.38 for a given value of x and y. It is only necessary to evaluate Equation 5.38 for $0 \leq \theta < \pi$ as the curve is symmetric around $\theta = \pi$.

If we consider three co-linear points, the HT of the family of lines passing through each point will produce three curves. The intersection of these three curves in Hough space at (ρ_0, θ_0), defines the line passing through those three points.

Figure 5.27 shows the HT of the radial/phase plot for an ideal spiral, see Figure 5.3. For each point (r_i, ϕ_i), the curve that represents all the possible lines passing through that point is determined. If n of these curves intersect at a given point in the Hough space, (ρ, θ), then the intensity at that point is set as the sum of the intensities at the n points in r/ϕ space, i.e.

$$I(\rho, \theta) = I(r_1, \phi_1) + \ldots + I(r_n, \phi_n) \quad . \tag{5.39}$$

Therefore, the points in Figure 5.27 with the highest intensities, describe the lines in r/ϕ space on which most points lie.

This is precisely what we are trying to determine when obtaining the best fit for k. As θ in Hough space parametrically describes the gradient k in r/ϕ space, we wish to find the value of θ, θ_m, that produces the most intense peaks. As we have defined that the spiral evolves in a clockwise direction, Section 5.1.1, we know that ρ need only be evaluated for the fourth quadrant, i.e. $-\frac{\pi}{2} < \theta < 0$. In Figure 5.27, ρ has been calculated for each of the 360 image pixels along the θ axis, so each pixel represents $\frac{1}{4}^\circ$. As the gradient of the lines is quite steep, θ_m will be a small negative angle. In order to illustrate the variations of $I(\rho, \theta)$ around θ_m, the HT has been carried out over the range $\frac{-\pi}{4} < \theta < \frac{\pi}{4}$.

As shown by the flat intensity distribution $I(\theta)$, in the side histogram in Figure 5.27, the total intensity integrated along any line of constant θ, is approximately constant. This indicates that almost all of the curves in Hough space for each of the points (r_i, ϕ_i) will have positive values of ρ at angles sufficiently close to θ_m. So almost every point in r/ϕ space will be represented and the total number of points will be constant for each value of θ in this region. The intensity distribution for the value of θ which contains the points with the maximum intensity, $I(\rho, \theta_m)$, will have the maximum modulation. The

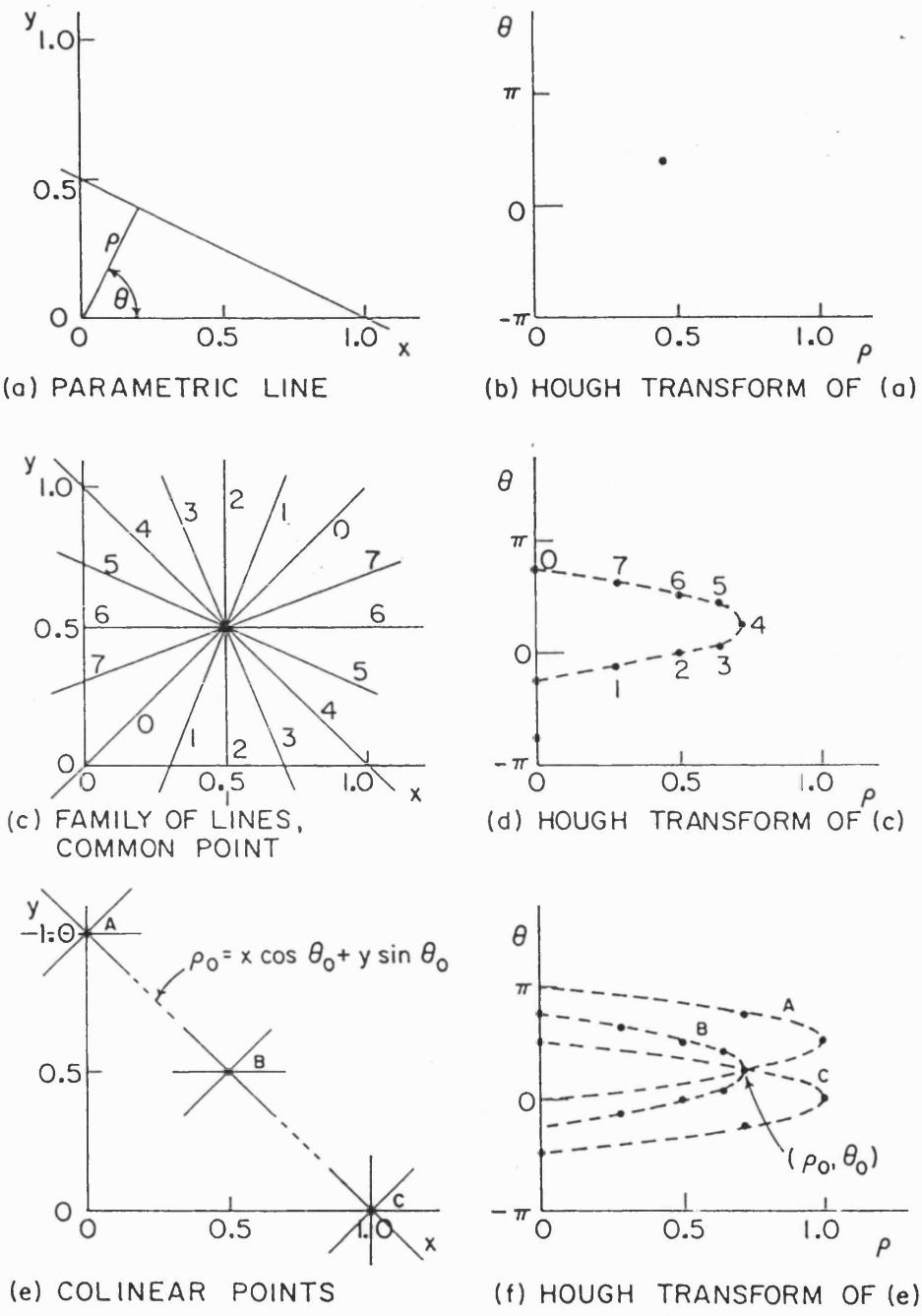

Figure 5.26: The Hough transform.

From Pratt (1978).

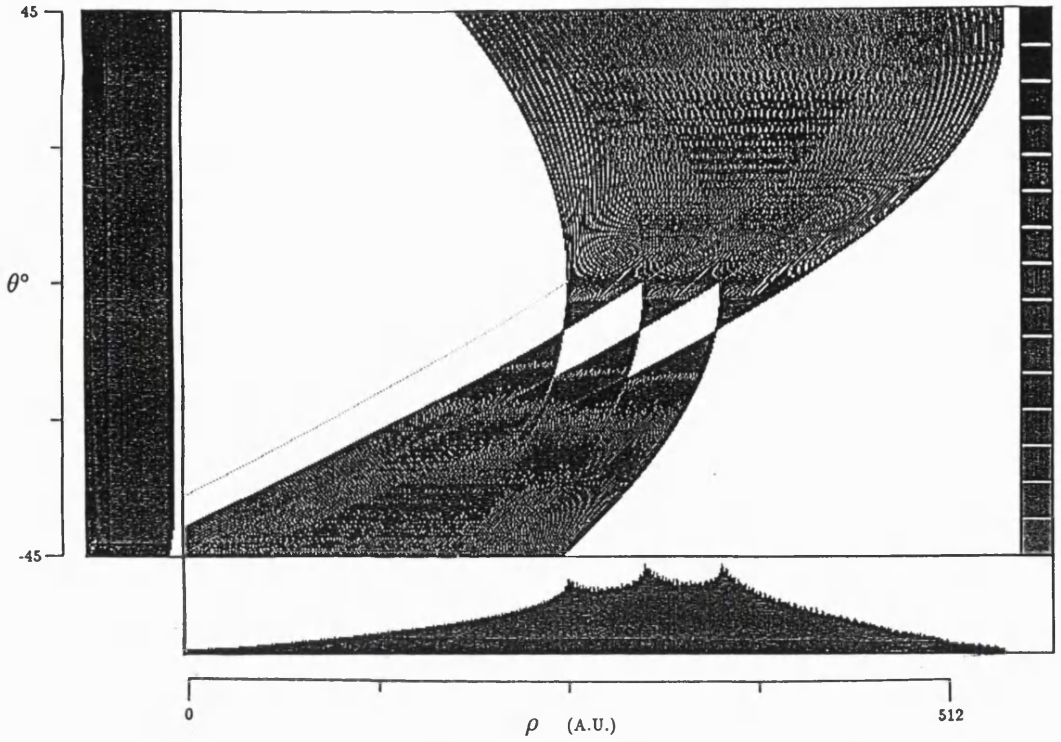

Figure 5.27: The Hough transform of the ideal spiral, Figure 5.3.
The greyscale corresponds to a logarithmic intensity scale with 6 db steps.

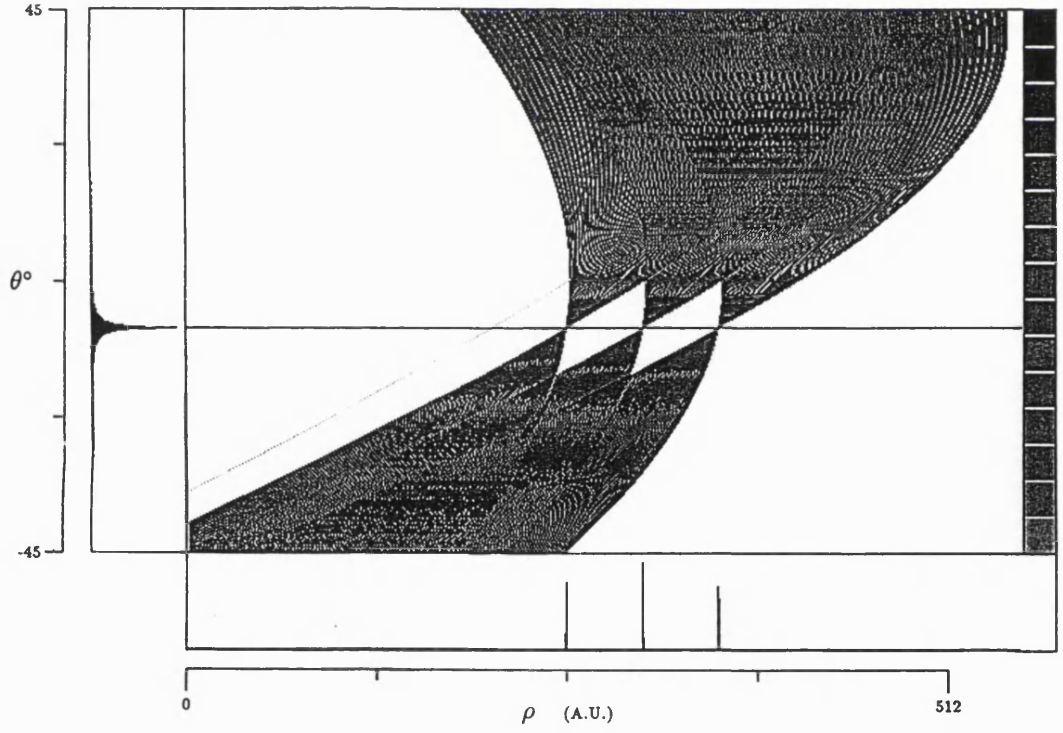

Figure 5.28: As for Figure 5.27, except the side histogram shows the variation of χ^2 with θ and the bottom histogram shows the distribution of ρ along the line $\theta = \theta_m$.

degree of modulation can be found by determining the χ^2,

$$\chi^2 \propto \sum_{i=1}^{m} \left[I(\rho_i, \theta_i) - \frac{I(\theta)}{m} \right]^2 \quad , \tag{5.40}$$

where m is the number of pixels along the ρ axis. Therefore, the value of θ that returns the largest χ^2 is the value that produces maximum modulation and represents the best fit of the spiral constant k.

Figure 5.28 shows the variation of χ^2 for Figure 5.27, in the side histogram. The section along the line $\theta = \theta_m$, $I(\rho, \theta_m)$ is shown in the bottom histogram. This distribution shows the number of points lying on all the lines of gradient k in r/ϕ space. The spiral phase shift angle ψ can be estimated by correlating a set of delta functions with this distribution. The spacing of the delta functions is determined by the value of θ_m. The point at which there is a maximum correlation between these delta functions and $I(\rho, \theta_m)$ represents the best estimate of ψ.

Figure 5.29 shows the HT of the r_n/ϕ plot shown in Figure 5.16 and demonstrates the information returned from the HT software. Of particular interest is how well the spiral arms are defined in the section along $\theta = \theta_m$ and how pronounced the χ^2 peak is. In the situation where the radius has been modified with radius independent correction, Figure 5.18, the definition of the arms is slightly improved on that for the central arm in this image.

The offset angle ψ has been estimated by the correlation of a 50% duty cycle square wave, of frequency determined by θ_m, with $I(\rho, \theta_m)$. A 50% width was chosen as the larger the duty cycle used in the correlation, the less modulation of the result will be produced but larger fractions would be used in practice. The estimate of ψ returned by the correlation determines directly whether the envelope for accepting data, should be symmetrical around the spiral arm or should be skewed to one side.

Evaluating the HT over 90° takes approximately 5 minutes. The majority of this time is used for calculating values of ρ, for the 360 values of θ, for each point. By limiting the range of θ over which ρ is evaluated, the HT can be sped up significantly.

The width of the r_n histogram in the r_n/ϕ plots gives a direct approximation of θ_m. If we assume that there is at least one spiral arm in the image and not more than the maximum number of arms defined by the anode design, m, then the range of θ is such that

$$\frac{-w_r}{w_\phi} < \tan\theta < \frac{-w_r}{w_\phi(m+1)} \quad , \tag{5.41}$$

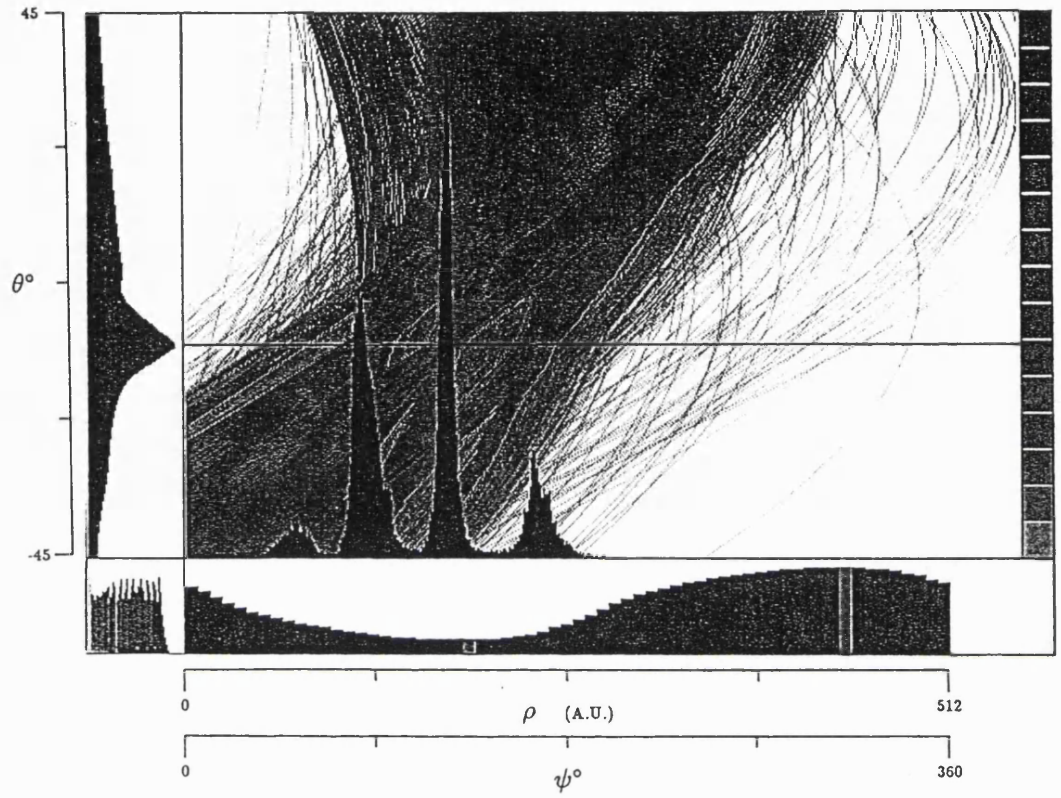

Figure 5.29: The HT of Figure 5.16.

The side histogram shows the variation of χ^2 with θ, the central region is a logarithmic intensity plot with 6 db steps, the histogram along the bottom of the central window is the distribution of ρ along the line $\theta = \theta_m$ and the bottom histogram is the correlation with the 50% duty cycle square wave with that ρ distribution to determine ψ. The two light regions in the bottom histogram represent the points with the maximum and minimum of the correlation.

where w_r and w_ϕ are the widths of the r_n and ϕ histograms, respectively, and $m+1$ is used to make allowance for the finite widths of the spiral arms.

Figure 5.30 shows the HT of Figure 5.16 over the reduced range in θ as determined by Equation 5.41, where w_r is the width of $I(r_n)$ at the $\overline{I(r_n)}$ level and w_ϕ is the total length of the ϕ axis, i.e. 360°. Both widths are in units of pixels. The range of θ is approximately 15° wide and the HT takes only 80 seconds. In this case the range of θ corresponds roughly to the FWHM of the modulation distribution, in the side histogram, and should be enough to demonstrate that the software has correctly located θ_m.

The HT could be sped up further by increasing the step in θ to more than $\frac{1}{4}°$. However with our computer, the algorithm could not be made to take less than approximately 40 seconds due to the time it takes to access the disk (approximately 400 kB must be read) and to plot the intensity distribution, both of which must be carried out twice.

Various other methods have been proposed to reduce the number of calculations in the HT (Ben-Tzvi & Sandler, 1990 and references therein) but given the limited gains to be made due to the computer speed, it is beyond the scope of this work to evaluate them.

The determination of θ_m and ψ take only an extra 15 seconds, so the spiral constants can be determined in approximately 1.5 minutes.

5.3.3 Comparison

The edge detection scheme is sensitive to noise, which can only be overcome by thresholding of the values returned by the ED. As the spiral arms are not edges but lines of finite width of almost constant intensity, thresholding will lead to fragmentation of the arms. This can lead to assigning points to the wrong spiral arm, although robust estimation of the line gradient can cope with this problem if it is not too severe.

The ED will only be successful if most of the points are assigned to the correct spiral arm in order to determine the correct position of that spiral arm. However, assigning points to arms is the very problem we are trying to overcome by determining the arm positions. So it is a rather circular technique.

The ED scheme is not stable enough to be used in a purely automatic manner but will require close supervision by the operator. The envelope containing the points that can be confidently assigned to either arm, as described by Equation 5.23, is symmetric about the centre of the spiral arms. However, this is not necessarily the best solution and an

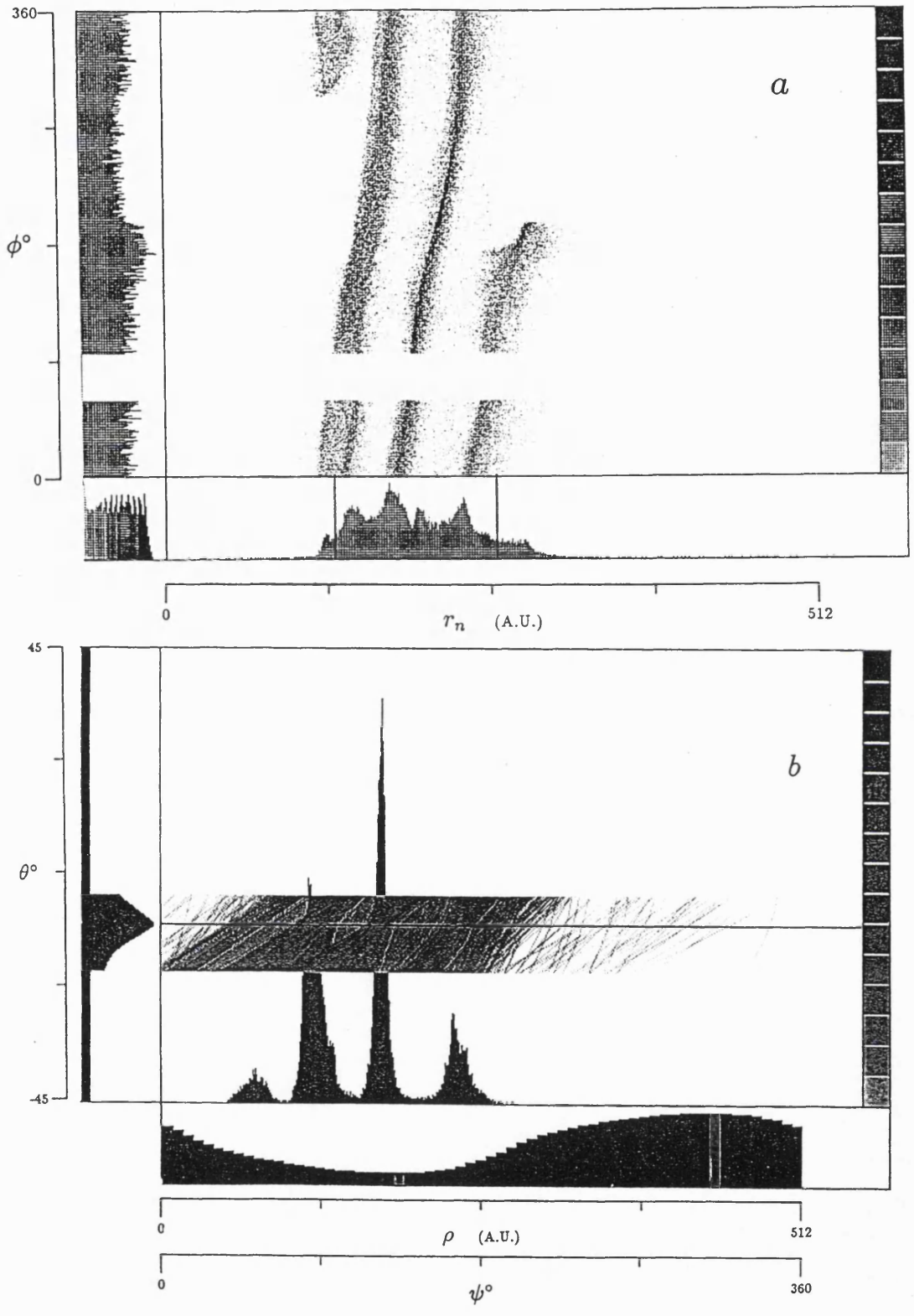

Figure 5.30: The reduced angle range for the HT determined by the r_n intensity distribution. The lines in the bottom histogram in Figure a show the region used in estimating the range in θ. Figure b has the same form as Figure 5.29 and shows the result of the HT performed over the limited angle range.

envelope skewed to one side might be better. Another convolution with the whole $I(r_n, \phi)$ distribution is necessary to determine where the centre of the envelope should lie. This takes approximately 2.5 minutes, giving a total computation time of 8 minutes.

As noise is uncorrelated in position, it won't be correlated in Hough space and for a given value of θ, noise will be spread over a wide range of ρ. The points associated with the arms are correlated in position and so will be concentrated into a smaller range of ρ than the noise. As each point in the image is represented for each value of θ in Hough space, the SNR will be improved as the entire two dimensional image will be integrated into one dimension. As θ more closely corresponds to the gradient of the spiral arm, the signal from the arms will be concentrated into smaller regions of ρ but the distribution of the uncorrelated noise will not be significantly affected. The SNR will therefore increase along with the definition of the spiral arms. The best SNR and arm definition will occur at θ_m.

As example of the enhancement of SNR, Figure 5.31 compares the Sobel ED with the HT for determining the gradient, α, of the $r(h)$ function, see Section 5.2.1 and Figure 5.11. As this is only a thin slice of the r_n/ϕ plot and the data is spread across 512 channels there are very few counts in each channel. EDs are suited for narrow lines such as these but as there are so few counts in each energy channel, the arms are fragmented again. More data are necessary for the ED to work and the problem still remains of how to determine which arm is which. The HT, however, has clearly resolved the three arms present and α has been determined once more by the modulation of $I(\rho, \theta)$.

Given the HT's tolerance of noise it is suitable for use in a highly automated procedure. It also takes one sixth of the time of the ED and has the potential for some speed improvement, while the ED cannot be improved very easily. Also, the author finds it particularly satisfying, philosophically, that the positions to which points are to be assigned, can be determined without actually having to first assign points to some distribution.

The HT however will only work if the r_n/ϕ plot consists of a series of curves which can be approximated by straight lines. If this is not the case, the ED method would have to be used. The continuous curve, consisting of all the parallel curves joined together, would then have to be fitted with a cubic spline because the curve could not be fitted with a straight line.

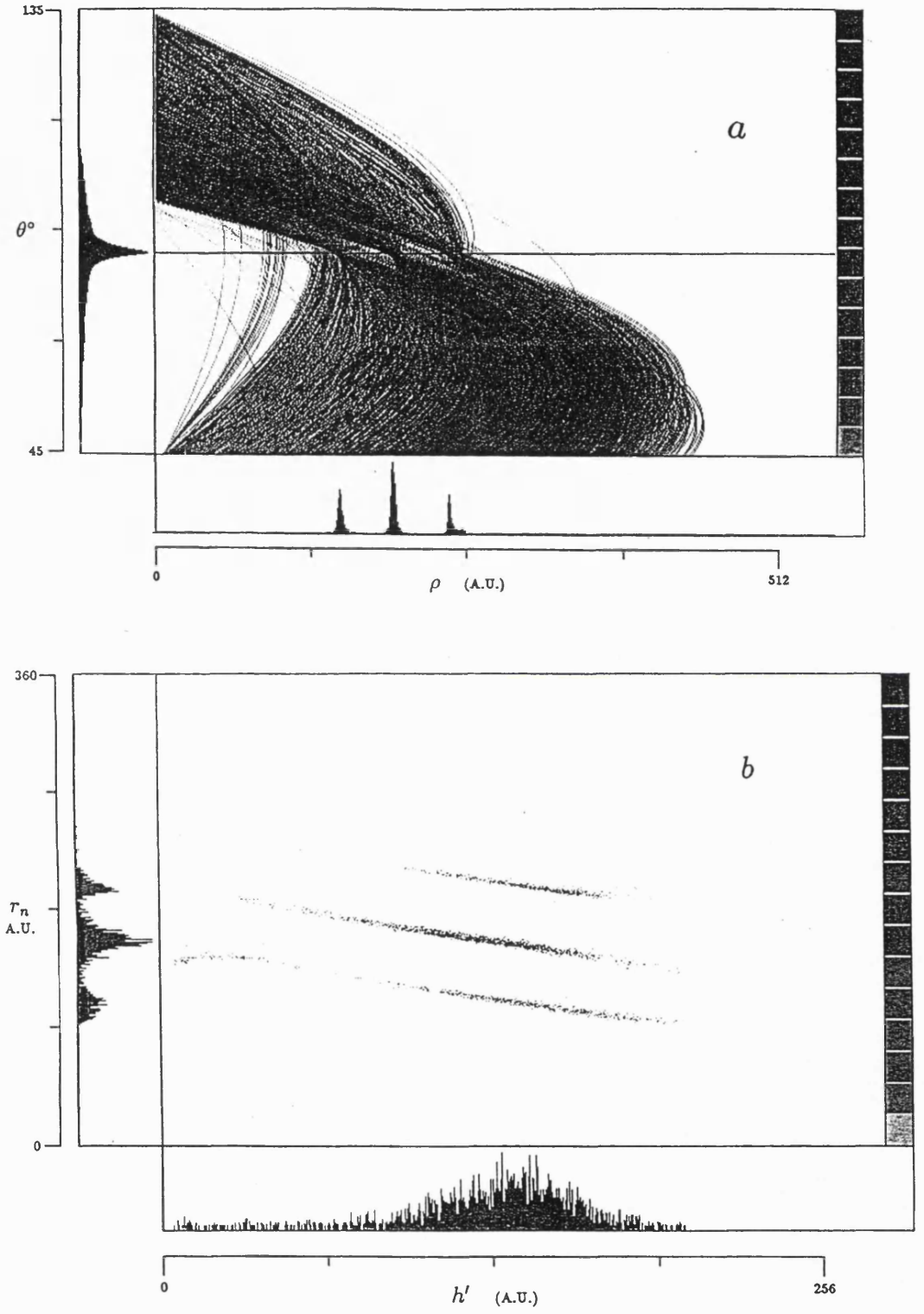

Figure 5.31: Comparison of the Sobel ED and the HT.
Figures a and b show the results returned by using the Sobel ED and the HT on the $r_n(h')$ plot shown in Figure 5.11, respectively.

5.3.4 Variation of Spiral Constants

Although the two spiral fit parameters are constant for any given anode design, the measured parameters vary with the plate operating conditions. As discussed in Section 5.2.1, the radius of the Lissajous figure produced by the three electrodes, is dependent on the charge cloud size. Any variation in that radius must significantly vary k and ψ. The spiral fit parameters are actually only constants for a constant set of operating conditions. For consistency's sake, I shall still refer to them as constants, although the variation of constants is a somewhat oxymoronic concept.

The constants presented in this section were all measured with the Hough transform, as discussed in Section 5.3.2. The uncertainty in k corresponds to the $\frac{1}{4}^\circ$ bins in the χ^2 distribution in Hough space, this corresponds to $\approx \pm 0.05$ in the arbitrary units of k. The FWHM of the χ^2 peaks is typically 5° corresponding to a width in k of ≈ 1.0 which is much larger than the observed k variations.

The distribution obtained by the correlation of the square wave with $I(\rho, \theta_m)$, is very broad which makes ψ prone to large uncertainties. The full width at the point half way between the maximum and minimum correlation is typically $180 - 240^\circ$. Also, all though k and ψ are quoted in units that suggest they are orthogonal, they are not: ψ is sensitively dependent on k.

Figure 5.32 shows how the constants vary with V_g. At the higher values of V_g, only small variations in k still occur, but there are still significant, progressive variations in ψ. The sizes of these shifts are large enough that if they were not corrected for, a large fraction of events would be mapped into the region between the spiral arms and discarded, severely degrading photometric linearity. Shifts in ψ larger than 90° can produce chronic ghosting.

Figure 5.33 shows how the constants vary with V_c. Once again there is relatively little variation in k at the higher values of V_g but significant variations in ψ occur in all cases.

Whenever photometric linearity is a consideration, new spiral constants should be calculated if varying the MCP operating conditions produces a significant variation in charge cloud size. As seen in Chapter 4.1, this occurs almost every time any of the operating conditions are changed.

The constants are sensitive to operating conditions but they appear to be reason-

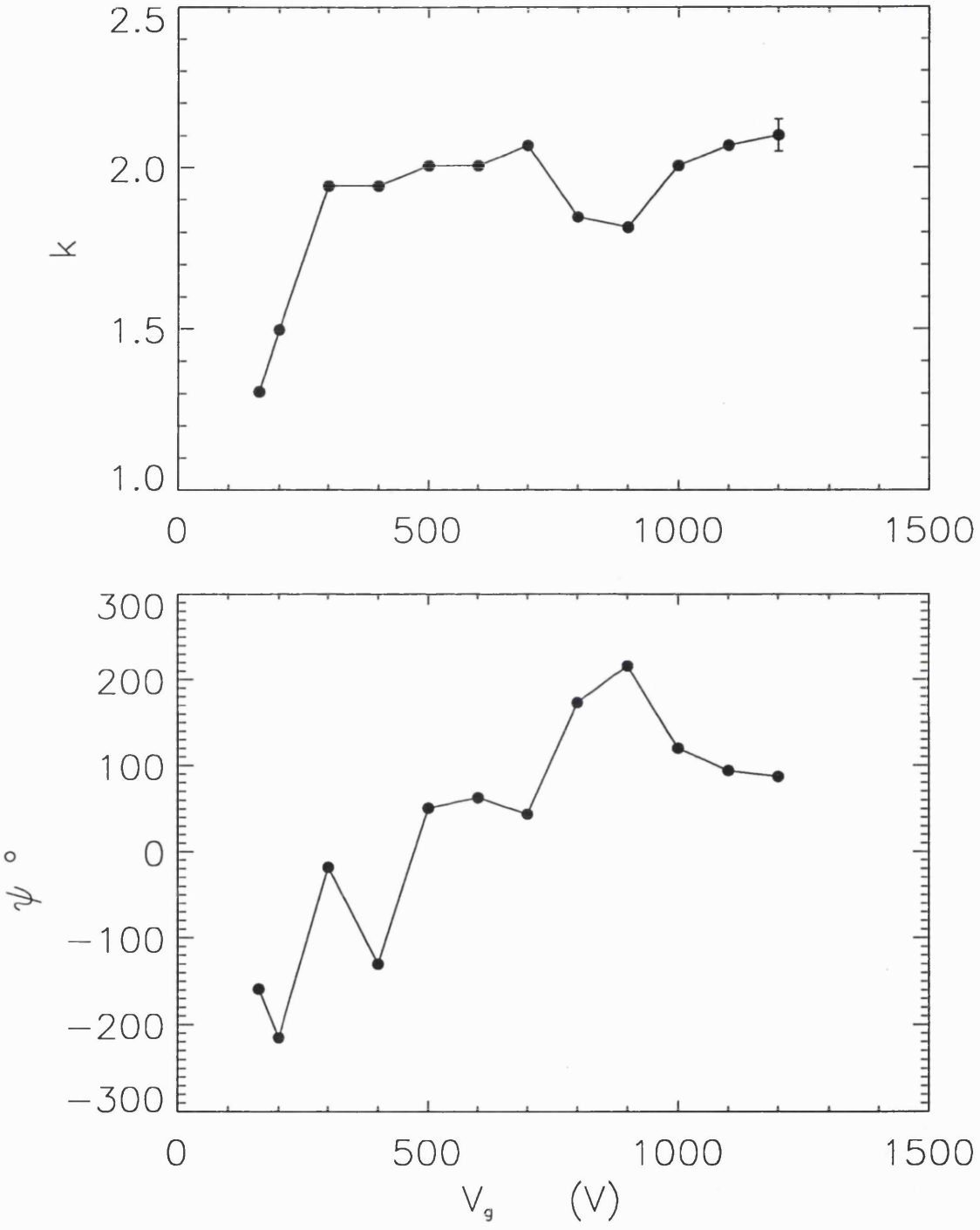

Figure 5.32: The variation of the spiral constants with anode gap voltage.
The data presented here are the k and ψ values for the same data sets for which α was displayed in Figure 5.14.

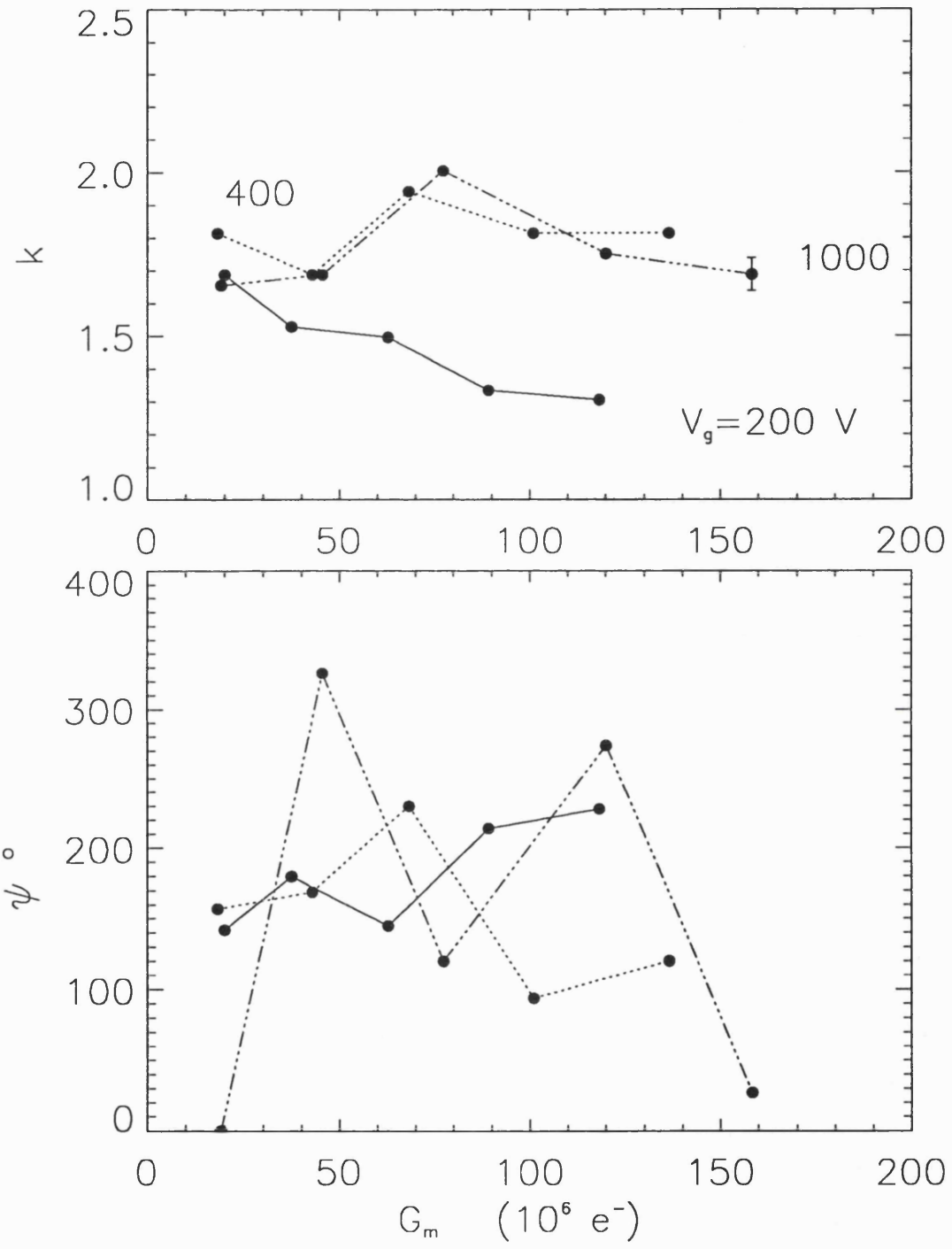

Figure 5.33: The variation of the spiral constants with plate voltage.
The data presented here are the k and ψ values for the same data sets for which α was displayed in Figure 5.15. The five different gains for each curve correspond to chevron voltages in the range 2.7 to 3.1 kV with 100 V steps.

ably stable with time. Although no detailed investigation of time variation has been carried out, I have used the same constants at constant plate operating conditions continuously for up to a month, without any appreciable degradation in photometric linearity or increase in ghosting.

5.4 Spiral Arm Assignment by Statistical Distribution of ρ In Hough Space

One further benefit of using the HT is that the distribution $I(\rho, \theta_m)$, see Figure 5.29, directly corresponds to the intensity distribution across the width of each spiral arm, for the whole length of each arm, i.e. every point associated with each arm is represented in the distribution.

This provides a convenient method of carrying out the spiral arm assignment. The operator need only select an intensity threshold in the distribution. The points above the threshold will be assigned to the appropriate spiral arm, those below will be discarded. Some care would have to be taken in the threshold selection, as partial spiral arms will have fewer counts in them, as shown in Figure 5.29. Alternatively, an acceptable width may be selected.

In either case, the operator may chose a scheme that will either eliminate the chance of "ghosting", retain the maximum number of events or a comprise between the two. Use of $I(\rho, \theta_m)$ would immediately allow a quantitative evaluation of the effectiveness of any decision criteria, such as percentage count loss or probability of ghosting.

The assignment could be implemented as a look-up-table (LUT) with the ρ value as input and the spiral arm number, a as output. The full width of the Hough transform plots, in this chapter, is always 550 pixels. Therefore, a 9 bit address should be adequate to describe the vast majority of possible ρ values. The memory could be configured as 4 bits deep, giving a total size of 256 bytes for the LUT. Figure 5.34 shows an example of $I(\rho, \theta_m)$ where data in between the spiral arms has been discriminated against and a representation of the values in the corresponding LUT. The rejected regions were chosen by eye. This image is presented only as an example and can in no way be claimed to represent an optimum case.

After the normalized data has been converted into polar space, (r_n, ϕ), it is trans-

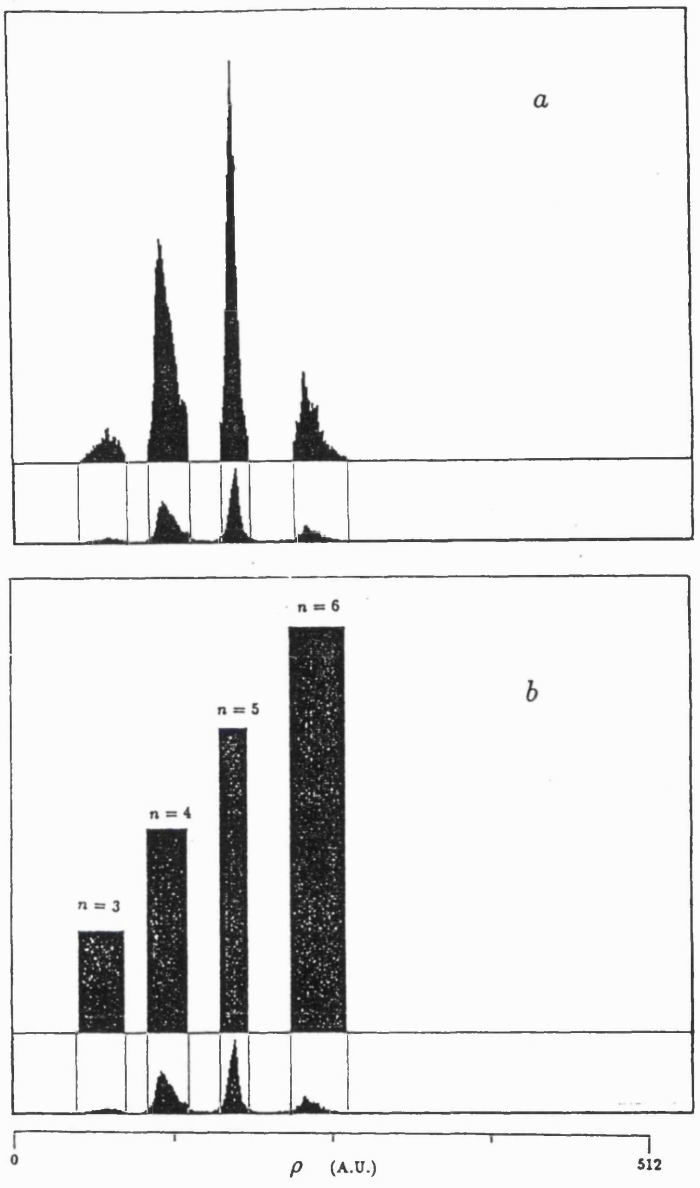

Figure 5.34: An example of spiral arm assignment by statistical distribution of ρ in Hough space.

Figure a demonstrates how the distribution of ρ along the line $\theta = \theta_m$ can be used to discriminate against events lying between the spiral arm. Figure b is a representation of the values in the ρ LUT. The value n is the number of the spiral arm, as in Equation 5.19. This anode has 4 spiral arms but only approximately three complete revolutions lie within the active diameter of the detector. The first complete arm in the active area is the fifth arm from the spiral origin, i.e. $n = 4$.

ferred into Hough space (ρ, θ). Since θ_m has already been determined from the flat PHD image, the data can be immediately projected into the line (ρ, θ_m) by Equation 5.38

$$\rho = r_n \cos\theta_m + \phi \sin\theta_m \quad . \tag{5.42}$$

Figure 5.35 shows an example of an image obtained using this assignment method.

5.5 Applications for Other Detectors

These techniques for spiral arm assignment are not just useful for SPAN alone. They are applicable for any cyclic readout in which the variable used for determining coarse position varies linearly and continuously with position across the detector, p.

For example, in the vernier anode, Section 2.2.2, coarse position is determined by the difference in the phase angles returned from the two sets of triplets, or the phase lag angle

$$\phi_{lag}(p) = \phi_2 - \phi_1 \quad , \tag{5.43}$$

$$= p(\omega_2 - \omega_1) \quad , \tag{5.44}$$

where ω_2 and ω_1 are the different angular frequencies associated with the two electrode triplets. From Equation 5.44 it can be seen that ϕ_{lag} varies linearly and continuously across the detector as long as $0 \leq p < \frac{2\pi}{\omega_2 - \omega_1}$. If the p exceeds the upper limit, ϕ_{lag} repeats itself.

Figure 5.36 shows the plot of ϕ_1 versus ϕ_{lag} for a simulated vernier anode where $\omega_2 = 1.1\omega_1$. It can be seen that it has the same general form as the r_n/ϕ plots for SPAN. If ϕ_1 and ϕ_{lag} were plotted in polar coordinates with ϕ_{lag} corresponding to the radius, the resultant curve is a spiral. Therefore, the technique of spiral arm assignment is applicable for the vernier anode.

In the case of double diamond readout, Section 2.2.1, the coarse position, ϕ_c is given by

$$\phi_c = p\omega_c \tag{5.45}$$

and

$$\omega_c = 0.1\omega_f \quad . \tag{5.46}$$

where ω_c and ω_f are the angular frequencies of the triplets encoding the coarse and fine positions (ϕ_f), respectively. The function $\phi_c(p)$ is linear and continuous over the range,

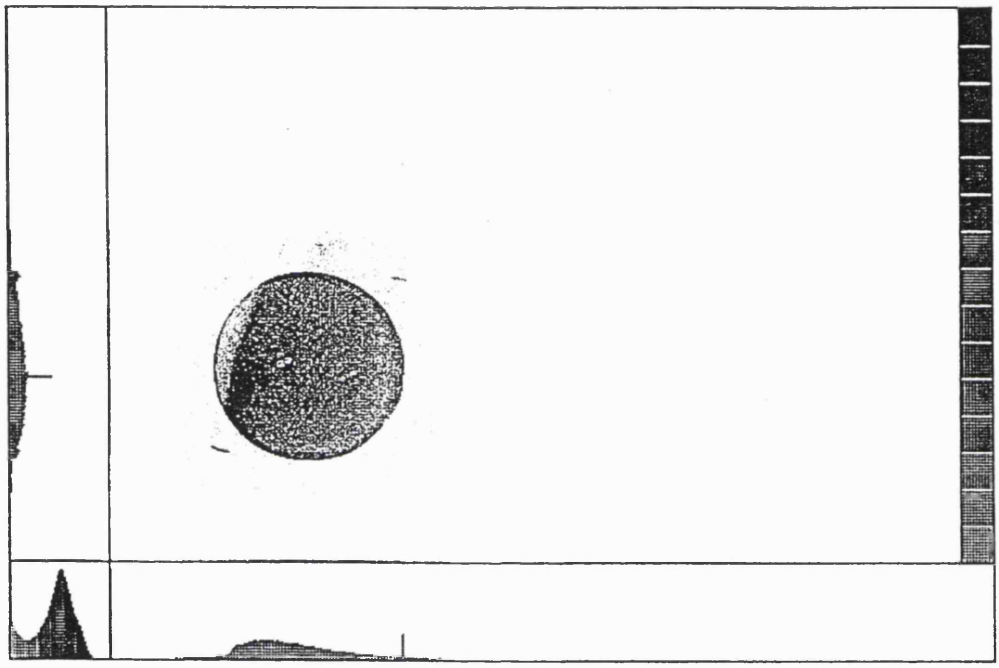

Figure 5.35: An example of the results obtained with spiral arm assignment by using the statistical distribution of ρ.
This figure uses the same data as represented in Figures 5.5 and 5.6. Even though it uses the whole PHD, the suppression of the ghosts is clearly superior to that obtained in Figure 5.6 and is comparable to that obtained by raising the level of the LLD, as in Figure 5.7.

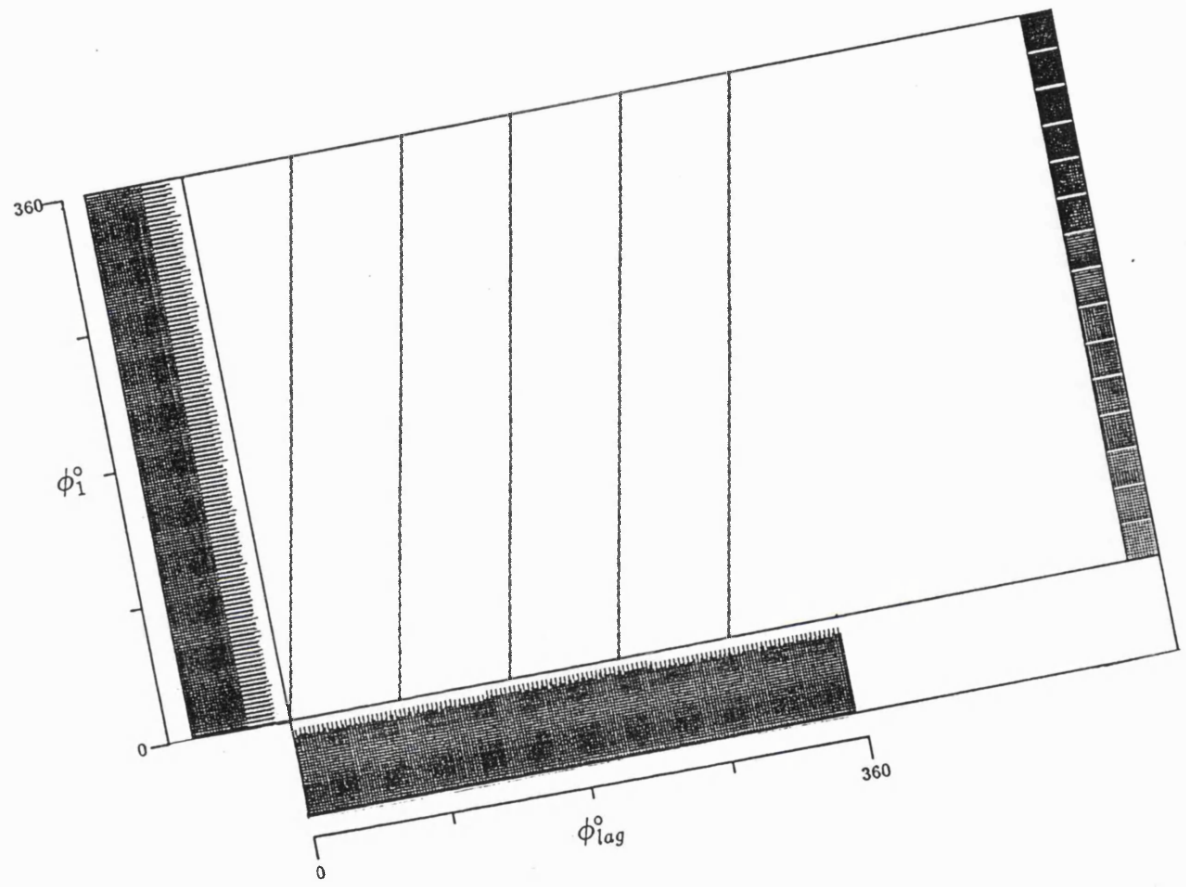

Figure 5.36: ϕ_{lag} plotted against ϕ_1, demonstrating that these two values define a spiral. The unevenness of the two subsidiary histograms is an artefact of the simulation software.

$0 \leq p < \frac{20\pi}{\omega_f}$. Even though the Lissajous figure produced by the triangular electrodes is a square, the double diamond readout will define a spiral if (ϕ_c, ϕ_f) are plotted as polar coordinates.

Spiral arm assignment should also be applicable for any readout in which the coarse position variable, c, varies continuously, provided $c(p)$ can be transformed into a linear, monotonic relationship.

5.6 How the Algorithm is Implemented

At present, all of the decoding for SPAN is carried out in software. The software runs on a Research Machines VX/2, PC compatible. This is an Intel 80386 based 16 MHz, IBM PC compatible computer with a 80387 maths co-processor. The 80386 is always operated in the "Real Mode". The software is written under the Microsoft MS-DOS operating system. The display standard is VGA, 640 × 480 pixels with 16 colours. The software is completely PC compatible and will run on any machine using MS-DOS 3.3, or later, and supporting VGA graphics.

Almost all of the software is written by the author in C and is approximately 3500 lines long. It is all written in the small memory mode and fits in the default data and code segments and therefore uses < 128 kB when loaded. However, in operation it uses a dynamically allocated array, 550 × 360 × 2 bytes deep, i.e. 396 kB. This array plus the default data and code segments add up to approximately 540 kB of the 640 kB RAM available under MS-DOS. Care must be taken in determining how much of this RAM other software packages on the machine use.

At present, data acquisition is carried out by 6 ADCs controlled through a Peripheral Interface Adapter by a routine written in assembler. Assembler was chosen for this phase because of its speed. This assembler routine is the only hardware specific part of the software.

Approximately 1000 events are acquired at a time and loaded into an array in the default data segment. Control is then returned to the main C calling routine and the decoding algorithm is carried out on the 1000 events, the pulse height of each event displayed and a histogramming memory for each pixel is incremented. Then another 1000 events are acquired and the process repeated.

At this stage the program is limited by the fact that the CPU has to control

data acquisition. As a result, data cannot be acquired and processed simultaneously and the results are only displayed in "pseudo-realtime". The decoding algorithm and the real-time display of events require much more time than the acquisition, limiting the speed of operation of the software to approximately 600 counts.s^{-1}

An important feature of the software is that the incoming digital data is converted into floating point numbers immediately after it has been read in. This is necessary to ensure that no spurious aliasing or fixed patterning is caused by roundoff errors during integer arithmetic.

The data is displayed in a central window of the VGA screen, with dimensions of 550 × 360 pixels. When the acquisition is complete the pulse height distribution is plotted in a small window (64 × 64 pixels). The integrated intensity across the x and y image axes can be plotted in two side windows 550 × 64 and 360 × 64 pixels, respectively. Any point on the screen can be interrogated by the mouse and the coordinates, the number of counts per pixel, per energy channel or per line is displayed on the screen. A zoom feature is available so any selected region of an image may be displayed using the full 550 × 360 array of pixels in the central window.

There are several modes of operation for the software :

1. Data can be displayed as it is acquired or from a stored image.

   Most of the following options are available for both modes.

2. The number of bits of digitization for the ADC can be varied but only for events that are actually being acquired.

3. A constant multiplication factor can be applied to individual channels for fine tuning of the image. This is only used while testing electronics.

4. The cartesian coordinates in the plane of the spiral, e.g. Figure 5.2, the r_n/ϕ space, for either dimension, or the two dimensional image can be displayed. Displaying the one dimensional data is necessary for spiral arm assignment. The plane of the spiral display is only used when investigating the gross shape of the spiral. It is sometimes easier to visualise the cause of gross distortions from the spiral in this mode than in the r/ϕ mode.

5. The pulse height of each event can be displayed in realtime. This is particularly useful

when high local count rates depress the gain of the MCP. A selection can be made either to display the cumulative total over all frames or just each individual frame.

6. The ratio of the total number of events plotted to the total number acquired is always displayed in real time. When acquiring two dimensional data, this provides a measure of the proportion of events that are not being mapped correctly to one of the valid spiral arms.

7. The cumulative count per pixel can be displayed in real time or after acquisition is complete. Intensity is shown with a 16 colours palette. The scale for the false colours can be selected to be either logarithmic or linear and step sizes and offsets are also selectable. The maximum number of counts per pixel is 64 k.

8. The whole active diameter or a selected region can be viewed in realtime. Similarly, the range of event pulse heights to be displayed can be selected.

9. The 6 ADC values, at 12 bytes per event, the decoded position and pulse height, 10 bytes per event, or just the histogrammed memory can be saved to disk. Files containing the 6 ADC values are used as inputs to a separate program to produce the $r(h)$ plots as in Figures 5.11. The histogrammed memory files are used as inputs to the Hough transform and edge detection spiral constant determining programmes.

5.7 SPAN Imaging Performance

The diagrams in this section were obtained with an open faced detector, the configuration of which is discussed in Section 7.2.1. They represent the best results obtained with a SPAN to date. Lapington *et al.* (1992) have presented examples of recent performance measurements with a two dimensional SPAN in a sealed tube detector.

The grey scales in all the diagrams in this section, correspond to intensity values with zero offset and unit steps.

5.7.1 Pulse Height Related Position Shifts

Figure 5.37 shows that there is a pulse height related shift in ϕ as well as in r_n. No correction for pulse height has been made on the radius in both figures, so that on each spiral arm, the lower pulse height events have the larger radii.

In the data plotted in the plane of the spiral, the low pulse height data always precedes the high pulse height data, i.e. ϕ is largest for the lowest values of h'. This is also apparent in the r_n/ϕ plot. If there was no variation of ϕ with h', the individual smears would be parallel to the r_n axis. Also, the gradient, $\frac{\phi}{r_n}$, does not vary significantly through 360°.

The cause of this shift is not known at present but the author thinks they are probably another charge cloud effect. If the variation in ϕ was due to a h' dependent shift of the spiral origin, the gradient would vary with angle and would have opposite signs for points separated by 180°, so this cannot be the explanation. Also, although the magnitude of the gradient is often not the same for each of the triplets, the sign always is. The data in this diagram are those obtained from the second triplet of electrodes of the two dimensional SPAN anode. The ϕ/r_n gradient for the first triplet is much smaller.

As the ϕ is used to determine the fine position, any h' related variation in ϕ will induce pulse height related position shifts in a two dimensional image. Figure 5.38 shows an example of two dimensional images produced with varying proportions of the PHD. The effect causes the low intensity tails extending in the positive y direction in the figure consisting of events distributed throughout the entire PHD. These tails are not visible where a smaller range of pulse heights are used. Also, the tails extend much further in the y direction than in the x which follows the behaviour of the ϕ/r_n gradients for the two triplets. The size of the pinhole images in the figure with the reduced pulse height ranges have diameters of ≈ 60 μm and the length of the tails are comparable. All though the shift in ϕ with pulse height is small, it can translate into significant positional shifts.

5.7.2 Positional Linearity and Resolution

Figure 5.39 shows an image of a pinhole array covering the whole active diameter of the MCP. It demonstrates the excellent spatial linearity of SPAN. In all but the extreme edges of the image, the maximum deviation from the expected position of the peak of the images is 30 μm across the active region. The best resolutions obtained were at voltages

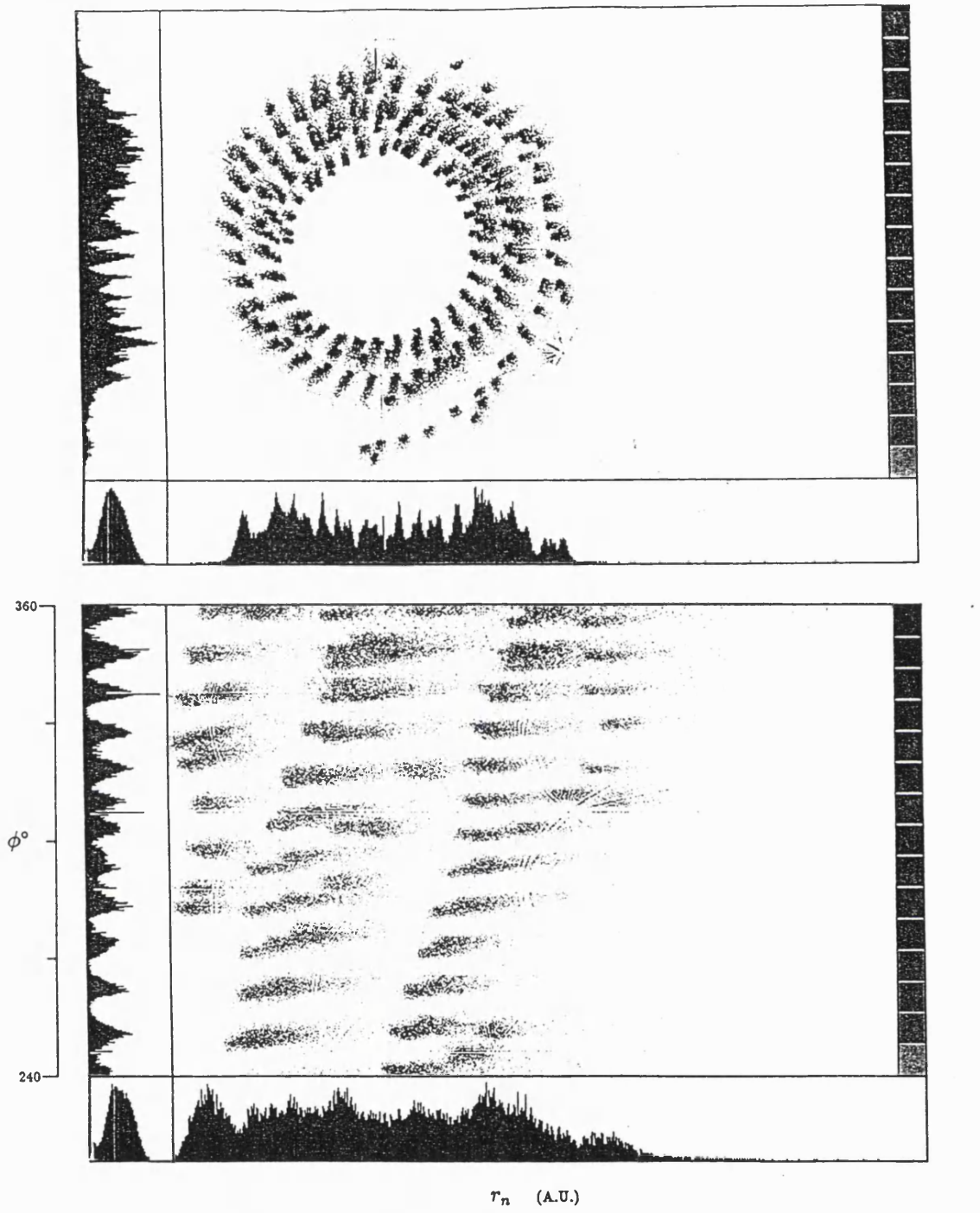

Figure 5.37: An example of pulse height related shifts in ϕ and r_n.
The top figure shows the data represented in the plane of the spiral and the bottom diagram shows a section of the r_n/ϕ plot in the range $240° < \phi < 360°$. No correction has been made for radius dependence on pulse height. The image was formed by illuminating the MCP through a uniform grid of pinholes, as described in the next section. Note the structure in the figures due to fixed patterning, which is discussed in the next chapter. This data was obtained with 9 bit digitization.

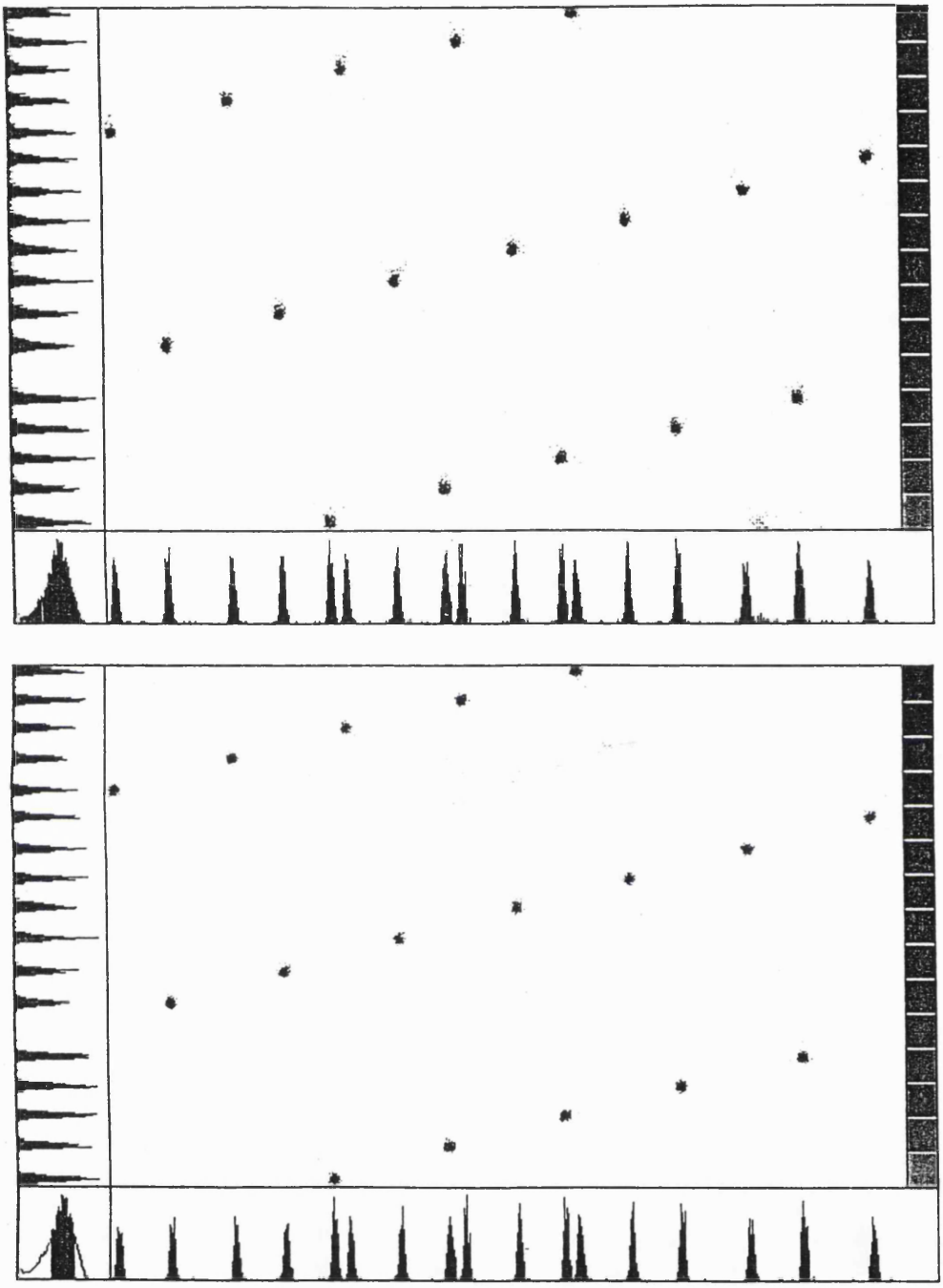

Figure 5.38: An example of positional shifts due to pulse height variation.
The figures are an enlarged image of the same pinhole array seen in Figure 5.39. The top image uses events with pulse heights distributed throughout the PHD, while the bottom diagram includes only those lying within a region defined by the PHD FWHM. The data displayed in the previous figure corresponds to the y axis in this diagram.

of $V_c = 2.9$ kV and $V_g = 400$ V. Figure 5.40 shows an image obtained at these operating conditions in which the MCP pores are visible. The image was acquired only using a limited range of pulse heights, $6 \pm 1 \times 10^7 e^-$, in order to overcome the h' related positional shifts. The resolution is approximately 17 μm FWHM which represents the centroiding PSF of the readout.

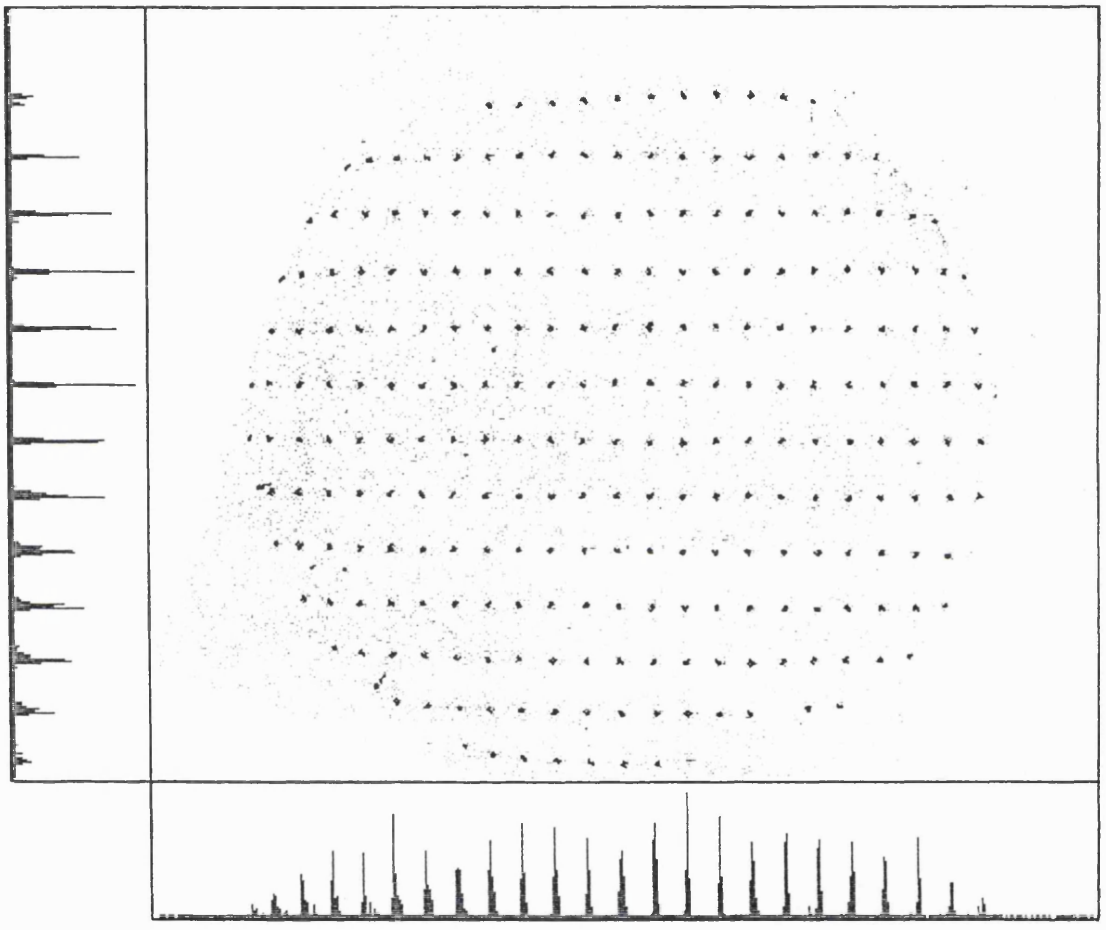

Figure 5.39: Image of an array of 50 μm pinholes demonstrating the linearity of the SPAN readout.

The array covers the entire 25 mm active diameter of the detector and has a spacing of 1.7 mm by 1.0 mm.

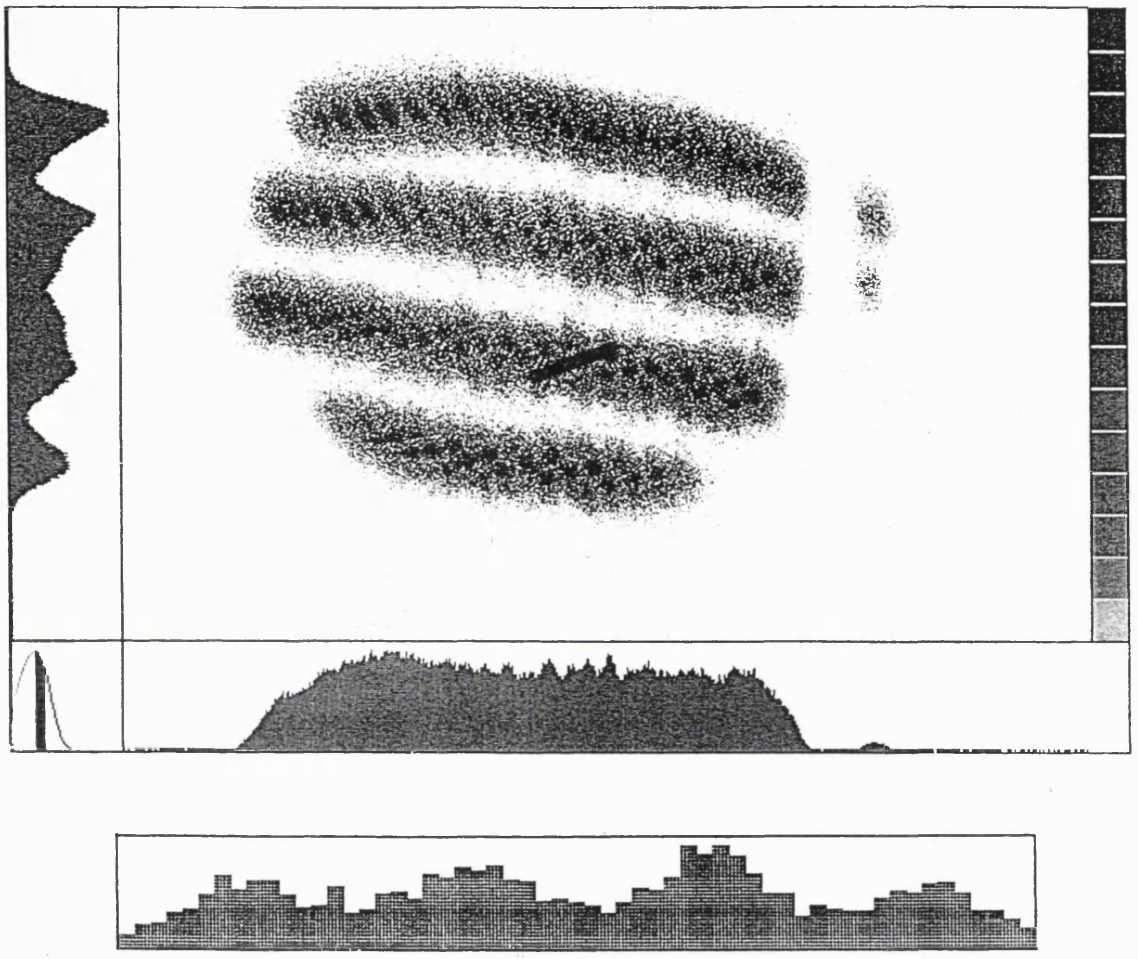

Figure 5.40: Image of a 37 μm bar mask in which the individual pores are clearly resolved. The lower panel shows the intensity distribution along the section indicated by the dark rectangle in the main figure. This demonstrates the level of modulation of the pore images. The image contains a total of 150,000 counts and represents approximately 16% of the total counts acquired. The total count rate was $\approx$ 100 Hz. The data was obtained with 14 bit digitization and a 2 μs time constant on the shaping amp.

Chapter 6

The Effects of Digitization for the SPAN Readout

The values returned by the ADC's represent the vertices of pixels and if we plot the three ADC values (x, y, z) as mutually orthogonal coordinates, the vertices define a cubic lattice. When this lattice is sectioned by the plane $x + y + z = c$, where c is a constant, the vertices are hexagonally packed and the pixels have been deformed into rhomboids, Figure 6.1.

This hexagonally packed lattice must be resampled into segments of equal arc length, S. This presents no problems for continuous data, but for discrete data it can introduce fixed patterning. This is illustrated in Figure 6.2. In this example, the hexagonally packed lattice is subdivided into 256 angle windows of constant width, $\Delta\phi$ and only those points lying within a finite radius window, Δr, are regarded as acceptable, a window centred on the minor axis of the lattice will contain 7 points while the adjoining window contains no points. For angular windows centred on an angle of inclination 15° to the minor axis, there are approximately equal numbers of points in adjacent windows. This effect arises due to the fact that for a finite Δr there are only a finite number of pairs of finite integers, (m, n), or states, that satisfy

$$\phi_0 < \arctan\frac{m}{\sqrt{3}n} < \phi_0 + \Delta\phi \quad , \tag{6.1}$$

$$r_0 < \sqrt{m^2 + n^2} < r_0 + \Delta r \quad . \tag{6.2}$$

The factor of $\sqrt{3}$ in the denominator of the arctan expression is due to the transformation into coordinates in the plane of the spiral, see Equations 5.4 and 5.5. In practice, the range

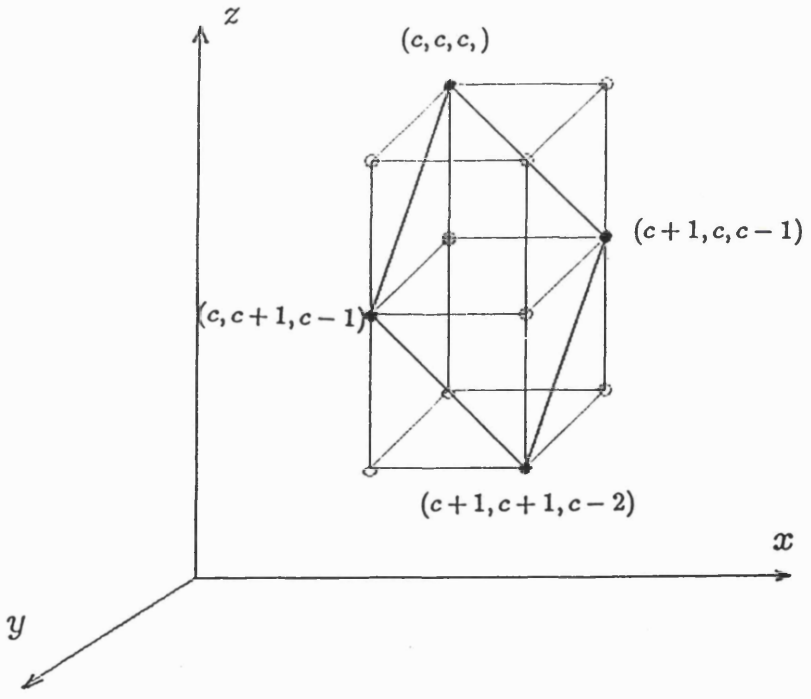

Figure 6.1: The cubic lattice defined by the digitization levels of the three ADCs, produces a hexagonally packed lattice when sectioned by the $x + y + z = c$, where c is a constant.

of m and n is limited by the number of digitization levels of the ADCs used.

This effect presents itself as a variation in the sensitivity, $s(i)$, from one pixel, i, to another. Figure 6.3 shows a simulation of the variation in $s(i)$ for a spiral anode containing three arms in the active region of the detector. The active region commences at the beginning of the fourth spiral arm, i.e.

$$n_a = 3 \ , \tag{6.3}$$

$$n_s = 4 \ , \tag{6.4}$$

$$\Rightarrow 8\pi < \theta < 14\pi \ . \tag{6.5}$$

This is the approximate configuration of the spiral in the active area of the detectors evaluated so far. There is only a phase shift of about 70° between this configuration and that displayed in Figure 5.18, etc. Every possible state lying within a radius envelope, with a relative width, w_r, half the spiral arm separation, i.e.

$$\Delta r = w_r 2k(h')\pi \ , \tag{6.6}$$

$$= k(h')\pi \ , \tag{6.7}$$

and centred on the centre of the spiral arms, has been illuminated just once.

The $s(i)$ values correspond only to data from one pulse height plane, i.e. the plane,

$$h' = \frac{3}{2}256 \ , \tag{6.8}$$

$$= 384 \ . \tag{6.9}$$

Choosing only one plane also constrains the values of k,

$$k(384) = 2.1 \ , \tag{6.10}$$

which corresponds to

$$k_n = k(256) \ , \tag{6.11}$$

$$= 1.4 \ , \tag{6.12}$$

which is typical of the spiral constants for the anodes that have been evaluated so far.

The inputs x, y and z have been digitized to 8 bits, $d = 8$ and the arc length, S, defined by this range of θ has been divided up into 2048 pixels, n_p, of equal width. This

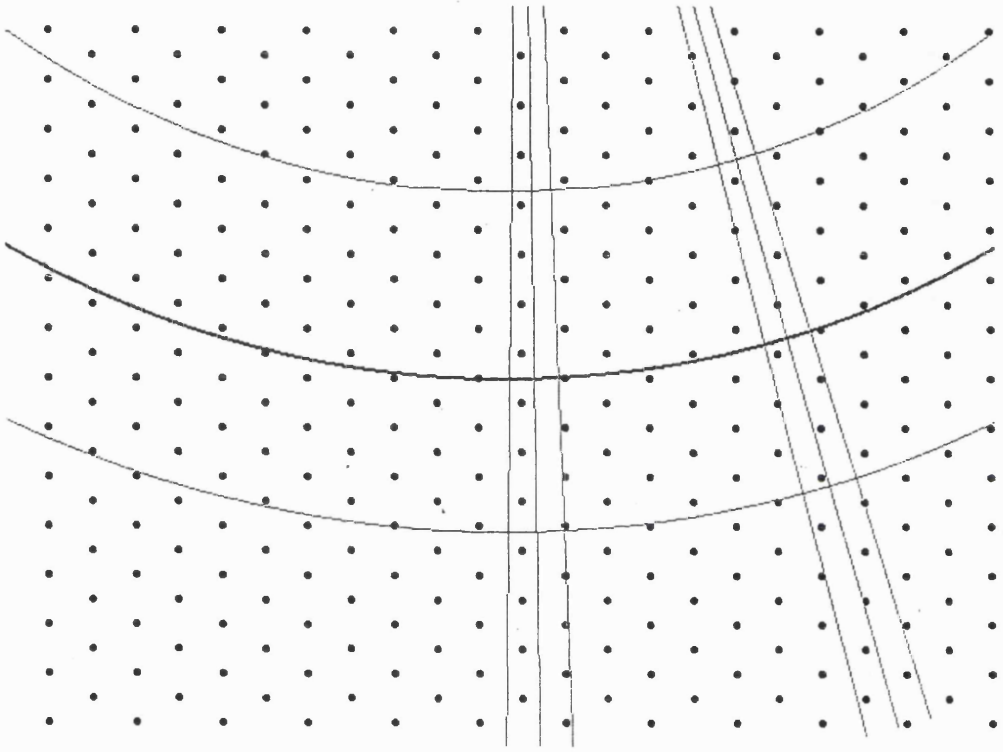

Figure 6.2: The variation of the number of lattice points lying within windows of constant finite width in both radius and phase angle.

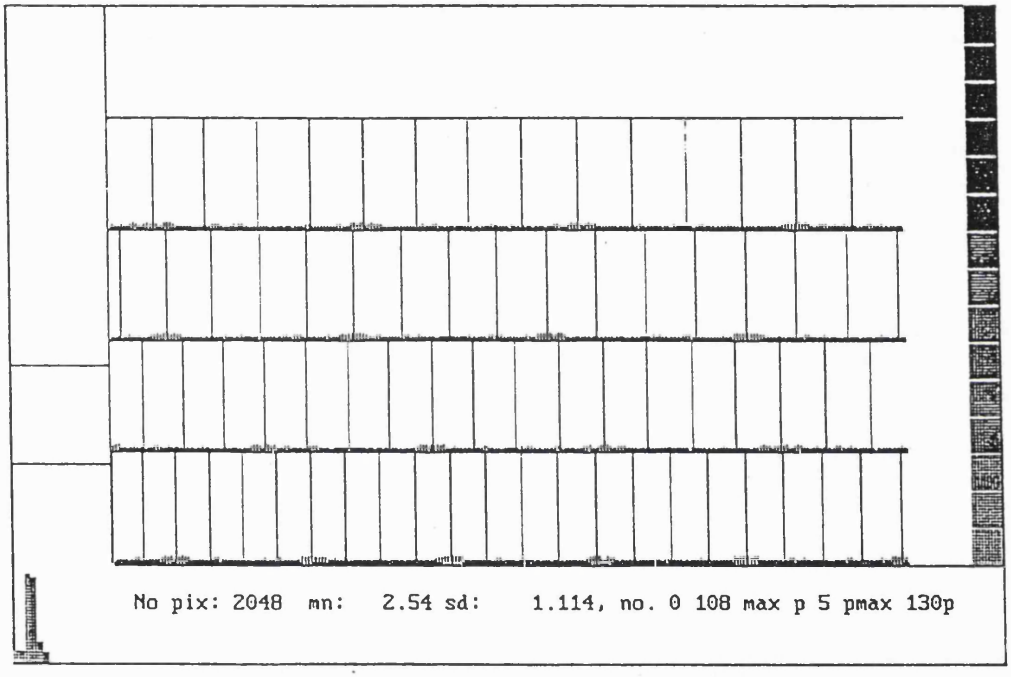

Figure 6.3: The fixed patterning produced when all the possible lattice points have been illuminated once and only once.
The vertical lines represent $s(i)$ for each of the pixels and the distribution on the bottom left corner represents the distribution in $s(i)$. There are 512 pixels represented in each of the horizontal lines. The mean and variance are quoted in the bottom panel together with the number of dead pixels, 108, the maximum value of $s(i)$, 5, and the number of pixels with that value, 130.

represents the baseline requirements for the Optical Monitor (OM) detector. Even though the pixels are of equal width in arc length, they behave effectively as though the width varies from pixel to pixel, i.e. they have a finite differential nonlinearity. The magnitude of the fixed patterning has a clearly defined cycle, becoming most prominent every 60° of ϕ. This occurs when a radial lies along one of the axes of the lattice, as along these lines, the separation of the states is at a minimum and so more points exist in a finite Δr and there are no points in the adjacent angle windows.

The intensity distribution of $s(i)$ varies between Poisson and Gaussian distributions, depending on average sensitivity, $\overline{s}$. The ratio of the standard deviation of s_i to $\overline{s}$ provides a useful measurement of the degree of fixed patterning and does not require *a priori* assumptions about the form of the distribution.

From the above description it can be seen that even in an ideal case, the ratio $\frac{\sigma}{\overline{s}}$ has seven degrees of freedom,

$$\frac{\sigma}{\overline{s}} = \frac{\sigma}{\overline{s}}(n_a, n_s, k, w_r, h', d, n_p) \quad , \tag{6.13}$$

which for the baseline configuration

$$\frac{\sigma}{\overline{s}}(3, 4, 2.1, 0.5, 384, 8, 2048) = 0.42 \quad . \tag{6.14}$$

The first three parameters in Equation 6.13 are defined by the pattern design while the last four are defined by the user and the electronics.

In this chapter, the fixed patterning is modelled assuming that all the electronic components behave ideally. Another model has been developed in which the performance of the readout is estimated for the presence of various effects such as noise and crosstalk. Results from this model are presented in Breeveld *et al.*, (1992b).

6.1 The Effects of Anode Design Parameters on Fixed Patterning

Even though the ratio $\frac{\sigma}{\overline{s}}$ is a useful measure of the degree of fixed patterning, it does not take into account the absolute limit set by $s(i) = 0$. Figure 6.4 shows the simulated variation of the ratio and $p(0)$, the measured probability of a pixel having zero sensitivity, i.e. a dead pixel, for variations of each of the three spiral parameters from the baseline specification described above. Also, as fixed patterning is produced by a combination of

allowable pairs of integers, the ratio $\frac{c}{s}$ will not be systematic over small ranges, indeed it could be described as "pathologically unsystematic". It is useful for a qualitative discussion or for describing gross variations but not for detailed predictions.

Increasing any of these parameters reduces the fixed patterning as the arc length is increased, i.e.

$$\Delta S \approx \frac{k(h')}{2}\Delta(\theta^2) \quad , \tag{6.15}$$

$$\approx 2k(h')\pi^2((n_a+n_s)^2-n_s^2) \quad , \tag{6.16}$$

$$\approx 2k(h')\pi^2(n_a^2+2n_an_s) \quad . \tag{6.17}$$

As described in Section 5.1.3 the radius of the largest r_{lim}, that can be drawn inside the equilateral triangle defined by the ADCs is given by

$$r_{lim} = \frac{x+y+z}{\sqrt{6}} \quad . \tag{6.18}$$

Therefore, a continuous spiral electrode has the constraint that

$$k(h')2\pi(n_a+n_s+\frac{1}{4}) < \frac{h'}{\sqrt{6}} \quad , \tag{6.19}$$

$$\Rightarrow k(h')(n_a+n_s+\frac{1}{4}) < 25 \quad , \tag{6.20}$$

where $h' = 384$. The $\frac{1}{4}$ term is included to allow for the finite width of the spiral arms.

Equation 6.20 shows that the options for improving the fixed patterning are limited. Figure 6.4 shows that for $k(384) = 2.1$, if the total number of arms is greater than 12, the magnitude of the fixed patterning increases rapidly. This is due to some parts of the simulated spirals having radii greater than r_{lim} and so the spiral is no longer continuous. A similar situation occurs when $k(384) > 3.5$ if all other parameters are set at their baseline levels.

6.2 The Effects of User Defined Parameters on Fixed Patterning

Figure 6.5 is similar to Figure 6.4 and shows the variation in fixed patterning for variation in the four user defined parameters. These four parameters h', w, d, n_p vary the number of lattice points included in each of the pixels.

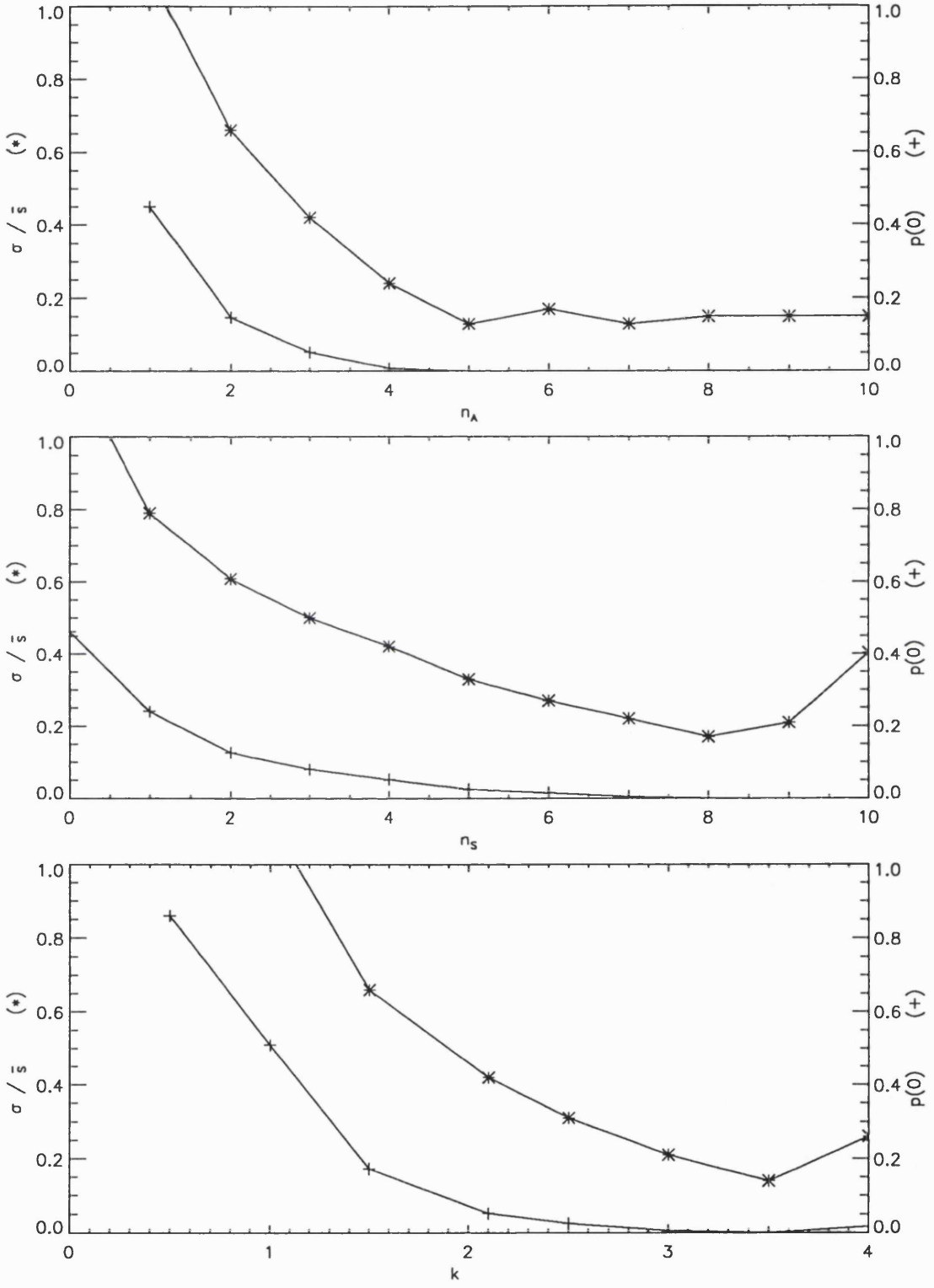

Figure 6.4: The effects of variation in the anode design parameters on fixed patterning. The asterisks represent $\frac{\sigma}{\bar{s}}$ and the crosses represent $p(0)$.

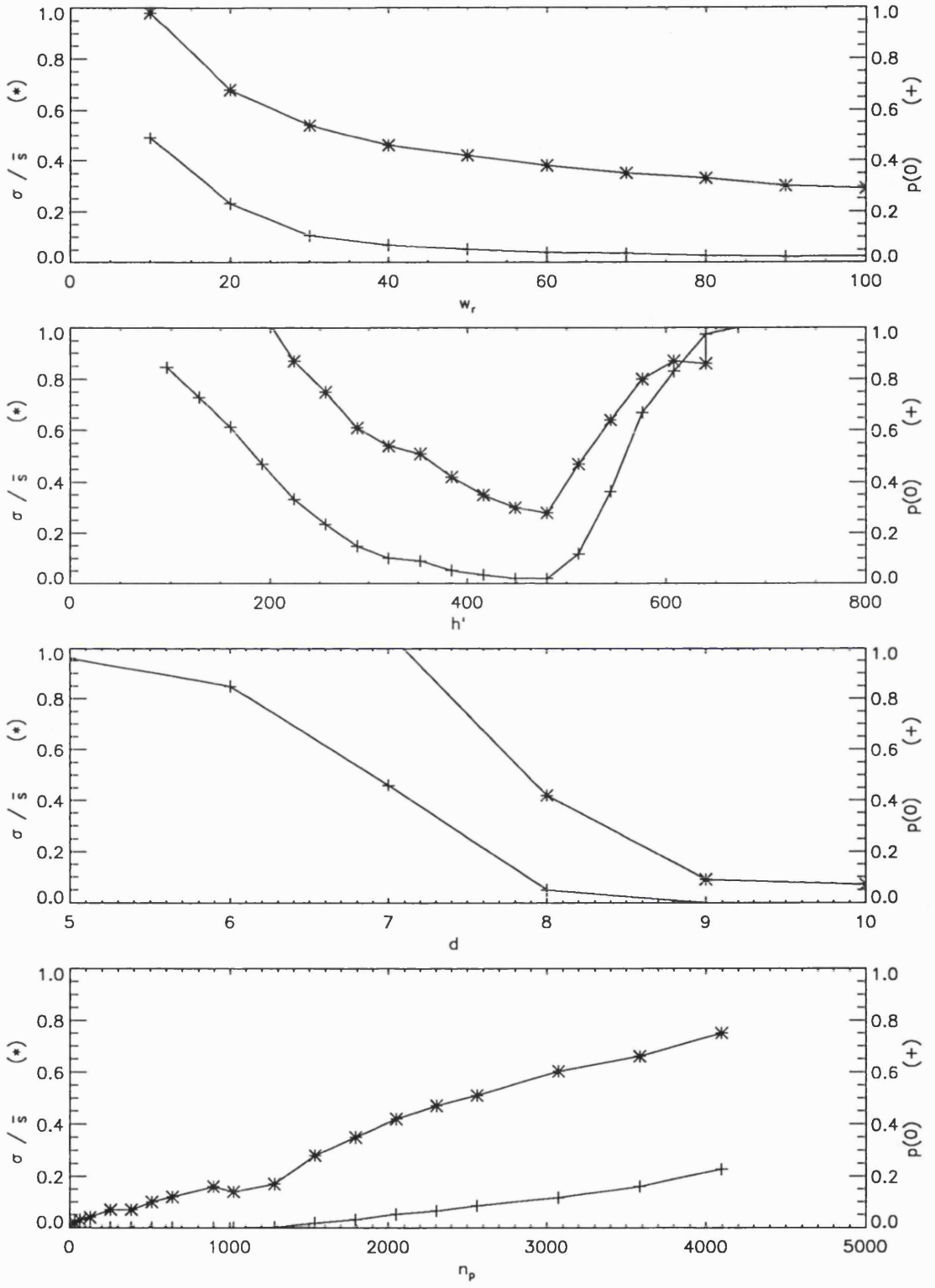

Figure 6.5: The effects of variation of user defined variables on fixed patterning.

It can be seen from the graphs that the most efficient way to reduce fixed patterning is to either reduce the number of pixels or increase the number of bits. In both cases there appears to be a point beyond which minimal gains will be made. If 10 bits are used the fixed patterning is comparable to that for 9 bits. Also, if the number of pixels is reduced fixed patterning does not reduce significantly below 1024 pixels. It is necessary to reduce the number of pixels to 8 to reduce $\frac{\sigma}{\bar{s}}$ to below 1%.

Increasing w_r increases the the number of states which are accepted as representing valid events, which increases $\bar{s}$. The graph in Figure 6.5 shows the width of the spiral arm cannot be set arbitrarily small but should be set as large as possible, bearing in mind the probability of ghosting.

The lattice points are hexagonally packed with constant spacing in all of the planes. This spacing is defined by the ADC digitization levels, which for an ideal ADC, are uniformly spaced. However, the size of the triangle containing all the possible lattice points varies with h', so the number of lattice points varies. Increasing h' therefore, increases the number of lattice points per unit angle, reducing the fixed patterning.

6.2.1 Pulse Height Related Vignetting.

Due to the finite number of digitization levels from an ADC, h' cannot be made arbitrarily large. As described in the previous section, for each value of h' there is a maximum radius, r_{lim}, for which a continuous curve can be drawn on the plane defined by three ADCs. The three points at which one of the three ADCs returns a zero value, lie on the circle with this radius. If we assume that the z ADC has returned 0, the coordinate of this point is $(\frac{h'}{2}, \frac{h'}{2}, 0)$, as the curve intercepts the xy plane halfway along the line $x+y = h'$.

For an 8 bit ADC, the maximum value for x, y and z is 255. Therefore, the maximum plane that can be addressed is $h' = 3 \times 255$ and the point (255,255,255) is the only point on this plane. Therefore, r_{lim} is at a minimum for $h' = 0$ and 765. From Figure 6.6 it can be seen that the plane on which r_{lim} is a maximum, is half way between the planes for which $r_{lim} = 0$, i.e. $h' = \frac{3}{2} \times 255$. Therefore,

$$r_{lim}(h') = \begin{cases} \frac{h'}{\sqrt{6}} & \text{if } h' \leq 382 \\ \frac{1}{\sqrt{6}}(765 - h') & \text{if } h' \geq 383 \end{cases} . \qquad (6.21)$$

This places a constraint on the maximum value of h' similar to those on k, n_a and n_s, discussed in the previous section. The maximum value of h' for which the spiral is continuous

is actually dependent on the three anode parameters, i.e. by Equation 6.19

$$k(h')2\pi(n_a + n_s + \frac{1}{4}) < r_{lim}(h') \quad , \tag{6.22}$$

inserting the values from the baseline configuration, maximum value of h' is given by

$$2.1\frac{h'}{384} \times 90 \approx \frac{1}{\sqrt{6}}(765 - h') \quad , \tag{6.23}$$

$$\Rightarrow h' \approx 500 \quad . \tag{6.24}$$

As pulse height increases beyond this level, the ADCs will be able to address smaller fractions of the spiral plane, i.e. the spiral will be vignetted. This effect can be seen in Figure 5.20 showing the hard limit on radius with pulse height and is demonstrated in Figure 6.5 by the rapid increase in the non-uniformity of s for $h' \geq 512$.

This effect will tend to filter out multiple, simultaneous events as these will usually be much larger than normal events. Very large events will only be addressable at small values of r_n and if these radii are significantly smaller than the radius of the first spiral arm, they will be effectively ignored. However, large events can also be incorrectly mapped into the active region of the normalized spiral plain, producing spurious events that will be accepted. It is thought that this is the cause of the extra noise apparent for large pulse heights in Figure 5.20. Therefore, extreme care must be taken in matching the PHD with the reference voltage when using fixed reference ADCs.

6.3 Fixed Reference ADCs

In conventional ADCs the reference voltage is fixed and the digital output is proportional to that fixed reference. Therefore, as the pulse heights vary, a series of planes is produced. After normalization with respect to h' (see Section 5.1.3), the areas of each of these planes are the same. Therefore, as the number of lattice points varies with h', data from lower planes will produce a larger lattice spacing in the normalized plane and data from higher planes will produce a smaller spacing.

If the lattice spacings are different, the states are not aligned and so there will be many more states in any finite area of the plane, reducing fixed patterning. Figure 6.7 is similar to Figure 6.3 but represents the effect of projecting many planes of different h' and constant lattice spacing into one plane. It is readily apparent that there are many more states in some areas of finite angular and radial width compared to Figure 6.3.

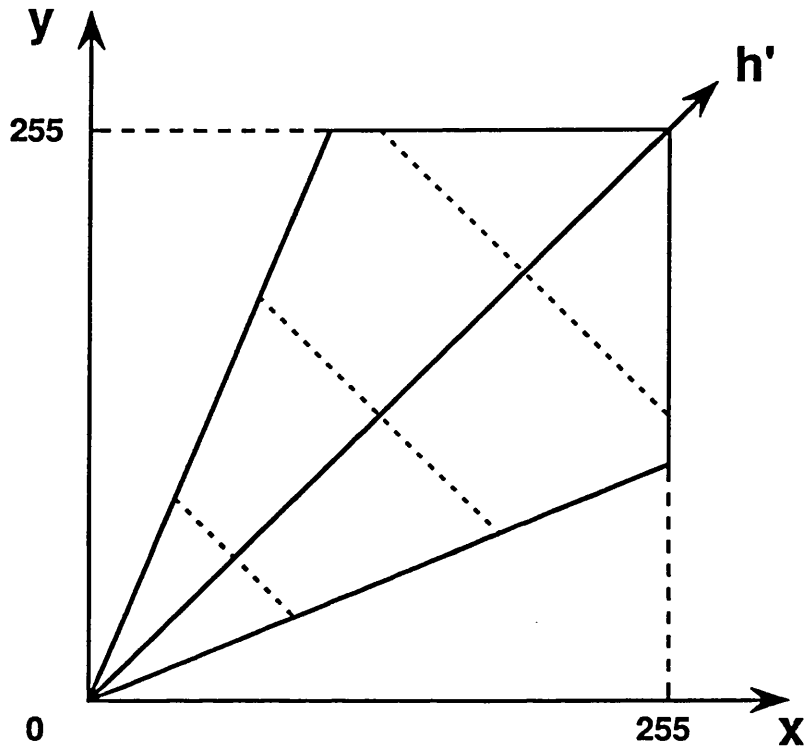

Figure 6.6: The variation of r_{lim} with h' for 8 bit ADCs.

The dotted lines normal to the h' vector represent the limiting diameters for a continuous circle at three pulse heights. The figure shows that below a certain pulse height, r_{lim} is determined by the anode design but above that level, r_{lim} is determined by the full scale digitization of the ADCs.

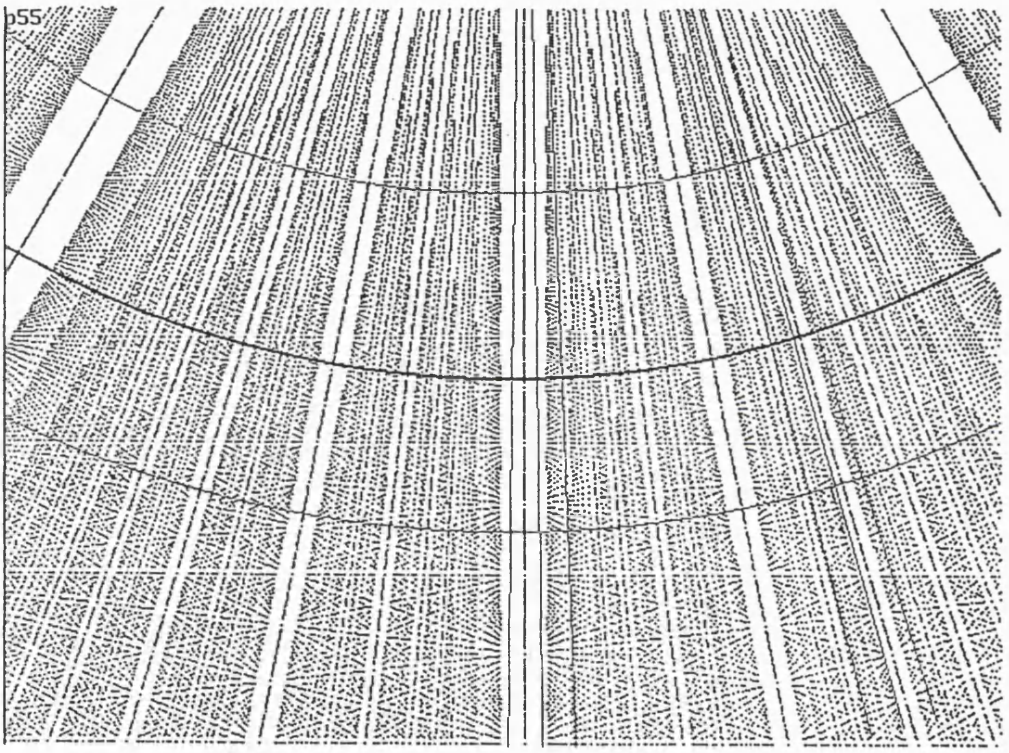

Figure 6.7: This diagram is similar to Figure 6.2 except that all of the lattice points from all of the pulse height planes have been projected into one plane.

However, even though the spacing varies the orientation of the lattice axes does not. The position along the axes vary for points from different planes, but the radial along which they lie does not. This gives rise to the variation of number of states with angle, which will produce variation in $s(i)$. So even though fixed patterning could be reduced in some areas, it is still a problem at precisely the same points that fixed patterning is most severe for data from a single plane.

Fixed reference ADCs do not digitize all events to the full dynamic range of the ADC. For example, an 8 bit ADC will only digitize an event with a pulse height of half the reference value to 7 bits. Given that even a well saturated MCP PHD has a saturation of the order of 50% and assuming that the PHD is Gaussian then there is a factor of 4 difference in the magnitude of the pulse height between $\pm 3\sigma$ and magnitude of the modal gain would be only approximately 60% of the $+3\sigma$ point. Therefore, a 9 bit ADC would be necessary to obtain the full 8 bit digitization at the modal gain without clipping the top half of the PHD.

Given that the gain will be depressed at high point source count rates, at least a 10 bit ADC is necessary to maintain the level of fixed patterning at that of the baseline configuration, as discussed in the previous section. Figure 6.8 shows an example of gain depression increasing the fixed patterning. The data was obtained with 9 bit Wilkinson ADCs. Data digitized at the full 9 bits would occupy the extreme right of the PHD display. As the PHD lies only in the left half of the display, the data has been digitized at less than 8 bits. The data at the lower count rate already shows severe variations in $s(i)$ but as the count rate increases the gain is depressed, leading to increased fixed patterning and almost total fragmentation of the image.

Figure 6.9 shows the results from a simulation of varying the number of bits digitization for a fixed reference ADC. The actual data was acquired with 14 bit Wilkinson ADCs, i.e. $d = 14$, and is also displayed. The other images are produced by the same data using only the d most significant bits of the original 14 bit data. The data has not been resampled into pixels of equal arc length but is the direct output as calculated by $S = \frac{k}{2}\theta^2$.

Each of the pixels in the image represents approximately 4 μm which is about half of the pixel width required by the OM. The SPAN used for these measurements has a diameter of 36 mm and contains 4 spiral arms. Only $\approx$ 3 arms lie in the 25 mm diameter of the MCPs. The OM requires an 18 mm square active area. Assuming that a pattern can be made with 4 spiral arms in this area, the fixed patterning for a given physical pixel

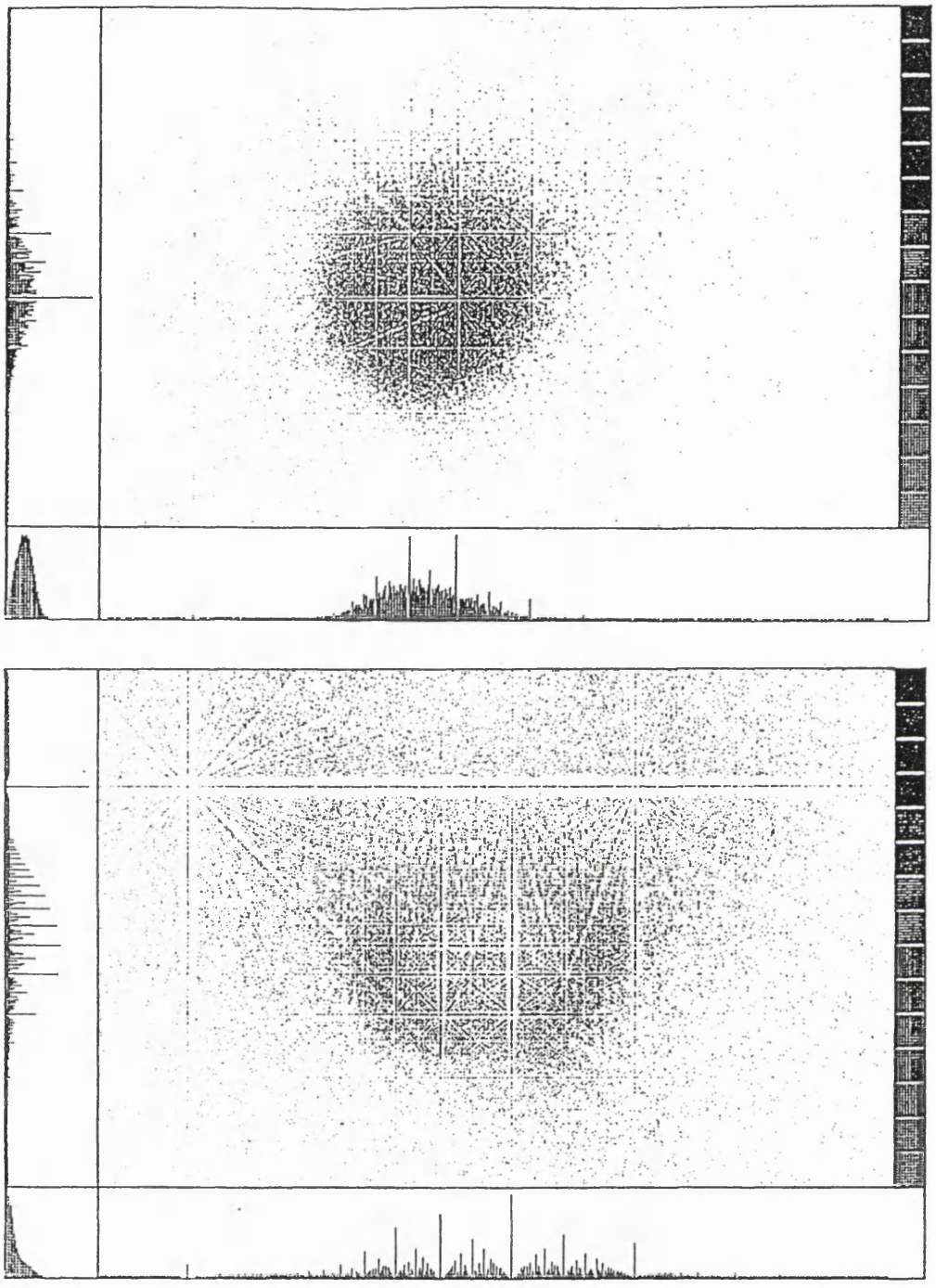

Figure 6.8: The variation of fixed patterning with gain depression for fixed reference ADCs. Both figures are images of a 180 μm diameter pinhole. The count rates were 250 Hz and 1 kHz for the top image and bottom images, respectively.

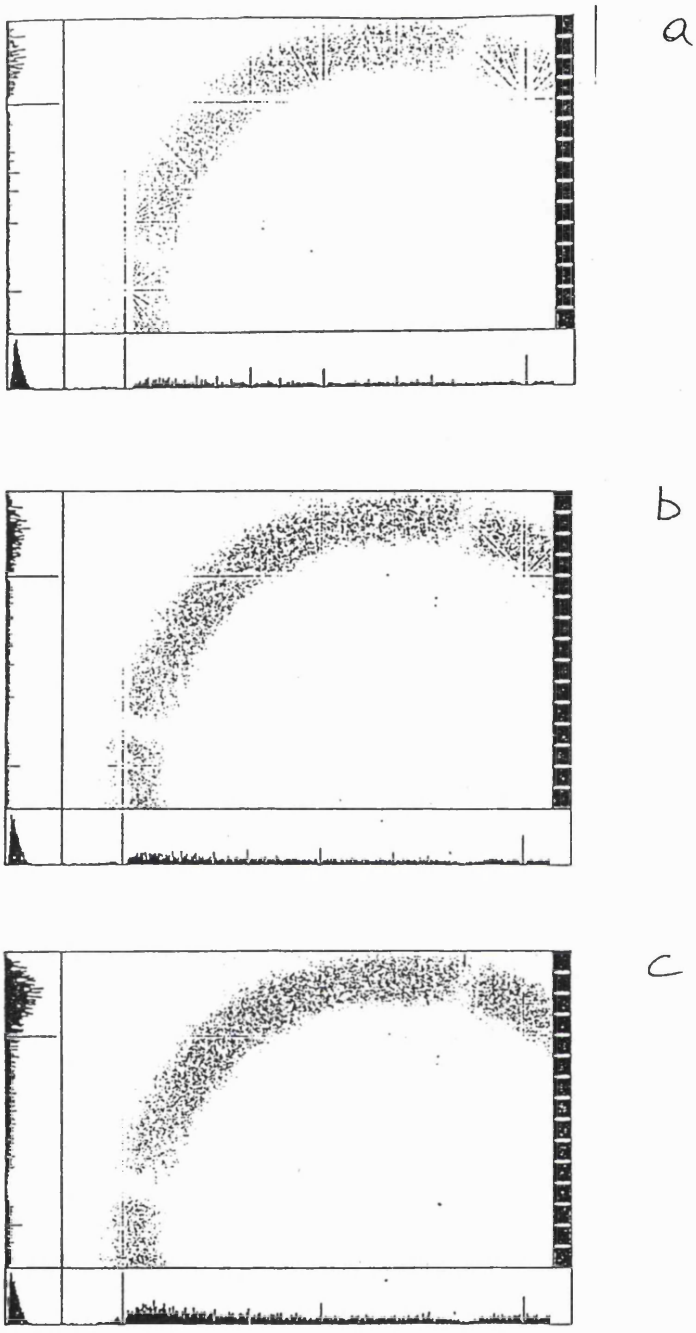

Figure 6.9: Simulation of the variation of fixed patterning with varying levels of digitization for fixed reference ADCs.

Figures a, b, c, d and e represent simulations of 8, 9, 10, 11 and 12 bit digitization, respectively. Figure f is the original data obtained with 14 bit digitization. Figures d, e and f are on the next page. The fixed patterning in these figures is due to the sampling of the discrete two dimensional image by the screen pixels. There are 360 screen pixels across the vertical axis in the central window and the image is of a 1 mm diameter ring.

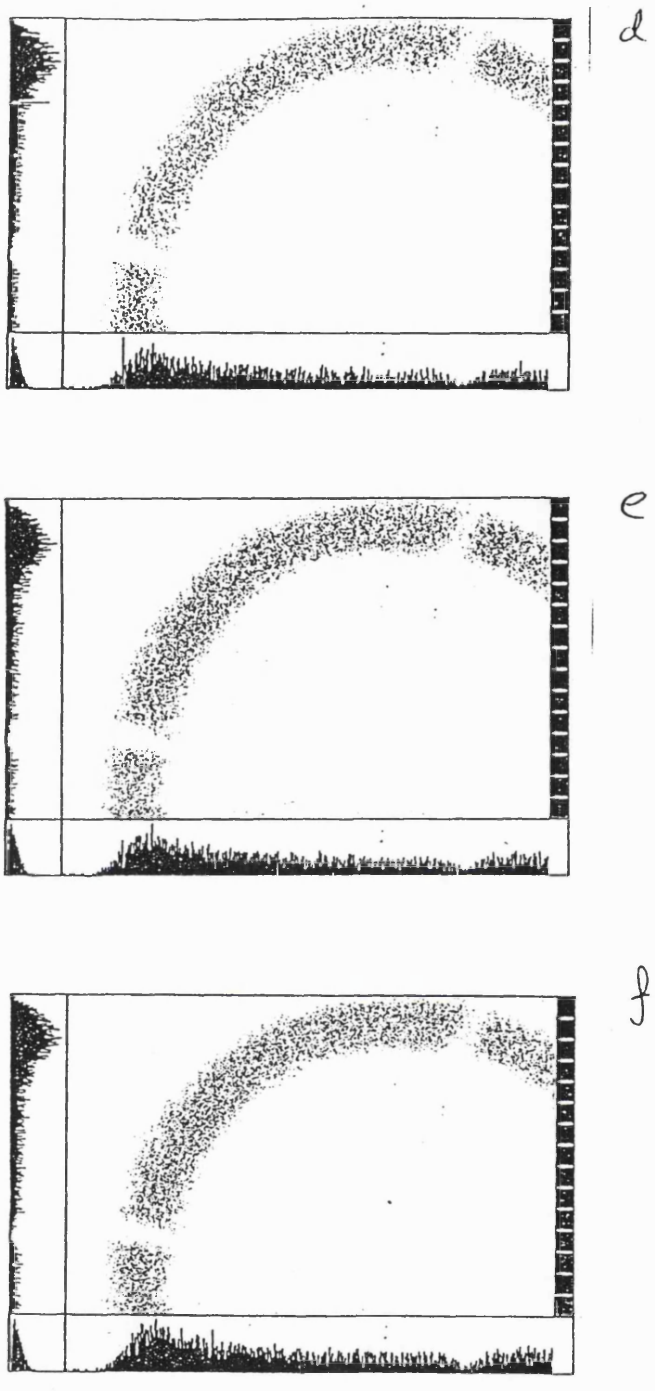

Figure 6.9 continued.

size should be reduced by a factor of two. Therefore, the fixed patterning displayed in Figures 6.9 and 6.10 is from 2 to 4 times worse than that for an anode designed specifically for the OM. These images should therefore be regarded as worse case scenarios.

The images demonstrate that although the fixed patterning varies in severity, its position remains constant. They also show that 12 bits are necessary to achieve a fixed patterning level similar to the original data.

6.4 Ratiometric ADCs

In ratiometric ADCs, the reference is driven by a varying voltage. The digital output is directly proportional to the ratio of the magnitude of the input to the magnitude of the varying reference signal at the time of conversion.

Ratiometric ADCs offer a potential major advantage over fixed reference ADCs for fixed patterning. If the reference is driven with the sum of x, y and z, then the data will be immediately normalized with respect to pulse height and all the data will be projected into one pulse height plane. This has four important consequences.

1. Fixed reference ADCs require that the normalization is carried out after digitization by a division by the sum of the three ADCs. At present, this is carried out in software as a floating point operation. In an actual realtime system used on the satellite, this division would most probably be carried out as a integer division. This would require either an Arithmetic Logic Unit (ALU) or look-up-table (LUT). In either case, it represents extra electronics that are not required for ratiometric ADCs. Also normalization by division with digitized values is itself, a source of fixed patterning (Koike & Hasegawa, 1988, Geesman *et al.*, 1991 and Phillips, 1992).

2. The number of lattice points will be constant for events with differing pulse heights, so fixed patterning should be independent of the PHD and count rate.

3. The data can be normalized into a plane of the user's choice by multiplying the reference by a constant factor. For example, consider an 8 bit ADC, if

$$Q_{ref} = Q_x + Q_y + Q_z \quad , \tag{6.25}$$

$$\Rightarrow x + y + z = 255 \quad , \tag{6.26}$$

however, if

$$Q_{ref} = \frac{2}{3}(Q_x + Q_y + Q_z) \quad , \tag{6.27}$$

$$\Rightarrow x + y + z = 382 \quad , \tag{6.28}$$

where Q_x is the output of the preamp for the x electrode etc. and Q_{ref} is the signal driving the reference. As discussed in Section 6.2, selecting a plane with a higher h' will reduce the fixed patterning. The limit on h' will be defined by the SNR on Q_{ref} or r_{lim}.

4. If we substitute h' into the expressions for the coordinate rotation, Equations 5.4 and 5.5, we obtain

$$x' = \frac{1}{\sqrt{2}}(h' - (x + 2y)) \quad , \tag{6.29}$$

$$y' = \frac{1}{\sqrt{6}}(3x - h') \quad . \tag{6.30}$$

As ratiometric ADCs normalize with respect to pulse height, h' is a constant. Therefore, for an ideal spiral, only 2 ratiometric ADCs are necessary per axis.

Figure 6.10 is similar to Figure 6.9 except that a ratiometric ADC has been simulated with the original 14 bit data. In each case the normalized plane is

$$h' = \frac{3}{2}(2^d - 1) \quad . \tag{6.31}$$

From the diagram it can be seen that a 10 bit ADC is needed to overcome fixed patterning. This represents a 2 bit improvement over the fixed reference ADC, which corresponds to the approximate expected pulse height dynamic range of 4.

The speed at which they can operate is limited by the analog bandwidth of the reference bandwidth. The one dimensional SPAN detector for SOHO is evaluating Micro Power Systems (1989) MP7683 8 bit, flash ADCs in the ratiometric mode (Breeveld *et al.*, 1992). These are low power chips, ≈100 mW, and space qualified. SOHO's count rate requirement is 100 kHz, approximately half that of the OM. At this stage it appears that these ADCs will meet the SOHO requirements but not the OM's.

Ratiometric, 8 bit ADCs are available with higher reference analog bandwidths, for example TRW's (1991) TDC 1058 is rated at 5 MHz, and Analog Devices' (1988) AD9002 at 10 MHz. These chips have higher power consumption, 600 mW and 750 mW, respectively and it is not known if they are space qualified but they do demonstrate that ratiometric

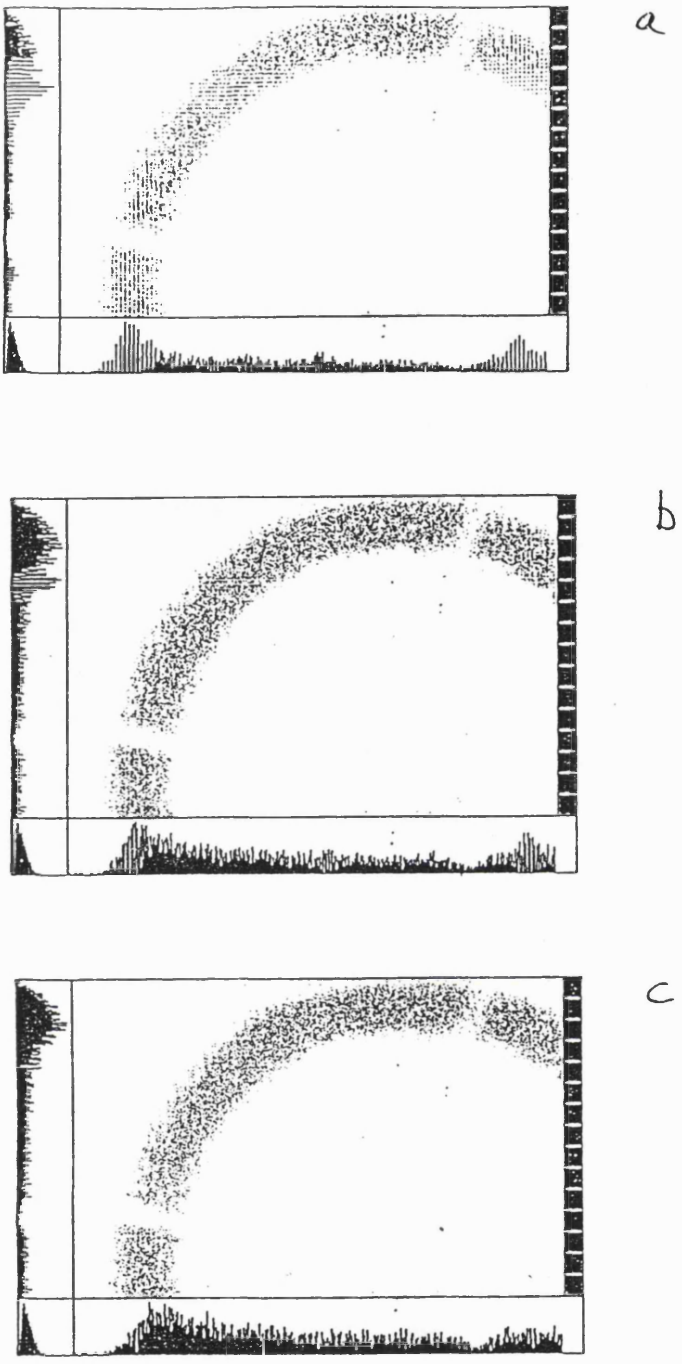

Figure 6.10: Simulation of fixed patterning with varying levels of digitization with ratiometric ADCs.

The figures are similar to those displayed in Figure 6.9. Figures a, b and c have 8, 9 and 10 bit digitization, respectively.

ADCs can meet the OM specification of 200 kHz, random. At present it appears that 8 bits is the maximum for a fast, ratiometric capable ADC. However, the MP7683 and AD9002 have overflow signals so it is possible to combine two chips to obtain 9 bit digitization.

If the reference input is not linear with respect to pulse height, it will produce variations in radius with respect to pulse height. It may be possible to overcome this variation in a similar manner as described in Section 5.2.2. However, if only 2 ADCs are used, the three dimensional xyz data has effectively been projected into the xy plane and is therefore susceptible to the pulse height proportional shift of the spiral origin, as discussed in Section 5.1.3. Figure 6.11 shows a simulation of nonlinear behaviour of the reference.

Using two ratiometric ADCs, this or any other pulse height related phenomenon cannot be corrected. If pulse height related effects are significant and need to be corrected, a third ADC is required. This ADC has to have a fixed reference in order to provide pulse height information from the sum of Q_x, Q_y and Q_z. In the software the pulse height has always been divided into 256 channels which has always been sufficient to correct any pulse height related effects. Therefore the third ADC requires a maximum of 8 bits.

6.5 Aliasing

In MCP based detectors, the image is hexagonally sampled by the MCP pores in the front plate. This produces a resolution limit of approximately twice the pore spacing, i.e. the Nyquist Limit. Any variation in the image with a spatial frequency higher than this limit will cause aliasing.

A gap between two MCPs allows the charge cloud from the first MCP to spread out and excite several pores in the back plate. Therefore, the charge cloud distribution from the front plate is sufficiently sampled by the rear plate so that aliasing between the MCPs does not occur.

Carter (1991a) has presented results of aliasing between 11 μm pixels and pores with a 15 μm spacing, see Figure 6.12. As the SPAN detector is capable of resolving the pores in the front plate and the dimensions are similar, aliasing could be a problem. However, the degree of modulation of the fringes is dependent on the PSF of the centroiding of the charge cloud. A finite PSF acts as a filter, reducing the power in the higher spatial frequencies of an image and therefore, the power aliased into the Nyquist frequency range.

Figures 6.13 and 6.14 show results of a computer model of fringing between pores

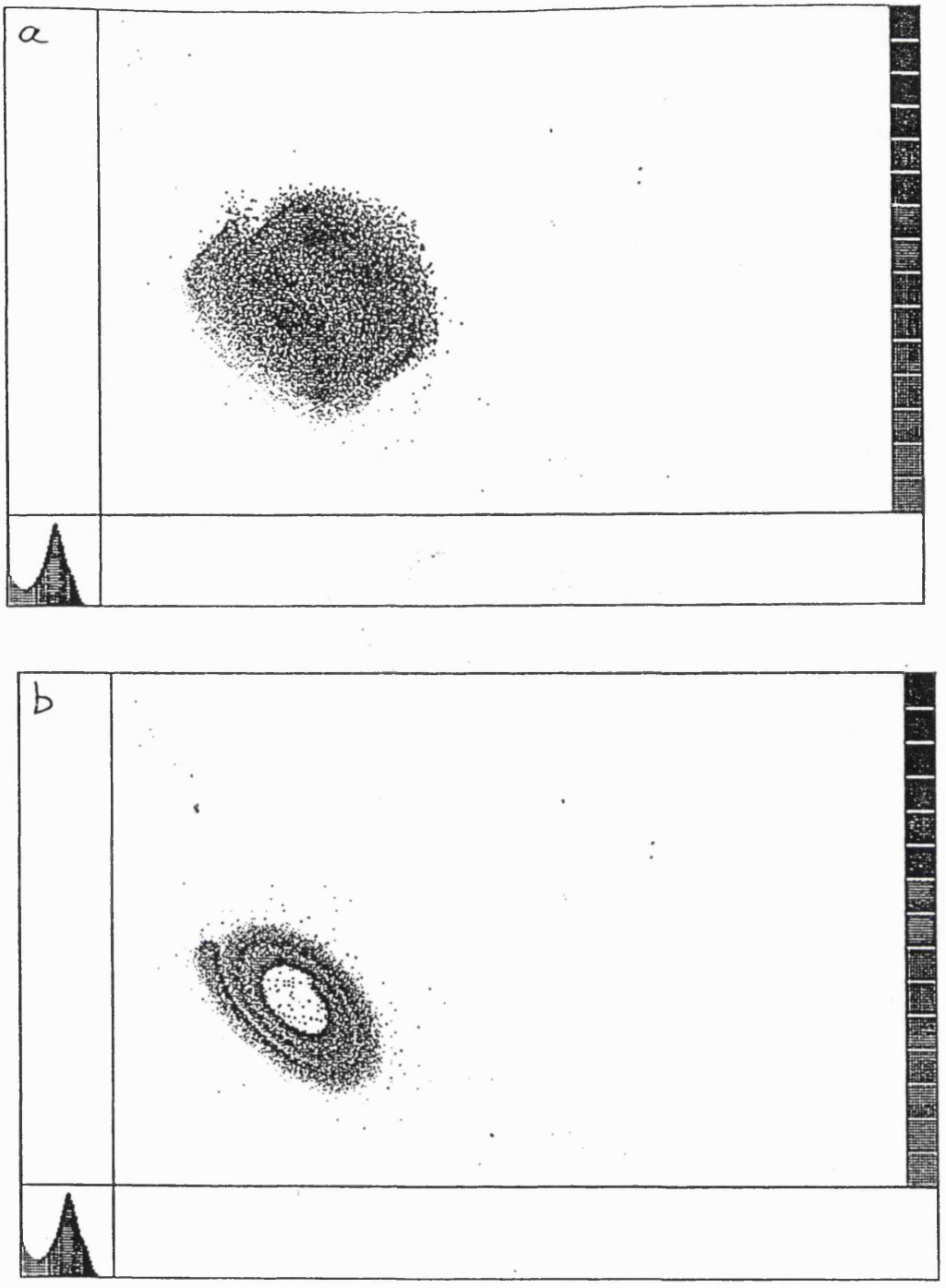

Figure 6.11: The shift of the spiral origin with pulse height in a system using ratiometric ADCs.

Figure a shows the origin shift that occurs when the reference has a nonlinearity with respect to pulse height of 5%. Figure b shows the correct case. The greyscale in images are proportional to the pulse height of each event and correspond to the colours displayed in the PHD.

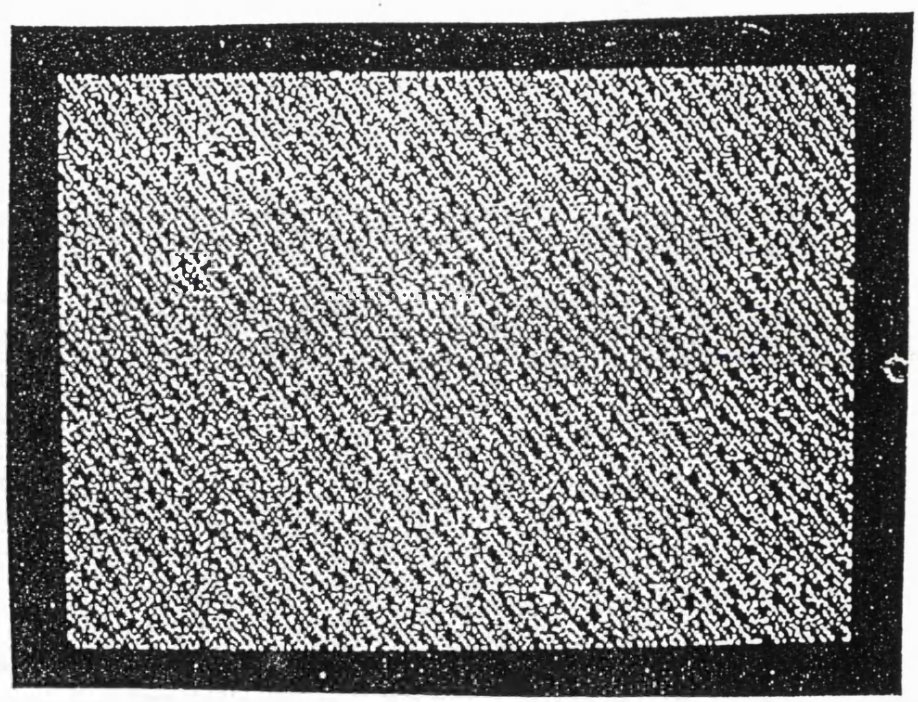

Figure 6.12: Aliasing between 11 μm pixels and pores on 15 μm centres as measured with a MIC detector.
From Carter, (1991a). The centroiding PSF in this image was 4 μm.

and a 9 μm pixel array (Smith, 1991). The fringing has been evaluated for the MCP we use at present, 15 μm pore spacing, and an MCP with approximately half the spacing, 8 μm, at a variety of centroiding PSFs. The figures show a 32 by 32 pore region of the MCP with the pixel grid inclined at an angle of 5° to the MCP array, for both pore spacings. These figures clearly demonstrate that larger PSFs reduce the intensity modulation of the fringes.

The only way to eliminate aliasing between the pores and the pixels is to have pixels either over twice or less than half the width of the pore spacing. However, it is possible that a broad enough centroiding PSF could reduce the intensity modulation of the fringes to acceptable levels. The results of the model suggest that SPAN should not have serious intensity modulation due to the aliasing for MCPs with either 15 or 8 μm pore spacing.

6.6 Chicken Wire Distortion

Several authors have reported a hexagonal modulation of intensity in flat field images in MCP detectors (e.g. Siegmund *et al.*, 1989, Barstow *et al.*, 1990 & Vallerga *et al.*, 1991). As shown in Figure 6.15 this produces an image that looks similar to a chicken wire fence.

This distortion is not due to digitization, but is thought to be caused by variations in the behaviour of the MCP at the boundaries of the multi-fibre bundles. However, this distortion would produce a variation in pixel sensitivity similar to fixed patterning. Vallerga *et al.* (1991) report that the distortion is not always present in flat fields and suggest that it might be due to the preconditioning of the plate.

Chicken wire distortion has not been observed with SPAN, however, we have not carried out many long flat fields over a large portion of the MCP. As the distortion depends on the two dimensional structure of the MCP and SPAN encodes the two dimensions independently, this problem, if present, cannot be overcome during the encoding. It could only be corrected in the final image.

6.7 Possible Techniques for Reducing Fixed Patterning

Geesman *et al.* (1991) proposed a method for reducing fixed patterning due to normalization with respect to pulse height for digitized data by tuning the shape of the PHD.

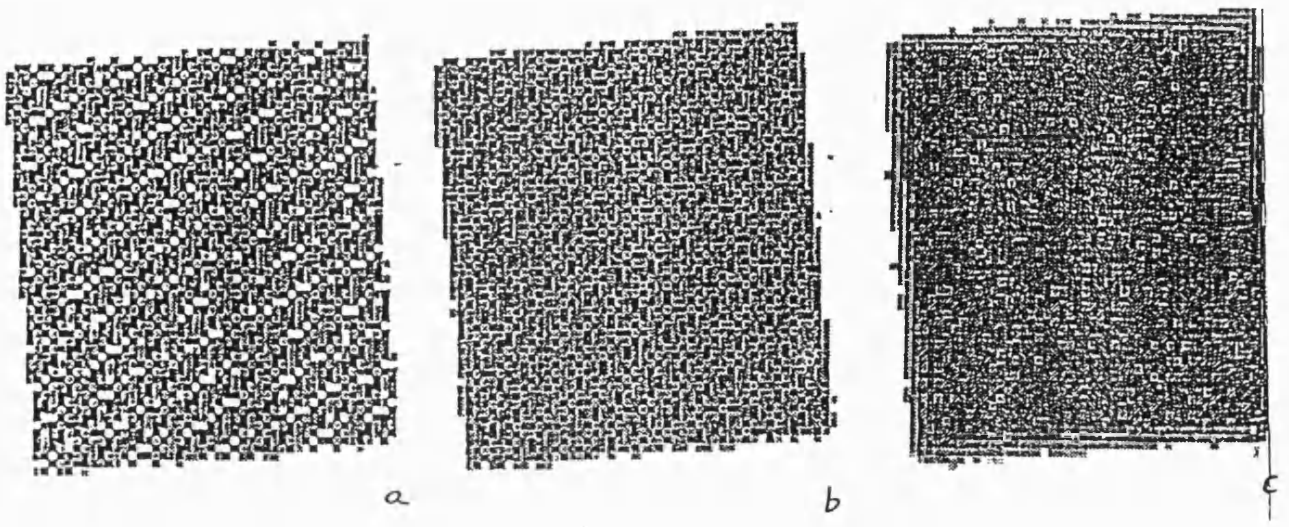

Figure 6.13: Simulation of aliasing between 9μm pixels and pores on 15 μm centres. From Smith (1991). Figure a represents a FWHM centroiding PSF of 2.5 μm, Figure b has 6 μm, comparable to the MIC PSF and Figure c has a FWHM of 18 μm, similar to SPAN.

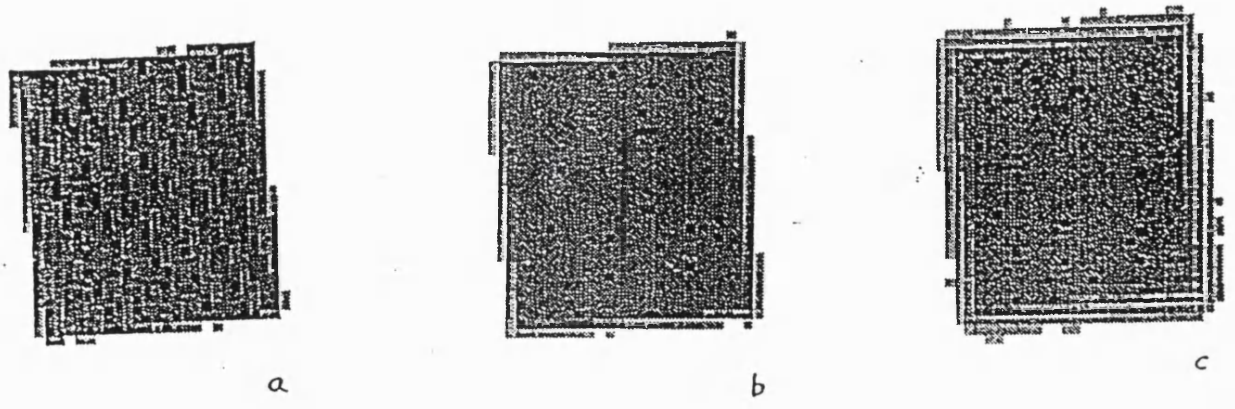

Figure 6.14: Simulation of aliasing between 9μm pixels and pores on 8 μm centres. From Smith (1991). Figures a, b and c have PSFs corresponding to those in Figure 6.13.

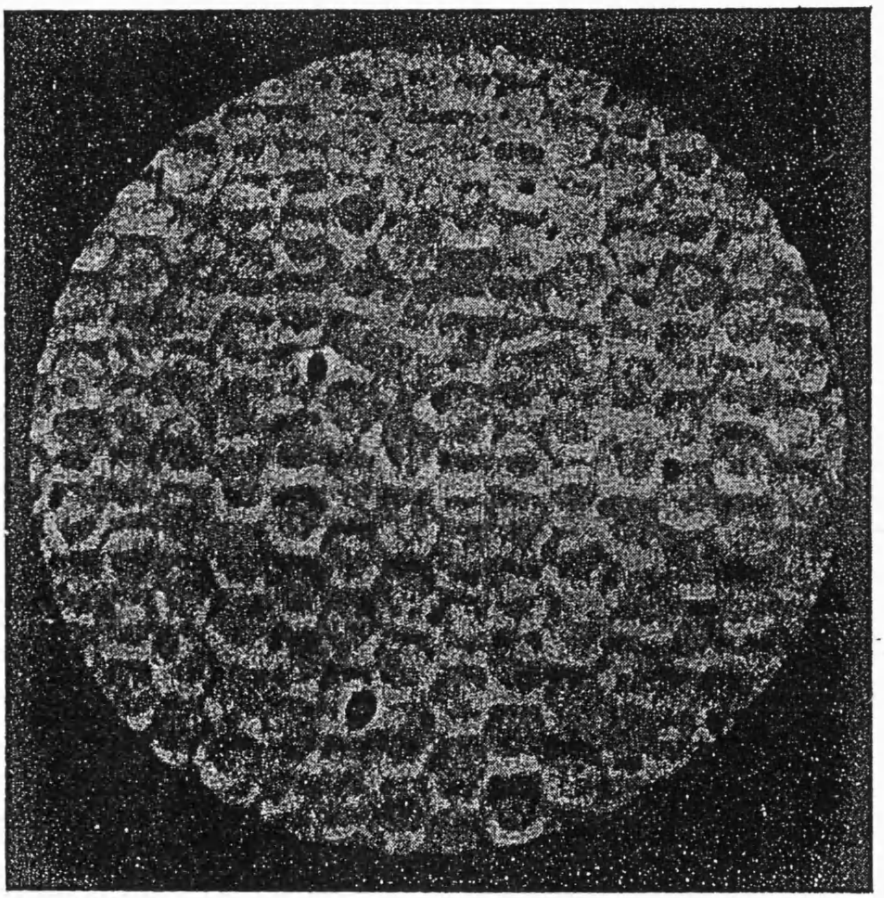

Figure 6.15: An example of chicken wire distortion.

Philips (1992) studied the effects of this method for actual fixed patterning obtained from backgammon readout, used in a gas proportional detector for the Bent Crystal Spectrometer on the Solar-A (later Yokoh) spacecraft. He found that when fixed patterning was present, this method does reduce the amplitude of the largest spikes but simultaneously increases the amplitude of the smaller deviations from the mean, i.e. it redistributes the power in the "spiketrum". The method requires that the PHD is constant and symmetric and is only applicable to normalization with respect to pulse height. Therefore, the technique is not applicable to situations in which gain depression will occur or for the fixed patterning due to the calculation of ϕ for SPAN.

Koike & Hasegawa (1988) have proposed a technique to reduce fixed patterning which is applicable to any situation in which digital division takes place. The success and accuracy of this technique has been studied analytically by Phillips (1992). The two digitized inputs are combined with n bit random numbers such that the n least significant bits of the two new numbers are random. The efficiency of this technique depends on the width of the PHD for use in normalization so it will be degraded by gain depression, but it does not require a constant or symmetrical PHD. It is applicable to the calculation of ϕ but does not take into account the nonlinear nature of atan or the effect of resampling of the hexagonally packed lattice into segments of equal arc length.

Figures 6.16 and 6.17 show an example of the effectiveness of a technique similar to the second method. Figure 6.16 shows the results of a model of SPAN showing the severe fixed patterning produced by this digitization when combined with 2048 pixels. This result is independent of the actual physical length of the SPAN pattern. The data was simulated using an actual PHD and simulated digitization ratiometric ADCs, so the fixed patterning is not due to normalization with respect to pulse height. Figure 6.17 was obtained under the same conditions as Figure 6.16 but with 3 noise bits added to both inputs. Addition of more than 3 bits does not significantly reduce the fixed patterning beyond this level.

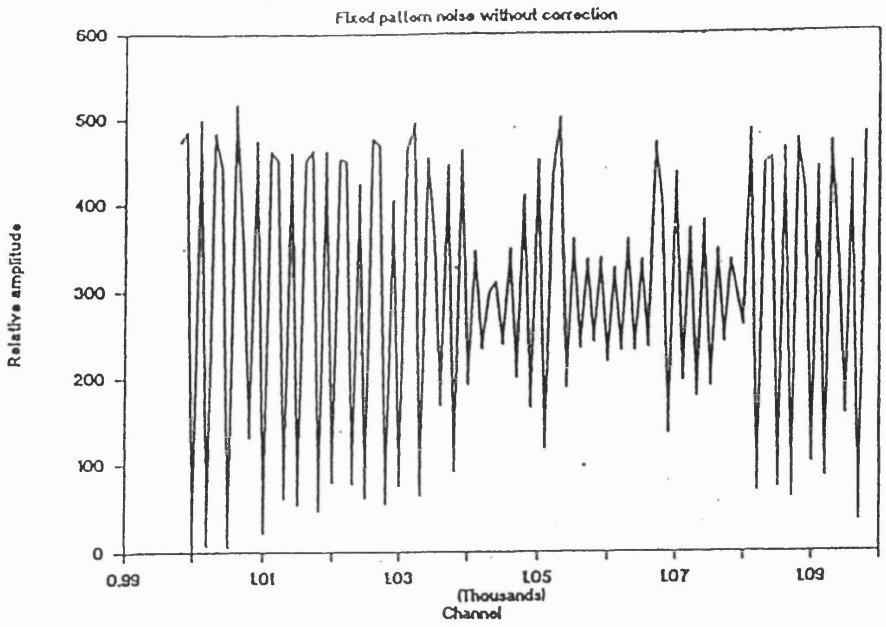

Figure 6.16: Simulated fixed patterning due to the interaction between 8 bit digitized inputs and the 2048 pixels. The image represents a flat field over 5% of the detector width located at the approximate centre.

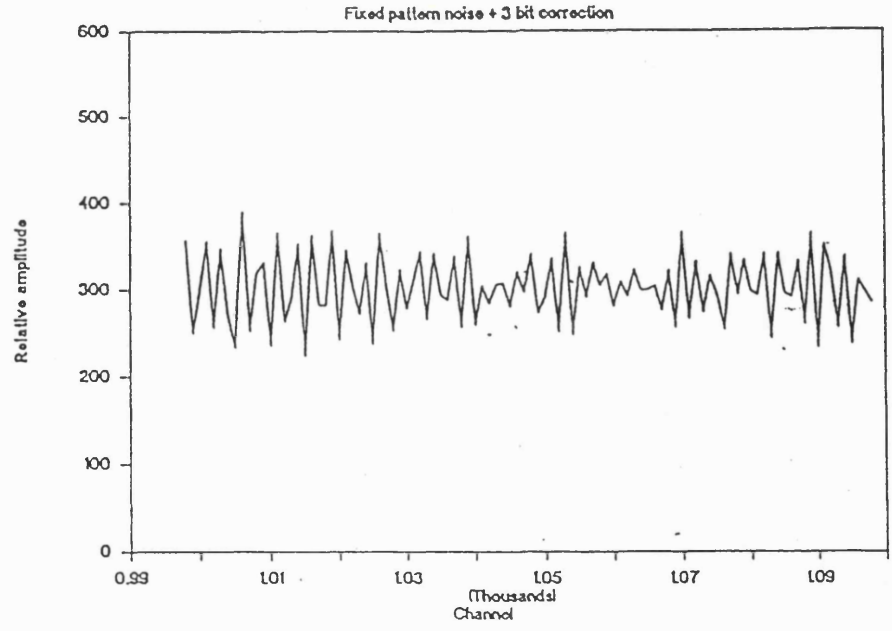

Figure 6.17: Simulated fixed patterning with 3 random, extension bits on each of the inputs. The image was generated under the same conditions as Figure 6.16 but with 11 bit inputs, of which the 3 least significant bits are random.

Chapter 7

The Long Range Interaction Between Pores

7.1 Introduction

7.1.1 Adjacency

The count rate performance of MCPs has been analysed extensively in terms of the deadtime due to the recharge of the wall after the channel has fired. MCPs have been analysed variously as paralysable (Nieschmidt *et al.*, 1982, Nicoli, 1985, Cho & Morris, 1988, Cho, 1989, Fraser *et al.*, 1991b and Sharma & Walker, 1990, 1992) and non-paralysable detectors (Sharma & Walker, 1989, 1992). The properties of paralysable and non-paralysable detectors are discussed in Section 1.3.1.

In detectors containing two or more MCPs in the gain stage, the magnitude of the gain depression at a given count rate is proportional to area of the region illuminated while the sustainable count rate is inversely proportional to the area (Cho & Morris, 1988, Pearson *et al.*, 1988, Cho, 1989, Nartallo Garcia, 1990 and Fraser *et al.*, 1991b), see Figure 7.1. This strongly suggests that there is some interaction between adjacent pores and that the recharging of the active pores is dependent on their number. This effect has been called "adjacency" (Sharma & Walker, 1989).

Adjacency effects are not present in single MCPs, for either straight or curved channels, (Cho, 1989 and Fraser *et al.*, 1991b). Statistical deadtime analysis by Cho (1989) showed that each of the illuminated channels of a single C plate could be treated as an

independent paralysable detector, similar to a CEM. However, when carrying out deadtime analysis of multi-stage MCP detectors, he found the illuminated area had to be treated as a single detector with the time constant being approximately linearly proportional to the number of channels illuminated.

Sharma & Walker (1989, 1990, 1992) have developed a two dimensional statistical deadtime analysis to take into account the effects adjacency. They postulate a spatio-temporal deadtime in which a group of firing channels induces a deadtime effect of arbitrary spatial extent in surrounding pores.

Fraser *et al.* (1991b) have carried out an extensive review of variation of gain with count rate. They model the recharge of the channel after firing as an exponential recovery from 0, i.e. the pore has been completely discharged during the electron cascade, to the low count rate gain with a time constant τ such that

$$\tau = k\tau_{MCP} \quad , \tag{7.1}$$

where k embodies the unknown properties of the recharge mechanism and τ_{MCP} represents the characteristic time constant of the MCP, i.e.

$$\tau_{MCP} = R_{ch}C_{ch} \quad , \tag{7.2}$$

$$= R_{MCP}C_{MCP} \quad , \tag{7.3}$$

where R_{ch} and R_{MCP} are the resistances of an individual channel and the entire MCP, respectively. The C variables with the corresponding subscripts are the associated capacitances. They have also measured the ratio of the current in output pulse current to the channel strip current, i.e. $\frac{I_p}{I_s}$.

In single plate detectors the value of k and $\frac{I_p}{I_s}$ are approximately constant irrespective of the area illuminated and have values of ≈ 5 and 0.48, respectively. Figure 7.2 shows the variation of the current ratio with count rate for illuminated areas with different sizes for a chevron pair with a rear plate resistance of ≈ 2 GΩ. It clearly shows that the current ratio and the best fit value for k depend strongly on the illuminated area and is a clear example of adjacency. The limit in k as the area approaches zero is approximately the value for a single plate but $\frac{I_p}{I_s}$ exceeds unity. Fraser *et al.* (1992) have determined that the current ratio, in multi-stage detectors, is an approximately linear function of the number of illuminated channels over 6 orders of magnitude.

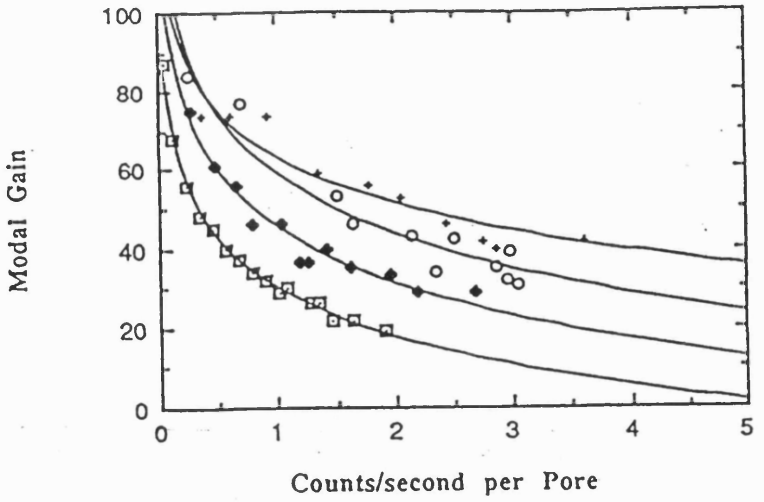

Figure 7.1: The effects of adjacency on gain depression. The magnitude of Gain depression is inversely proportional to the area illuminated.
This data was acquired using the same MCPs as were used during the experiments described in this chapter. The squares, diamonds, circles and crosses represent data acquired with pinhole images with approximate FWHM diameters of 1.5 mm, 600, 225 and 180 μm, respectively. From Nartallo Garcia (1990).

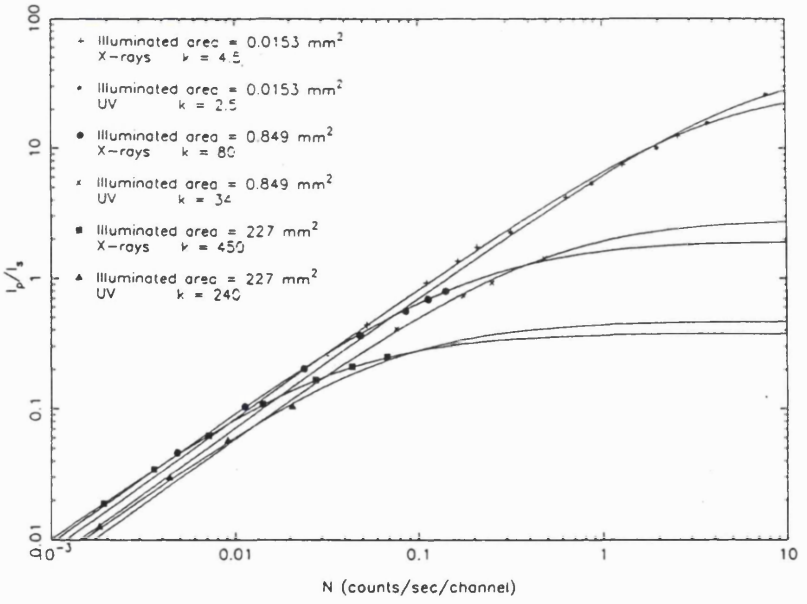

Figure 7.2: The variation of pulse current to strip current with count rate and size of illuminated area.
The symbols represent the measured points and the curves represent values calculated with the corresponding value of k shown in legend in the top left corner. From Fraser *et al.* (1991b).

7.1.2 Effects of Gain Depression

The most obvious, and probably the most important effect of gain depression is that as count rate per pore increases, the pulse heights of more of the events will lie below the discriminator of the measuring electronics and those events will not be detected. Therefore, the count rate linearity will be degraded progressively. In extreme cases, the gain may be depressed so much that almost all of the PHD lies below the discriminator effectively paralysing the pore.

Reduced gain also lowers the signal to noise ratio for charge measurement electronics, reducing the spatial resolution of charge division readout devices, e.g. Figure 1.20.

As discussed in Chapter 5, SPAN has pulse height related position shifts. The most serious problem is that gain depression will move a significant proportion of the PHD into the nonlinear region of the radius/pulse height function and so it will be impossible to reliably assign events to a spiral arm. Either the presence of ghosts must be tolerated or the discriminator level must be raised, aggravating the problem of photometric nonlinearity.

Other readouts also suffer from the variation of gain. As discussed in Section 3.1, variation of charge cloud size affects the positional linearity of the MIC and WSA detectors. Position shifts of approximately 50 μm have been observed for delay lines (Freidman *et al.*, 1990) over the range in gain of $1-4 \times 10^7\ e^-$. Count rate dependent shifts of approximately 10 to 20 μm have been observed with the HRI (Zombeck & Fraser, 1991). Gain depression can cause incorrect positional coding in the PAPA detector, producing spurious images (Sams, 1991).

If active pores have a long range effect on their quiescent neighbours it could pose a serious problem for the high speed operation of MCP based detectors. An intense point source might paralyse a pore and reduce the resolution for any images in the area surrounding it. Statistical analysis of data obtained with a MIC detector by Sharma (1991) indicates that an event in a single channel causes a spatio-temporal deadtime which extends into the group of 12 surrounding pores and causes them to remain inactive for 0.1 ms.

In an extreme case, a point source could paralyse a significant proportion of the MCP. The situation would be much worse for an image containing many bright features or a spectrum with many close lines. Sharma (1991) has also modelled the effect that a large "deadradius" would have on speckle images. He finds that once the deadradius becomes comparable to the size of the speckle, the speckle peak maybe obscured in the image. Similar

effects were seen experimentally with an MCP based image intensifier.

Gain related position shifts could also be produced in the region near a bright source. Friedman *et al.* (1990), using a two dimensional, transmission line, delay line readout, have observed shifts of position of up to 40 μm at distances of 400 μm from a bright source. At larger distances, smaller shifts were noticed. Gain depression with a long range component is a possible mechanism as their readout does have gain dependent positional shifts of this scale.

In this chapter, the results of direct measurements of the effect of active pores on quiescent, neighbouring channels are presented. These results were measured with a two dimensional imaging detector and some of these results were the first such measurements presented in the literature. Possible mechanisms are discussed in Section 7.7.

7.2 Experimental Procedure

In order to investigate the long range effect of active pores on quiescent pores we superimposed an intense source, concentrated on a small region, over a diffuse source covering the majority of the active area of the MCP. A schematic of the experimental setup is shown in Figure 7.3. The diffuse background illumination samples the gain in the quiescent pores of the MCP. Provided that the interval between the arrival of these sampling events at each individual pore is many times longer than the recharge time constant, i.e. many seconds between events, the diffuse illumination will not cause gain depression.

The diffuse source was produced by illuminating a 50 μm thick Al mask with 5.9 KeV X-rays from an Fe^{55} source placed approximately 2 cm away. The Al mask is not completely opaque to X-rays at this energy and transmits approximately 4% of the incident flux. The mask was placed 0.1 mm from the open face of the front MCP of a chevron pair. The X-rays produced a count rate of approximately 500 Hz spread over most of the 25 mm active diameter of the MCP. In the central region of the MCP this corresponds to an event rate of 2.5 $Hz.mm^{-2}$ or less than 2 $counts.pore^{-1}.hour^{-1}$.

The intense count rate was produced by illuminating the MCP through a 100 μm pinhole, in the centre of the Al mask, with UV light from a Hg lamp placed about 2 m away. The UV lamp had a fused silica envelope, therefore the MCP was illuminated mainly by light from the 253.7 nm Hg line. The intensity of the UV radiation was varied by moving the lamp with respect to the MCP.

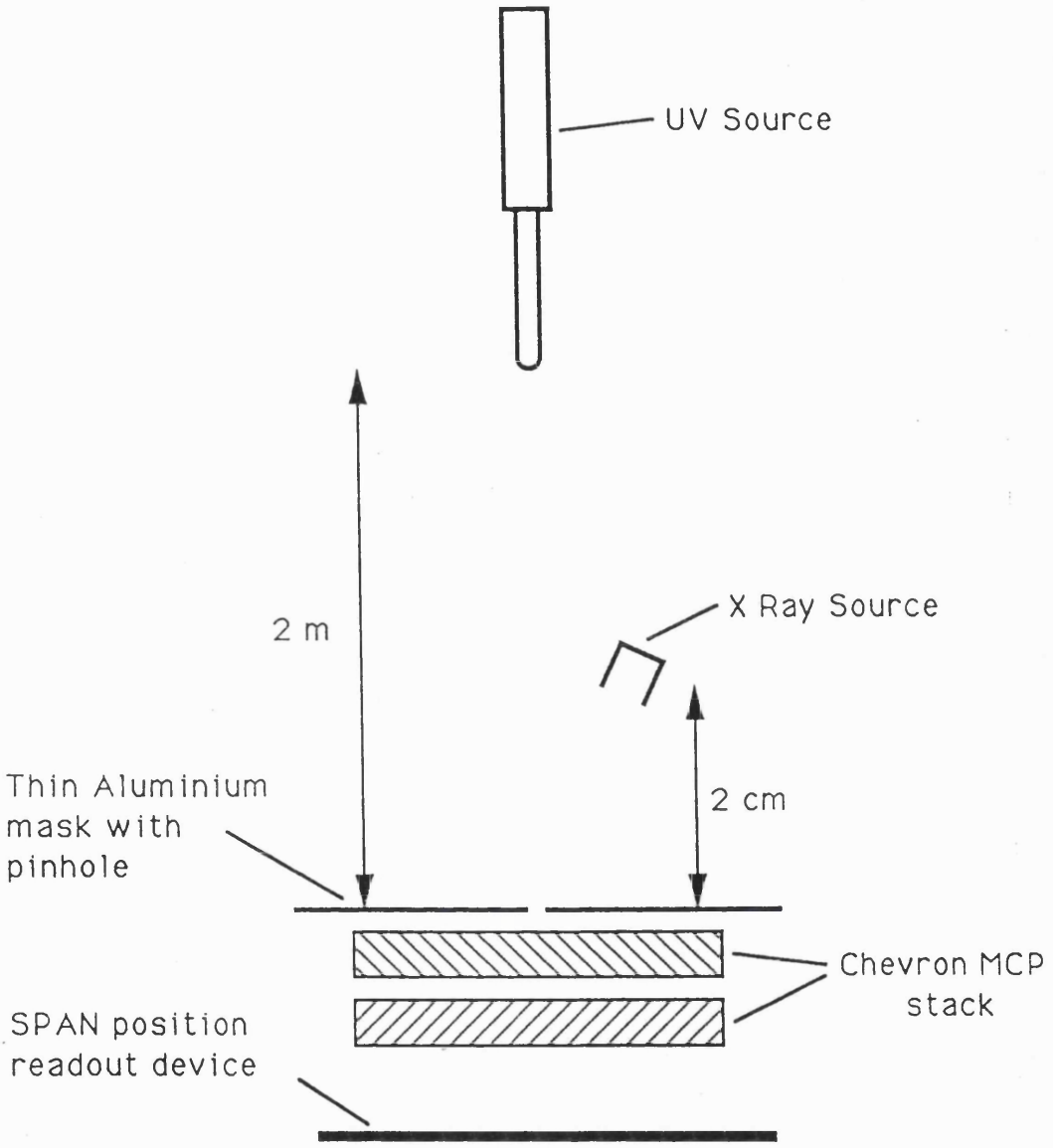

Figure 7.3: The Experimental Arrangement.

The X-Ray source provides a diffuse source of events, approximately 2.5 $Hz.mm^{-1}$ over most of the face of the MCP, while the Hg lamp provides an intense source illuminating the pinhole.

It is worth emphasising that this arrangement enabled the intensities of the sampling events and those causing gain depression to be independently varied. It allowed the quiescent gain in the region to be measured immediately before or after intense point source illumination and so provided a control. This was deemed to be a very important aspect in the design of the experiment as there was no *a priori* knowledge of the scale length over which the interaction between pores would act and only vague assumptions about the manner in which it would manifest itself. It also allowed the removal of any variation in the gain across the face of the MCP that was already present.

As adjacency appears as a count rate related phenomenon, one of the criteria chosen for deciding that any long range effect was actually caused by interaction between channels, was that the magnitude of effect should be dependent on the intense point source count rate. If the diffuse and point source intensities are coupled, they will vary together and any effects caused by increased intensity of sampling events could mistakenly be assumed to be due to the interaction between channels.

7.2.1 MCP Configuration

The MCP stack consisted of two, 36 mm diameter, 80:1 length to diameter ratio, Phillips plates with 12.5 μm pores on 15 μm centres and a measured resistance R_{MCP} = 640 MΩ. The capacitance of the MCPs has been calculated using the method described by Fraser *et al.* (1991b), as C_{MCP} = 15 pF, therefore $\tau_{MCP} \approx$ 10 ms. The MCPs have an open area ratio of 63% with $\approx$ 5100 pores.mm^{-2}. The plates had a bias angle of 13° and were arranged as a chevron pair with a 190 μm inter-plate gap. The voltage across this gap was held at 0 V. The MCP-anode gap was defined by three 6 mm diameter spacers separated by 120°. Therefore, both the front and the back of the MCP are open to vacuum. During all of the experiments described in this chapter, the anode gap and the applied voltage were held constant at 4.7 mm and 400 V, respectively.

The MCPs had been baked for 6 days at temperatures ranging from 200° to 240° C and scrubbed, extracting $\sim 3 \times 10^{-8}$ C.s^{-1}.cm^{-2} for 5.5×10^4 s. They have been cycled from vacuum to air on many occasions. Immediately prior to the experiment the MCPs were held at a pressure of 10^{-6} Torr for a week and were kept at this pressure throughout the experiment. The vacuum pump was an oil diffusion pump without a cold trap.

7.2.2 Readout and Electronics

The readout device was the two dimensional version of SPAN. The position co-ordinates were used to assign the event to one of 64 annuli of equal area, centred on the pinhole. All events lying outside of these annuli were discarded. Pulse height was determined from the sum of the charge measured on the six SPAN electrodes and was used to construct 256 channel PHDs for each annulus.

The electronics chain for each channel consisted of a charge-integrating preamp, shaping amp and 14 bit Wilkinson ADC. With Wilkinson ADCs, conversion time depends on the size of the digital output code for each event. The maximum conversion time of the ADCs at full 14 bit digitization is $\sim$ 37 μs giving a 10% coincidence loss at 2.7 kHz. In practice, the amplitude of the events is such that they are digitized to only approximately half of the full ADC range. The time constant on the shaping amp was 2 μs. Even allowing for a decay time of 10 time constants, the dominant contribution to the deadtime was the ADC conversion time.

7.2.3 Software

The software used was the same as that described in Section 5.6. For each of the measurements, 1 million events were acquired with x,y co-ordinates and pulse height being determined for every point. After the acquisition was complete the image was divided into 64 annuli of equal area, centred on the position of peak intensity of the pinhole. Constant area annuli were chosen to keep the number of events per annulus approximately equal. Pulse height distributions (PHDs) were obtained for each annulus.

Saving each event's position and pulse height on the hard disk placed a severe constraint on the number of events that could be acquired. The hard disk only had a capacity of 60 MB and each event required 22 bytes of storage. This effectively limited the total number of events to about 1 million. Also, as no selection was made on which events were stored during acquisition, these events were distributed over the full active diameter of the MCP. This limited the number of counts in each PHD to $\sim$ 300, which was insufficient for good statistics.

7.3 The Spatial Extent of Gain Depression

Measurements were carried out without UV illumination to provide a control, two measurements at a moderate UV count rate to test repeatability and one at a higher UV count rate. The UV fluxes used were 2700, 2900 and 5900 Hz.mm^{-2} corresponding to event rates of approximately 0.53, 0.57 and 1.2 Hz.pore^{-1}, respectively. The voltage across the chevron pair, V_c, for the three measurements was constant at 3.2 kV. The measurements have been described previously by Edgar *et al.* (1992a).

Figure 7.4 shows the mean gain, $\overline{G(r)}$, for annuli with middle points at radius r mm and areas of 0.54 mm^2. Curve "a" represents the situation in which the pinhole is not illuminated by UV photons and shows the intrinsic variation of MCP gain, independent of gain depression. The other three curves show the effect of gain depression combined with this intrinsic variation. Even so, the effects of gain depression are obvious at distances of up to 1.4 mm.

Figure 7.5 shows relative mean gain per annulus, $\overline{G'(r)}$ for the three cases when the pinhole is illuminated with UV radiation, normalized with respect to the intrinsic gain variation. It clearly demonstrates that gain depression is significant over a large distance scale with respect to the MCP pore size, i.e. at least 1.5 mm, which is 100 pores away from the centre of the pinhole and 1.5 times the length of the pore. The area within this radius contains over 1.5% of the total number of MCP pores. The significant increase in the magnitude of the gain depression with higher count rate is also apparent.

In Figure 7.6 the region up to a radius of 1.5 mm, has been resampled with annuli of a smaller area, 0.12 mm^2. The count rates for these annuli are shown in Figure 7.7 and the PHDs from selected annuli in this region are shown in Figure 7.8.

The difference in behaviour of the gain in the region of the graphs in Figure 7.6 with radius < 0.5 mm is due to the presence of UV photon events within those annuli. Figure 7.7 shows the excess counts present at these radii. As the UV photons have only a low energy compared to the X-rays, 5 eV compared to 5.9 KeV, UV events have a lower gain than the X-ray events. This is demonstrated in curve "a" in Figure 7.8 in which there are an excess of events below energy channel 80. The UV events will also be subject to gain depression producing even lower gain events. The occurrence of a significant number of UV events within an annulus will produce an anomalously low average gain. Therefore, meaningful measurements of the long range effects of gain depression can only be made in

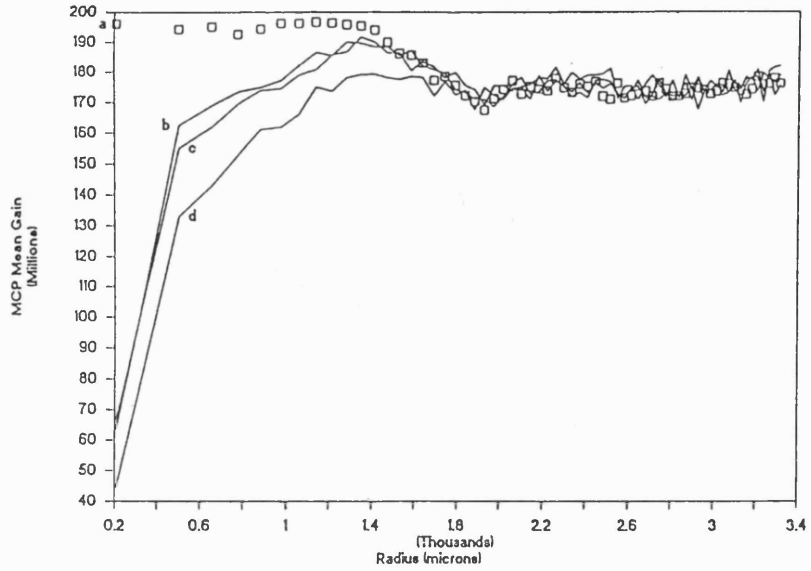

Figure 7.4: Mean MCP gain for each annulus, $\overline{G(r)}$.

The squares for curve **a** correspond to the midpoints of the annuli. Each annulus has an area of 0.54 mm^2. Curve **a** represents the quiescent state of the MCP, being illuminated only by the diffuse X-ray source. Curves **b**, **c** and **d** represent UV fluxes of 2700, 2900 and 5900 Hz.mm^{-2}, respectively.

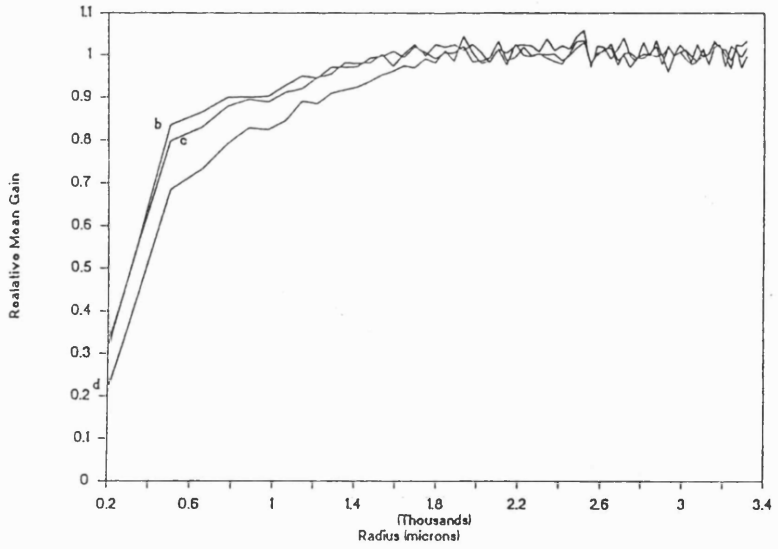

Figure 7.5: Relative mean gain versus annuli radius, $\overline{G'(r)}$.

Curves **b**, **c** and **d** are the same as in Figure 7.4 but have been normalized with respect to curve **a** of that figure.

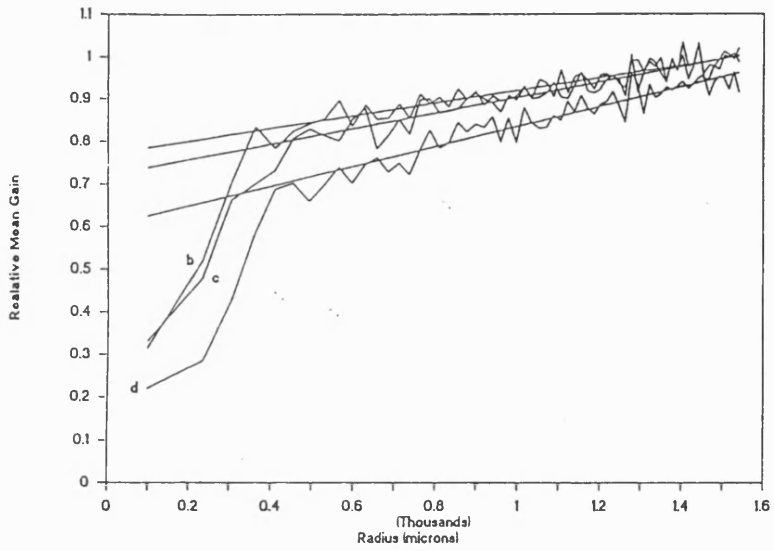

Figure 7.6: $\overline{G'(r)}$ for radii up to 1.5 mm.

All curves are the same as for Figure 7.5 but the data has been resampled with smaller annuli of area 0.12 mm^2. The scatter of the data points is representative of the errors associated with the mean. The linear regression fits to the lines are also shown.

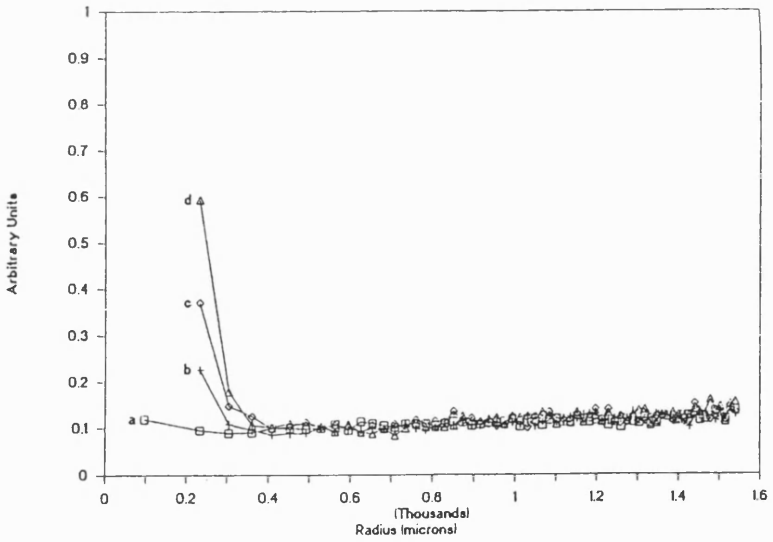

Figure 7.7: Normalized count rates per annulus for the curves in Figure 7.6.

Note the count rate excess below a radii of 0.5 mm due to UV events and that above this radius the three count rates are all within the scatter. The slight increase in the count rate with radius is probably due to the oblique illumination of the MCP.

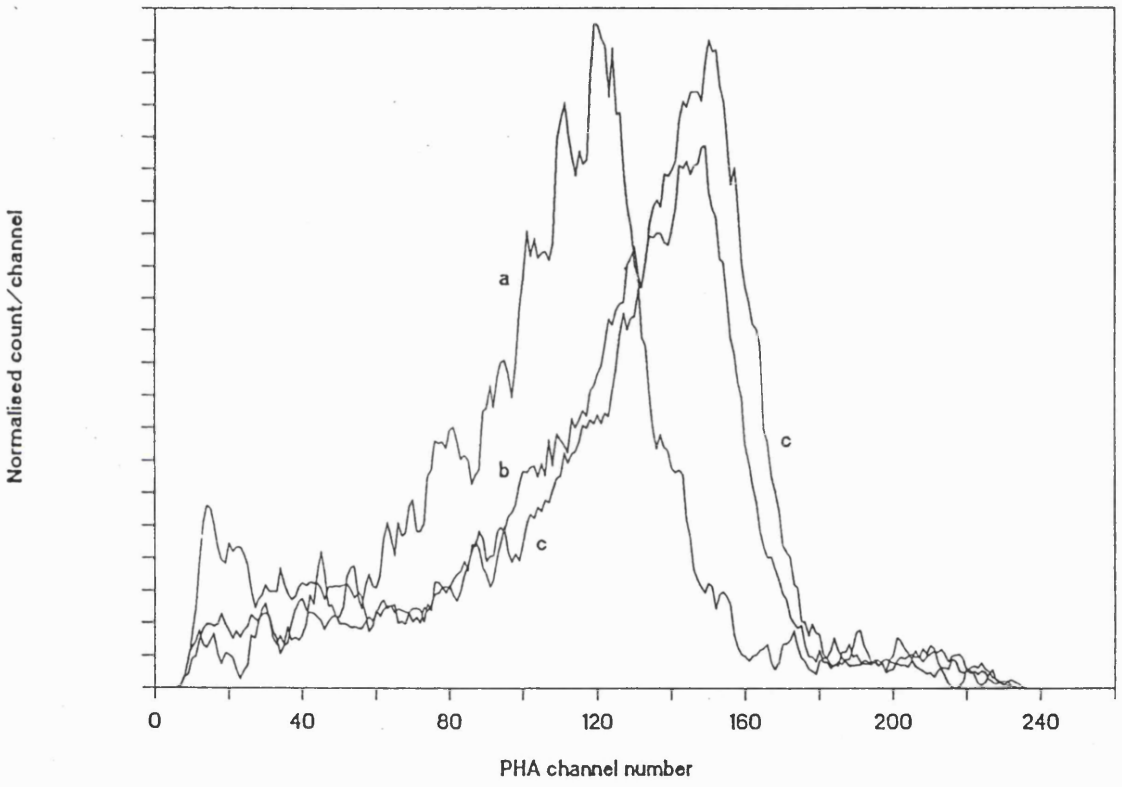

Figure 7.8: Pulse Height Distributions at selected radii.

Curves **a**, **b** and **c** are the pulse height distributions at radii of 0.230, 0.56 and 1.07 mm, respectively. Curves **b** and **c** are the sum of the annulus at that radius and its neighbours. Note the shift in modal gain with radius. Also note the excess of events below channel 80 in curve **a**, due to UV events.

Curve	UV Flux $Hz.mm^{-2}$	Gradient k mm^{-1}	Offset $\overline{G'(0)}$
b	2700	0.149	0.772
c	2900	0.182	0.722
d	5900	0.233	0.602

Table 7.1: Fit parameters for relative mean gain versus radius curves in Figure 7.6 parameters are the same as in Equation 7.4.

the absence of UV events and so we restricted our study to radii greater than 0.5 mm.

We were able to obtain good linear regression fits for $\overline{G'(r)}$ for radii in the range 0.5 to 1.5 mm. The fits are of the form

$$\overline{G'(r)} = kr + \overline{G'(0)} \quad . \tag{7.4}$$

where k is the gradient in mm^{-1}. The fits are shown in Figure 7.6 and the fit parameters are given in Table 7.1.

The linear fits showed that the long range gain depression (LRGD) decreased linearly with radius, at least over the range 0.5 to 1.5 mm. Also the two measurements carried out with comparable UV fluxes, cases "b" and "c" have similar gradients and offsets, while the higher count rate case has, as expected, lower value for $\overline{G'(0)}$ and a steeper gradient indicating larger gain depression.

Fraser *et al.* (1992) have carried out similar measurements with Philips MCPs of identical resistance and geometry. They also find that gain depression has long range effects and that the "zone of influence" extends over the range of 1.5-2.0 mm.

7.4 Measurements of the Long Range Effects of Gain Depression

Another series of measurements was made to further study the effects of LRGD. Measurements were made with illuminated regions with two different geometries; the pin-

hole, as described in Section 7.2 and a ring.

The X-ray event rate was reduced to $\sim$ 1 Hz.mm^{-1} in order to reduce the probability of the sampling events interacting with each other. An area of at least 7 mm^2 is affected by the illumination of the pinhole and it was assumed that a similar area would be affected by the group of pores fired by one photon. At an event rate of 1 Hz.mm^{-2} and given that $\tau_{MCP} \approx 10$ ms, at least 7 % of sampling events will occur in the affected area of another, earlier sampling event within one τ_{MCP} of the earlier event's arrival.

Immediately prior to the experiments the MCPs were held at a pressure of 5×10^{-7} Torr for at least a week and were kept at this pressure throughout the experiments.

7.4.1 Further Measurements with the Pin Hole

As the characteristic scale of LRGD had been determined, a set of annuli for use in the further experiments could be pre-selected. Once again, 64 annuli were chosen. The size of the annuli selected varied slightly for each of the three plate voltages. The radius of the 64th. annulus was approximately 1.8 mm for plate voltages of 3.0 and 3.1 kV and 2.1 mm for 2.9 kV. These radii correspond to an area of approximately 0.22 and 0.16 mm^2 per annulus, respectively.

Approximately 1000 contiguous events were acquired at a time, then all the position decoding calculations for each event were carried out. If an event lay within one of the pre-selected annuli, the corresponding PHD was incremented and events lying outside the set of annuli were discarded. Then another 1000 events were acquired and the process repeated. Only the 64 PHDs were stored. This had the advantage that it required only a small amount of memory for each measurement, i.e. 64 kB, but meant that the data could not subsequently be binned into a different set of annuli.

In a typical flat field measurement, i.e. with no UV illumination of the pinhole, a 6 hour integration was carried out, in which data was acquired for a total of approximately 4 hours. During a flat field integration, approximately 10^7 events were incident on the MCP of which about 1% were assigned to one of the annuli, i.e. approximately 1500 counts per annulus. When the MCP was illuminated, the deadtime associated with the calculations required longer integration times, typically 7 to 8 hours, to acquire the same number of events in the non-illuminated annuli.

Count rates were determined by counting the busy signal on one of the shaping

amplifiers. Therefore, the absolute UV flux through the pinhole is not known, due to pile-up events in the shaping stage or due to very small pulse height events caused by gain depression. However, this method is much more sensitive, at higher count rates, than that used in the measurements described in Section 7.3, i.e. counting the events lying above the ADC LLD. Therefore, similar, quoted count rates in the two sections do not correspond to the same flux levels. Both sets of count rates represent lower limits on the UV flux but the rates quoted in Section 7.3 will underestimate the flux to a larger extent than those in the rest of this chapter.

Ghosting is a problem for these measurements. When gain depression occurs many events lie in the nonlinear region of the r_n/h' relationship and so are mapped into the wrong spiral arm, see Section 5.2.2. This reduces the photometric linearity in the gain depressed regions. However, the vast majority of the ghosted events are low pulse height events, so ghosting leads to an underestimate of gain depression. There is very little ghosting when using just X-ray illumination, the data set used as the example throughout Chapter 5 was obtained during this set of measurements. The ghosts of the measured region are mapped into a region of the image that lies far outside the set of annuli and so they do not corrupt the data sets. Any events mapped into the set of annuli are from unaffected regions of the MCP and so will only lead to a slight underestimate of the magnitude of any gain depression.

The region illuminated in these measurements was exactly the same as that which was illuminated in Section 7.3. The new measurements were made approximately 5 months after the earlier measurements. During that time the MCPs had undergone several cycles from vacuum to air and had also been exposed to laboratory air for several weeks.

7.4.2 Measurements with a Ring

In order to investigate the interaction between more than one illuminated region we also illuminated the MCP with UV photons through an annulus. I shall henceforth refer to this annulus as a ring in order to distinguish it from the annuli that sample the PHDs at various radii. An image of one quadrant of the ring can be seen in the figures showing the simulated effects of different levels of digitization on fixed patterning, i.e. Figures 6.9 and 6.10.

When choosing the radius of the ring, a compromise had to be struck between

making the ring large enough so that not all of the interior would be illuminated by scattered UV light and that a point on the ring would be close enough to interact with most other points on the ring. The ring had an interior radius of 0.9 mm and a width of 100 μm and was laser machined into a 50 μm Al sheet, as was the pinhole. Typical integration times for the images were 7 hours and 12 hours for flat fields, both yielding $\approx$500 counts in the annuli inside the ring.

The software for the ring measurements was similar to that used for the pinhole experiments except that 128 annuli were used, 64 inside the ring and 64 outside. The annuli were aligned with respect to the ring by selecting 16 points, distributed around the internal circumference of the image of the illuminated ring, from which a statistical estimate of the ring centre and radius were determined. The outer radius of the 64th. annulus and that of the 128th. annulus always corresponded to the estimate of the ring internal radius and 3 times that estimate, respectively. The 64 annuli inside the ring all have equal areas and those outside the ring internal radius also have constant areas, 8 times those inside the ring.

7.5 Dynamic, Long Range Gain Depression

Figure 7.9 shows the mean gain, $\overline{G(r)}$, for each annulus with a middle point at a radial distance of r mm from the centre of the pinhole for 3 different plate voltages. This data represents the intrinsic gain variation of the MCP and was obtained only with the diffuse X ray, sampling illumination. The saturations for each plate voltage are similar to those quoted in Section 7.6.2.

I shall use the term "dynamic LRGD" to refer to the LRGD in an area surrounding a group of pores which are undergoing intense UV illumination but not including the gain depression in the UV illuminated channels themselves.

Figure 7.10 shows the relative mean gain, $\overline{G'(r)}$, when the pinhole was illuminated with UV at various count rates. The gains have been normalized with respect to the corresponding $\overline{G(r)}$ curves in Figure 7.9.

Figure 7.10d shows the $\overline{G'(r)}$ curve obtained at 3.0 kV at a UV count rate of 4.5 kHz. As we observed previously, the $\overline{G'(r)}$ curve consists of three regions. Beyond a radius of approximately 1.6 mm, the curve appears to reach a plateau. The curve is linear with respect to radius between this point and $r \approx 0.6$ mm. Below this point the curve diverges sharply from the gradient in the linear region. The curves show the same overall

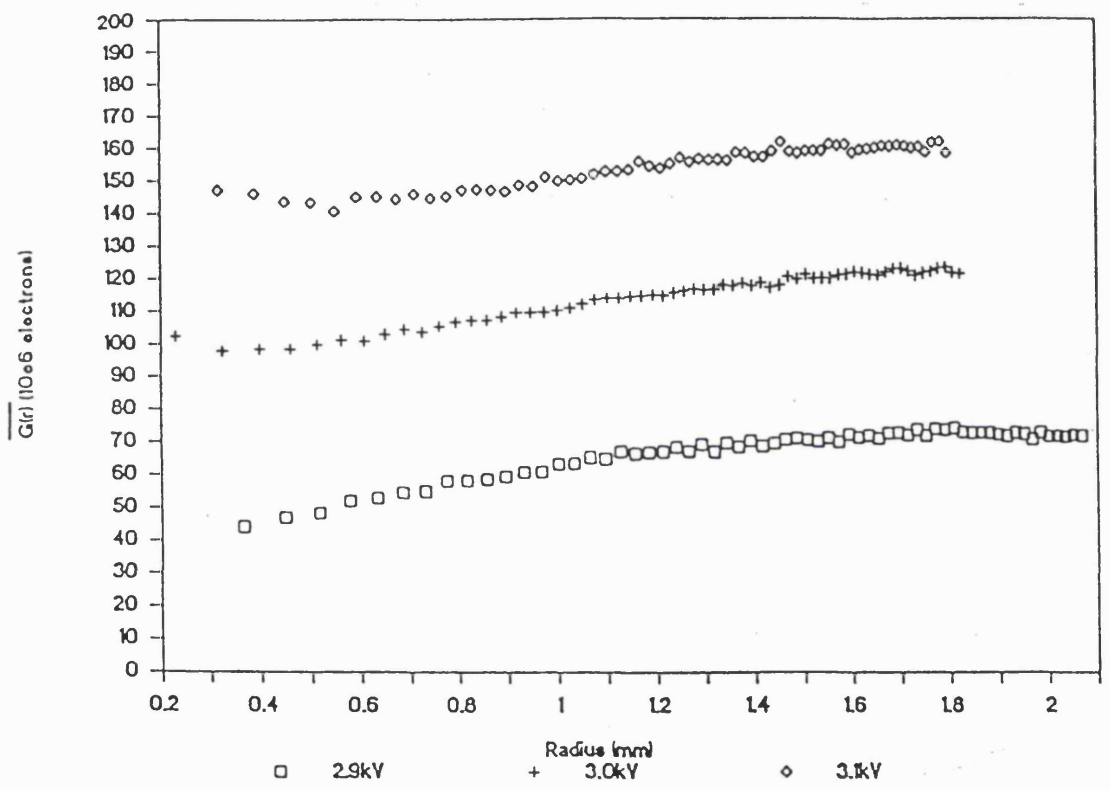

Figure 7.9: The intrinsic variation of the mean gain with radial distance, $\overline{G(r)}$, from the centre of the pinhole for 3 plate voltages. The curves represent flat fields, i.e. the MCP was illuminated only by the diffuse X ray source.

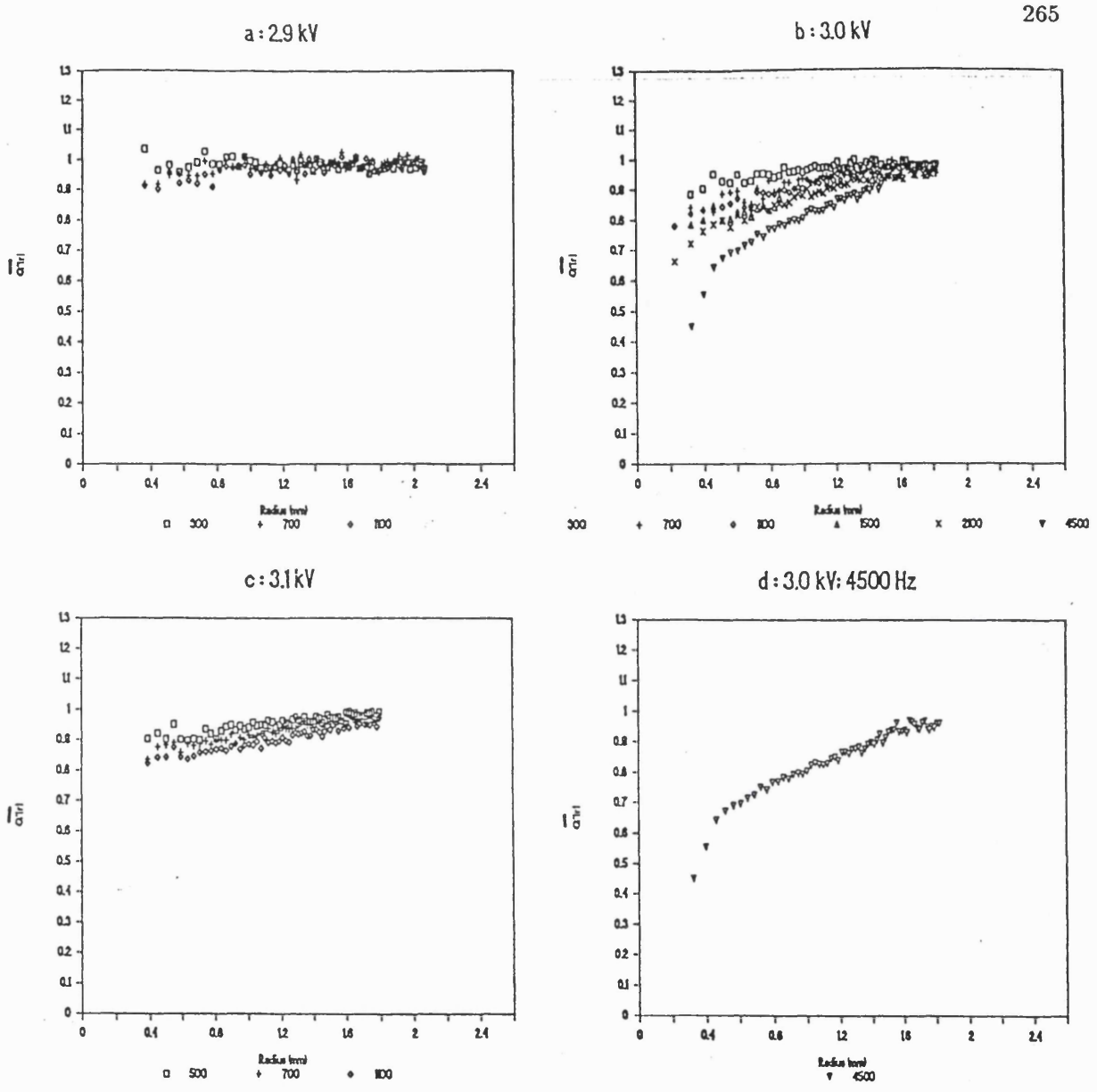

Figure 7.10: The variation of normalized average gain with radial distance from the centre of the pinhole, $\overline{G'(r)}$, for 3 plate voltages.

The gains have been normalized with respect to the corresponding flat field, as shown in Figure 7.9. The UV fluxes associated with the curves are 300, 700 and 1100 Hz for each voltage and extra count rates of 2100 and 4500 Hz at a plate voltage of 3.0 kV. The gain depression is largest for the highest count rates. Figure 7.10d shows the three different regions of the 4500 Hz curve obtained at 3.0 kV. The data from the first annulus, which contains the PHD for the image of the pinhole, is not included for any of the curves.

behaviour for all plate voltages and count rates but the magnitude of the effects varies.

We carried out linear regression fits for $\overline{G'(r)}$ only in the region where the gains always varied linearly, i.e. over the range $0.6 < r < 1.6$ mm. Examples of the fits are shown in Figure 7.11. Note that the two fits intersect at the point where $\overline{G'(r)} \approx 1.0$.

Figure 7.12 shows the two fit parameters, the gradient k and zero intercept $\overline{G'(0)}$, plotted against each other. This indicates that the function $k(\overline{G'(0)})$ is approximately linear.

If a set of lines $y = m_i x + c_i$ has a linear relationship between c and m such that,

$$c_i = d - nm_i \quad , \tag{7.5}$$

$$\Rightarrow y = m_i(x - n) + d \quad , \tag{7.6}$$

for all i and where n and d are constants, then all the lines must intersect at the point (n, d).

Therefore, by carrying out a linear regression fit on the data in Figure 7.12 we can estimate that all the lines defined by the fits to the data in Figure 7.10 intersect at a radius of 1.74 mm at $\overline{G'(r)} = 1.00$.

This result indicates that gain depression only occurs within a constant, limiting radius for all of the plate operating conditions and UV fluxes that we measured. The LRGD can be described as the surface of a hollow, right circular cone with a constant diameter base but in which the height of the apex varies. In this case given a constant limiting radius, the important independent parameter is the extrapolated gain at the pinhole centre, i.e. $\overline{G'(0)}$.

Figure 7.13 shows the fit parameters obtained from two sets of curves acquired at two constant count rates compared to the linear fit obtained in Figure 7.12. They give some indication of the uncertainties associated with the single data points in Figure 7.12. An important point is that although some points lie some distance from the fit, the scatter parallel to the fitted line is significantly larger than the scatter normal to the line. The 900 Hz and 500 Hz data were acquired approximately 4 and 5 weeks after the data shown in Figure 7.10. Different flat fields were used for the normalization. These are discussed in the next section.

The 3.2 kV data in Figure 7.12 represent the fits to the $\overline{G'(r)}$ curves as given in Table 7.1. These data were obtained approximately 5 months before the rest of the data in the figure, at a gain of $\approx 1.8 \times 10^8\ e^-$. These data are displayed only as a comparison and were not used in determining the fit to $k(\overline{G'(0)})$.

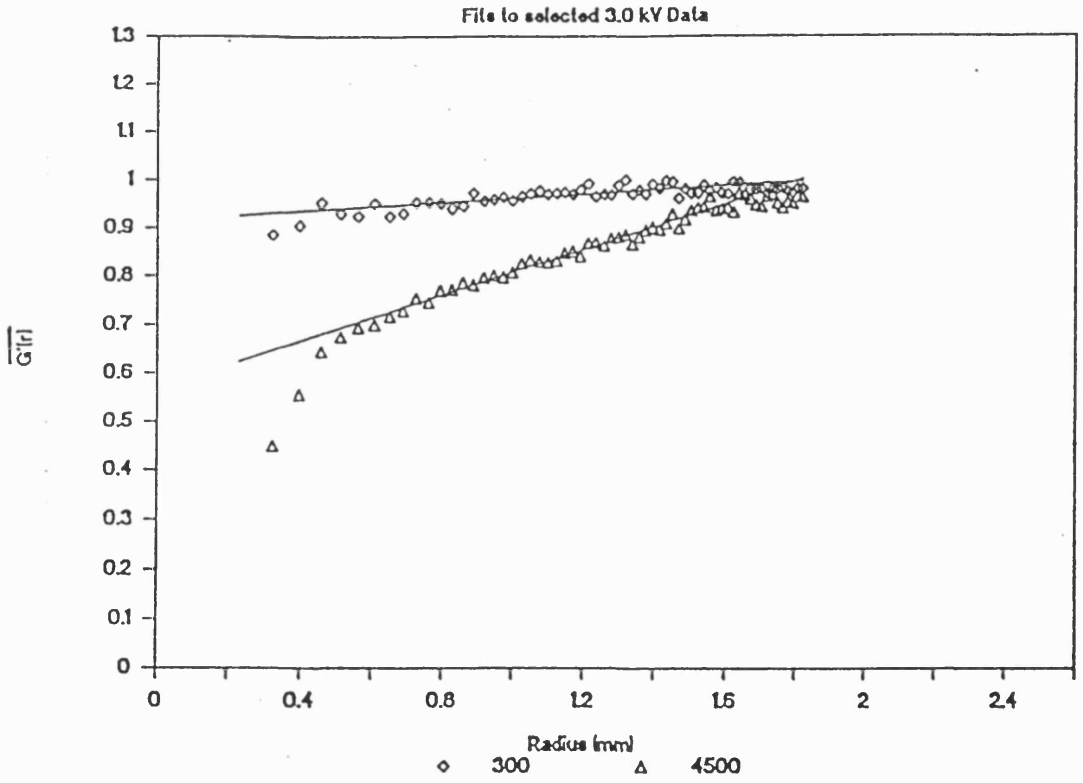

Figure 7.11: Examples of linear regression fits for data obtained at UV fluxes of 300 and 4500 Hz for a 3.0 kV plate voltage.

The fit is only carried out for data in the region which is linear in all of the curves.

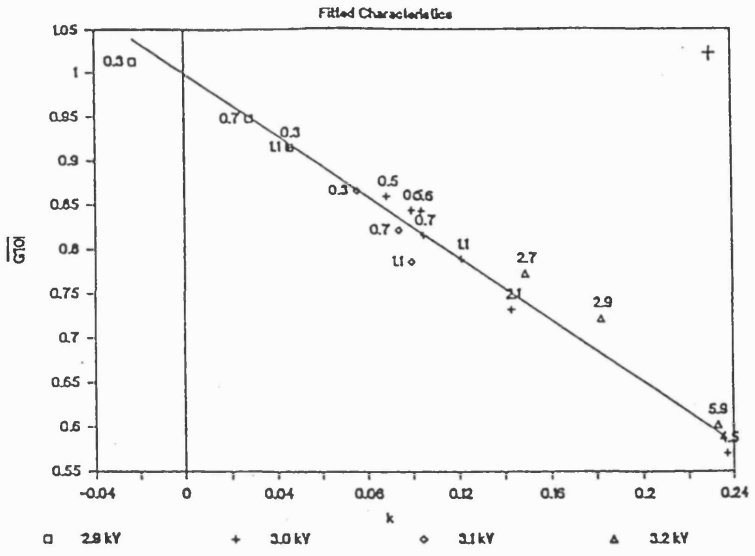

Figure 7.12: The gradient and offset terms from the linear regression fits for 15 data sets, including data presented in Figure 7.10.

The error bar in the corner is typical of the errors associated with each of the individual points. The gradient of the fit to this data is -1.74 ± 0.08 mm and the zero intercept is at $\overline{G'(0)} = 1.00 \pm 0.02$.

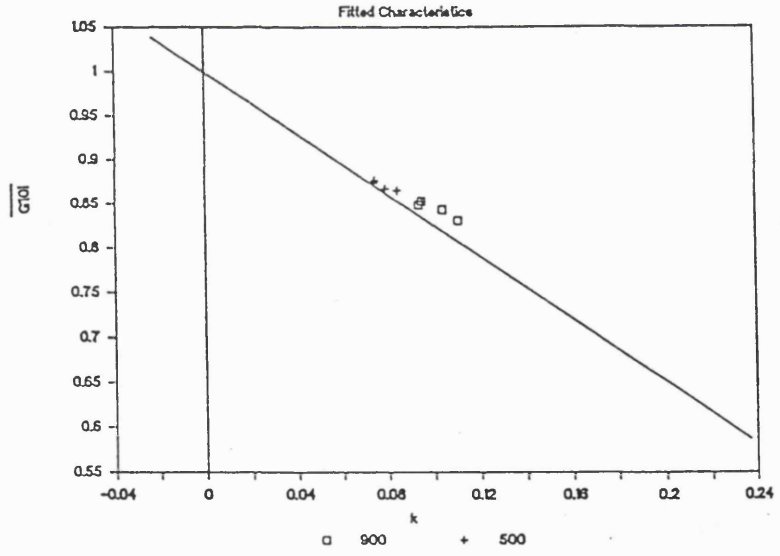

Figure 7.13: Gradient and offset terms for linear regression fits for 4 data sets obtained at UV count rates of 500 and 900 Hz with a plate voltage of 3.0 kV.

The scatter is a demonstration of the probable uncertainty associated with data points in Figure 7.12. Although there is a scatter the points all lie approximately on the linear regression fit for the whole data set as shown in Figure 7.12.

The linear nature of the data in Figure 7.12 shows that the limiting radius of the gain depression does not vary significantly over a factor of 3 in gain, an order of magnitude in UV flux, a long period of time or cycling the MCPs between air and vacuum.

Figure 7.12 also shows that the magnitude of the gain depression varies monotonically with UV flux. Although $\overline{G'(0)}$ varies monotonically with flux, it is not always monotonic when flux and plate voltage are considered together. Gain depression appears to be monotonic with plate voltage at a UV flux of 300 Hz, but at higher fluxes it reaches a maximum at 3.0 kV and reduces at 3.1 kV. This is also the case for 3.2 kV when compared to the high flux measurements.

7.5.1 Measurements of the Dynamic, Long Range Gain Depression with the Ring

The ring was used to observe the behaviour of the LRGD when the MCP was illuminated by an extended image. Figure 7.14 shows the $\overline{G'(r)}$ and relative count rates as measured at various radii. The relative radius refers to the ratio of the annuli radius to the interior radius of the ring. The relative gains and count rates were determined by normalization with respect to a flat field, acquired separately, consisting solely of X-ray events. To allow for small variations in the acquisition times of the various data sets, the count rates were normalized with respect to the count rate in the 128th. annulus.

A count rate significantly greater than 1 indicates the presence of UV events. Unfortunately, all the PHDs inside the ring contain a significant proportion of UV events, which, as discussed in Section 7.3 produces anomalously low values of $\overline{G(r)}$. So the gain variations in this diagram are not proof of LRGD.

The total average gain $\overline{G_t}$ for a PHD containing UV and X-ray events with mean gains $\overline{G_{uv}}$ and $\overline{G_x}$, respectively, is given by

$$\overline{G_t} = \frac{\overline{G_{uv}}(n_t - n_x) + \overline{G_x} n_x}{n_t} \quad , \tag{7.7}$$

$$= \overline{G_{uv}} - \frac{n_x}{n_t}(\overline{G_x} - \overline{G_{uv}}) \quad , \tag{7.8}$$

where n_x and n_t are the number of X-ray events and the sum of X-ray and UV events, respectively. In the absence of gain depression, $\overline{G_t}$ is inversely proportional to n_t.

Figure 7.15 shows the same data as in Figure 7.14 with $\overline{G'(r)}$ plotted against the inverse of the relative rate. Each of the three curves show divergence from a straight line

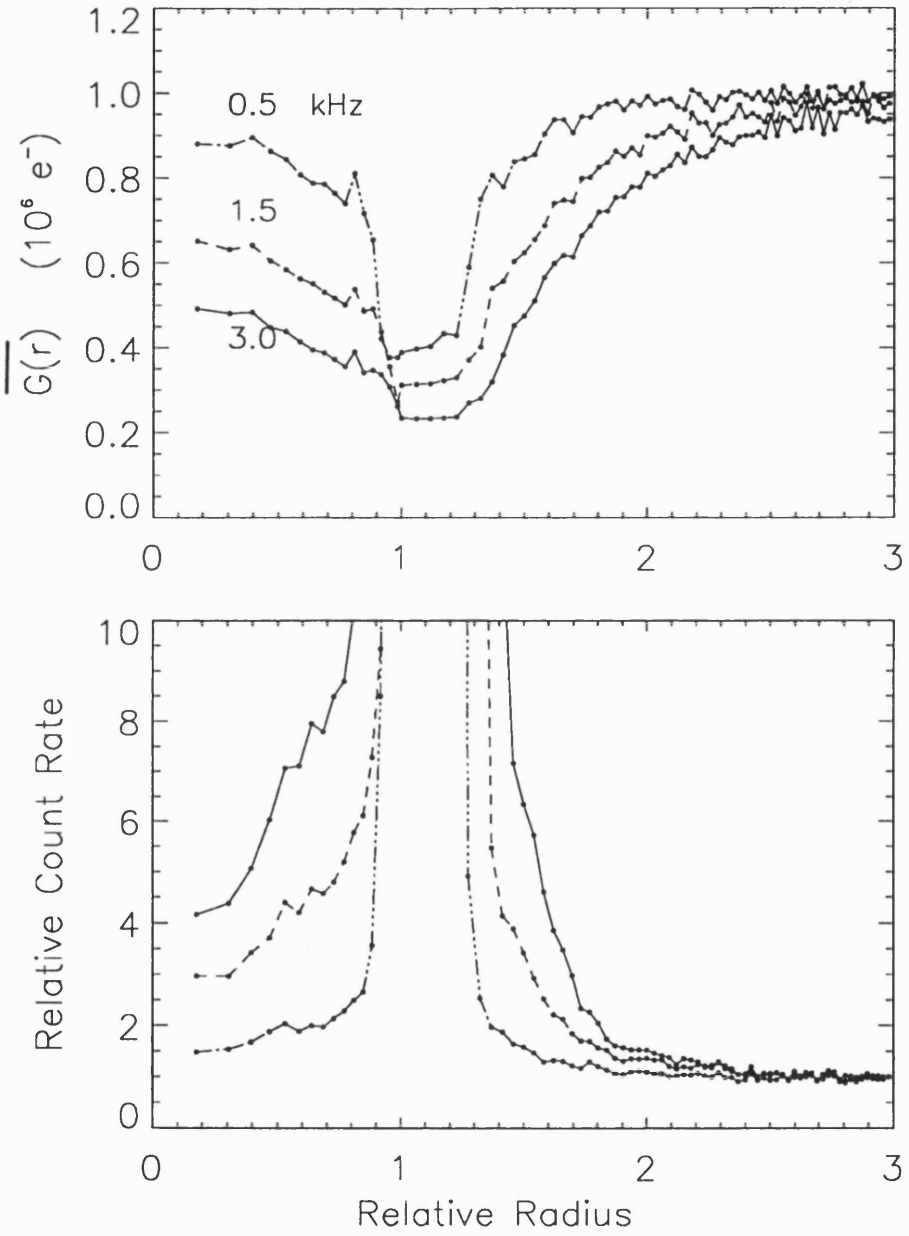

Figure 7.14: The variation of $\overline{G'(r)}$ and relative total event rates for three UV count rates, as measured with the ring.

Relative radii less than 1 represent the annuli included within the interior radius of the ring. The 64 interior annuli have been rebinned into 16 annuli with an area of 0.16 mm^2 each to improve SNR. The count rates quoted in the top figure are the approximate total UV rates. The line types correspond to the same count rates in both diagrams.

relationship which indicates the presence of gain depression.

The gain depression inside and outside the ring cannot be due solely to increasing interaction between the events in these regions with increasing rate because the magnitude of the gain depression is dependent on the total UV flux, not the local flux. Also, the gain depression near the ring is always greater on the inside than the outside, even though the local UV fluxes are the same. Therefore, LRGD is present and depresses the gain more near the inside edge of the ring than on the outside. In the centre of the ring the depression is similar to that on the outside of the ring for the same local flux. This demonstrates the magnitude of LRGD is dependent on the morphology of the illuminated region.

7.6 Long Term, Long Range Gain Depression

Until now, it has been assumed that LRGD has no long term effect on the MCP, i.e. the gain should recover almost immediately after the point source illumination is removed. Given the long integration times necessary to obtain a reasonable signal to noise ratio in the PHDs of the annuli illuminated only by X-rays, we cannot measure any rapid variation of the gain in quiescent pores. While it is expected that prolonged, intense UV exposure would permanently reduce the gain in the region of the MCP illumination, there should be no long term effect in the rest of the MCP.

I shall use the expression "long term LRGD" to refer to the LRGD in an area surrounding a region that has undergone intense UV illumination, many $\tau_{MCP}s$ after the UV illumination has finished. As in dynamic LRGD, it does not refer to gain depression in the region that was actually UV illuminated.

Figure 7.16 shows examples of the MCP gains at various stages during the experiment, obtained with X-ray illumination only. Curve "a" was obtained at the start of this experiment, 5 months after the last UV illumination. The total UV exposure through the pinhole and the time between when the curves were obtained is shown in Table 7.2.

It is apparent that the gains in the annuli that were not UV illuminated up to a radius of at least 1 mm, have not returned to the pre-experiment levels. This clearly demonstrates that gain depression has a component that is both long term and long range.

The gain in the first annulus, or more accurately the disk, which contains the region that was UV illuminated, has returned to approximately the same level as at the start of the experiment, while the gain in many of the non-illuminated annuli has not. This

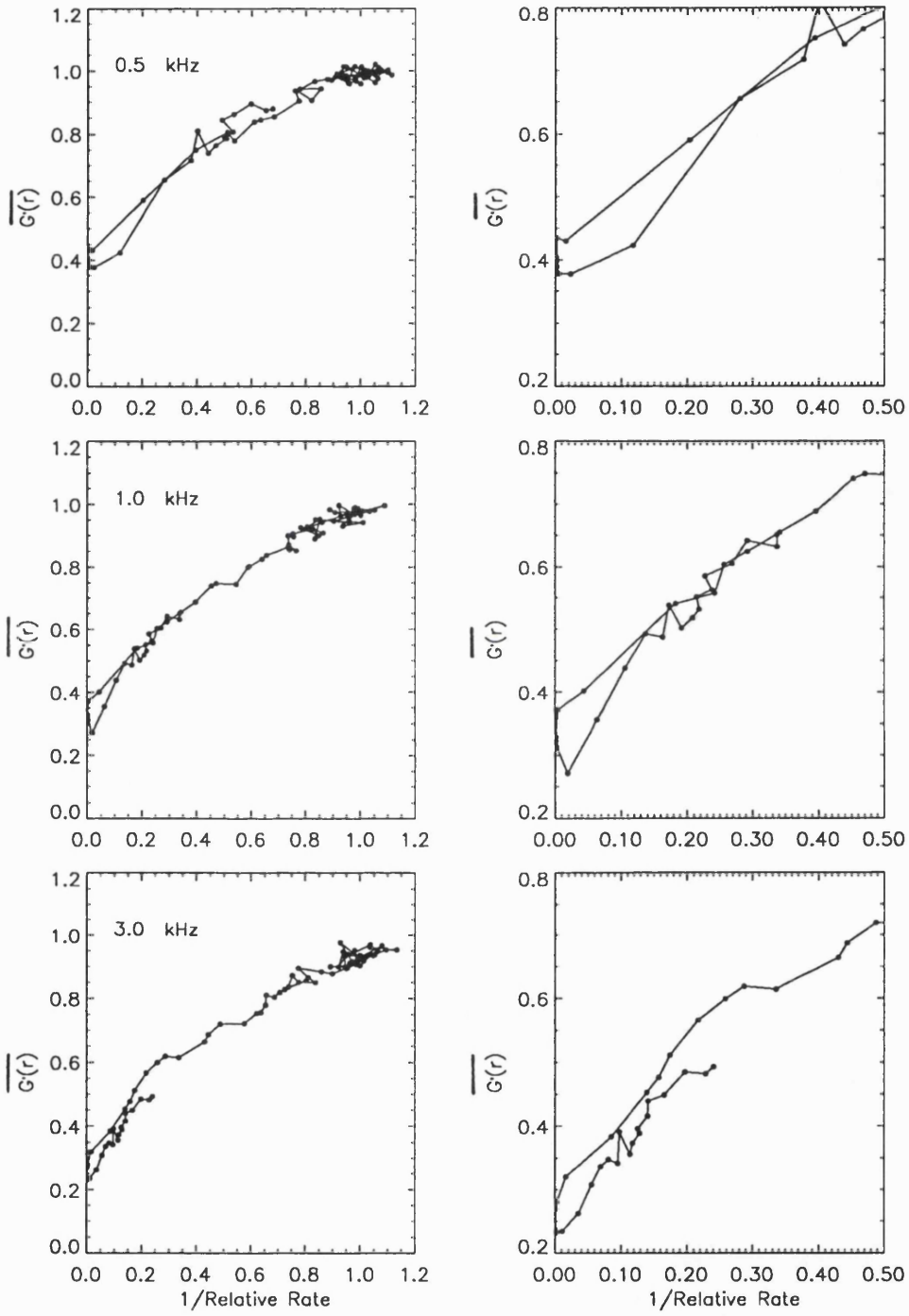

Figure 7.15: Variation of $\overline{G'(r)}$ with relative total count rates.

The data is the same as shown in Figure 7.14. The shorter of the curves in the diagrams on the left, represent the data from inside the ring. The graphs on the right side of the pages are a subset of the data in the curves on the left.

is precisely the opposite of expected behaviour.

This long term LRGD complicates the experiment. As the intrinsic gain of the MCP can change, we cannot be sure what the flat field was actually like during the measurements with UV illumination. Normalizing with respect to Curve "a" produces higher values of $\overline{G'(0)}$ than if we use Curve "c" as the flat field. However, we obtain very nearly the same fit for $k(\overline{G'(0)})$ irrespective of which of the flat fields we use. The difference between the limiting radius of the gain depression for the two fits, was less than 0.1 mm. Curve "c" was used as the flat field to normalize the data in Figure 7.10 and is the same data as the 3.0 kV curve shown in Figure 7.9.

The 2.9 and 3.1 kV flat fields in Figure 7.9 were taken immediately prior to the series of measurements with UV illuminations for each voltage. The probable cause of the negative value for $\overline{G'(0)}$ for a UV flux of 300 Hz at 2.9 kV in Figure 7.12 is that there was a slight variation in the intrinsic gain of the MCP during the measurement of either the flat field or the illuminated image. The gradient of the gain depression for this data set is very shallow and only a very small increase in the intrinsic MCP gain would be necessary to change the gradient's sign.

Curve "d" was used to normalize two of the gain curves for the 900 Hz data sets represented in Figure 7.13. Curve "e" was used to normalize the other two 900 Hz data sets. Curve "f" is the average of 4 flat fields taken alternately with 4 UV illuminations at a UV flux of 500 Hz. The flat fields were started within 10 minutes of the UV lamp being extinguished. The flat field taken directly after each UV measurement was used to normalize the corresponding 500 Hz data as shown in Figure 7.13. The total UV exposure time was approximately 27 hours.

It must be stressed that in each case, the gain depression with UV illumination was significantly greater than that in the flat fields measured after the illumination. All of the data presented for 3.0 kV was normalized with a flat field taken after the UV measurement. After the UV illumination was extinguished, the MCP gain returned to some intermediate value between the illuminated and pre-experiment cases.

Curves "d", "e" and "f" are very similar, even though there is a total of 43 hours UV exposure between "d" and "f". This demonstrates that the effect of long term LRGD has saturated, i.e. further UV exposure does not increase the magnitude of the gain depression. Also the magnitude of the gain depression with respect to Curve "a" for these three curves is approximately twice that for Curves "b" and "c".

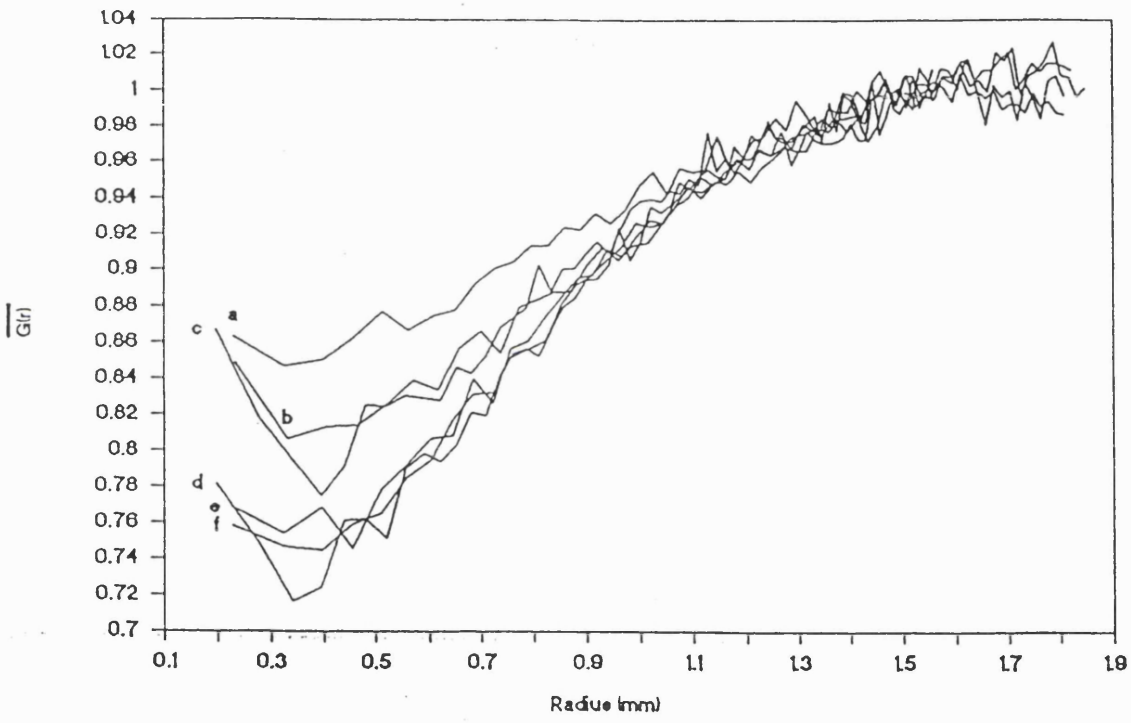

Figure 7.16: Flat fields obtained at various stages of the experiment.
All of the curves were obtained at a plate voltage of 3.0 kV and have been normalized so that the average gain at 1.5 mm is equal to 1. The variation in $\overline{G(1.5)}$ for the 3.0 kV curves was approximately 3%. The individual curves are described in the text and in Table 7.2.

Curve	UV Exposure (hours)	Total Time Since Last Exposure (hours)
a	96 @ Various V_c and rates.	3700 Including exposure to air for several weeks.
b		771
c	16 @ $V_c = 3.0$ kV and 900 Hz.	12
d	16 @ $V_c = 3.0$ kV and 900 Hz.	146
e	27 @ $V_c = 3.0$ kv and 500 Hz, composite of 4 measurements separated by $\approx$ 7 hrs exposure each.	
f		

Table 7.2: Total UV exposure and the intervals between the times at which the curves in Figure 7.16 were acquired.
Time increases down the page, i.e. an item directly below another occurred immediately after the upper item.

One possible explanation for this behaviour is that the intrinsic gain is progressively depressed until the long term effect saturates. This is unlikely to cause the variation between Curves "b", "c" and Curves "d", "e", "f", as the total UV exposure time between "a" and "c" was 6 times longer than that between "c" and "d". While it is true that the 96 hour exposure consisted of various fluxes at various gains, it would require that the magnitude of the gain depression would be strongly nonlinear with respect to integrated UV exposure. Also, it would be serendipitous, to say the least, if we had randomly chosen to measure a flat field at the critical point just before saturation occurred.

Another possibility is that the long term effect saturates relatively quickly, i.e. in less than 16 hours, and the intrinsic gain slowly recovers to an intermediate point such as Curve "c". The recovery would have to be quite slow. Curves "d", "e" and "f" are very similar but the time elapsed between extinguishing the UV and starting the flat field acquisition, was of the order of minutes for Curves "d" and "f" while it was 6 days for Curve "e". Therefore, no significant recovery occurs over approximately a week. Also, if recovery is the cause of the variation in the magnitude of gain depression, then it has taken approximately 1 month to recover to approximately halfway between the saturated and pre-experiment intrinsic gains. Another interesting phenomenon is that the gain appears to recover faster in the illuminated annulus than in the non-illuminated annuli.

A flat field obtained at 3.2 kV, see Figure 7.4 before the MCP was illuminated with UV and before the experiment described in Section 7.3, indicates that the intrinsic gain was relatively flat up to approximately 1.2 mm. Assuming that the general form of the gain curve would be the same for 3.0 kV as for 3.2 kV, Figure 7.16 shows that the intrinsic gain of the MCP has not fully recovered over a period of 5 months which included prolonged exposure to air.

7.6.1 The Variation of Long Term, Long Range Gain Depression with Time

Measurements of the evolution of long term LRGD with time were carried out using the ring. In these measurements a section of the MCP that had not previously undergone intense UV illumination was used, i.e. a different region than used with the pinhole and the ring measurements as described in Section 7.5.1.

A series of 14 measurements were made to investigate how LRGD varies during

progressive UV illumination. Each measurement consists of data obtained with 2 hour long, X-ray only flat fields obtained at various stages during a cumulative UV exposure. The initial flat field was obtained after only 15 minutes exposure, which represents the time that was necessary to setup the spiral fit parameters and select the annuli positions. This data is shown in Figure 7.17a. As in most of the diagrams in this section, the 64 annuli inside the ring have been resampled into 16 equal area annuli to improve the SNR.

After each flat field was obtained, the MCP was illuminated with UV through the mask, typically for 35 minutes. After the UV illumination was finished another flat field was taken. Flat fields and UV illuminations were both begun within 2 minutes of the end of the previous measurement. A series of 13 UV illuminations was carried out and the total UV exposure time after the initial flat field was 27430 s, $\approx$ 7.5 hours. Figure 7.17b shows the combined average X-ray and UV count rates per pore within each of the 80 annuli. The count rate has been corrected for the acquisition deadtime, i.e. the proportion of the integration time for which the ADCs were not sampling data, which was over 90%. No correction has been attempted for losses below the LLD, due to ghosting or coincidence loss in the electronics. No significant variation in UV intensity with time was noticed.

Figure 7.17c shows the dynamic gain depression, produced during the first and last UV illumination. It shows that there was no significant variation in the magnitude during the 13 UV exposures. Figure 7.17d shows the average charge extracted per pore during UV exposure after the initial flat field. These values have been corrected in the same manner as the count rates.

After the sequence of UV exposures, a series of flat fields was obtained at various times over a period of 2 weeks. The MCPs were kept in vacuum throughout the entire series of measurements. The MCPs and electronics were run for at least two hours before acquiring any of the flat fields.

Figure 7.18 shows the average relative gains as measured in the flat fields both during and after the sequence of UV illuminations. Times quoted on the left half of the diagram refer to the total UV exposure and times on the right side of the figure represent the time elapsed since the last UV exposure. The two scales share the same origin but represent two different times. The original 128 annuli were rebinned so that there are 8 interior and exterior annuli. The various curves are a selection of these 16 annuli and correspond to the annular regions indicated in the table in the bottom left corner, for flat fields acquired at various stages during the experiment. All data was acquired with V_c = 3.0 kV and have

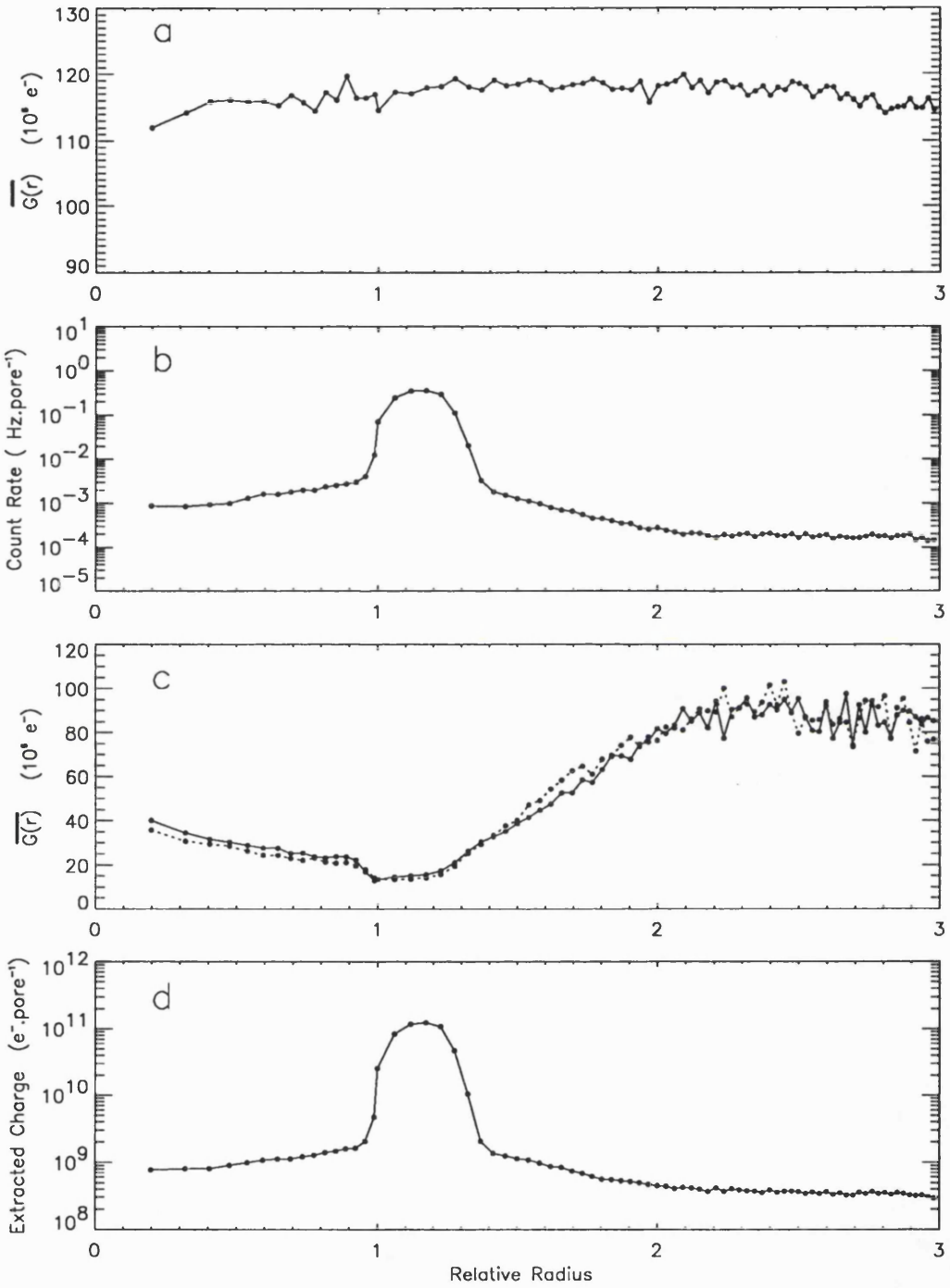

Figure 7.17: Details of the UV illumination of the ring.

Figure a shows the flat field for $V_c = 3.0$ kV at the start of the experiment which was measured immediately before the first data point in Figure 7.18. Figure b shows the combined X-ray and UV event rate during the UV illuminations. Figure c shows the variation in $\overline{G(r)}$ as measured during the first (solid line) and last (dotted) exposure. Curve d shows the total charge extracted during the series of UV exposures.

been normalized such that $\overline{G(r)} = 1$ for the 16th. of the new annuli, to allow for drifts in the amplifier gains with time. These drifts were only noticeable for the flat fields taken over several days after the last UV exposure. The error bars on the right half of curve 8 correspond to total integration times for those data sets.

Figure 7.18 shows clearly that the magnitude of the gain depression increases with UV exposure and that the gain recovers slowly. This is the behaviour that was suggested by the flat fields displayed in Figure 7.16. The maximum magnitude of the gain depression in the two diagrams is comparable. The rate of recovery is much faster here than was suggested by Curves **"b"** and **"c"** in Figure 7.16, however, there was much more extensive UV illumination between Curves **"a"** and **"b"** in that figure than in the present case.

The figure also shows the magnitude of the long term, gain depression is greatest on the inside of the ring and not in ring itself. A similar effect is seen in Figure 7.16 where the maximum long term, gain depression is located approximately 0.4 mm from the pinhole. The magnitude of the long term LRGD is also greater on the inside of the ring than on the outside, as was seen for the dynamic LRGD in Figure 7.15. It is extremely unlikely that this long term gain depression is due to the increased count rate caused by the local UV flux inside the ring. As shown in Figure 7.17, the maximum event and charge extraction rates inside the ring, Curves 1-4 in Figure 7.16, are $\sim$ 100 times smaller than those in the Curve 5, which represents the ring, yet the rate of change of the magnitude gain depression in all of these curves is comparable.

An interesting feature is that while there is a large variation in the magnitude of the long term LRGD between the first and last UV exposure, the absolute gain measurements for the dynamic LRGD do not vary significantly.

Figure 7.19 shows the same data as in Figure 7.18 but plotted linearly with time. Figure 7.19a clearly shows that the rate of change in the magnitude of long term LRGD decreases with progressive UV illumination and it also appears to saturate after about 6 hours. This figure and Figure 7.18 show that neither the progressive increase in the magnitude of gain depression nor the gain recovery follow straight forward power law or linear relationships.

The PHDs shown in Figure 7.20 correspond to the data points in these curves obtained $\sim$ 100 hours after the last UV exposure. The modal gain is reduced by $\sim$ 25 channels inside and near the ring compared to PHD 9 located at the edge of the measured

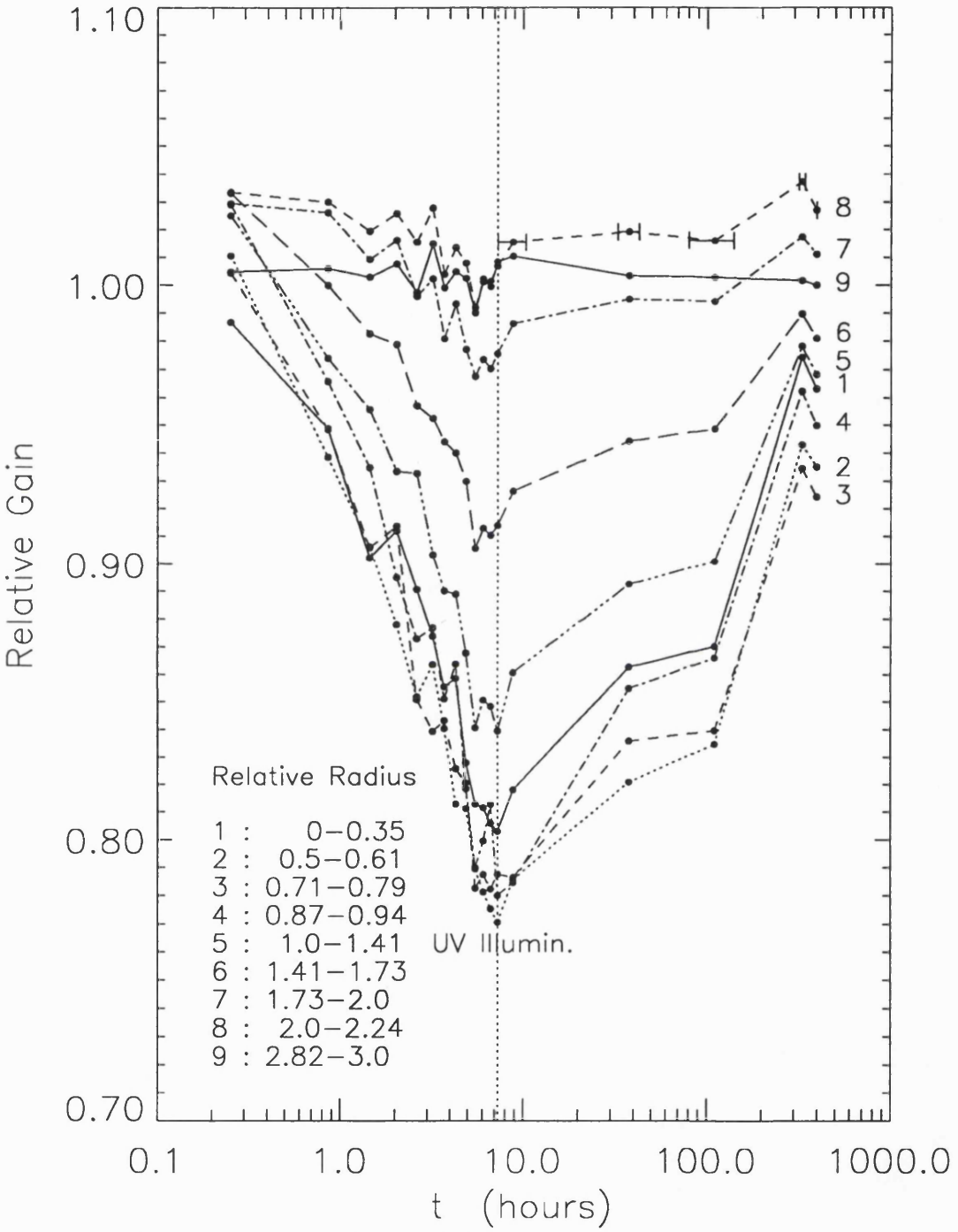

Figure 7.18: The variation of the magnitude of long term LRGD with time. Times to the left of the vertical dotted line correspond to cumulative UV exposure time. Times to the right of the line indicate the total time elapsed since the end of the UV illumination, the origin is the same for both cases. The data have been rebinned into a total of 16 annuli and the gains have been normalized with respect to the gain in the 16th. of these new annuli. The data is discussed in detail in the accompanying text.

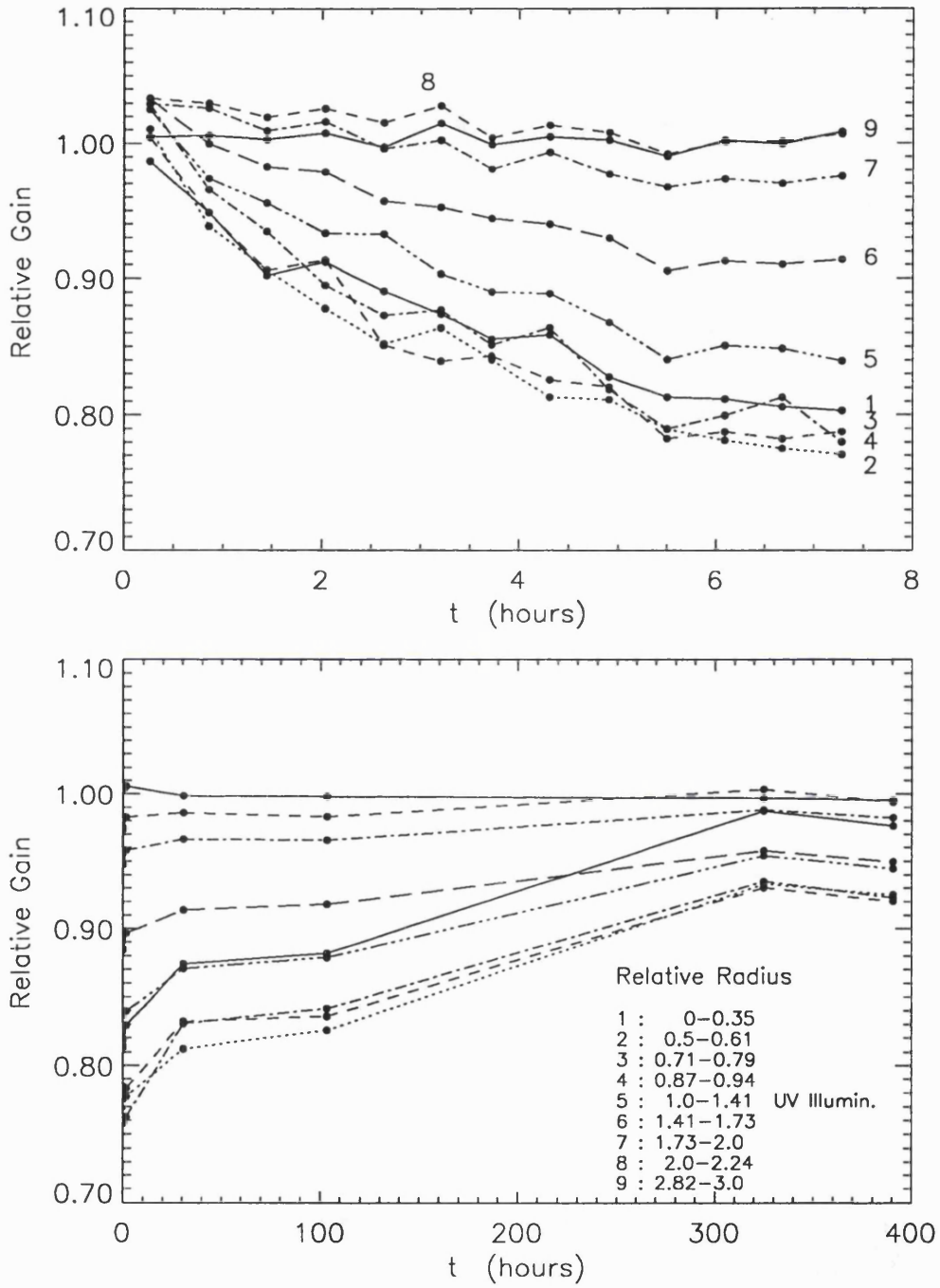

Figure 7.19: The data presented in 7.18 plotted linearly with respect to time. Figure a shows the progressive gain depression with UV exposure and Figure b shows the recovery of gain after the UV illumination was stopped. Figure b has been renormalized with respect to the gain for the first point in Figure a and shows the magnitude of the gain depression for each curve. The last point in Figure a corresponds to the first point in Figure b.

area. The PHDs obtained before UV exposure are essentially the same as PHD 9. As was also seen with "conventional" gain depression, see Section 1.1.4, the absolute width of the PHD does not vary significantly between the annuli. Note how the intersection between the main peak and the high energy tail changes with position with respect to the ring.

7.6.2 The Variation of Long Term, Long Range Gain Depression with Plate Voltage

Figure 7.21 shows a series of flat fields measured after the UV exposure obtained at 5 different values of V_c. All the curves were obtained in the interval from 25 to 60 hours after the end of UV illumination. The curves were obtained in the order 3.0 (10 hour integration), 2.8, 2.9, 3.1 (6 hours each) and 3.2 kV (7 hours). The saturation in the 128 th. annulus for each voltage, in increasing magnitude from 2.8 to 3.2 kV, is 145, 75, 46, 32 and 27%.

Although all UV illumination took place at $V_c = 3.0$ kV, significant differences are observed in the magnitude for the gain depression for each value of V_c. Unfortunately, the author did not have the foresight to measure flat fields at all values of V_c before the start of the experiment. However, the initial 3.0 kV flat field, as shown in Figure 7.17, is essentially flat as is the 3.2 kV curve and the curves all behave similarly at relative radii greater than 2.0. It is, therefore, highly probable that the reduction in the gain in these curves is an accurate measurement of the variation in gain due to long term LRGD.

Although the absolute difference is greater for higher voltages, except for 3.2 kV, the maximum gain depression as a fraction of the quiescent gain, as shown in the bottom diagram of Figure 7.21, is a monotonic relationship with V_c. The 2.8 kV flat field has a maximum gain depression of 30% while the 3.2 kV curve shows almost no evidence of gain depression. Also the point at which maximum gain depression occurs also moves further from the ring and closer to the centre of circle with increasing V_c

It is extremely unlikely that the order in which the flat fields were measured causes the variation in these flat fields, as the recovery between this 3.0 kV flat field and that measured 110 hours after UV illumination, is small compared to the difference in gain depression between the 3.0 kV and flat fields obtained at the other voltages. Also, the two lowest voltages exhibit larger gain depression but were acquired after the 3.0 kV flat field. Therefore, long term LRGD can induce large variations in the gain across the MCP and

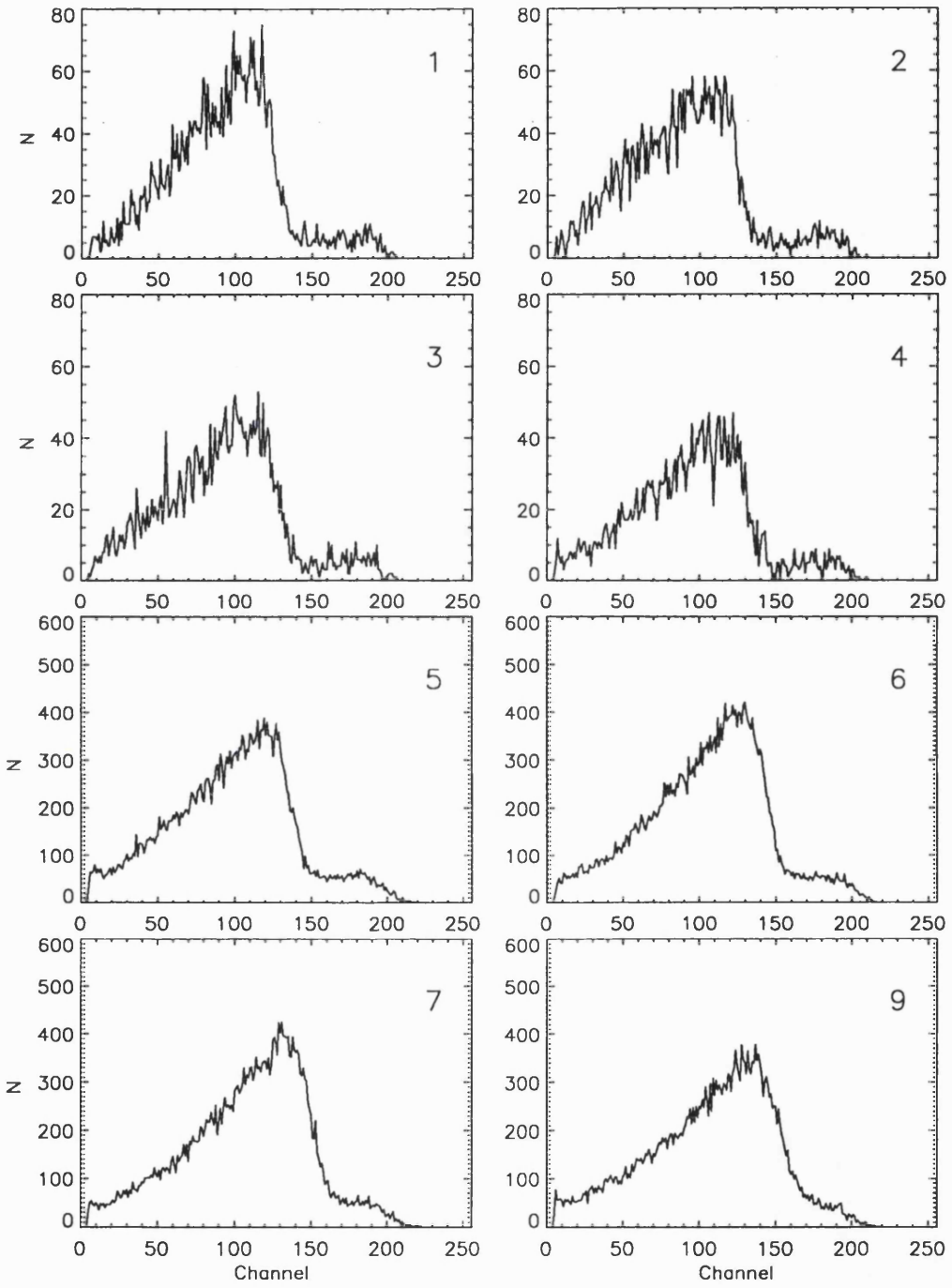

Figure 7.20: The PHDs acquired for various different regions approximately 100 hours after the last UV exposure of the ring.

These PHDs were acquired during a 24 hour integration and are represented by the data point at approximately 100 hours in Figures 7.18 and 7.19. The PHDs correspond to the curves with the same numbers in those two diagrams. Channel 100 corresponds to a gain of 1.1×10^8 e^-.

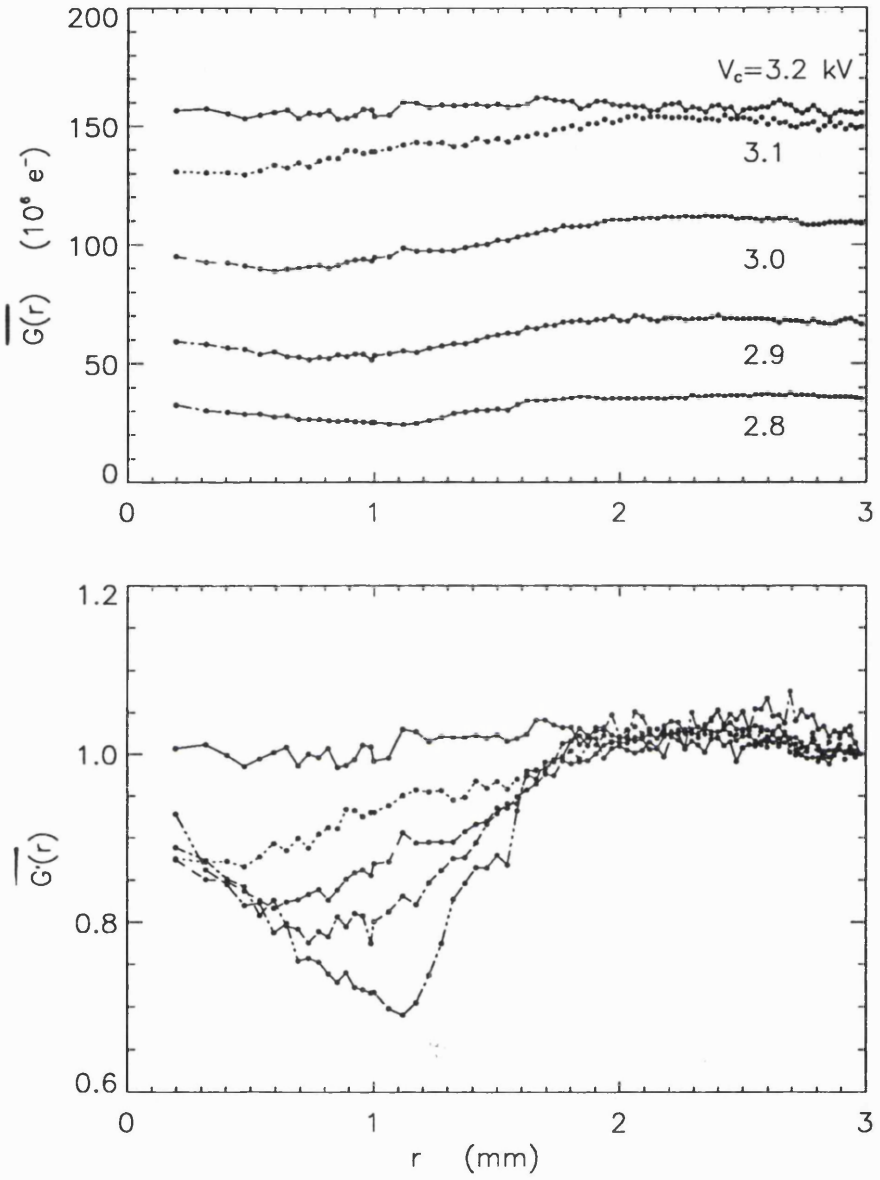

Figure 7.21: Variation in gain for flat fields obtained at various chevron voltages after prolonged UV illumination of the ring.

The curves in the bottom diagram have been normalized with respect to $\overline{G(r)}$ for the 128th. annulus. In the bottom figure V_c increases from bottom to top, as in the top figure. The interior 64 annuli have been rebinned into 16 annuli.

these variations will be change significantly with plate voltage.

The variation of the magnitude of gain depression with V_c is strong evidence that long term LRGD is essentially a radial phenomenon. As discussed in Section 1.1.3, as saturation increases, the region of unity gain extends further back up the channel. Therefore, at higher values of V_c, the last dynode that contributes effectively to the gain lies further up the channel. If the last dynode has been affected permanently by operation at one saturation, the gain will be reduced more while operating at saturations lower than that initial saturation than for higher saturations. At lower saturations, more of the affected region will lie in the region of the channel that is effectively providing electron multiplication, while at higher saturations, a larger proportion of the affected region will lie in in the unity gain region and so will have little effect on the overall gain of the channel. Therefore, although long term LRGD has a large radial extent, it has only a small extent axially.

7.6.3 Image Distortions Due to the Long Term Effects of Long Range Gain Depression

As was seen in Figure 7.18, after a period of two weeks, the gain had recovered to a level at least 90% of the initial values in all areas. However, even though the gain has almost completely recovered, the long term effects of LRGD are still sufficient to produce significant image distortions.

Figure 7.22 shows an image of a bar mask obtained with the same MCPs approximately 1 month after the measurements with the ring. The MCPs had been cycled from vacuum to air on several occasions since the ring measurements were completed. The pinhole was located in the region lying between the 9th. and 10th. bars from the top of the image in the column containing the second largest bars in the top figure. These bars have a centre separation of 400 μm. This region of the MCP had not undergone intense UV exposure for $\approx$ 6 months before this image was acquired. The region that was used in Section 7.6.1 is indicated by the dotted circle in the bottom figure, which is an expanded image of the fine series of bars in the top figure.

Clear distortions of some of the images of the bars are visible in the bottom diagram. The opposite ends of bars are offset up to 60 μm vertically from each other and obvious distortions extend up to 600 μm from the position of the ring. Also the two bars that lie either side of the position where the pinhole was located show evidence of distortion

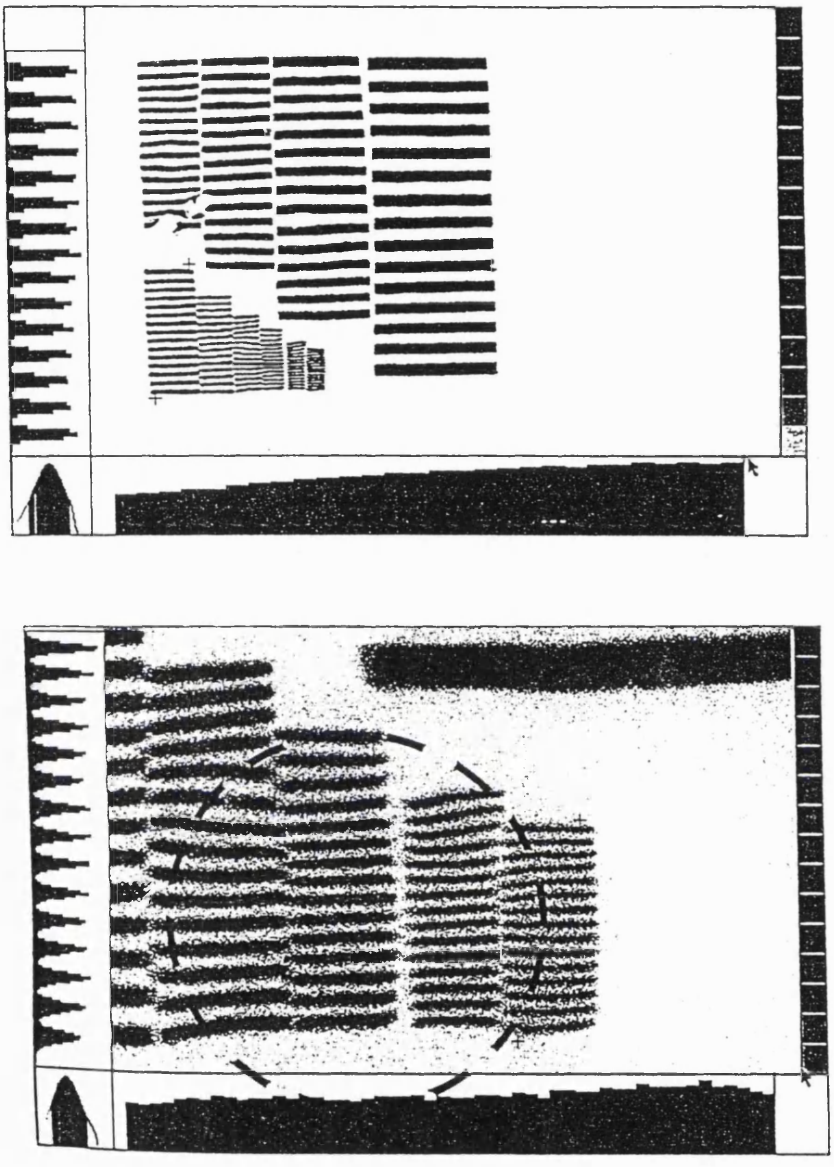

Figure 7.22: Image distortions in a two dimensional image produced by long term LRGD. The image includes the regions illuminated during the LRGD experiments. The dotted line in the bottom diagram shows the position where the ring was located. The bottom diagram is an expanded image of the fine series of bars in the top figure, the sequence of centre separation of these bars is 64, 74, 98, 120, 158 and 200 μm. From Lapington *et al.* (1992).

and its possible that the adjacent bars are also slightly distorted. As the distortions are present at relatively large distance from the regions that underwent prolonged UV exposure, these distortions are a long term effect of LRGD.

Although SPAN has pulse height related position shifts, see Section 5.7.1, it is unlikely that the distortions are caused solely by the difference in gain due to long term LRGD. The position shifts due to gain are most noticeable over a large range of pulse heights. In this image, the extreme edges of the PHD have been removed. Also, the positional shifts are always in one direction, wherehas these distortions appear to have a strong dependence on the azimuthal angle around the circumference of the ring.

The existence of long term effects of LRGD raises the possibility that a localized region of the readout has been affected, rather than the MCP. Upon examination of the readout after the MCPs were subject to intense localized UV exposure, a brown discolouration was observed. This is probably due to a chemical reaction caused by intense electron bombardment of residual pump oil molecules. The MCP stack was rotated in one piece, 120° with respect to the readout. The mask was not moved with respsect to the MCP and so was also rotated with respect to the anode. As shown in Figure 7.23, the distortions have not moved during rotation, with respect to the deadspots visible in the left edge of the bar mask but they have moved with respect to the anode, as shown by the inclination of the bar masks to the x and y axes of the diagram. Therefore, the distortions are phenomenon of the MCP not the readout and as their most likely cause is LRGD, this is also true for LRGD itself.

The presence of the deadspots was found to have no effect on the experiment. Care was taken to make sure that they lay outside the set of annuli. When all the events acquired across the whole active diameter of the MCP were saved, as in the initial experiment described in Section 7.2.3, measurements were carried out to the determine the effect of the deadspots. A set of annuli was chosen such that the outer radius of the last annulus was located just outside the closest region obviously affected by the deadspots. Gain and gain depression measurements were compared for the full annuli and for annuli in which the octant in the direction of the deadspots was masked out in software. No significant variation was noticed between the two sets of measurements.

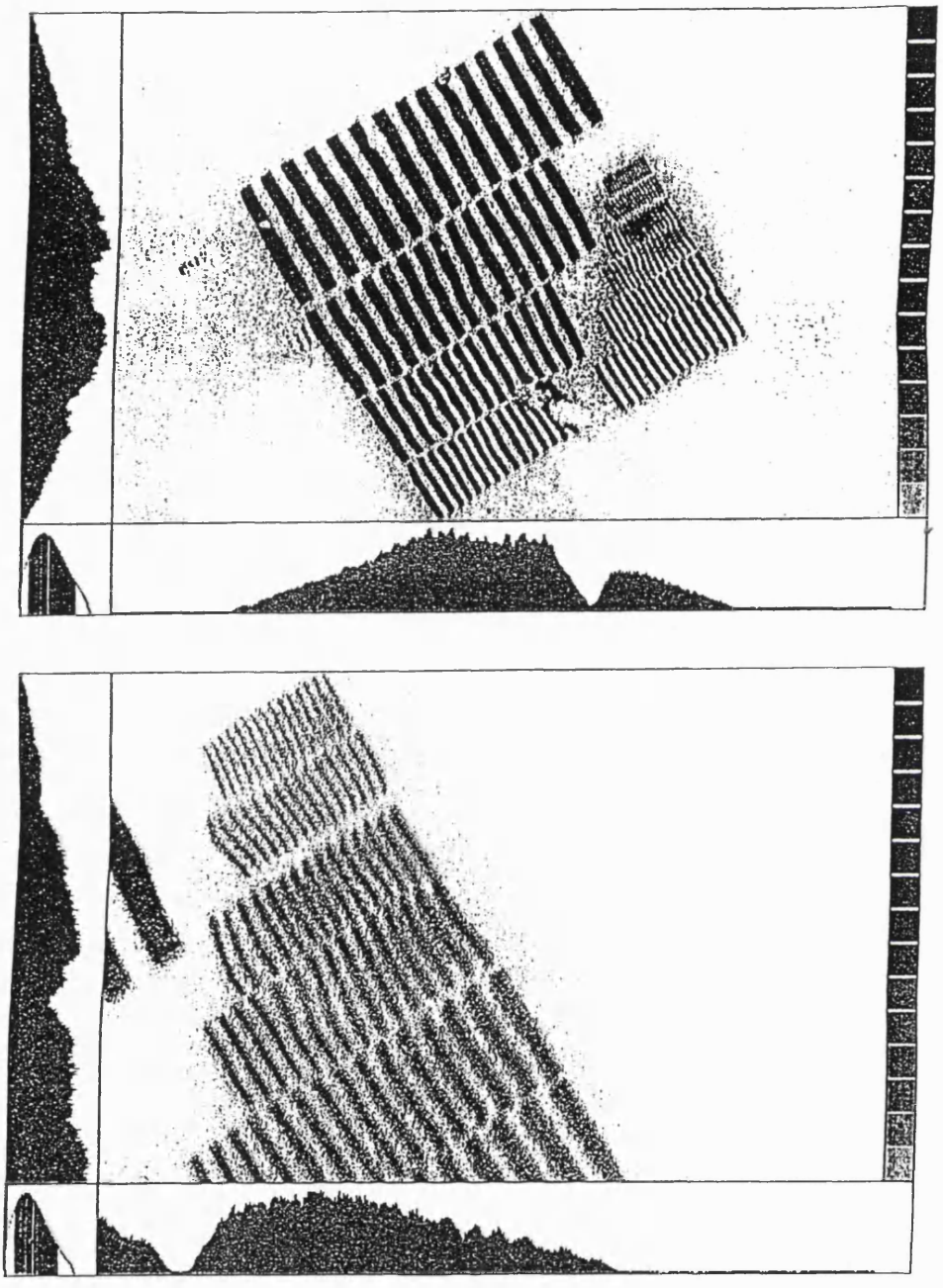

Figure 7.23: Image distortions similar to those in Figure 7.22 after the MCP stack has been rotated by 120° with respect to the readout.
The distortions have not moved with respect to deadspots visible on at the left edge of the bar mask during rotation of the MCPs. The significance of the deadspots on the experiment is discussed in the accompanying text.

7.7 Possible Mechanisms for Long Range Gain Depression

7.7.1 Dynamic, Long Range Gain Depression

In the "dynodised" MCP model developed by Eberhardt (1979, 1980, 1981), the wall collisions inside the pore occur over a preferred distance and the pore behaves as though it were a discrete electron multiplier with a fixed number of dynodes. Most of the charge comes from the last dynode, located at $\sim$ 95 % of the pore length. The equivalent circuit of the dynode, see Figure 7.24, consists of a capacitance and resistance to ground, C_{cl}, approximately 10^{-16} F and $R_{cl} = R_c/(n+1)$ where R_c is the resistance of the pore, $\sim 10^{15}$ Ω, for the plates used in this work. In a chevron pair, it is the last dynode of the bottom plate that provides most of the charge and it is at this point where gain depression would be most severe.

Eberhardt also invokes a lateral capacitance, $C_L \sim 50 \times C_{cl}$ and parallel to C_{cl} in order to explain high gains achieved with Z stacks compared with single plates (Eberhardt, 1980, 1981). The extra charge is provided by a lateral storage capacitance between each of the active pores in an MCP and the quiescent pores surrounding them, see Figure 7.25. This process has been used to explain the adjacency phenomenon (Pearson *et al.*, 1988). Maximum sustainable count rates were obtained when the ratio of quiescent channels to active channels was at a maximum. It was proposed that the lateral capacitance was proportional to the circumference of the excited area and the ratio of circumference to enclosed area increases as the area decreases.

In a simple model, the MCP can be described as a large array of RC circuits in parallel. All quiescent pores should be at the same potential and so the network of parallel elements can be replaced by one RC circuit of equivalent magnitude. This equivalent circuit would be coupled to the active regions of the MCP through lateral capacitance.

This model does not explain the results reported in this work. Charge would be extracted equally from all the quiescent pores. However, in order to be consistent with results displayed in Figure 7.6, charge would have to be removed preferentially from nearby pores, and the amount removed would have to reduce linearly with radius for up to 100 pore diameters. This would require that some series component be present, such as a resistive path in the conductor on the face of the MCP or a variation with distance for the capacitance between pores.

The linear variation of the magnitude of gain depression, suggests that it is sym-

metric around the pinhole. In this work, the pinhole was placed at the centre of the MCP, so we cannot determine what effects the edge of the MCP would have on the symmetry of gain depression. Fraser *et al.* (1991b) have investigated adjacency for a pinhole by illuminating a spot at the MCP centre and at the edge and measuring the ratio $\frac{I_p}{I_e}$. No variation was found and as this is the most likely method of varying the capacitance between the active region and the MCP edge, they conclude that adjacency is independent of relative position of an image on the MCP and that lateral capacitance is unlikely to be the cause. They also point out if adjacency is caused by lateral capacitance it should be present in single plate detectors, which it is not.

Anacker & Erskine (1991) have carried out Kirchoff analysis of the equivalent recharging circuit for the last dynode and found that $\tau \gg 9$ ms. However, using electron time of flight measurements they observed the occurrence of gain depression within 500 ns. The group from Rutherford Appleton Laboratory measured the gain extracted from a MIC detector subjected to an intense flash of 60 μs duration over a 5 × 5 mm square (Carter, 1991b). They find the amount of charge extracted varies across the square, with the maximum extracted at the edges and an approximately constant amount extracted in the centre. This is a direct measurement of interaction between channels occuring in less than 0.1 ms, so charge removal by lateral capacitance is too slow to be a viable mechanism.

A second proposed mechanism for gain depression is pore de-activation, in which the electric field from an active pore interferes with the field in several quiescent channels. In an isolated quiescent pore, the electric field vector $\vec{E}$ is aligned with the channel axis. If they become unaligned the gain is reduced as the electrons will be accelerated for shorter distances and will collide with the channel walls with less energy producing fewer secondary electrons. Gatti *et al.*, (1983) have measured the effect of the inclination of $\vec{E}$ and the pore axis on modal gain by applying an external magnetic field to the MCP. The modal MCP gain $G(\theta)$, as a function of the angle, θ, between $\vec{E}$ and the pore axis, is a nonlinear relationship and very sensitive to θ, see Figure 7.26. They have also shown that the positive wall charge in one channel after the electron cascade can introduce potential changes in the neighbouring pores, which alters the electric field.

When an event occurs in a chevron pair, the positive charge present on the walls of the cluster of active pores in the rear MCP decays exponentially with a time constant proportional to the characteristic time constant of the MCP, τ_{MCP}. Approximating the wall charge as an infinite line of charge with uniform charge density, this charge produces

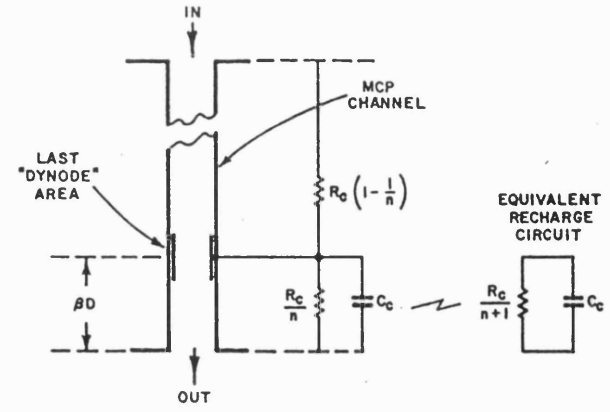

Figure 7.24: The equivalent circuit of the last dynode.
From Eberhardt (1981).

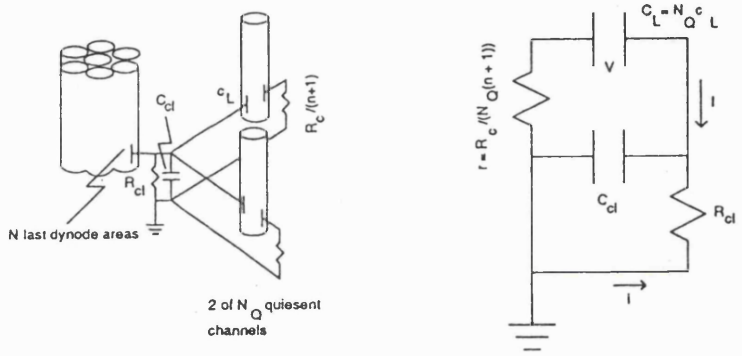

Figure 7.25: Schematic diagram and equivalent circuit of coupling by lateral capacitance between N active pores and N_Q quiescent pores.
From Anacker & Erskine (1991).

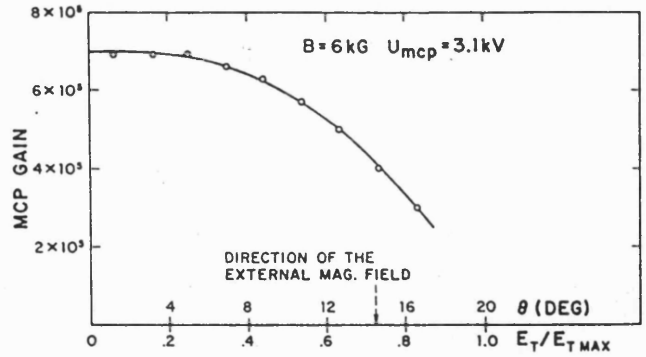

Figure 7.26: The variation of modal gain as a function of the inclination between the electric field the channel axis.
From Gatti *et al.* (1983).

a radial electric field, $E(r) \propto G/r$, where G is the gain of the event, outside of the cluster of active pores (Anacker & Erskine, 1991). This field perturbs the alignment of $\vec{E}$ with the pore axes in the surrounding quiescent pores. If one of these disturbed pores is fired in the presence of $E(r)$, the gain of the pore will be depressed.

Anacker & Erskine (1991) have estimated that there is significant gain depression at radii up to $\sim$ 20 pores for a chevron pair of 40:1 L/D ratio plates with 10 μm pores operated at a gain of 5×10^6 e^{-1}. This is approximately one seventh of the size that observed in this experiment. However, the MCPs were operated at much higher gains in this work.

The perturbing field decreases with radius as was the case for the gain depression that we measured. However, given the nonlinear nature of $G(\theta)$, it is not obvious that there would be a linear relationship between gain depression and radius.

Fraser *et al.* (1992) used a Hg lamp to provide both the intense point source and diffuse source. As a result, they avoided the problem in the difference of gains between the UV and X-ray photons that is a feature of the procedure used in this chapter. Therefore, they could measure the gain depression much closer to the UV illuminated region. They achieved good fits to a gain depression law proportional to $\frac{1}{r}$.

The linear regression fits, such as those shown in Figure 7.11 are carried out only for $r > 0.5$ mm. Its quite possible that we are fitting to an approximately linear region of a $1/r$ curve and the divergence from the linear is much more obvious closer to the pinhole. However, the mixing of the UV and X-ray events prevents measurements in this region where the difference between the two types of law would be most evident. The determination of the size and sign of the index on the power law in the relationship between LRGD and radius was the major motivation for the measurements with the ring. Unfortunately, the mixing of UV and X-ray events in the PHDs made this impossible.

Neither mechanism has an inherent limit on the distance over which gain depression would be significant. Anacker & Erskine (1991) predict that the radius of the region in which the $E(r)$ significantly disturbs trajectories will be $\propto \frac{G}{I_s}$, where I_s is the length of the saturated region of the channel and they predict that this radius increases by a factor of ≈ 2 when the plate voltage is increased from 880 to 930 V. Their model implicitly assumes that the positive wall charge is uniformly distributed along the saturated region. However, the MCPs are being operated at very low saturation as the authors require linear operation for their TOF spectrometry.

As discussed in Section 1.1.3, the wall charge can reduce the secondary emission coefficient, δ, to 1, either by reducing the strength of the electric field or preventing the low energy electrons escaping from the surface. Once unity gain occurs, the local charge density on the channel wall can no longer increase with continuing electron bombardment. Therefore, there will be a maximum wall charge density defined by the intrinsic properties of the glass. As the channel is driven further into saturation or with increasing gain depression, the length of the pore with this maximum charge density will change but the actual charge density will not.

As the perturbing electric field can be approximated as a purely radial phenomenon with magnitude dependent on the charge density, the maximum wall charge defines a maximum electric field strength and therefore a maximum radius over which trajectories will be perturbed. So the length over which the trajectories are disturbed in the neighbouring, quiescent pores will increase but not the distance at which pores are affected. Therefore, the magnitude of the gain depression could vary with plate voltage and count rate but the spatial extent will remain approximately constant.

This is the behaviour indicated in Figure 7.12 where the limiting radius of the gain depression is a constant over a wide range of operating conditions but the magnitude of the gain depression, as indicated by $\overline{G'(0)}$ does vary with operating conditions. At low count rates, i.e. 300 Hz, $\overline{G'(0)}$ does reduce monotonically with plate voltage.

Fraser *et al.* (1992) have measured the gain depression profile for a variety of front plate voltages keeping the rear plate at 1300 V. They find no significant variation at varying from 1250 to 1350 V. The combination of their measurements and those presented in this chapter cover a range in gain of approximately 5 and 300 V in plate voltage for similar MCPs and produce gain depressions with similar scales.

Fraser *et al.* (1992) also investigate a recharge model with a reservoir of charge of fixed depth, G_{max}, which is the maximum deliverable or stored charge, as proposed by Nicoli (1985) and Cho (1989). In this model, the channels do not discharge completeley for each event and the gain for a given pulse depends on the magnitude and temporal spacing of the previous pulses in that channel. Their model predicts that at high count rates the PHD will lose its peaked profile. However, as discussed in Section 1.1.4, the saturation remains essentially constant with increasing count rate. They also observe that the value of G_{max} decreases with increasing count rate. They conclude that the central assumption of the reservoir model is incorrect and that the reduction of G_{max} is due to a perturbing,

radial electric field.

The variation of $\overline{G'(0)}$ is only monotonic with count rate for a given plate voltage. However, the measurements of gain depression are averages of samples taken at various stages of the recharge in the active channels. The higher the count rate, the higher the probability of sampling events occurring sooner after the active channel events and therefore being exposed to a larger radial electric field during the cascade. So the variation of $\overline{G'(0)}$ with count rates is not necessarily evidence of an increased length in the saturated region.

7.7.2 Long Term, Long Range Gain Depression

Given that the spatial extent of the long term gain depression is comparable to that of the dynamic LRGD, it is reasonable to assume that one mechanism causes both the long range effects. MCP gain can be permanently reduced by baking and scrubbing. Baking causes outgassing of molecules adsorbed to the walls of the pore. Rager *et al.* (1974) reported that MCPs baked at 200° C had their gains depressed by 40% and when they were exposed to air once more, the gain recovered over a period of 2 months. When baked at 250°, the gain was depressed by 70% but did not recover when the plates were subsequently exposed to air.

During scrubbing the channels are exposed to prolonged electron bombardment to remove the excess gas from the surface of the MCP that was absorbed during reduction. The MCP surface is exposed to uniform illumination to minimize variation of gain across the MCP. The most prevalent gas desorbed during scrubbing is hydrogen with amounts of water vapour and methane (Hill, 1976). A side effect of scrubbing is the reduction of gain, after $\approx$ 0.05 C.cm^{-2} has been extracted, the gain is reduced by a factor 2-3 (Siegmund, 1989) and extraction of $\approx$ 1 C.cm^{-2} can reduce the gain by a factor of 20 (Read *et al.*, 1990). The later scrub can reduce the partial pressure of hydrogen desorbed during bombardment by a factor of approximately 70 to 0.2 $\times$ 10^{-9} Torr.

Authinarayanan & Dudding (1976) have investigated the effect of electron bombardment on the surface of a reduced lead glass as used in channel electron multipliers. They find that δ varies progressively with electron bombardment, see Figure 7.27.

The only mechanism which could cause the long term LRGD by gas desorption is heat, since there was no prolonged electron bombardment of the channel walls in regions that were not exposed to intense UV. The only source of heat is the Joule heating due to

the strip current and, possibly, the current due to charge transferral between quiescent and active pores.

If charge extraction is the cause of dynamic LRGD, we can estimate the total amount of charge transferred from the quiescent pores by combining the values of $\overline{G'(0)}$ from Figure 7.12. It can only be estimated for the pinhole as a much larger proportion of the area measured for the ring images had considerable UV flux. The total "missing" charge can be estimated from the volume of the cone with base radius 1.7 mm and height $1 - \overline{G'(0)}$ times the quiescent gain as measured in the flat field. This value represents an approximation as it extrapolates the linear range of the gain to zero radius, i.e. into the region where there is significant UV illumination. The "missing" charge would be transferred from each of the groups of channels that are fired in the bottom plate by one X ray event. Carrying out a calculation similar to that in Section 4.4.5, approximately 25 pores are fired in the bottom plate for each sampling event and it is assumed that the charge is transferred equally from each of these pores.

The maximum, total current transferred from the quiescent pores would be associated with the 4.5 kHz data, as shown in Figure 7.12, and is < 10 nA. The estimate of the total charge transferred from the affected area during the experiment is $\approx 2 \times 10^{-4}$ C which corresponds to $\approx 2 \times 10^{-3}$ C.cm^{-2}. A total extracted charge comparable to this estimate, can introduce long term gain depression of the order of 10 % during scrubbing (Barstow & Samson, 1990).

The strip current is estimated by using the measured resistance when no high voltage was applied to the MCPs, i.e. 640 MΩ, and estimating the number of channels which yields $R_{ch} \approx 3.3 \times 10^{15}\Omega$. The resistance could have reduced appreciably when high voltage was applied due to heating by the strip current (Pearson *et al.*, 1987).

The current transferring the charge to the active pores should flow through the same regions of the pore walls as the strip current, i.e. the conducting layer in the channel wall which is approximately 100 times larger than emissive layer (see Section 1.1). Also, the average current per pore in the affected area, due to charge transfer, during the most severe gain depression we measured, would be < 20 % of the strip current (not 10 % as I reported in Edgar *et al.*, 1992b).

Pearson *et al.* (1987) have calculated that the strip current raises the temperature of an MCP approximately 4° C above the ambient temperature. It is unlikely that the extra currents due to charge transferral could produce enough heat to produce the high

temperatures and the rate of gas desorption that occur during baking. And as most of any extra current would flow through the conduction layer in the channel wall, it is unlikely that charge transfer could cause gas desorption from the surface layer of the channel except by heat. Also, if charge transferral was raising the channel temperature a significant amount, R_{ch} should be reduced more as the number of illuminated channels is increased. Therefore, $\frac{I_p}{I_e}$ should increase with illuminated area which is the opposite of what is actually observed (Fraser *et al.*, 1992).

Although outgassing occurs during scrubbing, it has been argued that the gain depression is due, at least in part, to continuous, prolonged electron bombardment changing the emissive properties of the surface layer of the pore walls (Rager *et al.*, 1974 and Siegmund, 1989). Authinarayanan & Dudding (1976) found that K was removed from the surface of the glass during electron bombardment, see Figure 7.28. As shown in Figure 7.29, δ is sensitive on the K concentration in the surface layer (Hill, 1976). Removal of K from the surface layer will reduce δ and hence, the gain.

The Potassium is present in the glass as K_2O. Authinarayanan & Dudding (1976) point out that direct momentum transfer from the bombarding electrons is insufficient for disassociation of the K_2O. They and Hill (1976) propose a mechanism where the positive charge built up on the glass surface produces a large electric field which causes K^+ ions to move away the surface into the bulk material. Therefore, direct electron bombardment is not necessary to remove K from the surface layer, but only exposure to an electric field. Therefore, the positive wall charge in an active channel could induce an electric field in the neighbouring pores and thereby remove K from the emissive layers of these quiescent channels.

If a electric field is causing K to migrate out of the surface layer of neighbouring pores, the amount of K removed probably varies with azimuthal angle around those pores. It is possible this is the cause of the image distortions seen in Figures 7.22 and 7.23.

The radial electric field could explain why gain depression is less in the region actually illuminated, than in the surrounding quiescent areas. The active pores should have a similar amount of positive wall charge, and so large potential differences, and therefore electric fields, should not be present within the active areas.

Fraser *et al.* (1992) did not observe long term LRGD. The only long term gain depression that they observed was in the region that was actually exposed to the intense point source. As the long term LRGD appears to be closely associated with plate pre-

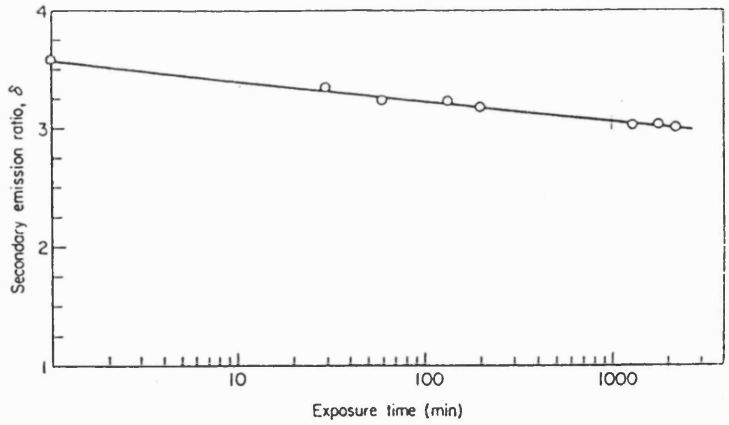

Figure 7.27: The reduction in δ for reduced lead glass with progressive electron bombardment.

From Authinarayanan & Dudding (1976).

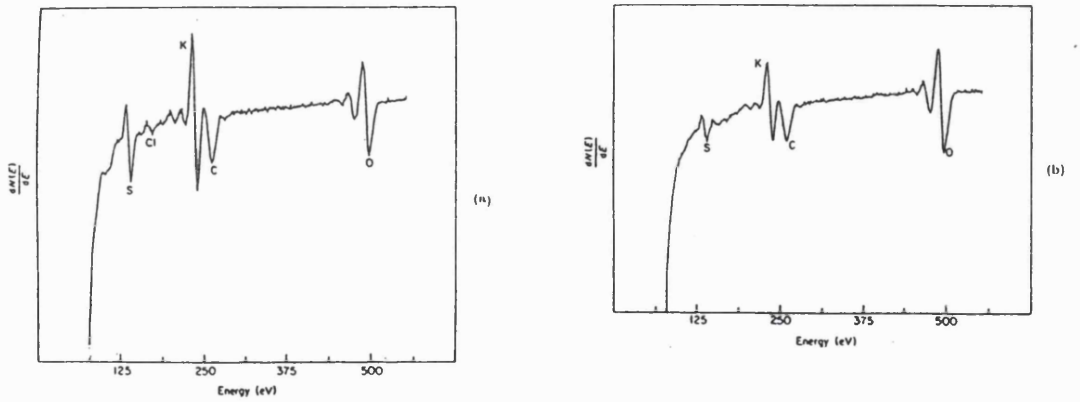

Figure 7.28: Auger spectrum of regions of reduced lead glass that are unexposed figure a, and that have undergone intense electron bombardment, figure b, which shows that K has been removed from the surface layer as its concentration has been reduced compared to C.

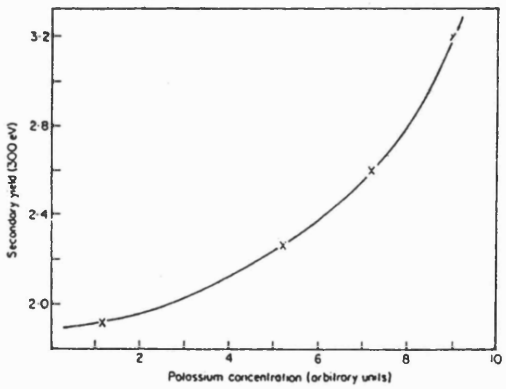

Figure 7.29: Variation in δ with K concentration in the surface layer.

From Hill (1976).

conditioning, it is highly probable that variation in the preconditioning will produce large variations in the magnitude of the observed long term, gain depression. More extensive scrubbing almost certainly removes the effect completely otherwise it would have definitely been observed previously. The MCPs used in this chapter only had a light scrub and it appeared that the gain depression appeared to saturate after a relatively short UV exposure. It would certainly be interesting to carry out a series of measurements with sets of MCPs that have undergone a variety of preconditioning procedures.

Long Term Recovery of Gain

Authinarayanan & Dudding (1976) and Hill (1976) have found that if after the bombardment, the surface is exposed to a hydrogen atmosphere, δ, and therefore the gain, will recover by approximately 10 %. The two experiments used partial pressures of $\approx 10^{-6}$ and 10^{-3} Torr, respectively. Exposure of the glass to a partial atmosphere of oxygen did not lead to a recovery in δ. Hill (1976) also failed to find any recovery when exposing the glass to air or methane.

The recovery of the gain over a period of weeks, as seen in Figures 7.18, would require that there was a substantial partial pressure of hydrogen present over this period. The chamber was pumped continuously during the experiment and the MCPs were open to the vacuum at both ends of the stack. Although our vacuum (5×10^{-7} Torr) is not particularly good, it is unlikely that a high partial pressure of hydrogen is present. The partial pressure of hydrogen released during initial scrubbing is of the order of 10^{-8} Torr. Even assuming that gas desorption is the cause of long term LRGD, the 2 mm radius area affected represents only 0.3% of the MCP surface area. Therefore, only an extremely small amount of hydrogen would be desorbed.

The major component of the gas present in the vacuum chamber is laboratory air. It is extremely unlikely that this will cause recovery, as Hill (1976) found no effect. Also, exposure to laboratory air for several weeks did not lead to a more complete recovery of the gain for the region surrounding the pinhole, see Figure 7.16, than that surrounding the ring.

One possible mechanism is that after the K has migrated out of the surface layer under the influence of the electric field and when the surface charge is removed, the K can diffuse back to the surface over a long period of time. The author is unaware of any

discussion of this in the literature. At present, the cause of gain recovery remains a mystery.

7.7.3 Conclusion

It appears that there are severe problems with explaining either dynamic or long term LRGD with charge transferral from quiescent to active channels. However, there are plausible mechanisms for both types of LRGD with the transverse electric field model. Therefore, in line with the conclusion of Edgar *et al.* (1992a), rather than my more timid discussion in Edgar *et al.* (1992b), the most probable mechanism for interaction between pores is the perturbation of the axial electric field, established by the plate voltage, by a transverse electric field due to the positive wall charge developed in active channels during the electron cascade.

It is particularly interesting that various phenomena in MCPs, saturation, "conventional" gain depression, dynamic LRGD, which is the mechanism causing adjacency, and long term LRGD can all be explained in terms of the wall charge.

Chapter 8

Conclusions and Future Work

8.1 The Size of the Charge Cloud

In Chapter 3, techniques and analysis that can successfully determine the size and form of the radial distribution of the electron cloud leaving the MCP were demonstrated. The underlying assumptions, necessary conditions and limitations of these methods were also analysed in detail.

Measurements of the distribution of the charge cloud for a wide variety of MCP operating conditions were presented in Section 4.1. These are the only measurements of the radial distribution and the most extensive set of measurements of the size of the charge cloud that have been presented in the literature.

At least two components are always necessary to successfully describe the distribution; a narrow central component and a broad wing component. These two terms are sufficient for a successful fit in almost all cases.

Under most of the MCP operating conditions the radial distribution of both these components has an exponential form, the scale size of the central component being approximately one third that of the wing component. However, this may not necessarily always be the case. The form of the central component appears to become progressively more Gaussian with increasing electric field strength across the MCP-anode gap, E_g. In most instances, the central component is dominant, containing most of the charge.

At high values of E_g, the form of the wing term also changes and it can be best described as a constant amplitude offset. The manifestation of this flat wing appears to be closely associated with the onset of modulation. Measurements suggest that modulation is

not just a function of the charge cloud size but arises from the actual form of the radial distribution. It is possible that the modulation is caused by the introduction of higher spatial frequency terms into the distribution or that the flat term is itself an artefact of modulation. As modulation is a problem for all centroiding readouts with a repeat pitch, the origin of this flat term and its link with modulation are worthy of further intensive investigation.

The electric field in the MCP-anode gap is the operating parameter that has the largest effect on the size of the charge cloud. The size reduces by a factor ≈ 3 as E_g increases by a factor of ≈ 40.

It was found that a simple ballistic model could not explain the relatively large charge cloud size. Mutual repulsion between the electrons in the charge cloud as they cross the anode gap is, most probably, the most important factor in determining the size of the charge cloud.

However, variation in gain alone does not explain the variations in charge cloud size when varying plate operating conditions other than E_g, e.g. plate voltage and inter-plate gap voltage. This strongly suggests that the initial conditions of the charge cloud, i.e. the distribution of the electrons' exit velocities and the complex interaction of electric fields at the end of the pore, significantly affect the charge cloud size. The combination of space charge and variation of the initial conditions would make any predictive model exceedingly complex.

The charge cloud is slightly elliptical, the average ratio of the major to minor axis is ≈ 1.1. Prehaps unexpectedly, the major axis is in the plane of the channels, rather than normal to this plane.

Variations in the properties of individual MCPs, in particular the endspoiling, and the stack geometry would be expected to produce large variations in the distribution of the charge cloud. For example, the results presented are probably only applicable to detectors using charge division anodes. The large voltages applied across the small MCP-phosphor gaps in light amplification detectors, will produce very small electron transit times and so the mutual electron repulsion will have less time to accelerate the electrons to high transverse velocities. Therefore, these detectors will operate in a region closer to the purely ballistic effects limit. This could explain why the charge clouds measured for the MIC detector are more elliptical than in the case measured here, due to the variation of electron velocity distribution with azimuthal angle around the pore. The form of the radial distribution

for these detectors may also be much better described by a Gaussian rather than by an exponential.

A truly quantitative, predictive model would require a large data set containing measurements obtained for many types of MCPs, configurations and at a wide range of operating conditions. If it was possible to develop such a model, it would have to be exceedingly complex to accommodate the large number of degrees of freedom. Therefore, while the techniques demonstrated can successfully measure the radial distribution of the charge cloud for a given, or similar, detector, the resulting measurements will be of limited utility for anything other than qualitative extrapolations to other detectors.

8.2 The Interaction Between Pores

In Chapter 7 a novel and successful technique for directly measuring the spatial extent of gain depression was presented. Measurements of the long range effects of gain depression were also presented. These results included the first direct measurements of the long range effects of gain depression published in the literature.

Gain depression is a long range phenomenon. When a group of pores fires in the bottom plate of a chevron stack, the gain is significantly depressed in channels up to 1.7 mm away, i.e. more than 100 pores for the MCPs used. The spatial extent of the gain depression is constant over a wide range of operating conditions but the magnitude of the depression varies. The magnitude of the gain depression also depends on the morphology of the illuminated region.

The most probable cause of the long range gain depression is the positive wall charge that is developed on the wall of the channel during the electron cascade. This produces a radial electric field that perturbs the electron trajectories in the quiescent channels, reducing the kinetic energy the electrons acquire between collisions with the wall and thereby reducing the number of secondary electrons emitted in the collisions.

The perturbing, radial electric field can explain the adjacency phenomena. As the area illuminated with a constant flux increases, there will be an increased probability of subsequent events arriving in the affected area surrounding a group pores that have fired, sooner after those pores have fired. Therefore, these subsequent events will be subject to a larger perturbing electric field and the magnitude of gain depression will be larger. If the gain depression is large enough, a spatio-temporal deadtime would be produced which

would cause the variation of the sustainable count rate with illuminated area.

The maximum spatial extent of the gain depression is probably set by the maximum positive wall charge that the channel wall can sustain that does not reduce the secondary electron emission coefficient to 1. The magnitude of the gain depression increases monotonically with count rate in the active region of the MCP but increases monotonically with plate voltage only at low count rates.

Gain depression can also be a long term and long range phenomenon. Prolonged, intense illumination in one region can produce a gain reduction of $\approx 20\%$ in surrounding pores, at distances of ~ 0.5 mm. The gain recovers over a period of weeks but can still be seen up to several months later, after repeated cycling between air and vacuum and prolonged exposure to air. This long term gain depression can introduce significant image distortions, $\sim 60\ \mu$m, even after a month. The mechanism of this long term, long range gain depression is unlikely to be gas desorption but is most probably due to the radial electric field induced by the positive wall charge in active pores, causing potassium ions to diffuse from the thin emissive layer of the wall into bulk material. This reduces the secondary emission coefficient of the wall which reduces the gain.

At present the only direct measurements made of the spatial extent long range gain depression have been carried out with two similar sets of plates. Further measurements of long range gain depression should include different types of MCPs, particularly those with lower resistance. In order to determine the index on the power law with radius, measurements should be made for rings with as many diameters as possible. This would also confirm whether the mechanism is due to an electric field or not, as the electric field should cancel at the centre of the ring.

The technique used in this work was satisfactory for determining the spatial extent of gain depression but it should be modified for further work. At present there is some uncertainty about the index on the power law in the gain depression versus radius relationship. Using the same energy photons for the intense illumination and the diffuse, sampling events should help determine this value by removing the problem of the mixing of UV and X-ray events in the PHD. However, it would still be important to retain two independent light sources so that there is no coupling in the intensities between the two types of events and so that flat fields can be obtained immediately preceeding and after intense illumination.

The values of gain used in the analysis in this work are the average gain of the PHD in each annulus. However, the events arriving in these annuli are arriving at various intervals

after an active channel has fired, so they also contain the effects of temporal variation in the electric field strength. In order to fu rther investigate adjacency, it will probably be necessary to time tag individual events. This would require a realtime system and the ability to acquire many times more contiguous events than the 1000 that can be acquired at present. It would also be necessary to provide an intense source of illumination with accurately known flux. Given its property of ghosting low pulse height events, SPAN would not be the ideal readout for examining deadtime effects. High spatial resolution would not be necessary but photometric linearity, in a region of severe gain depression, would, so a WSA would be appropriate.

It would also be worth carrying out a series of measurements with some plates that have not undergone scrubbing. Ideally, this should carried out in a very clean, high vacuum system with the ability to measure the partial pressure of the desorbed gas. This would allow measurements of the long term, long range gain depression during progressive scrubbing of the plate and should provide further evidence that potassium migration is the mechanism.

Measurements of dynamic gain depression during a progressive scrub would also confirm whether the magnitude of the positive wall charge determines the maximum spatial extent of dynamic gain depression. If this is the case, the spatial extent should vary during progressive scrubbing of the plate.

8.3 The Spiral Anode

In Chapter 2 mathematical analysis of cyclic, continuous anodes was presented. This demonstrated the principles of operation of three examples of these detectors and established the suitability of treating electrodes as orthogonal oscillators and the resultant Lissajous figures.

In Chapter 5 the method of operating SPAN was described. For the SPAN anode, mapping into polar coordinates produces a series of parallel lines and the major difficulty is identifying with which of these lines each event is associated. It was also demonstrated that this problem occurs in each of the other types of cyclic, continuous readouts considered and can be solved in a similar manner. Two different methods for determining the position of the lines were evaluated in detail for real data. The Hough transform offers superior performance over methods based on various types of edge detectors.

The spiral anode (SPAN) has exhibited good spatial resolution. The centroiding PSF is equivalent to that of the delay lines and only the MIC detectors have significantly better resolution. It also exhibits excellent positional linearity, ≈ 30 μm which is comparable to the best achieved with other charge division detectors.

8.3.1 Problems with SPAN

The major problem with the SPAN detector has been identified and the probable mechanism determined. The SPAN readout relies on accurate measurement of the radius of the spiral Lissajous figure, r, which is needed to determine the coarse position. However, there can be a strong variation of r with pulse height. The most probable cause of these differences in r is variations of the charge cloud size with varying gain. If uncorrected, the r variations produce significant ghost images. Two methods have been demonstrated that can correct for this variation but there is a lower limit in pulse height for which they are effective. It is at this level which the LLD should be set to eliminate ghosts. For future development of SPAN, it will be necessary to understand precisely what determines the magnitude of these variations and why they vary from detector to detector.

The problems of ghosting cannot be overcome with only a tight PHD, as intense point illumination of a given region of the MCP will depress the gain and move the modal gain to lower pulse heights. Therefore, the readout must be able to cope with a wide range of pulse heights. The position of the LLD necessary to reduce ghosting will determine the photometric linearity of the detector. However, the LLD is usually set quite low, and the events lying below it would produce low resolution due to their low gain.

Significant position shifts, ≈ 60 μm, are also produced by variation in gain. They are caused by a shift in the spiral phase angle, ϕ, with gain. In this work, I have concentrated on variation of r, as this is the fundamental problem with SPAN. These position shifts are also probably caused by the interaction of the electrode geometries with the charge cloud but will require further study. As the gradient between ϕ and gain appears to be constant around the spiral, the position shifts could be corrected in a similar manner to the corrections for r.

The variation of r with gain is much larger than the variation of ϕ. Therefore, the Vernier and the Double Diamond readouts should not suffer from ghosting as the separation of the parallel lines would be much larger than their widths. As the lines would be much

narrower, it should also be possible to fit more cycles on each pattern and so simultaneously increase the resolution and reduce the fixed patterning.

8.3.2 Proposed Real Time Operating Systems

All measurements carried out in this work with the SPAN have been hampered by the low speed of the data acquisition. A real time data acquisition system is the most urgent requirement for the continued development of SPAN.

Large Look Up Table Decoding

The most straight forward data decoding system is to use a single, look up table (LUT). Assuming that an 11 bit address is output, the minimum practical depth of this LUT will be 12 bits, i.e. 1.5 bytes. This is the depth of the LUT that will be used throughout the rest of the discussion in this section.

The three ADC values cannot be used as the inputs to the LUT as this would require 1.5×2^{3n} bytes, where n is the number of bits digitization, i.e. 24 MB for 8 bit digitization. This is clearly impractical. As discussed in Section 6.4, after normalization with respect to pulse height, the third ADC value is redundant. Therefore, the LUT only requires 1.5×2^{2n} bytes, i.e. 96 kB for 8 bit digitization. An algorithm for generating this smaller LUT has been developed by the author. It only requires the spiral constants k and ψ and the width of the envelope from which events will be accepted.

The digital electronics of this type of decoding has been simulated using a Motorola 56001 Digital Signal Processor (DSP) mounted on a VME bus. There are First In First Out (FIFO) memories on the digital inputs, which derandomize the event arrival times. Each event cycle consists of combining two 8 bit numbers from the ADCs into a 16 bit address, presenting this address to the LUT and storing the 11 bit output in a register. This part of the cycle is carried out twice, for the two dimensions, and the two 11 bit values in the registers are combined into a 22 bit address. This address is passed down the VME bus to a 8 MB RAM card configured as 2048 x 2048 histogram, 2 bytes deep. The value stored at this 22 bit is incremented by one. Throughput rates of 250 kHz have been achieved with this system (Kawakami, 1992).

However, this system makes no allowances for any pulse height variations. Measurements made with LUTs generated for the two dimensional SPAN used in this work,

indicate that if the PHD is subdivided into at least 4 bins, ghosting can be eliminated. Thus 4 LUTs would be required, one for each PHD window. As a consequence the pulse height related position shifts would be reduced to the level of the pore spacing. These 4 LUTs could be combined into one large LUT of size $1.5 \times 2^{2(n+1)}$ bytes, i.e. 384 kB for 8 bit digitization.

Increasing the digitization by 1 bit will increase the amount of memory required by a factor of 4. Its therefore impractical to use the LUT method for larger digitizations. Similarly adding three noise bits to reduce fixed patterning is also impractical.

Hough Transform Decoding

Figure 8.1 shows a proposal for a real time decoding system not based on large LUTs. It is based on the decoding method using the Hough transform in realtime, see Section 5.4. It has not been constructed but the decoding segment has been simulated in software.

In the example in Figure 8.1, ratiometric ADCs are used and a SPAN with a phase difference of 90°. The 90° SPAN is used to simplify the coordinate transformation. No floating point operations are required and so the transformation can be carried out with simple digital electronics. This example shows a one dimensional detector, for simplicity. In a two dimensional detector the two sets of ADC values would probably be multiplexed through the same sets of digital electronics, so a FIFO would be placed after the ratiometric ADCs. This has the added advantage of derandomizing the data arrival times. It would require four ratiometric ADCs and a fifth conventional ADC to provide pulse height information for both dimensions.

The heart of this system is the Pythagoras Processor which carries out realtime conversion from Cartesian to polar coordinates. Two manufacturers currently supply such chips; the PDSP 16330 (GEC Plessey, 1990) and the TMC 2330 (TRW, 1991). Both chips offer similar performance and carry out the conversion of two 16 bit inputs into a 16 bit magnitude, r, and a 12 (the PDSP 16330) or 16 bit (TMC 2330) phase angle, ϕ, at 25 MHz.

Both of the outputs on each of these chips have an accuracy greater than that required. The r_n/h' plots in Chapter 5 contain only 550 pixels across the entire r_n axis and not all of the axis is used. So 9 bits gives sufficient accuracy for the radius measurement. An accuracy of 10 bits on the phase angle is sufficient to ensure that each of the 2048 output

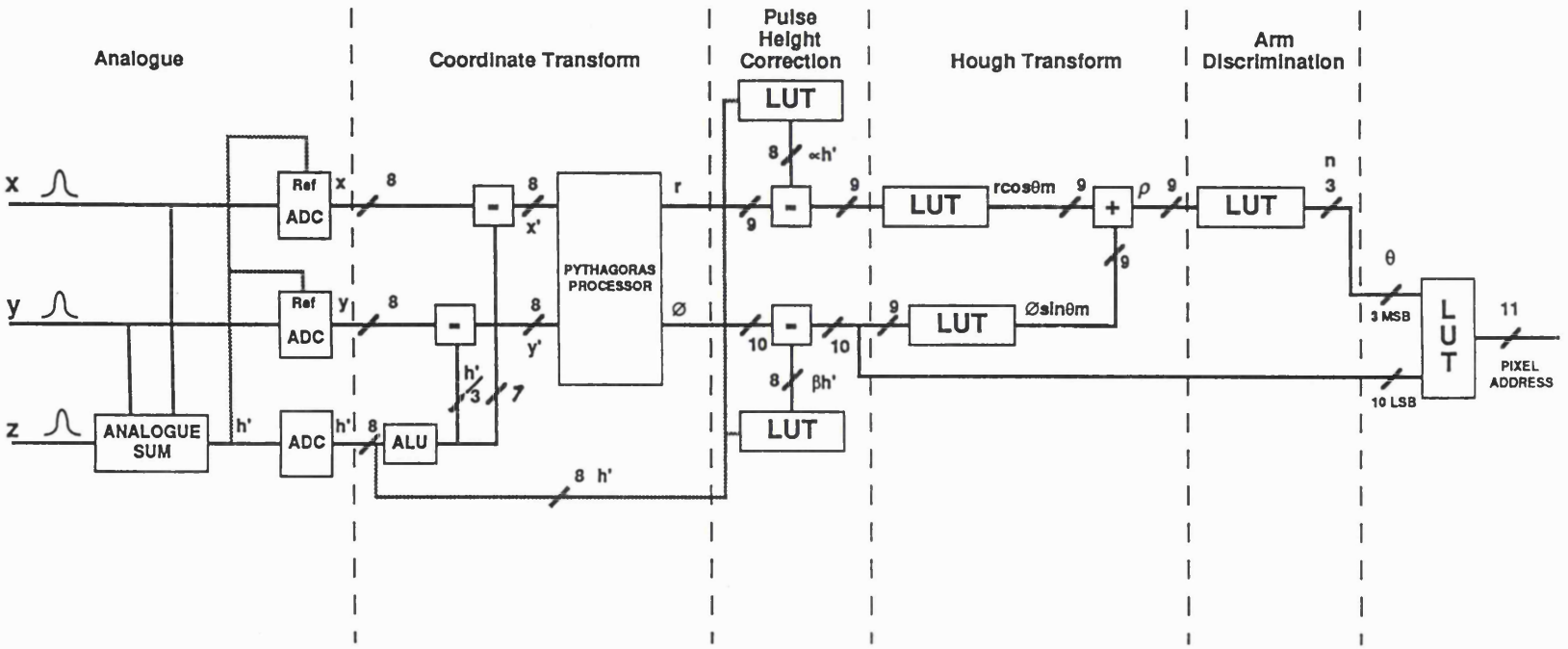

Figure 8.1: Schematic diagram of a proposed realtime decoding system based on the Hough transform.

This decoding system is discussed in detail in the accompanying text.

pixels are addressable by combining the coarse and fine positions.

The correction for pulse height related effects would be performed using LUTs providing a correction value which is then subtracted from r and ϕ. The subtraction would be a straight forward operation on two binary numbers and could be carried out in simple digital circuitry. As the corrections will be much smaller than the full range of the values of these two parameters, an 8 bit correction will be more than sufficient. Therefore, the correction can be carried out with two 256 byte LUTs. The values in the LUT would be calculated separately by using the pulse height/parameter gradients which would be measured in a manner similar to that described in Section 5.3.3.

The Hough transform would be carried out with three LUTs and a binary addition. As the value θ_m that corresponds to the gradient of the spiral arms would have been determined separately, the Hough transform would be reduced to

$$\rho = r\cos\theta_m + \phi\sin\theta_m \quad . \tag{8.1}$$

The LUTs would be loaded with the appropriate values corresponding to the two parameters multiplied by the trigonometric values. As discussed in Section 5.4, only 9 bits are necessary for arm discrimination, so the two LUTs need only be 512 × 1.5 bytes each, giving a total of 1.5 kB. The actual arm discriminator LUT would only require 512×0.5 bytes as only 2-3 bits would be necessary for the spiral arm number, n.

The values of n and ϕ would be combined to form a 13 bit value of θ, the spiral angle; n forms the 3 most significant bits and ϕ the 10 least significant bits. This value would be used as the address for a last 12 kB (8 k×1.5 bytes) LUT which contains the final image pixel address.

Therefore, a system could be built that will run fast enough for the 200 kHz random event rate required by the Optical Monitor. The total memory requirement, including pulse height related corrections, is $\sim$ 14 kB, approximately 25 times less than that required for the large LUT decoding. Also, the number of bits on the inputs can be increased without increasing the total memory requirements. Therefore, up to 16 bit ADCs could be used for this system, which would require 24 Gigabytes for the large LUT method, or random extension bits could be added to reduce fixed patterning.

8.3.3 The Analogue Front End

The largest problem with respect to the count rate performance of SPAN is the analogue front end. Fast flight qualified preamps have been developed for the SOHO CDS Grazing Incidence Spectrometer (GIS) (Breeveld & Thomas, 1992). The preamps use a shaping stage with a 148 ns shaping time and have a maximum count rate of 175 kHz. The equivalent input noise with this shaping constant is 1.5×10^4 e^-, which corresponds to a SNR of $\sim 1000:1$ assuming an average MCP gain of 5×10^7 e^- distributed evenly between the three anodes. While the two dimensional SPAN has demonstrated a centroiding PSF of 17 μm, this was with non-flight electronics and a time constant of 2 μs. The PSF has not been measured while using high speed electronics and this should be carried out as soon as possible.

As discussed in Section 6.4, another limitation is the analogue bandwidth on the reference input of ADCs. However, devices are available that can probably operate at count rates up to 200 kHz.

8.3.4 The Suitability of SPAN for Use in Space

In May 1992, due to failure of two image tube manufacturers to deliver working tubes, of the five tubes delivered five failed, SPAN was withdrawn from consideration for the Optical Monitor and the MIC detector was chosen.

SPAN requires relatively high gain to achieve good resolution. Therefore, the MCPs cannot undergo extensive scrubbing before the tube is sealed. The best spatial resolution obtained with a sealed tube containing SPAN was only 60 μm FWHM. This was due to the low gain, 3×10^6 e^-, approximately 10 times less than that used for the detector described in this work, as the MCPs had undergone a scrubbing regime similar to that used for the MIC detector. As MIC requires lower gains than SPAN, it can therefore undergo more extensive scrubbing and so should have major advantages with respect to tube lifetime. The spatial extent of long range gain depression may also be reduced.

The point source count rates for SPAN, and most other charge division anodes, is limited only by the recharge time of the channels. This is the major advantage of these readouts over scanned readout devices such as the CCD. Low resistance plates would have to be used to meet the specifications for the Optical Monitor, although the effects of these plates on tube lifetime have no been determined. Charge division anodes are also inherently

radiation tolerant.

The amount of power available for the detectors is quite small, 7 W for the blue detector on Optical Monitor (Bray, 1992) and 13 W between four detectors for the GIS on SOHO CDS (Breeveld *et al.*, 1992). The small power allocations are the critical problem for the SPAN detector. It requires that 8 bit ADCs are used as both these authors conclude there are no radiation tolerant, high reliability ADCs with more than 8 bit digitization and low enough power consumption. There is also insufficient power to allow combining two 8 bit ADCs together to attain 9 bit digitization.

Power constraints also place constraints on the amount of memory that can be used for each detector. The GIS requires a LUT for each detector and so requires a total of 256 x 2 kB of RAM (McCalden, 1992). This is without any pulse height correction and so requires that SPAN behaves ideally. Unless the MCPs can be operated in a regime where the pulse height radius gradient is extremely small, which has been achieved on some occasions, the detectors will either be plagued by severe ghosting or a significant degradation in the photometric linearity of the detector will have to be accepted.

The size of the LUT also precludes telemetering the LUT contents from Earth. A flat field will be telemetered to Earth and the spiral constants determined. This will be sent to the satellite. An algorithm, based on one written by the author, will be used to calculate the LUT on board. This algorithm consists of approximately one quarter of the total memory space required for on board software for the GIS due to need to use floating point software libraries.

The Hough transform method of decoding could reduce the amount of memory required while still providing pulse height related corrections. At a rate of 10 MHz, the PDSP 16630 dissipates 400 mW. As only a 200 kHz throughput would be required, a significant reduction in power consumption would be expected. MIL-Spec versions of both of the chips are available, but they are both fabricated using 1 μm CMOS technology. Therefore, their radiation tolerance must be suspect. However, Inmos Transputers have passed radiation tolerance tests for the GIS (McCalden, 1992), so it is feasible that a radiation tolerant batch of these chips could be selected. The power consumption and radiation tolerance of these chips should be evaluated in the near future.

As was shown in Chapter 6 and by Breeveld *et al.* (1992a), the largest single problem associated with low bit digitization is fixed patterning. Both the SPAN detectors have a requirement for 2048 pixels but the SOHO detector has 4 spiral arms and the

Optical Monitor detector 3 in the active diameter. However, they both exhibit severe fixed patterning. Constraints on the anode designs will probably prevent any further significant reduction in the magnitude of fixed patterning through varying anode design parameters.

With the constraints on digitization and resolution there is almost no prospect of reducing fixed patterning by using a different set of user defined parameters than those used at present. Limitations on memory size also preclude the use of extension bits. The only remaining the option is to iteratively reassign the vertices in the hexagonally packed lattice in the spiral plane to different output pixels, in order to produce uniform pixel sensitivity. A similar method is used in the MIC detector (Carter *et al.*, 1990, 1991b) but the correction is reliable for only a given set of MCP operating conditions and for a localized region. Varying these conditions, such as gain and charge cloud size can reintroduce fixed patterning. The stability of such a correction in SPAN is unclear, as it must hold across the entire width of the detector even when some regions are driven into severe gain depression.

SPAN has the potential to be a high speed, high resolution detector. It probably needs only $\sim$ 8 bit accuracy on the analogue charge measurement to attain good resolution. This has yet to be confirmed experimentally but it is suggested by the lack of variability in the image sizes in the simulations of fixed patterning in Figures 6.9 and 6.10. However, it requires at least true 9 or, preferably, 10 bit digitization to overcome fixed patterning.

Using the Hough transform decoding scheme, a fast, high performance ground based detector could be built using 12 bit fixed reference ADCs, e.g. the THC 1201 (TRW, 1991) which is a 10 mega samples per second device that consumes 4.5 W. While power budgets for detectors are so low or until high reliability, radiation tolerant, low power ADCs with more than 8 bits are available, SPAN (and any other charge division readout that uses charge or time measurement) is unsuitable for a high speed, large format, high resolution, satellite based detector.

Bibliography

Adams, J. & Manley, B. W., 1966, *IEEE Trans. Nucl. Sci.* **NS-13**, 88.

Allemand, R. & Thomas, G., 1976, *Nucl. Instrum. Meth.* **137**, 141.

Allington-Smith, J. R. & Schwarz, H. E., 1984, *Q. Jl. R. astr. Soc.* **25**, 267.

Allison, J., 1985, *Nucl. Instr. Meth.* **A 236**, 284..

Allison, J., Ashton, P., Baines, J. T. M., Barlow, R. J., Chrin, J. T. M., Davies, O. W., Duerdoth, I. P., Hinde, P. S., Banks, J. N., Hughes-Jones, R. E., Lafferty, G. D., Loebinger, F. K., Macbeth, A. A., Moss, M. W., Murphy. P. G., O'Dowd, A., Pawley, S. J. & Stephens, K., 1991, Proc. 2nd. London Position Sensitive Detectors, London ,U.K. 1990, *Nucl. Instr. and Meth.* **A310**, 527.

Anacker, D. C. & Erskine, J. L., *Rev. Sci. Instrum.*, **62**, 1247, 1991.

Analog Devices, 1988, *Data Conversion Products Databook*, Norwood, MA, USA, 3-339.

Arfken, G., 1970, *Mathematical Methods for Physicists* 2nd. Ed., Academic Press, New York, pg. 725 and pp. 737-741.

Authinarayanan, A. & Dudding, R. W., 1976, Photo-Electronic Image Devices, Proc. Third. Symposium, London, 1975, *Advances in Electronics and Electron Physics* **40A**, 167.

Barstow, M. A. & Sansom, A. E., 1990, *SPIE* **1344**, 244.

Baum, W. A., 1966, Photo-Electronic Image Devices, Proc. Third. Symposium, London, 1965, *Advances in Electronics and Electron Physics* **22A**, 617.

Bendat, J. S. & Piersol, A. G., 1966, *"Measurement and Analysis of Random Data"*, John Wiley & Sons, New York, pg. 15.

Ben-Tzvi, D. & Sandler, M. B., 1990, *Pattern Recognition Letters*, **11**, 167.

Bevington, P. R., 1969, *"Data Reduction and Error Analysis for the Physical Sciences"*, McGraw-Hill, New York, pp 187-203.

Bray, N., 1992, *"Comparison of MIC and SPAN Electronics for Engineering into the Space Environment"*, MSSL Optical Monitor Technical Report, XMM-OM/MSSL/RV/004.

Breeveld, A. A., 1992, *Ph. D. Thesis*, University of London, *in preparation.*

Breeveld, A. A., Edgar, M. L., Smith, A., Lapington, J. S. & Thomas, P. D., 1992a, Proc. 4th. Int. Conf. Synchrotron Radiation Instrum., Chester, U.K., 1991, *Rev. Sci. Instrum.* **63 Part II**, 673.

Breeveld, A. A., Edgar, M. L., Lapington, J. S. & Smith, A., 1992b, *SPIE*, **1743**, 315.

Breeveld, A. A. & Thomas, P. D., 1992, *Proc. Int. Symp. Photon Detectors for Space Instrumentation*, ESA Special Publication **SP-356**, *in press.*

Bronshteyn, I. M., Yevdokimov, A. V., Stozharov, V. M., & Tyutikov, A. M., 1980, *Radio Eng. Electro. Phys.* **24**, 150.

Bryant, D. A. & Johnstone, A. D., 1965, *Rev. Sci. Instrum.* **36**, 1662.

Carter, M. K., Cutler, R., Patchett, B. E., Read, P. D., Waltham, N. & van Breda, I. G., 1990, *SPIE* **1235**.

Carter, M. K., Patchett, B. E., Read, P. D., Waltham, N. & van Breda,I. G., 1991, Proc. 2nd. London Position Sensitive Detectors, London ,U.K. 1990, *Nucl. Instr. and Meth.* **A310**, 305.

Carter, M. K., 1991a *"Data Processing Requirements in a Centroiding Photon Counting System", private communication.*

Carter, M. K., 1991b, *private communication.*

Chapman, H. N., Nugent, K. A. & Wilkins, S. W., 1991, *Rev. Sci. Instrum.* **62**, 1542.

Chappell, J. H. & Murray, S. S., 1989, *SPIE* **1159**, 460.

* Briel, U., Brinkman, A. C., Ellwood, J. M., Fraser, G. W. de Korte, P. A. J., Lemmon, J., Lumb, D. H., Manzo, G., Peacock, A. Pfeffermann, E., Rocchia, R., & Westergard, N. 1987, "The High Throughput X-Ray Spectroscopy Mission, Report of the Instrument Working Group" ESA Special Publication, SP 1092, 49.

Cho, D. J. & Morris, G. M., 1988,*SPIE* **976**, 172.

Cho, D. J., 1989, *Ph.D. Thesis*, University of Rochester.

Clampin, M. & Edwin, R. P., 1987, *Rev. Sci. Instrum.* **58**, 167.

Clampin, M., Crocker, J., Paresce, F. & Rafal, M., 1988, *Rev. Sci. Instrum.* **59**, 1269.

Corben, H. C. & Stehle, P., 1974 *"Classical Mechanics"* 2nd. Ed., Robert E, Krieger, New York, pg. 140.

Culhane, J. L., 1991, Proc. 2nd. London Position Sensitive Detectors, London, U.K. 1990, *Nucl. Instr. and Meth.* **A310**, 1.

deBoor, C., 1970 , "CADRE: An Algorithm for Numerical Quadrature", in *Mathematical Software*, edited by John R. Rice, Academic Press, Orlando, Florida, pp. 417—442.

deBoor, C., 1971 , "On Writing an Automatic Integration Algorithm", in *Mathematical Software*, edited by John R. Rice, Academic Press, Orlando, Florida, pp. 201—209.

Eberhardt, E. H., 1977, *Appl. Opt.* **16**, 2127.

Eberhardt, E. H., 1979, *Appl. Opt.* **18**, 1418.

Eberhardt, E. H., 1980, ITT Electro-Optical Products Division, Technical Note, **No 127**, ITT Tube and Sensor Laboratories, Fort Wayne, Indiana.

Eberhardt, E. H., 1981, *IEEE Trans. Nucl. Sci.* **NS-28**, 712.

Edgar, M. L., Kessel, R., Lapington, J. S. & Walton, D. M., 1989 *Rev. Sci. Instrum.* **60**, 3673.

Edgar, M. L., Lapington, J. S. & Smith, A., 1992a, Proc. 4th. Int. Conf. Synchrotron Radiation Instrum., Chester, U.K., 1991, *Rev. Sci. Instrum.* **63 Part II**, 816.

Edgar, M. L., Smith, A. & Lapington, J. S., 1992b, *SPIE*, **1743**, 283.

Evans, D. S., 1965, *Rev. Sci. Instrum.* **36**, 375.

Feller, W. B., 1991, Proc. 2nd. London Position Sensitive Detectors, London ,U.K. 1990, *Nucl. Instr. and Meth.* **A310**, 249.

Firmani, C., Ruiz, E., Bisiachi, G. F., Salas, L., Paresce, F. & Carlson, C. W., 1984, *Astron. Astrophys.* **134**, 251.

Colson, W. B., Mc Pherson, J. & King, F. T., 1973, *Rev. Sci. Instrum.* **44**, 1694.

Fordham, J. L. A., Bone, D. A., Read, P. D., Norton, T. J., Charles, P. A., Carter, D., Cannon, R. D. & Pickles, A. J., 1989, *Mon. Not. R. astr. Soc.* **237**, 513.

Fordham, J. L. A., 1990, *private communication.*

Fraser, G. W. & Mathieson, E., 1981, *Nucl. Instrum. Meth.* **180**, 597.

Fraser, G. W., Pearson, J. P., Smith, G. C., Lewis, M. & Barstow M. A., 1983, *IEEE Trans. Nucl. Sci.* **NS-30**, 455.

Fraser, G. W., 1989, *"X-ray Detectors in Astronomy"*, Cambridge University Press, Cambridge, pp 169-170.

Fraser, G. W., Lees, J. E., Pearson, J. F. & Barstow, M. A., 1991a, Proc. 2nd. London Position Sensitive Detectors, London ,U.K. 1990, *Nucl. Instr. and Meth.* **A310**, 292.

Fraser, G. W., Pain, M. T., Lees, J. E. & Pearson, J. F., 1991b, *Nucl. Instr. Meth.* **A306**, 247.

Fraser, G. W., Pain, M. T. & Lees, J. E.,1992, preprint.

Friedman, P. G., Martin, C. & Rasmussen, A. 1990, *SPIE* **1344**, 183.

Floryan, R. F. & Johnson, C. B., 1989, *SPIE* **1072**, 30.

Gatti, E., Oba, K. & Rehak, P., 1983, *IEEE Trans. Nucl. Sci.*, **NS-30**, 461.

Gear, C. W., 1969 *Proc. Skytop Conf. USAEC Conf. No.670301*,. 552, (as quoted in Fraser, 1989).

GEC Plessey, 1990, *"Digital Signal Processing IC Handbook"*, Chenney Manor, Swindon, Wiltshire, UK, 73.

Geesman, H., Hanne, G. F., Stauffer, A. D. & Stauffer, J. A., 1991, *Nucl. Instr. and Meth.* **A307**, 413.

Goodrich, G. W. & Wiley, W. C, 1961, *Rev. Sci. Instrum.* **32**, 846.

Goodrich, G. W. & Wiley, W. C, 1962, *Rev. Sci. Instrum.* **33**, 761.

Guest, A. J., 1971, *Acta Electronica* **14**, 79.

Guest, A. J., 1978, *Philips Research Laboratory Annual Review*, 15.

Guest, A. J., 1988, *Proc. of SID* **29**, 193.

Guggenheimer, H. W., 1977, *"Differential Geometry"*, Dover, New York, pp 11-12.

Hamamatsu, 1987, *Technical Data Sheet*, **T-114**, Hammamtsu Photonics, Electron Tube Division, Iwata-gun, Shizuoka-ken, Japan.

Harris, L. A., 1971, *Rev. Sci. Instrum.* **42**, 987.

Hatfield, J. V., Burke, S. A., Comer, J., Currel, F., Goldfinch, J. & York, T. A., 1992, *Rev. Sci. Instrum.* **63**, 235.

Hill, G. E., 1976, Photo-Electronic Image Devices, Proc. Third. Symposium, London, 1975, *Advances in Electronics and Electron Physics* **40A**, 153.

Hynecek, J., 1988, *IEEE Trans. Electron. Device* **ED-35**, 646.

Jelinsky, P., 1979, *"The Size and Distribution of Electron Clouds from an MCP Detector", private communication.*

Kawakami, H., 1992, *private communication.*

Keller, H., Klingelhofer, G. & Kankeleit, E., 1987, *Nucl. Instrum. Meth.* **A258**, 221.

Kessel, R., 1988, *private communication.*

Klinowski, J., 1990, *Nature* **346**, 509.

Knibbeler, C. L. C. M., Hellings, G. J. A., Maaskamp, H. J., Ottevanger, H. & Brongersma, H. H., 1987, *Rev. Sci. Instrum.* **58**, 125.

Koike, M. & Hasegawa, K., 1988, Nucl. Instr. and Meth. **A272**, 840.

Koshida, N. & Hosobuchi, M., 1985, *Rev. Sci. Instrum.* **56**, 1329.

Koshida, N., 1986, *Rev. Sci. Instrum.* **57**, 354.

Kowalik, J. & Osborne, M. R., 1968, *"Methods for Unconstrained Optimization Problems"*, American Elsevier, New York.

Kume, H., Muramatsu, S. & Iida, M., 1986, *IEEE Trans. Nucl. Sci.* **NS-33**, 359.

Lampton, M., & Paresce, F., 1974, *Rev. Sci. Instrum.* **45**, 1098.

Lampton, M., & Malina, R. F., 1976, *Rev. Sci. Instrum.* **47**, 1360.

Lampton, M. & Bixler, J., 1985, *Rev. Sci. Instrum.* **56**, 164.

Lapington, J. S., Kessel, R. & Walton D. M., 1988, *Nucl. Instr. Meth.* **A273**, 663.

Lapington, J. S. & Edgar, M. L., 1989, *Proc. SPIE* **1159**, 565.

Lapington, J. S., Breeveld, A. A., Edgar, M. L., Tandy, J. A. & Trow, M. W., 1990, *Proc. SPIE* **1344**, 324.

Lapington, J. S., Breeveld, A. A., Edgar, M. L. & Trow, M. W., 1991 Proc. 2nd. London Position Sensitive Detectors, London ,U.K. 1990, *Nucl. Instr. and Meth.* **A310**, 299.

Lapington, J. S., Breeveld, A. A., Edgar, M. L. & Smith, A., 1992, *SPIE*, **1743**, 303.

Lombard, F, J., & Martin, F., 1961, *Rev. Sci. Instrum.* **32**, 200.

Loty, C., 1971, *Acta Electronica* 14, 107.

Lyons, A., 1985, *J. Phys. E.: Sci. Instrum.* **18**, 127.

Mc Calden, A. J., 1992, *Proc. Int. Symp. Photon Detectors for Space Instrumentation*, ESA Special Publication **SP-356**, *in press.*

Martin, C., Jelinsky, P., Lampton, M., Malina, R. F. & Anger, H. O., 1981, *Rev. Sci. Instrum.* **52**, 1067.

Martin, C. & Bower, S., 1982, *Appl. Opt* **21**, 4206.

Massey, H. S. W. & Kestelman, H., 1964, *"Ancillary Mathematics" 2nd ed*, Pitman & Sons, London, 261, 523, 847.

Mathieson, E., Smith, G. C. & Gilvin, P. J., 1980, *J. Phys. E: Sci. Instrum.* **13**, 792.

Mc Clintock, W. E., Barth, C. A., Steele, R. E., Lawrence, G. M. & Timothy, J. G., 1982, *Appl. Opt.* **21**, 3071.

McKee, B. T. A., Duffy, A. G., Feller, W. B. & Stewart, A. T., 1991, Proc. 2nd. London Position Sensitive Detectors, London ,U.K. 1990, *Nucl. Instr. and Meth.* **A310**, 256.

Mc Kinley, M. S., 1986, *private communication.*

Micro Power Systems, 1989, *Full Line Catalog*, Santa Clara, CA, USA, 2-50.

Murtagh, F. & Heck, A. , 1987, *"Multivariate Data Analysis"* D. Riedel, Dodrecht, Chapter 4.

Nakamura, T. & Matsumoto, K., 1992, *preprint.*

Nartallo Garcia, R., 1990, *M.Sc. Thesis*, University of London.

Neischmidt, E. B., Lawrence, R. S. & Gentillon, C. D., 1982, *IEEE Trans. Nucl. Sci.* **NS-29**, 196.

Nicoli, A.M., 1985 , M.S. Thesis, Massachevbetts Institute Technology.

Norton, T. J., 1990, *Ph.D. Thesis*, University of London.

Norton, T. J., Airey, R. W., Morgan, B. L., Fordham, J. L. A. & Bone, D. A., 1991, *Conf. on Photoelectonic Image Devices*, London, 1991, IOP Publishing Ltd., 97.

Oba, K. & Rehak, P., 1981, *IEEE Trans. Nucl. Sci.* **NS-28**, 683.

OPAL Collaboration, 1991, *Nucl. Instr. Meth.* **A305**, 275.

Papaliolos, C., Misenson & Ebstein, 1985, *Appl. Opt.* **24**, 287.

Pearson, J. F., Fraser, G. W. & Whitley M. J., 1987, *Nucl. Instr. Meth.* **A258**, 270.

Pearson, J. F., Lees, J. E., & Fraser, G. W., 1988, *IEEE Trans. Nucl. Sci.* **NS 35**, 520.

Phillips, A., 1992, *Ph. D. Thesis*, University of London, *in preparation.*

Pratt, W. K., 1978, *"Digital Image Processing"*,
John Wiley & Sons, New York.

Press, W. H., Flannery, B. P., Teukolsky, S. A & Vetterling W. T., 1986,
"Numerical Recipes, The Art of Scientific Computing", Cambridge University Press, Cambridge.

Purshke, M., Nuxoll, W., Gaul, G. & Santo, R., 1987, *Nucl. Instrum. Meth.* **A261**, 537.

Rager, J. P., Renaud, J. F. & Tezenas du Montcel, V., 1974, *Rev. Sci. Instrum.* **45**, 927.

Rasmussen, A. & Martin, C., 1989, *SPIE* **1159**, 538.

Randall, R. P., 1966, Photo-Electronic Image Devices, Proc. Third. Symposium, London, 1965, *Advances in Electronics and Electron Physics* **22A**, 87.

Read, P. D., 1990, *private communication.*

Read, P. D., van Breda, I. G. & Norton, T. J., 1990, *Proc. SPIE* **1235**,305.

Richter, L. J. & Ho, W., 1986, *Rev. Sci. Instrum.* **57**, 1469.

Rodgers, A. W., King, D., Conroy, P. & Harding, P., 1988, *preprint.*

Sams, B. J. III, 1991, *Rev. Sci. Instrum.* **62**, 595.

Samson, J. A. R., 1984, *Nucl. Instr. and Meth.* **A222**, 215.

Schecker, J. A., Schauer, M. M., Holzschetter, K. & Holzschetter, M. H, 1992, *Nucl. Instrum. Meth.* **A320**, 556.

Schmidt, K. C. & Hendee, C. F., 1966, *IEEE Trans. Nucl. Sci.* **NS 13**, 100.

Sharma A. & Walker, J. G., 1989, *Quant. Opt.* **1**, 11.

Sharma A. & Walker, J. G., 1990, *SPIE* **1235**, 474.

Sharma A., 1991, *Ph.D Thesis*, University of London.

Sharma A. & Walker, J. G., 1992, *Rev. Sci. Instrum., in press.*

Siegmund, O. H. W., Coburn, K. & Malina, R. F., 1985, *IEEE Trans. Nucl. Sci.* **NS 32**, 443.

Siegmund, O. H. W., Lampton. M. L., Chakrabarti, S., Vallerga, J., Bower, S. & Malina, R. F., 1986a, *SPIE* **1159**, 476.

Siegmund, O. H. W., Lampton. J., Bower, S. & Malina, R. F., 1986b, *IEEE Trans. Nucl. Sci.* **NS 33**, 724.

Siegmund, O. H. W., 1989, *Proc. SPIE* **1072**, 111.

Siegmund, O. H. W., Lampton. M. L. & Raffani, R., 1989a, *SPIE* **1159**, 476.

Siegmund O. H. W., Chakrabarti, S., Cotton, D. M. & Lampton, M., 1989b, *IEEE Trans. Nucl. Sci.* **NS 36**, 916.

Siegmund, O. H. W., Cully, S., Warren, J., Gaines, G. A., Priedhorsky, W. & Bloch, J., 1990, *Proc. SPIE* **1344**, 346.

Siegmund, O. H. W. & Stock, J., 1991, *SPIE* **1549**, 81.

Slater, D. C. & Timothy, J. G., 1991, *SPIE* **1549**, 68.

Smith, A. D. & Allington-Smith, J. R., 1986, *IEEE Trans. Nucl. Sci.* **NS-33**, 295.

Smith A., Kessel, R., Lapington, J. S. & Walton, D. M., 1989, *Rev. Sci. Instrum.* **60**, 3509.

Smith, A. & Bavdaz, M., 1992, Proc. 4th. Int. Conf. Synchrotron Radiation Instrum., Chester, U.K., 1991 *Rev. Sci. Instrum.* **63 Part II**, 689.

Smith, P. J., 1991, *private communication.*

Sobottka, S. E. & Williams, M. B., 1988, *IEEE Trans. Nucl. Sci.* **NS 35**, 348.

Stümpel, J. W., Sanford, P. W. & Goddard, H. F., 1973, *J. Phys. E: Sci. Instrum.* **6**, 397.

Tanaka, N., Hashimoto, S., Shinohara, M., Sugawa, S., Morishita, M., Matsumoto, S, Nakamura, Y. & Ohmi, T., 1990, *IEEE Trans. Electron. Device* **ED-37**, 964.

Timothy, J. G., 1974, *Rev. Sci. Instrum.* **45**, 834.

Timothy, J. G. & Bybee, R. L., 1975a, *Appl. Opt.* **14**, 1632.

Timothy, J. G. & Bybee, R. L., 1975b, *Rev. Sci. Instrum.* **46**, 1615.

Timothy, J. G., 1981, *Rev. Sci. Instrum.* **52**, 1131.

Timothy, J. G., Mount, G. H. & Bybee, R. L., 1981 *IEEE Trans. Nucl. Sci.* **28**, 689.

TRW, 1991, *"Data Converters - DSP Products Databook"*, La Jolla, CA, USA, A-163, A-287 and F-65.

Trap, H. J., L., 1971, *Acta Electronica* **14**, 41.

Turner, M. J. L., Smith, A. & Zimmerman, 1981, *Sp. Sci. Rev.*, **30**, 513.

Vallerga, J. V., Kaplan. G. C., Siegmund, O. H. W., Lampton, M., & Malina, R. F., 1989, *IEEE Trans. Nucl. Sci.* **NS 36**, 881.

Vallerga, J. V., Siegmund, O. H. W., Vedder, P. W.& Gibson, J. L., 1991, Proc. 2nd. London Position Sensitive Detectors, London ,U.K. 1990, *Nucl. Instr. and Meth.* **A310**, 317.

Veaux, J., Cavailler, C., Gex, JP., Hauduceour, A. & Hyvernage, M., *Rev. Sci. Instrum.* **62**, 1562.

Washington, D., Duchenois, V., Polaert, R. & Beasley, R. M., 1971, *Acta Electronica* **14**, 201.

Weast, R. C., *"Handbook of Chemistry and Physics"*, 47th. Ed.,
The Chemical Rubber Co., Cleveland, 1966.

Wilkins, S. W., Stevenson, A. W., Nugent, K. A, Chapman, H. & Steenstrup, S., 1989, *Rev. Sci. Instrum.* **60**, 1026.

Williams, M. B. & Sobottka, S. E., 1989, *IEEE Trans. Nucl. Sci.* **NS 36**, 227.

Wiza, J. L., Henkel, P. R. & Roy, R. L., 1977, *Rev. Sci. Instrum.* , **48**, 1217.

Wiza, J. L., 1979, *Nucl. Inst. Meth* **162**, 587.

Yamaguchi, N., Aoki, S. & Miyoshi, S., 1987, *Rev. Sci. Instrum.* **58**, 43.

Yusa, A., Nishizawa, J., Imai, M., Yamada, H.,Nakamura, J., Mizoguchi, T., Ohta, Y. & Takayama, M., 1986, *IEEE Trans. Electron. Device* **ED-33**, 735.

Zombeck, M. V.,& Fraser, G. W., 1991, *SPIE* **1549**, 90.

Acknowledgements

I would like to express my sincere appreciation to Prof. Len Culhane for the opportunity to carry out the research for this thesis, which I know caused him not inconsiderable inconvenience then and since. I would also like to thank him for being my supervisor and for all his help and encouragement throughout my time at MSSL.

I gratefully acknowledge the award of a Dean's Studentship by University College London.

I also wish to thank the members of the Detector Physics Group for their support, encouragement and friendship: Alice Breeveld, Hajime Kawakami, Jon Lapington, Alan Smith and especially Matt Trow. And I would like to particularly thank those who suffered terribly during the proof reading.

I would like to thank the members of my panel, Prof. Alan Johnstone and Dr. Keith Mason, for their advice and assistance, particularly in two hopeless, though different, causes. I would also like thank the following people for useful discussions and/or making unpublished material available: Martin Carter and Pete Read form Rutherford Appleton Lab, Abhay Sharma from King's College, Tim Norton from Imperial College and George Fraser from The University of Leicester.

I would like to thank the ladies in the office, particularly Ros and Libby, the gentlemen in the workshop and in the electronic engineering group, especially Gary Legge, Alec McCalden, Kerrin Rees, Jason Tandy and Steve Welch. And I'm happy to express gratitude to all those who showed me many personal kindnesses during my stay in England, in particular Eva Alam, Khalid al Janabi, Chris Alsop, Mark Birdseye, Charon Birket, the Breevelds, Francisco Carrera, the Fosters, the Kessels, Ronghui Lui, Dave Rodgers, the Rosens, Mike Tidy, the Waltons (especially for the sandwiches), Dave Wonnacott, the staff and patrons of the "King's Head" and "The Live and Let Live" and especially Ata Etamadi.

Finally, I wish to thank my fellow students during my stay here, for their friendship and encouragement: Steve Broadmeadow, Ady James, Ramon Nartallo Garcia, Vito Graffagnino, John Mittaz, George Papatheodorou, Liz Puchnarewicz, Gavin Ramsey, Phil Smith, Lee Sproats, Sarah Szita, and my fellow non-persons, Mark Garlick, Chris Jomaron, Sri Moorthy and Andy Phillips. Good luck to those still going and I hope that your own private calvary will not be as protracted as was mine.